Cylinder Liner Bore Form And Distortion Measurements Using Ultrasound

Sushil Simkhada

A thesis submitted in partial fulfilment of the requirements for the degree of

Doctor of Philosophy

The University of Sheffield

Faculty of Engineering

Department of Mechanical Engineering

Submission Date

Winter 2021

This thesis is dedicated to my family and my friends for being a great source of inspiration.

Abstract

Piston ring conformability to the cylinder liner wall during combustion, to form a seal for combustion pressure, is a critical parameter that dictates the efficiency of an internal combustion engine. Improving the ring-liner conformability would enable a potential reduction in friction through reduced contact forces, and thus reduce wear. It would also reduce the fuel consumption and the oil carryover, reducing the unburnt hydrocarbon particles in the exhaust, leading to reduction in harmful emissions. Unburnt hydrocarbon particles can also have a detrimental impact on the catalyst system, through its detergent constituents.

Conformability is affected by various factors, among which the distorted bore form and the initial bore form of the cylinder liner are major contributors. Attributes that control bore distortion are the machined profile of the bore, the pressure applied by cylinder head clamping bolts, the temperature distribution around the bore, and the dynamic loading during the combustion process.

The thesis presents the outcome of feasibility studies which evaluated the use of ultrasound through sensors that monitor the form of cylinder liner bores during the honing process, and sensors that measure the extent of bore distortion in operational engines.

Currently, bore form measurement is carried out using air gauges that give an indication of whether the bore diameter is within or outside 10 µm. The bore form quality assurance process still requires an additional step during manufacturing of the engine. The bore distortion measurements in running engines are, currently, typically performed using sensors mounted on the piston. This requires significant modifications to various engine components, while the distortion measurement obtained consists of high errors that result from difficulty in knowing the exact position of the piston.

The design and evaluation of ultrasonic sensors to be used for the bore form measurement in honing machines is presented. Several air-coupled ultrasonic probes working at 0.7MHz-1.5MHz were manufactured, costing under £20, and with transmission loss of 74dB and bandwidth of 20% (excited using 5-10 cycle sine waves). The bore form of a cylinder liner was measured using an ultrasonic probe, in a custom-built rig to mimic the honing process. The measurements were conducted at spindle speeds of 60RPM and 200RPM, and were found to be within ±3.48µm and ±3.79µm of the reference measurements, respectively.

A method to measure bore distortion, in-situ, using ultrasonic transducers bonded to the outer surface of cylinder liners, is presented. The impact of temperature variation on wave propagation velocity of bulk (through-thickness) and surface waves were investigated. The proposed method uses local temperature measurement to mitigate against the impact of temperature variation. The error in velocity measurement using the proposed method was around 0.2%.

Acknowledgements

I would like to take this opportunity to thank Prof. Rob Dwyer-Joyce for his support, supervision, encouragement, guidance, as well as at times for his patience. Without his help this thesis would not have been possible. I would also like to thank Dr Bryn Littlefair and Dr Tom Slatter for their supervision, support, and guidance. I will forever be grateful for the opportunity offered to me and for what I have learned during the process.

I would like to thank Dr Robin Mills, Dr Xiangwei Li, Dr Andy Hunter, and Dr Henry Brunskill for their advice and assistance in overcoming various challenges in experimental work, as well as the software and programs they have designed and made available to the Leonardo Centre for Tribology.

I would like to thank Mr Dave Butcher and Mr Luke Callaghan for their technical support, especially their suggestions for the design of the two rigs. I would equally like to thank Mr Jack Johnson for evaluating and suggesting changes for the design of the in-situ bore form measurement rig.

I would like to thank my friends in the tribo-acoustics group. They have all been of great support, both in and out of the sphere of university work. Specially, I would like to thank Mr David Fort and Mr Jack Rooke for their time in discussing the project as well as pointing me to helpful material.

I would like to send my special thanks to my friend Himesh Bilimoria for his support and mentorship. My friend Rabin Bhatta for his words of encouragement. My cousin Dilisha Simkhada for her support and mentorship. My uncles and aunts for accommodating me when I've been in need, for their positive words of encouragement and for general love and support.

Finally, I would like to thank my brother, my mum and my dad, for their support and encouragement throughout.

Contents

Nomenclature

σ_{ij}	Stress tensor
B	Wave number
s	Quantised signal
Δ	Sampling period
A	Transducer surface area
A_{min} ,A_{max}	Minimum and maximum amplitudes
B	Bulk modulus
c, c_1, c_2	Wave propagation velocity
c_0	Wave velocity
C_0	Transducer capacitance
C_k	Discrete Fourier transform of s_k
C_L	Longitudinal wave propagation velocity
C_T	Transverse wave velocity
d	Distance travelled by the wave
E	Young's modulus
e_m	Measurement error
F	Force
$f_{k,max}$	Maximum fundamental frequency
f_r	Resonant frequency
F_s	Sampling frequency
G	Shear modulus
i	Imaginary number
k	Wave number
k_{ijkl}	Stiffness tensor
l	Length
P	Pressure
P_-	Pressure in the backward direction (right to left)
p, p_i, p_r	Pressure
p_i, p_r, p_t	Incident, reflected and transmitted pressures
P_+	Pressure in the forward direction (left to right)
r	Distance travelled by the wave
R	Distance from the transducer
R, R_v	Pressure and velocity reflection coefficient
R_I	Intensity reflection coefficient
$r1$	Nearfield distance
s	Signal
s_k	Discrete inverse Fourier transform of C_k
t	Time
T	Time period, temperature
T	Pressure transmission coefficient
T_I	Intensity transmission coefficients
V^*	Complex phase velocity
K^*	Complex modulus
x	Displacement
Z	Impedance

z_1, z_2	Specific acoustic impedance
z_c	Characteristic impedance
z_s	Specific acoustic impedance
ν	Poisson's ratio
ρ	Density,
ρ_0	Initial density
C_{33}^{D}, C^{*D}_{33}	Free stiffness, complex free stiffness
C_{qr}	Correlation
D	Transducer diameter
E_R	Repeatability error
E_L	Linearity error
K	Compressibility, stiffness
N_I	Count channel i
N_A	Count channel a
Q	Loss factor
W	Windowing function
X_1, X_2, X_i	Error parameter
k_t^*	Complex electromechanical coupling factor
v	Particle velocity
zin	Input impedance
α	Attenuation coefficient
α_s	Attenuation coefficient of shear wave
α_l	Attenuation coefficient of longitudinal wave
γ	Phase change
δ_{ij}	Kronecker delta
$\varepsilon_{33}^{S}, \varepsilon^{*S}_{33}$	Clamped permittivity, complex clamped permittivity
ε_{ij}	Strain tensor
θ_{wheel}	Angular position of the code wheel
λ	Lamé elasticity constant
λ	Wavelength
μ	Lamé elasticity parameter
μ_{Xi}	Mean
σ_{Xi}	Standard deviation
ω	Angular frequency
ϕ	Phase of the wave

Abbreviations

1D	One Dimensional
2D	Two Dimensional
3D	Three Dimensional
BAW	Bulk Acoustic Wave
BDC	Bottom Dead Centre
ICE	Internal Combustion Engine
IML	Intermediate Matching Layer
LHS	Left Hand Side
OML	Outer Matching Layer
P2P	Peak to Peak
Rayls	Rayleigh
RHS	Right Hand Side
SAW	Surface Acoustic Wave
SNR	Signal to Noise Ratio
TDC	Top Dead Centre
TOF	Time of Flight
LDP	Laser Displacement Probe
DOF	Degree Of Freedom

1 Introduction

Reciprocating internal combustion engines (ICE) power applications ranging from large scale generators in electrical power stations, to ships, lawn mowers, and many other machines and devices. However, they are most well known for their use in automobile engines. At present, there are two main reciprocating ICEs in use in the automotive industry; spark ignition engines using petrol as fuel, and diesel engines using diesel as the fuel. The most popular design of reciprocating ICEs run in a four-stroke cycle, i.e., 2 complete revolutions of the engine to complete a full cycle. Figure 1-1 shows a cross-section of a four stroke Spark Ignition (SI) engine.

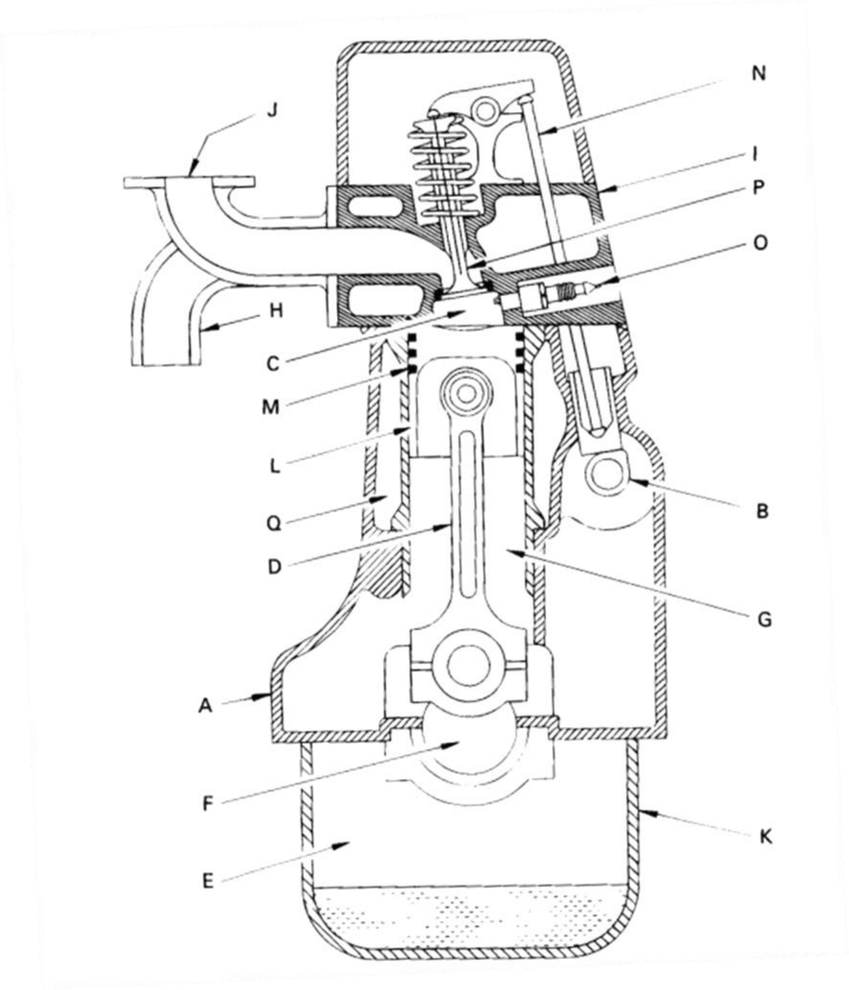

Figure 1-1: Cross-section of four stroke cycle SI engine showing engine components –(A) Block; (B) Camshaft; (C) Combustion chamber; (D)Connecting Rod; (E) Crankcase; (F) Crankshaft; (G) Cylinder; (H) Exhaust manifold; (I) Head; (J) Intake Manifold; (K) Oil Pan; (L) Piston; (M) Piston Rings; (N) Push Rod; (O) Spark Plug; (P) Valve; (Q) Water jacket. Figure adapted from Pulkrabek (1997).

Figure 1-2 shows a schematic of the combustion process inside a combustion chamber (region enclosed by the cylinder liner, piston, and the engine block head) undergone by an engine such as the one depicted in Figure 1-1.

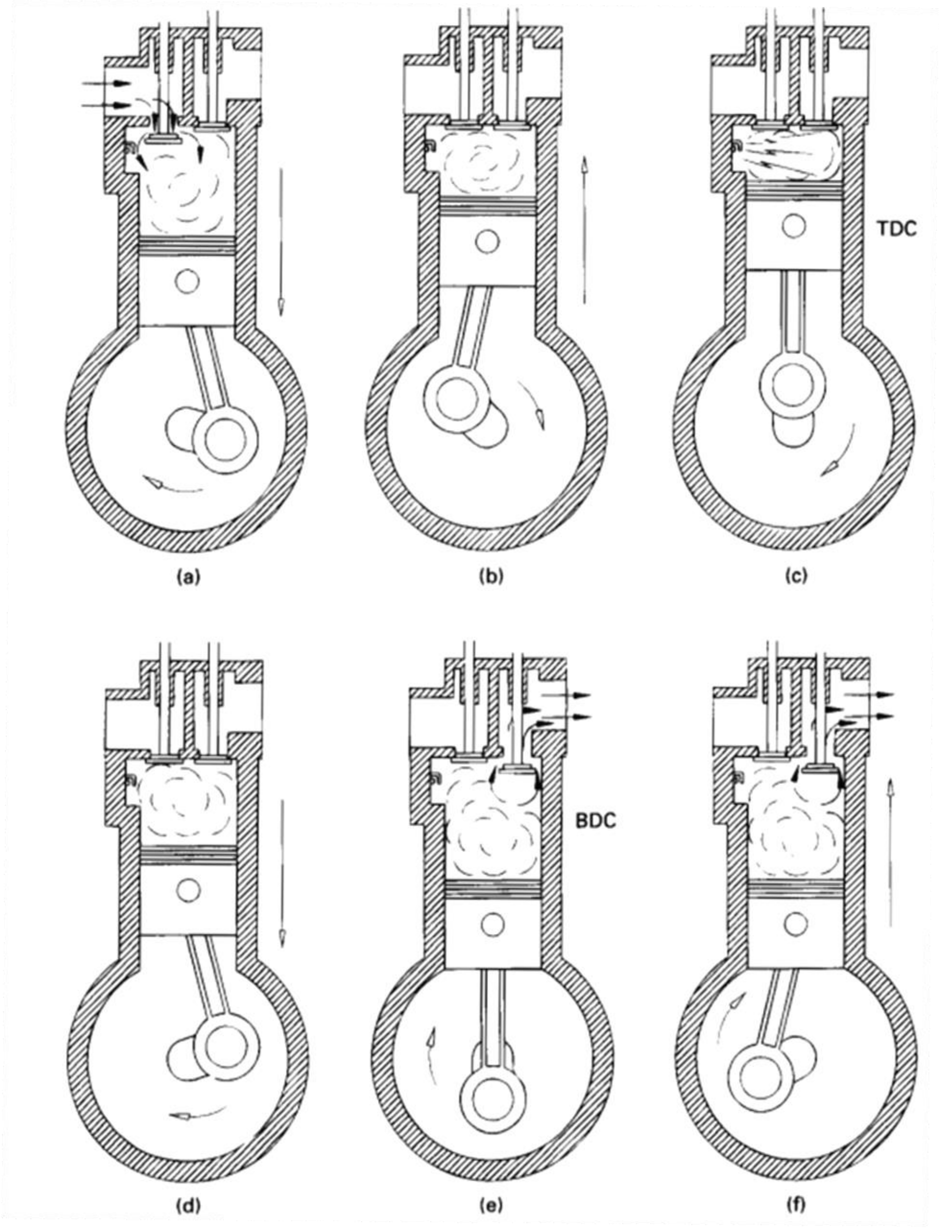

Figure 1-2: Four stroke SI Engine operating cycle. (a) Intake stroke; (b) Compression Stroke; (C) Combustion at or near Top Dead Centre (TDC); (d) Expansion Stroke; (e) Exhaust Blowdown as piston reaches close to the bottom dead centre (BDC); (f) Exhaust Stroke. Figure adapted from Pulkrabek (1997).

During the intake stroke, air is drawn in or forced in through the intake manifold using a turbo charger/super charger, while also being mixed with atomised fuel in the manifold, and subsequently injected into the engine through the intake valve (label 'P' in Figure 1-1).

This is followed by the compression stroke, where the piston compresses this fuel-air mixture. As the piston approaches its highest point (top dead centre (TDC)), the spark plug ignites the air-fuel mixture and causes it to combust. A diesel engine varies from the petrol engine in that it relies on just the pressure during compression to initiate the combustion.

The TDC reversal marks the start of the combustion stroke, where the combustion chamber experiences very high temperatures and pressure. The pressure inside the chamber can reach 18+ MPa (for diesel engine) and 10+MPa (for a gasoline engine) and a temperature of 2200°K for a four cylinder diesel engine (Kaźmierczak, 2004); an engine design that is commonly in use in family cars. The high pressure pushes the piston down, and the combustion chamber expands. Work done on the piston by the expanding fluid, through the motion of the connecting rod, turns the crankshaft. The crankshaft drives the powertrain, which in turn drives the wheels and moves the vehicle.

Once the piston reaches the bottom most point of the cylinder (BDC) — the furthest point from the cylinder head and the largest volume of the combustion chamber — the exhaust valve opens to let the gas inside the combustion chamber escape. This marks the start of the last stroke, known as the exhaust stroke. The gas by-product from combustion is pushed out from the cylinder as the piston moves towards the TDC. At TDC the intake stroke begins, and the cycle starts again. Readers are referred to books such as Engineering Fundamentals of the Internal Combustion Engine (Pulkrabek, 1997) for more detailed information on the workings of an engine.

1.1 Ring-Liner Conformability

The piston assembly consists of multiple piston-rings, typically three, where the top two are known as compression rings which help seal the combustion pressure. The second ring also cleans the liner surface of excess oil. The third (bottom) ring, known as the oil control ring, controls the supply of lubricant oil to the cylinder wall that is used to lubricate the contact between the piston skirt, piston rings and the cylinder wall. Figure 1-5 shows the piston rings on a piston.

The ring-liner conformability is defined as the degree to which the piston rings can change in shape to match the local shape of the cylinder bore profile. The piston rings are designed to maintain a good seal between the piston and the cylinder liner bore, such that maximum energy can be used to push the piston outwards. The sealing properties of the rings are activated by the combustion pressure that pushes the ring outwards on its attempt to escape from the gap between piston and liner; see Figure 1-3.

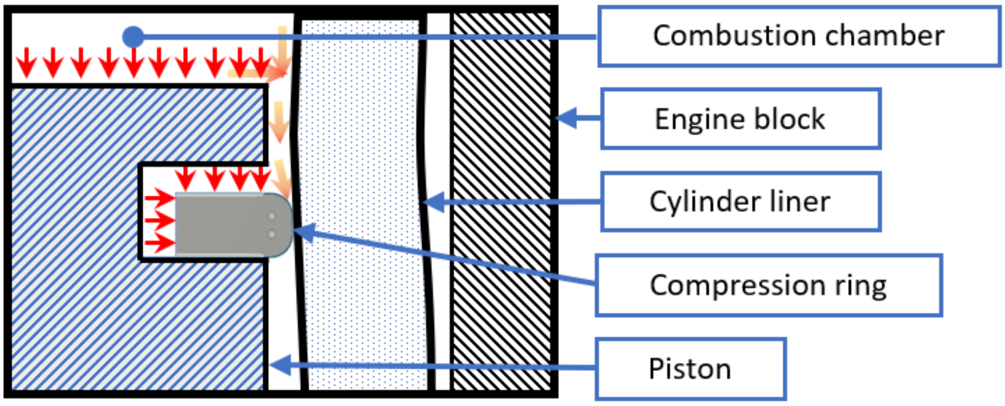

Figure 1-3: Top piston ring shown pushed down and outward by the pressure (red arrows) of combustion gasses (reddish-orange arrows), and in the process activating the sealing mechanism. Piston has blue 45° cross hatch, while liner is filled with blue dots.

The rings are subjected to radial and axial forces which causes them to deform in both in-plane (radial) and out of plane (axial) directions; the rings deform in-plane or out-of-plane, to a different degree along its angular position. While a stiffer ring would lead to lower undesired deformation, the higher stiffness also limits how easily the ring can conform around the bore. The final design of the piston rings finds it challenging to conform to higher order distortions due to high bending stresses required to overcome the elastic force stopping it from deforming; see Figure 1-4.

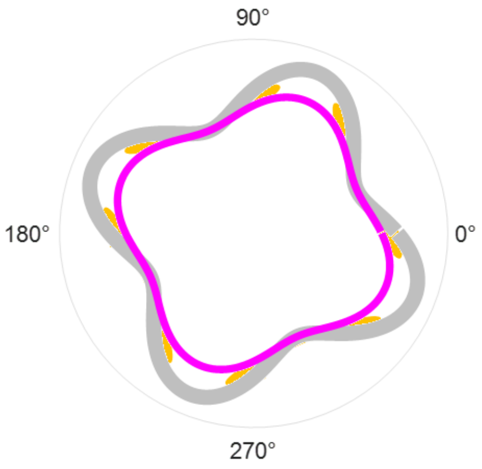

Figure 1-4: Schematic showing a liner in 4th order distortion and ring conforming partially around it. Regions of overlap are shown to depict the ring scraping the liner.

1.1 Bore Distortion and Ring-Liner Conformability

Figure 1-5 shows a schematic depicting the cross-section of an operational ICE. The block head clamping bolt force leads to non-uniform pressure distribution on the gasket and at the top end of the liner. This results in distortion of the liner bore. Other factors, such as the dynamic thermal and mechanical loading, also result in bore distortion. This leads to conformability issues between the bore and the piston rings. There are regions where a ring is not in contact with the bore and pressure leakage can occur. In other regions meanwhile the local pressure can be very high, leading to high frictional losses, or issues such as lubricant failure and the ring scrapes the bore surface. See Figure 1-4.

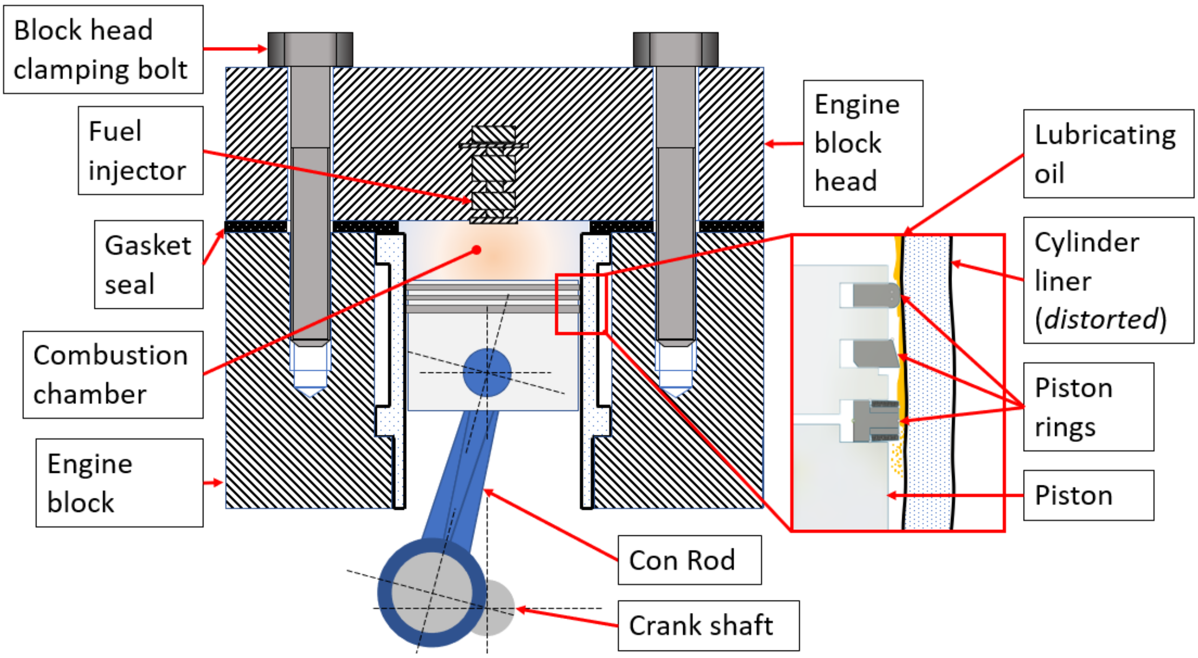

Figure 1-5: Schematic of an engine liner inside an engine showing the components that affect bore distortion.

Table 1-1 shows the various processes/mechanisms which contribute to bore distortion, while the engine is running.

Table 1-1: Parameters which contribute to bore distortion in an automotive engine and their magnitude. An email (B. Littlefair 2020, email communication, 2 October).

Type	**Distortion magnitude**	**Description**
Machining error	25µm (cylindricity)	Error in manufacturing processes such as bore honing
Clamping Load	20µm (≥4th order)	4/6 clamping head bolts, that are commonly used, result in higher clamping pressure nearer the location of the bolts.
Thermal expansion	30µm (3rd order)	Temperature variation in the inner face of the bore causes some areas to expand more, thereby causing the bore to distort.
Dynamic load	50µm (2nd order)	Small clearance between the piston skirt (lower part of the piston) and the cylinder liner allows small lateral and rotational motion of the piston during operation. The piston rings do not fully supress the motion, leading the piston to tilt, and change in the tilt angle, while in up and down motion.

1.2 Initial Bore Form and Ring-Liner Conformability

Figure 1-6 shows a sketch depicting the bore honing process used to machine the required cylinder liner bores' form in an automotive assembly line. The tolerance on the bore form is typically defined in terms of roundness, cylindricity, and straightness. The honing process is also used to achieve surface characteristics which retain a high quantity of lubricant and results in minimum friction between itself and the piston rings.

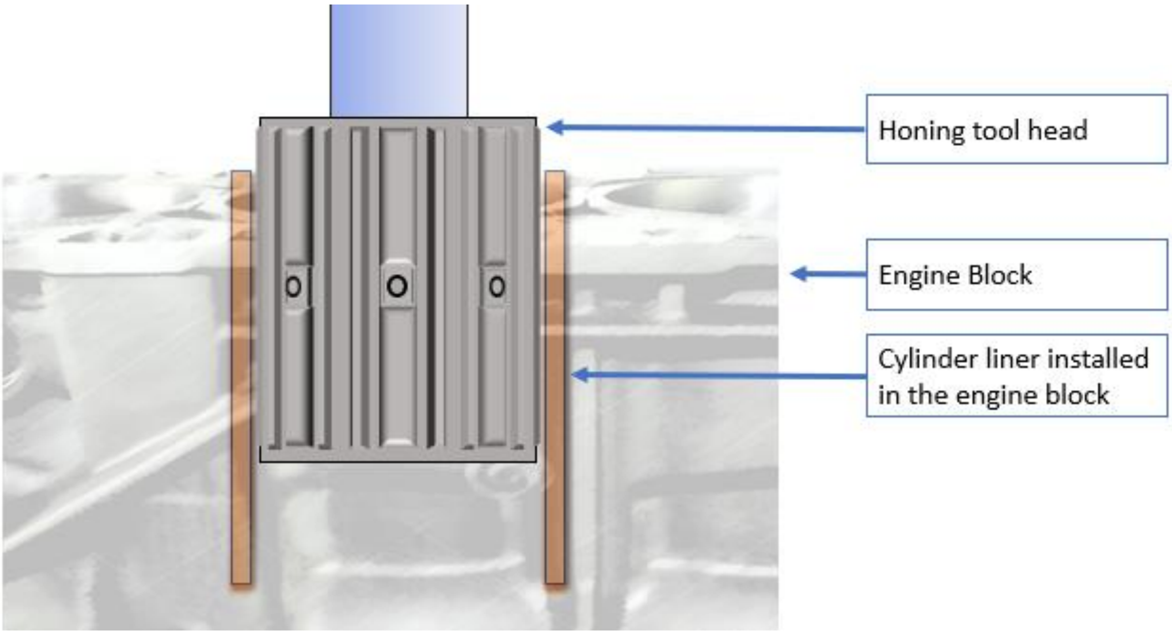

Figure 1-6: Mock-up sketch of the bore honing machine with a liner being honed.

The bore profile during honing is generally monitored using air gauges. However, errors in machining that are missed during the inspection process can lead to direct conformability issues or surface characteristics which increases frictional losses, during engine operation.

1.3 Industrial motivation

On average, only around 21.5% of the energy from combustion of fuel by ICEs is extracted for the use of driving automobiles. The remaining energy is attributed to combustion losses, overcoming air resistance, rolling friction losses, and frictional losses between various components within the driven parts inside an automobile. Figure 1-7 shows a breakdown of a passenger car engine consumption.

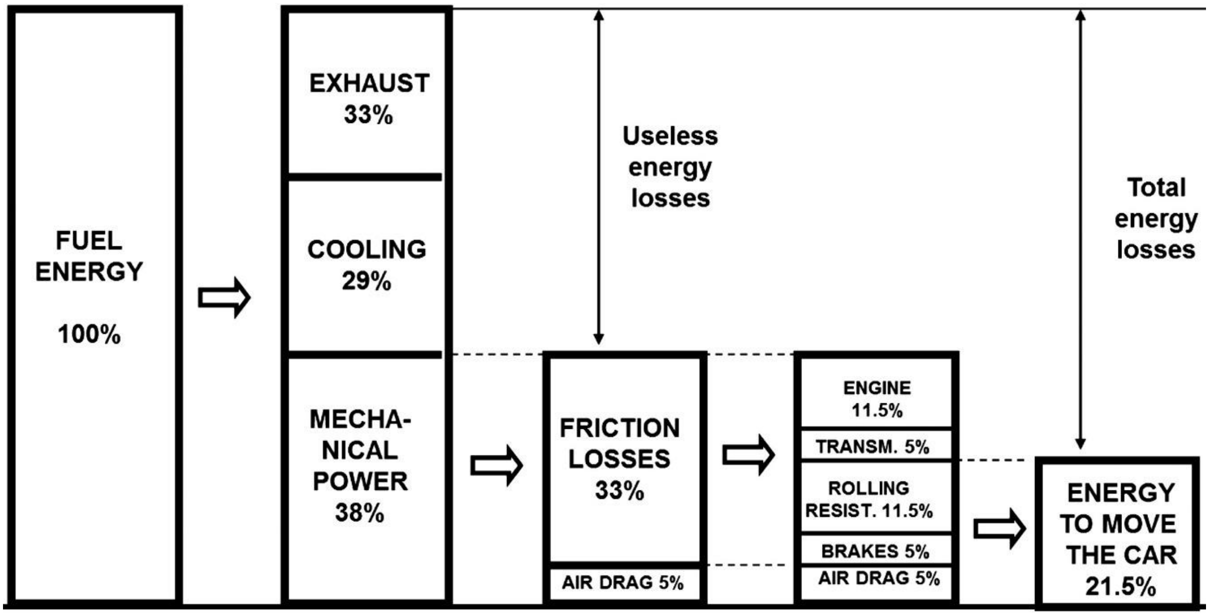

Figure 1-7: Breakdown of passenger car energy consumption. Figure obtained from Holmberg et al.(2012).

From the 11.5% loss within an ICE that is attributed to friction (Holmberg, Andersson and Erdemir, 2012), ~23% of the energy can be attributed to friction between piston and liner (Ghasemi, 2012). Therefore, it is evident that work on reducing the energy lost to conformability issues between the cylinder liner bore and the piston rings could lead to significant improvements.

The desire for making ICE more efficient has been a topic of interest since the invention of the first engine. At present, this area of research has mostly been fuelled by a desire to increase efficiency and reduce operational costs. Automotive manufacturers are also bound by government legislation to meet emission standards, in a bid to reduce the environmental impact from automobile vehicles. The legislations vary worldwide and are generally made more stringent every few years in a push to achieve net-zero greenhouse gas emissions. Thus, the work done to meet the legislation has been one of the driving factors for innovation within the automotive engine research sector.

With fossil fuels becoming scarcer, and predicted to last only for another 50 years or so, as well as considering the growing concern of the harmful impact of using fossils, there is an increasing interest in alternative means of driving automobiles. One of the main proponents is the electric vehicle. However, at present the electric vehicle (EV) technology and other technologies are still unable to meet most consumer demands. The current drawbacks of the EV technology include (but are not limited to): capacity of charge stored by the batteries used in the vehicles; speed at which the batteries are recharged; insufficient infrastructure (charging stations) to allow long distance journeys; and the capacity to produce the quantity required by the market. However, proposals have been made by governments around the world to invest in infrastructure to support EV, incentivising consumers to use EV, as well as investing in research and development and production of EV (Transitioning to zero emission cars and vans: 2035 delivery plan, The UK Government, 2021).

Vehicles using ICEs are still predicted to be in use for several more decades states Kalghatgi (2018). With major infrastructural challenges of mass adoption of electric vehicles in developing nations it is likely that the production and sale of ICE engines is still expected to continue for few decades. Furthermore, the research into improving the efficiency of the ICE is likely to continue, given their wide scale use in sectors such as marine, mining and farming, which all would benefit from more efficient engines.

The out-of-roundness of cylinder liner bores in honing machines are measured using air pressure-based gauges, to around ±10μm; an additional post gauging is required to ensure bore shape. Bore distortion are measured in static and dynamic running engines, for research and verification purposes. Static tests use instruments such as PAT inclinometers, or CMM machines; these are only feasible for use in static tests. Dynamic tests are performed using pistons with proximity sensors mounted on their ring land; slots for the sensors are machined on the piston. The setup for the dynamic tests is complex, while the distortion measurements are implicit as it requires predicting the piston tilt, axial position, and deformation.

Improving the accuracy of out-of-roundness measurements would reduce the frequency of machining errors, and could eliminate the post gauging stage to further save manufacturing cost. Establishing a less complex, explicit, bore distortion measurement method could lead to higher confidence in test results, while also reducing the cost of preforming such tests.

1.4 Aims and Objectives

The work reported within the thesis was in line with the industrial drive to reduce ring-liner conformability issues. The problem is tackled from the perspective of:

1. Reducing machining errors during the honing process by improving the existing measurement tool.
2. Developing a principal and technique that allows a bore distortion measurement to be performed.

The aims for the work conducted with these objectives can be outlined as follows:

1. To study the feasibility of using ultrasound to measure bore form during the honing process.
    a. Development of cost-effective air-coupled probes working in the MHz region that can be used for research purposes.
    b. Evaluation of the probe developed, to quantify its measurement accuracy. Building of a benchtop rig to enable the measurement to be carried out.
    c. Evaluation of the probe for in-situ bore form measurement of the bore of a cylinder liner. Design and build a rig which mimics the honing process for use in the in-situ measurement experiment.
2. To establish a method by which ultrasonic waves can be used in bore distortion measurements:
    a. Study the impact of variation in temperature of the cylinder liner on measurements conducted by bulk waves and surface waves.
    b. Develop a method to overcome the measurement uncertainty that the changing temperature of the cylinder liner would cause.

1.5 Thesis Layout

The thesis is written in a manner such that each experimental chapter (Chapters 4 to 8) can be read separately. Chapters 2, 3, 9 and 10 are generic and are relevant to the experimental chapters.

The theoretical background knowledge required for the use of ultrasonic waves as a measurement method of the bore form and cylinder liner distortion is presented in Chapter 2.

Chapter 3 outlines the various equipment used in the experimental setups. This includes the information on the design of the two rigs that were built. The chapter then outlines the experimental apparatus and their workings, and the generic methods in processing the acquired signal (ultrasonic waveform) to obtain measurement — generally the distance travelled by the wave from emission to detection.

Chapter 4 focuses on sensor development of high frequency air-coupled ultrasonic probes working at 0.7 to 1.5MHz, i.e. the sensor developed to perform bore form measurement. Current developments in the field of high frequency air-coupled ultrasonic transducers are reviewed to aid in finding a suitable design. The working characteristics of the probe are presented, and include the time domain waveform, the frequency domain response, and the bandwidth and insertion loss (measurement of efficiency).

Chapter 5 explores the various parameters of the probe design which could have been used to improve the probe performance by using the KLM model, an analytical model that is widely used by ultrasonic sensor manufacturers to predict the response of ultrasonic probes. In particular, the chapter is concerned with exploring the impact of varying thickness, impedance, and attenuation of an intermediate matching layer in a probe that consists of one outer layer, one intermediate layer, one piezoceramic transducer and a backing media.

Chapter 6 reports the investigation into methods in obtaining high measurement accuracy of the distance/range measurement. The chapter also presents some of the limitations of using air coupled probes in high accuracy range measurement which are highlighted in the literature. Finally, the accuracy of an air coupled probe that was developed (outlined in Chapter 4) is presented.

Chapter 7 presents the findings of the experiments conducted in the use of air-coupled ultrasonic probe to perform in-situ bore form measurement, using the rig built to mimic the honing environment. The ultrasonic measurements are compared with reference measurements from a 3D Coordinate Measurement Machine (CMM). The chapter concludes with the findings of the feasibility of using air coupled ultrasound as a bore form measurement sensor.

Chapter 8 concerns bore distortion measurement using ultrasound. The limitations of using through-thickness waves (bulk waves) are presented, along with the outcome of similar evaluations of surface waves. Discovering the possibility of using a method which utilises surface waves to perform bore distortion measurement whilst mitigating against the temperature effects is presented.

Chapter 9 presents the conclusions.

Chapter 10 investigates the various avenues of research that are possible for the continuation of the work reported within the thesis.

2 Background on Ultrasonic Waves

In this chapter the theory behind propagation of ultrasonic waves in an elastic medium relevant to the work carried out for the thesis is presented. The characteristics of ultrasonic waves and the various modes of wave propagation are explored. The equations used to calculate the properties of a medium which impacts wave propagation, such as the acoustic impedance, attenuation, and velocity are presented. The chapter also presents the theory of reflection and transmission of ultrasonic waves incident to an interface, or to a layer that is sandwiched between two mediums.

2.1 Ultrasound

Ultrasound is a term given to subset of elastic waves that have their frequency, f, greater than 20,000 Hertz, i.e. greater than the range of human hearing. Ultrasound has a wide range of applications in various sectors such as medicine, non-destructive testing (Krautkrämer and Krautkrämer, 1987), tribology (Dwyer-Joyce, 2005), and many more, where it is used as a measurement tool. Existing applications relevant to the work presented in this thesis would be proximity sensors used to detect objects by automotive vehicles (Canali *et al.*, 1982; Hickling and Marin, 1986), or tribological applications such as measuring oil film thickness (Dwyer-Joyce *et al.*, 2006; Avan, Mills and Dwyer-Joyce, 2010; Mills, Avan and Dwyer-Joyce, 2012) between two surfaces in contact. A similar approach was taken to studying the properties of ultrasonic waves.

2.2 Elastic Media

According to the classic theory of linear elasticity, an elastic body subjected to an external force will deform proportionally to the force it is subject to. When the force is removed, it returns to its original shape and size. A 3D elastic body deforms according to Hooke's law:

$$\sigma_{ij} = k_{ijkl}\varepsilon_{ij} \qquad \text{Equation 1}$$

Where, the stiffness coefficient k_{ijkl}, is a rank four tensor (with 81 components), and the stress, σ_{ij} (shown in Figure 2-1), and strain, ε_{ij}, are second rank tensors with 9 components.

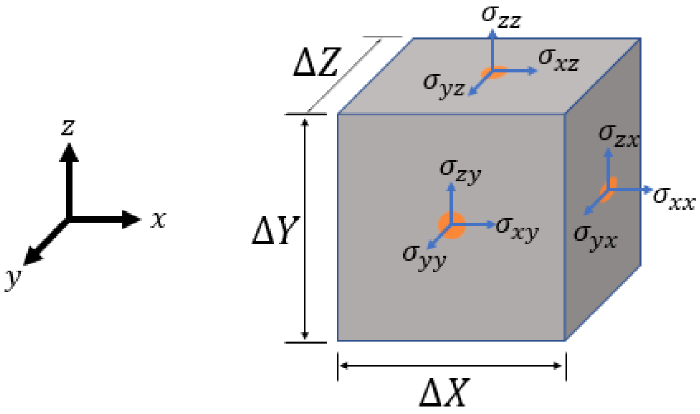

Figure 2-1: Cube elastic body with 9 stress components possible on surfaces perpendicular to 3 orthogonal directions. At the limit $\Delta \rightarrow 0$, the 9 components completely define the state of stress at the "3D point".

Elastic bodies with k_{ijkl} of only 2 independent coefficients are said to be isotropic, i.e. deformation remains constant with change in direction of tensile stress, or change in direction or polarisation of shear stress. If k_{ijkl} of a medium has more than 2 independent coefficients, the deformation varies with direction of application of stress, and the material is said to be anisotropic. Most materials have uniform *homogeneous* composition at any given point, but materials such as carbon fibre composites are *inhomogeneous*.

Fluid and amorphous solids are mostly isotropic. Polycrystalline (most engineering) materials consisting of grains joined at grain boundaries, are isotropic when grain shape and orientation have no pattern and are anisotropic otherwise (said to have *texture*). The degree of anisotropy and inhomogeneity can in some instances be scale dependent and may change with varying levels of magnification.

Most material can be assumed to behave as a homogeneous isotropic medium when trying to understand the wave propagation characteristics. Equation 2 for homogenous isotropic medium can be simplified as (Leonid M. Brekhovskikh and Godin, 1990):

$$\sigma_{ij} = \lambda \frac{\partial u_k}{\partial x_k} \delta_{ij} + \mu \left(\frac{\partial u_i}{\partial x_j} + \frac{\partial u_j}{\partial x_i} \right) \qquad \text{Equation 2}$$

Where, $\boldsymbol{u} \equiv (u_1, u_2, u_3)$ is the displacement vector; $\boldsymbol{x} \equiv (x_1, x_2, x_3)$ is the initial position vector; i, j are live indices and change only in new expressions and the equation represents 9 expressions, one for each stress component; k is a dummy index - dummy indices are always present in pairs in a term and invoke the Einstein summation convention[1]; δ_{ij} is the Kronecker delta, $\delta_{ij} = \begin{cases} 1, & i = j \\ 0, & i \neq j \end{cases}$; λ and μ are the Lamé constants - μ is the shear modulus of the medium. As fluids offer no resistance to shear in the above expression for fluid medium, $\mu = 0, \lambda = K$, $\sigma_{ij} = -p\delta_{ij}$, and p is the pressure at a point. Relation between the Lamé constants to common elastic parameters are given in Table 2-1.

Table 2-1: Relationship between elasticity parameters and the Lamé constants, λ and μ.

Young's modulus	$E = \frac{\mu(3\lambda+2\mu)}{\lambda+\mu}$
Poisson's ratio	$\nu = \frac{\lambda}{2(\lambda+\mu)}$
Bulk modulus	$K = \lambda + \frac{2}{3}\mu$
Rigidity	$\tau = \mu$
Lamés elasticity constant	$\lambda = \frac{\nu E}{(1+\nu)(1-2\nu)}$
Lamés elasticity parameter	$\mu = \frac{E}{2(1+\nu)}$

2.3 Elastic Waves

In an elastic medium, any disturbance to displace a particle from its equilibrium position will result in it being subjected to restorative forces - proportional to stiffness coefficient and distance from equilibrium. The displaced particle starts accelerating back to equilibrium under restorative forces and gains momentum - proportional to mass and velocity - in the process. Another force acting on the particle is the dissipative force, for instance due to frictional losses. The particle motion is like mass on a mass-spring-damper (see Figure 2-2).

---

[1] Einstein summation convention for the term $A_i^i \equiv \sum_{i=1}^{N} A_i^i = A_1^1 + \cdots + A_N^N$ for tensor of X^N dimensions; therefore $\frac{\partial u_k}{\partial x_k} \equiv \frac{\partial u_1}{\partial x_1} + \frac{\partial u_2}{\partial x_2} + \frac{\partial u_3}{\partial x_3}$ for 3D space.

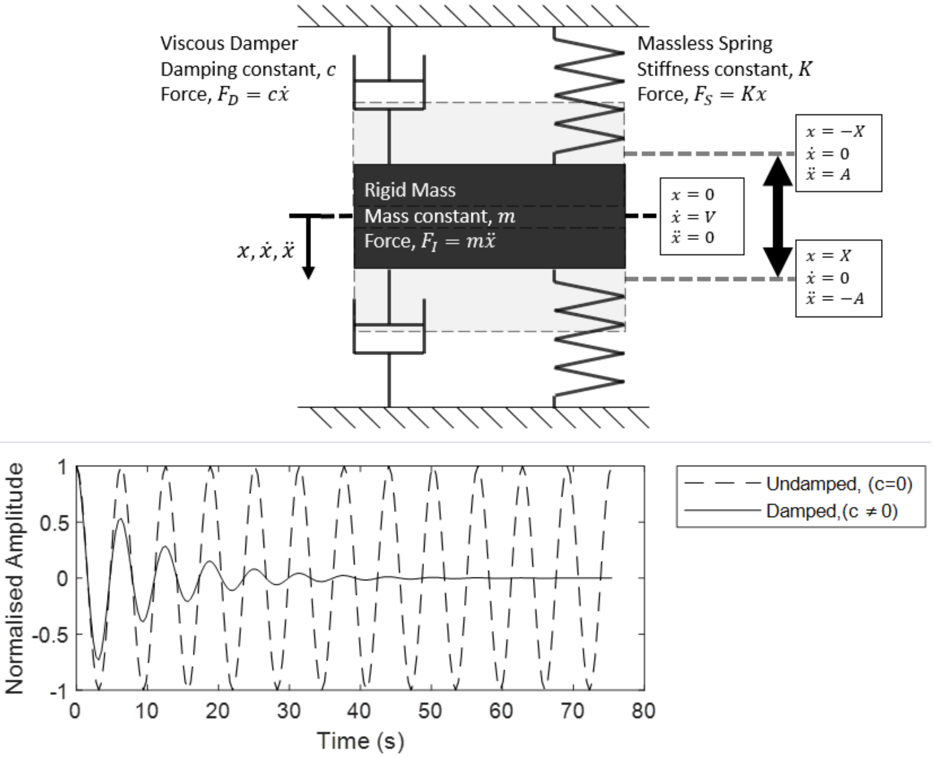

Figure 2-2: (Upper figure) - Mass with 1Degree-Of-Freedom (1DOF) connected to rigid planes with spring and damper on both sides; X, V and A are magnitudes of displacement, velocity, and acceleration, respectively. (Lower figure) - Vertical position of the mass vs time of damped and undamped systems.

Unlike the mass in Figure 2-2 above, particles in an elastic medium can transfer their kinetic energy to their neighbours, or vice versa. This process of particles oscillating under opposing inertial and restorative forces whilst transferring kinetic energy through the medium is known as an elastic wave; see Figure 2-3. The particles propagating the waves move with *acoustic velocity*, $v(x,t)$, while the energy propagation happens at *wave propagation velocity*, c.

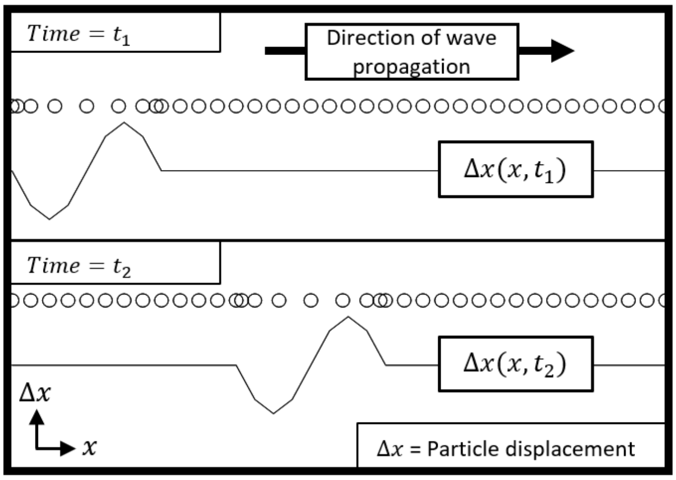

Figure 2-3: Propagation of elastic wave through 1D medium, forward in the x-direction. Discrete particles are used to exaggerate particle motion, while in reality the medium would be continuous. The line-plots below show particle displacement, Δx in x-direction.

Elastic waves starting at a point within the medium propagate outwards in all directions (Figure 2-7). The kinetic energy spreads over a larger area with increasing time; it can also be described as a function of distance travelled by the wave as c is independent of time.

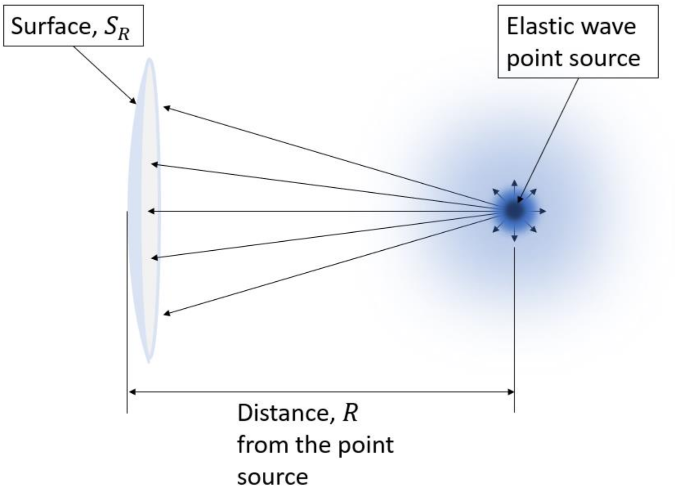

Figure 2-4: Point source disturbance spreading out through an elastic medium. Variation in colour of surface S_R to represent reduction in intensity $I(R)$ due to beam spread by inverse square law, $I(R) = I_0/R^2$.

2.4 Plane Wave Propagation

When using ultrasound to conduct measurement within short distances that are outside the diffraction range, ignoring wave dispersion can give a reasonable approximation (Krautkrämer and Krautkrämer, 1990b). Such approximation results in a theoretical type of waves known as *plane waves*.

In plane waves, particles in the plane perpendicular to the direction of wave propagation have the same displacement and velocity vectors. Figure 2-5 shows the two modes of wave polarisation possible in an isotropic medium; longitudinal and shear. Shear force is attenuated rapidly by fluid and therefore fluid media cannot support shear elastic wave propagation. Therefore, fluids are assumed only to support longitudinal polarisation mode, while solids support longitudinal and shear polarisation modes.

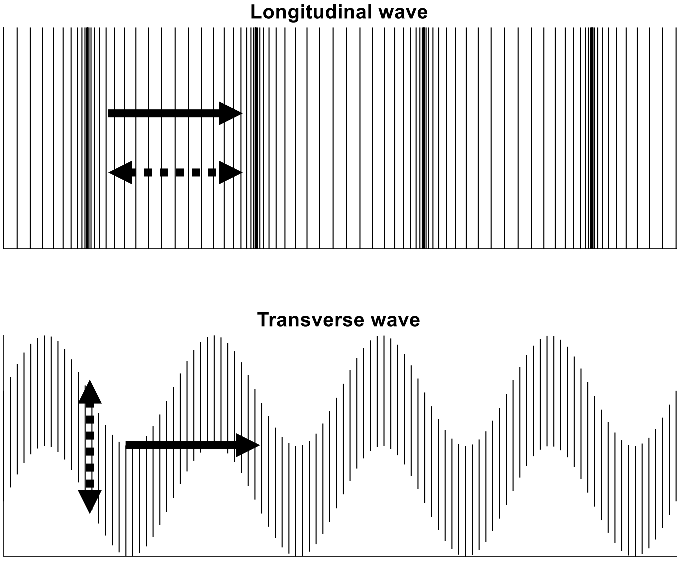

Figure 2-5: Plane waves polarised to longitudinal mode (top) and shear mode (bottom). Parallel lines represent the particles of the plane perpendicular to direction of wave propagation - the particles are fixed to the plane.

Due to the stiffness coefficient of anisotropic solids, the particle motion in the perpendicular directions can cause elastic deformation in directions other than that of the fundamental mode. Therefore, the polarisation modes in anisotropic solids are said to be quasi-longitudinal and quasi-shear.

2.4.1.1 The Wave Equation

Elastic wave propagation in elastic media is given by the wave equation — a partial differential equation varying in temporal and spatial domains. Limiting exploration to plane wave propagation in 1D fluid medium, the wave equation can be derived from the linearised continuity equation and the linearised Newton's second law of motion, in terms of pressure, p fluctuation of the medium as follows (Kinsler *et al.*, 2000):

$$\frac{1}{c^2}\frac{\partial^2 p}{\partial t^2} = \frac{\mathrm{d}^2 p}{\mathrm{d}x^2} \qquad \text{Equation 3}$$

c is the wave propagation velocity; and t is the time. c is the rate of pressure fluctuations with density:

$$c^2 = \left(\frac{\partial p}{\partial \rho}\right)_{\rho_0} \qquad \text{Equation 4}$$

Similarly, wave equation in Equation 4 can be presented in terms of the changing particle velocity, v as follows:

$$\frac{1}{c^2}\frac{\partial^2 v}{\partial t^2} = \frac{\mathrm{d}^2 v}{\mathrm{d}x^2} \qquad \text{Equation 5}$$

Figure 2-6 shows a plane wave emitted by a piston, one travelling away from the piston while the other is travelling towards it.

$$v_+ = \frac{P_+}{\rho_0 c} e^{j(kx - \omega t)} \qquad v_- = -\frac{P_-}{\rho_0 c} e^{-j(kr - \omega t)}$$

$$p_+ = P_+ \mathrm{e}^{j(kx - \omega t)} \qquad p_- = P_- e^{-j(kr - \omega t)}$$

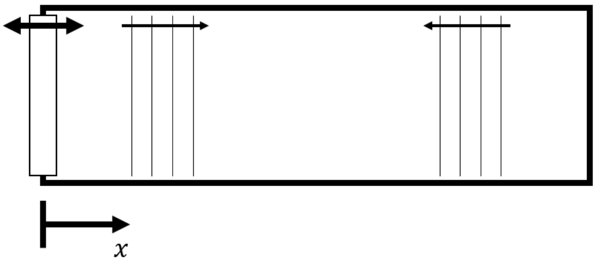

Figure 2-6: Plane wave propagating through 1D medium. v_+, p_+ and v_-, p_- are the local particle velocity and pressure of the forward and backward propagating waves, respectively.

Solution for wave propagation, i.e. the local particle pressures and velocity, as shown in Figure 2-6 is given as follows (Kinsler *et al.*, 2000):

$$p(x,t) = \left(P_+ \mathrm{e}^{j(kx - \omega t)} + P_- \mathrm{e}^{-j(kx - \omega t)}\right) \qquad \text{Equation 6}$$

$$v(x,t) = \left(\frac{P_+}{\rho_0 \boldsymbol{c}} \mathrm{e}^{j(kx - \omega t)} - \frac{P_-}{\rho_0 \boldsymbol{c}} \mathrm{e}^{-j(kx - \omega t)}\right) \qquad \text{Equation 7}$$

Where k, is the complex wavenumber vector $\left(k = \frac{2\pi}{\lambda} \pm j\alpha\right)$, α is the wave attenuation coefficient, λ is the wavelength; $\omega = 2\pi f$ is the angular frequency; P_+ and P_- are the pressure amplitudes of the forward and backwards travelling waves, respectively.

The solution to wave equation of a wave propagating the direction $\mathbf{n} = (n_x, n_y, n_z)$ in a 3D medium can be found by extending the above presented 1D equation, however the 1D model is sufficient for the qualitative understanding required at present.

2.4.1.2 Attributes of a Wave

Top plot in Figure 2-7 shows a plot of pressure variation of an elastic wave in fluid. The amplitude, A_0 is the magnitude of pressure variation at *anti-nodes*. The equilibrium position (ambient pressure) can have a '*0 shift*', i.e. the medium is subjected to static pressure. The wavelength, λ is the spatial distance between two *nodes* or *anti-nodes* - *nodes* are position-vectors (location in *x-axis*) where the particles are momentarily at ambient (static-equilibrium) pressure, *anti-nodes* are position-vectors where particles are momentarily at maximum pressure variation. The phase, ϕ of the wave is the arccosine of the ratio of local pressure of the wave at $x = 0$, and the maximum pressure, A_0, $\phi = \arccos(A(0)/A_0)$. The four variables and the wave propagation velocity, c gives the expression for pressure variation, $A(x)$ as follows:

$$A(x) = A_0 \sin[x\ (c/\lambda)\ - \phi] \qquad \text{Equation 8}$$

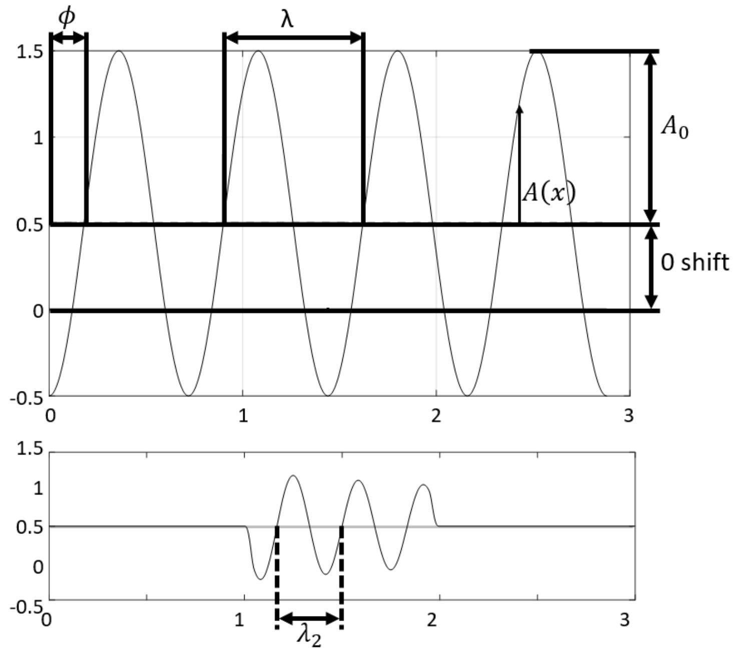

Figure 2-7: (Top Plot): Pressure distribution (*y-axis*) vs spatial position (*x-axis*) of 1D particles at a time instant, with the system subjected to sinusoidal pressure fluctuation of constant magnitude. (Bottom Plot) A wave packet (of spatial duration $3\lambda_2$) that is subjected to energy loss (attenuation).

Figure 2-7 also shows the propagation of a discrete wave packet that is subjected to attenuation. Constant rate of attenuation is generally modelled as an exponential decay function of space with a decay constant (attenuation coefficient), α. Equation 8 equivalent for discrete length wave subjected to attenuation is given as:

$$A(x) = W(x) \times A_0 \sin\left[x\left(\frac{c}{\lambda}\right) - \phi\right] \times e^{-\alpha x} \qquad \text{Equation 9}$$

$$W(x) = \begin{cases} W', & 1 < x \leq 2 \\ 0, & 1 \geq x, \quad x > 2 \end{cases}$$

Where, W' is the amplitude modulating window function.

The rate of oscillations of the particles, i.e. the *frequency, f* is defined as the number of oscillatory cycles completed by the particles in one second. The time taken for the wave to complete one cycle is known as the period of the wave, $T (= 1/f)$.

Given wavelength, λ is the distance travelled by waves during one cycle, the wave propagation velocity, c (the distance travelled by the wave in one second) is defined as the product of one wavelength and the time taken for one complete oscillation by the particle, i.e. its frequency, f.

$$c = f\lambda \qquad \text{Equation 10}$$

In polar form, after one period, T the wave completes 2π radians angular distance. The total angular distance covered by the wave in one second is known as the angular frequency, $\omega = 2\pi f$.

The *angular* distance covered by the wave while it propagates *one-unit* of physical distance is known as the *wave number*, k.

$$k = \frac{\omega}{c} = \frac{2\pi}{\lambda} \qquad \text{Equation 11}$$

Figure 2-8 shows regions of constant phase of plane wave and spherical wave. The surfaces with constant phase of the wave are known as *wavefronts*.

Figure 2-8: Regions of constant phase of spherical wave and plane wave. Each curved and straight lines represent surface where the phase of the wave is constant, i.e. they are wavefronts.

The intensity of the wave is the energy content in the wave and proportional to the square of the sound pressure (the product of the amplitude of particle displacement, x and angular frequency, ω) as follows:

$$I = \frac{1}{2}\frac{p^2}{\rho c} = \frac{1}{2}\rho c \omega^2 x^2 \qquad \text{Equation 12}$$

2.5 Wave propagation modes

Waves propagating through the inside of the medium are known as bulk waves; waves that are confined to a surface are known as surface waves; waves propagating through thin plate media causing the thickness of the plate to oscillate are known as Lamb waves. Figure 2-9 shows various modes of waves which exist in an elastic solid medium. Discussion within this chapter is limited to bulk waves.

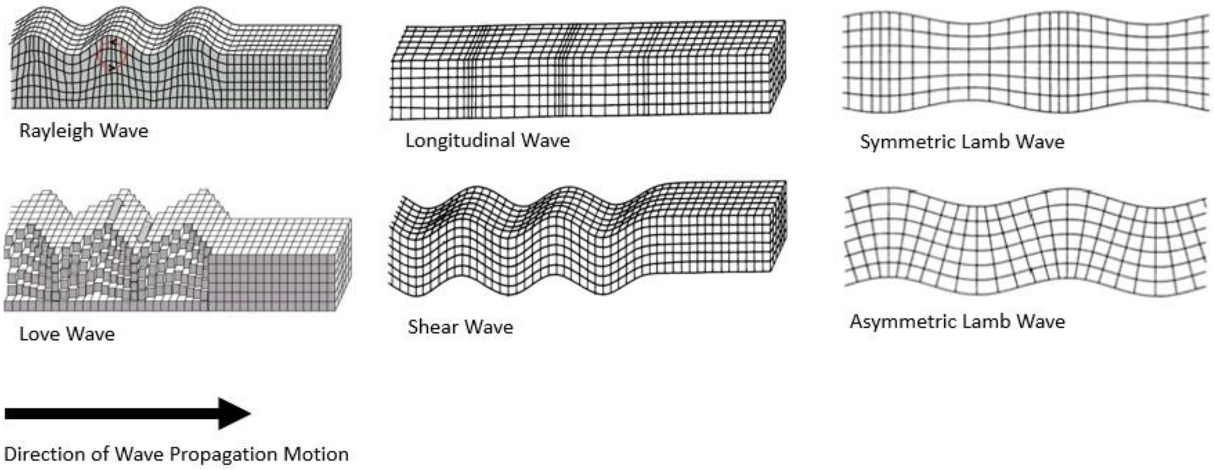

Figure 2-9: Various modes of waves propagating through a solid medium. (LHS pair): surface waves, (Centre pair): bulk waves; (RHS pair): plate waves.

When oscillations of the particles are in the same direction as the direction of wave propagation, the wave mode is known as *longitudinal* wave. If the direction of particle motion is perpendicular to the direction of wave propagation, then the wave mode is known as *transverse* or *shear* wave.

Isotropic media supports one longitudinal and one transverse mode, while transverse mode attenuates rapidly in fluids, the spatial rate of attenuation depending on viscosity and other properties. The number of modes of wave propagation possible through anisotropic solid media in any one direction depends on the degree of anisotropy - generally there is one independent longitudinal mode and 2 or more independent transverse modes. Wave propagation velocity tends to vary for different *propagation* modes.

Waves that travel along the surface of a solid, along a solid-fluid boundary or solid-solid boundary are known as guided waves. Generally, waves that travel along the surface of a solid (boundary with vacuum) are known as Rayleigh waves. Waves travelling between the solid and solid boundary are known as Stoneley waves.

2.6 Wave Velocities

The velocity at which *wavefronts* propagate is known as the *phase velocity,* c_p. The velocity at which the envelope of modulated wave propagates is known as the *group velocity,* c_g.

$$c_p = \frac{\omega}{k} \qquad \text{Equation 13}$$

$$c_g = \frac{\partial \omega}{\partial k} \qquad \text{Equation 14}$$

The phase and group velocities are equal in a homogenous isotropic medium, while they vary in dispersive media. Expressions for wave propagation velocities in an isotropic medium are presented below and have been obtained from Krynkin (2015).

Longitudinal wave propagation velocity in fluids is given by:

$$c = \sqrt{\frac{B}{\rho_0}} \qquad \text{Equation 15}$$

Where, B is the *bulk modulus* of the fluid, and ρ_0 is the density of the medium at equilibrium. Longitudinal wave propagation velocity in solids is given by:

$$c_L = \sqrt{\frac{E(1 - \nu)}{\rho_0(1 + \nu)(1 - 2\nu)}} \qquad \text{Equation 16}$$

Where, ν is the *Poisson's ratio*. Transverse wave propagation velocity in solids is given by:

$$c_T = \sqrt{\frac{G}{\rho_0}} \qquad \text{Equation 17}$$

Where, G is the shear modulus; $G = E/2(1 + \nu)$. The speed of propagation of Rayleigh waves is given by:

$$c_R = \frac{0.87 + 1.12v}{1 + v}\sqrt{\frac{E}{2\rho_0(1 - \nu)}} \qquad \text{Equation 18}$$

2.6.1 Variations in Wave Propagation Velocity

Any change in temperature of a medium impacts the stiffness coefficients as well as the existing residual stress of solids or ambient pressure of fluids. These factors impact the wave propagation velocity. The various media of interest are air, cast iron, oil on the internal face of the liner, or the coolant on the external face of the liner. At present the thesis focuses on air and cast iron (specimen cut out from cylinder liner) as the media through which the waves propagate.

For air, the wave propagation velocity is also dependant on humidity and CO_2 content of the atmosphere, although the impact is not as significant as temperature. Equation 19 presents the acoustic wave velocity in air as a function of temperature.

$$c^2 = c_0\left(1 + \frac{T}{273.16}\right) \qquad \text{Equation 19}$$

Where, c_0 (the speed of sound in air at 0°C) is a function of CO_2 content, humidity, and pressure.

The topic of change in wave propagation velocity with temperature in anisotropic solids, namely cast iron, is covered in Chapter 8.

2.7 Attenuation

As elastic waves propagate through natural materials, the energy content per unit area of the wave decreases (attenuates) with the distance the wave propagates. The three main factors contributing to attenuation are:

1. Beam spreading (diffraction).
2. Absorption - kinetic energy is converted to heat. This is a function of distance travelled as well as of the medium.
3. Scattering at boundaries between media.

Intensity reduction due to 1. is proportional to the inverse square of distance travelled; for 2. intensity is a function the medium; and for 3. reduction depends on interface between two media - 3. dominates attenuation in polycrystalline material.

Attenuation, accounting for the energy loss per unit surface area, for all modes, can be represented as an exponential decay of initial amplitude, A_0 (when the distance travelled, $x = 0$) and the material specific decay constant (*attenuation coefficient*), α as follows (Silk, 1984):

$$A = A_0 e^{-\alpha x} \qquad \text{Equation 20}$$

Attenuation coefficient, α can be calculated in *nepers* (Np) per unit distance, d as:

$$\alpha d = \ln\left(p_0/p(x)\right) \text{ [Np/d]} \qquad \text{Equation 21}$$

It is also common to present α in the *decibels* per meter (dB/m) as:

$$\alpha = \frac{1}{x} \times 20 \log_{10}\left(p_0/p(x)\right) \text{ [dB/m]} \qquad \text{Equation 22}$$

Where, x is in meters and $p(x)$ is the pressure after the wave has travelled the distance, x.

2.8 Wavefield Generated by a Circular Piston

For most applications, if the reflecting face is close to the source, then the wave can be approximated as plane waves, while if it is far away, then it is treated as a circular wave emitted by a point source; see Figure 2-10. The behaviour of wave emitted by a circular piston source, in the "near-field" region i.e. close to the probe, is of interest for the present work and is explored in this section.

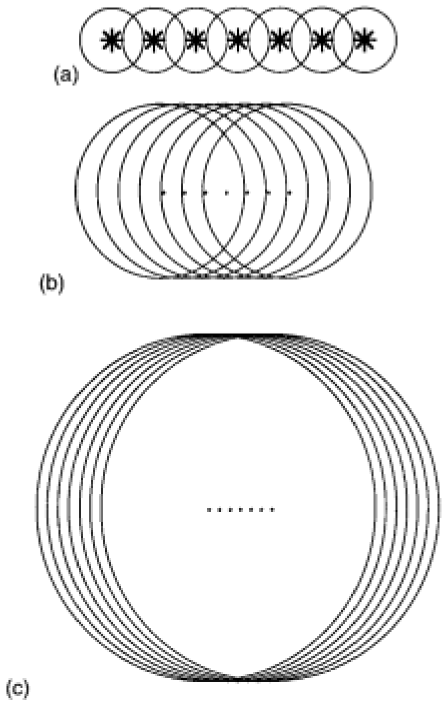

Figure 2-10:Wavefronts at 3 different times after generation by a line array of impulsive point sources showing progression from quasi-cylindrical to quasi-spherical fields. The dots represent the transducer while the circular lines are the wavefronts which have propagated outwards, getting larger (further away from the transducer) with increasing time. Figure acquired from reference (Fahy, 2003).

Using Huygen's principle, whereby each point on the transducer can be treated as a point source of the wave, we can obtain a waveform emitted by a circular piston oscillator, as a function of the distance from the oscillator, as shown in Figure 2-10. Figure 2-11 shows an acoustic pressure field around a circular piston obtained using the Huygen's principle, with and without the impact of attenuation.

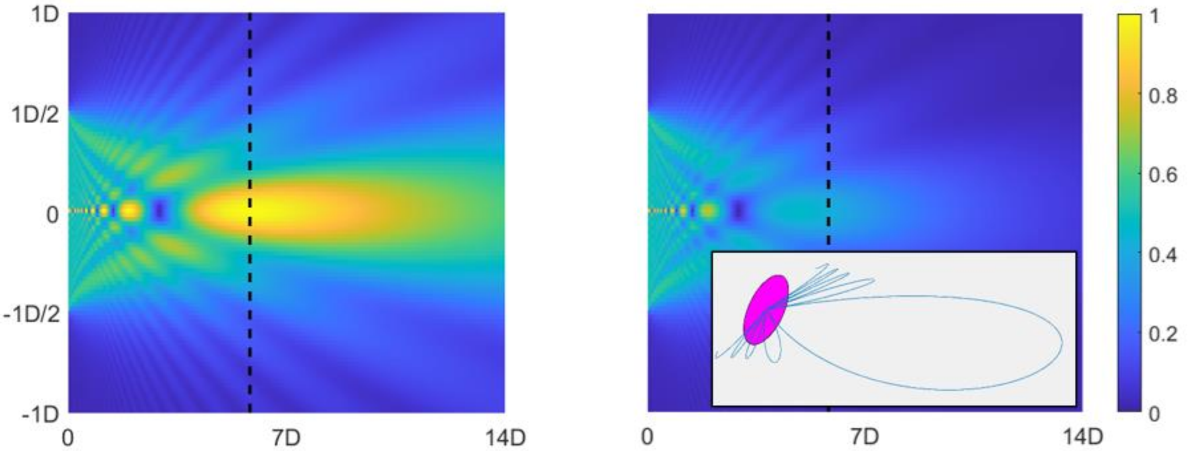

Figure 2-11: Normalised map of pressure field generated by a circular piston of diameter 8mm in air (assumed isotropic), at 1MHz. The wave is allowed to attenuate in the RHS plot. Pressure values in both the plots are normalised by the same intensity value; all axes are normalised by piston diameter, D. The schematic at the bottom of the RHS plot depicts pressure of sound wave emitted by a circular piston, at fixed radial distance away.

The pressure profile along the axial direction of wave emitted from a circular piston can be calculated using Equation 23 (Silk, 1984). Figure 2-12 shows the relationship between the amplitude and the axis perpendicular to the transducer face, calculated at the centre of the transducer using Equation 23.

$$P(R,0) = \left| P(0,0) \times 2\sin\left[\frac{\pi}{\lambda}\left(\sqrt{\frac{D^2}{4} + R^2} - R\right)\right]\right|$$

Equation 23

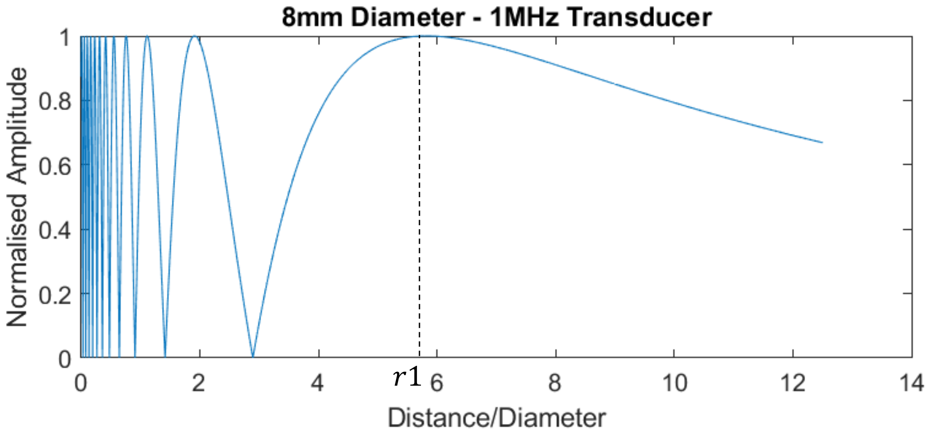

Figure 2-12: Axial pressure amplitude for baffled circular plane piston of radius 8mm and central frequency of 1MHz, emitting wave into air. $r1$ represents the transition from the near-field to far-field zone.

2.8.1.1 Near-field and far-field

In Figure 2-12, past a certain distance, $r1$, the pressure decreases monotonically, approaching an asymptotic $1/R$ dependence. For a distance less than $r1$, there is a strong interference effect which causes a modulation in the amplitude of the wave. The region within the distance r1 from the transducer is known as the *nearfield region*, while the region past this location is known as the *far field*. Nearfield distance, $r1$ can be calculated using Equation 24 (Silk, 1984). Transducers are normally designed such that the measurement is made outside the nearfield when possible.

$$r1 = \frac{D^2 - \lambda^2}{4\lambda} \qquad \text{Equation 24}$$

2.9 Acoustic Impedance

Mechanical impedance is defined as the measure of the ratio of external force to resulting velocity of a mass:

$$Z = \frac{F}{v} \qquad \text{Equation 25}$$

Acoustic impedance is a measure of resistance to motion when particles are subjected to external force. Specific acoustic impedance for a medium is related to the density and wave propagation velocity as follows:

$$z_s = \sqrt{\frac{k_{ii}}{\rho_0}} = \rho_0 c \qquad \text{Equation 26}$$

Specific acoustic impedance is measured in Rayl where 1 Rayl $= 1\,\frac{\text{N.s}}{\text{m}^3} = 1\,\frac{\text{Pa.s}}{\text{m}} = 1\,\frac{\text{kg}}{\text{s.m}^2}$. For fluids, k_{ii} is the bulk modulus, B.

Characteristic acoustic impedance is the relationship between particle velocity and force acting on it per unit area, presented as follows:

$$z_c = z_s A \qquad \text{Equation 27}$$

2.10 Reflection and Transmission of Plane Acoustic Waves at a Boundary

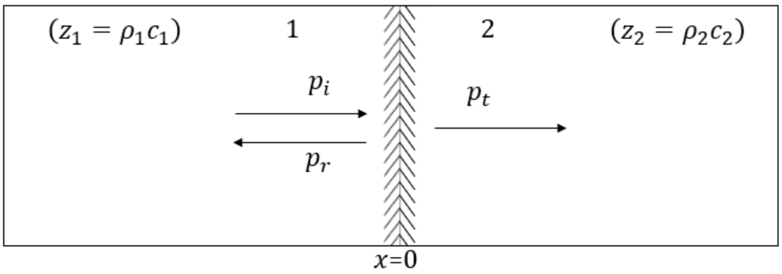

Figure 2-13: Reflection and transmission of a plane wave normally incident on a boundary between two media. Figure adapted from Kinsler et al. (2000).

As an acoustic wave travels from one medium to another, a portion of it is reflected while the remainder is transmitted. At the interface between the two media, 2 boundary conditions are satisfied: (1) continuity of pressure, p, and (2) continuity of normal component of particle velocity, v, across the boundary. These boundary conditions can be presented as Equation 28 and Equation 29.

$$p_i + p_r = p_t \quad \text{at x=0} \qquad \text{Equation 28}$$

$$v_i + v_r = v_t \quad \text{at x=0}$$ Equation 29

Dividing Equation 28 by Equation 29 we get Equation 30.

$$\frac{p_i + p_r}{v_i + v_r} = \frac{p_t}{v_t} \quad \text{at x=0}$$ Equation 30

As presented earlier, the specific acoustic impedance $z = \frac{p}{v}$; substituting this into Equation 30 and rearranging gives Equation 31.

$$R = \frac{z_2 - z_1}{z_2 + z_1} = \frac{z_2/z_1 - 1}{z_2/z_1 + 1}$$ Equation 31

Where, z_1 and z_2 are the specific acoustic impedances of the two media the sound wave travels from and into, respectively; R is known as the pressure reflection coefficient of the boundary and gives the portion of the wave energy reflected depending on the acoustic impedances of the two media. A similar process can be followed to show the reflection coefficient for velocity, R_v, given as follows:

$$R_v = \frac{z_1 - z_2}{z_2 + z_1}$$ Equation 32

The pressure transmission coefficient, T is defined as $T + R = 1$; we get the term for transmission coefficient as Equation 33.

$$T = \frac{2z_2}{z_2 + z_1} = 2\frac{z_2/z_1}{z_2/z_1 + 1}$$ Equation 33

The intensity reflection and intensity transmission coefficients are given by Equation 34 and Equation 35, respectively.

$$R_I = R^2 = \left(\frac{z_2 - z_1}{z_2 + z_1}\right)^2 = \left(\frac{z_2/z_1 - 1}{z_2/z_1 + 1}\right)^2$$ Equation 34

$$T_I = T^2 = \left(\frac{2z_2}{z_2 + z_1}\right)^2 = 4\frac{z_2/z_1}{(z_2/z_1 + 1)^2}$$ Equation 35

2.11 Plane Wave Propagating though a Sandwich Layer

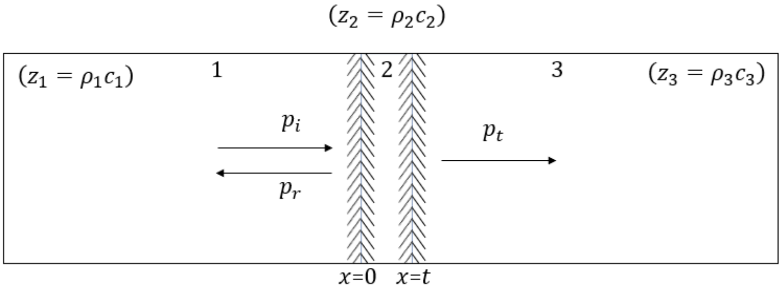

Figure 2-14: Reflection and transmission of a plane wave normally incident on a boundary layer (no. 2) between two media. Figure adapted from Kinsler et al. (2000).

A sandwich layer between two media is shown to transmit maximum energy when its impedance is a geometric mean between the two layers on either side:

$$z_2 = \sqrt{z_1 z_3}$$ Equation 36

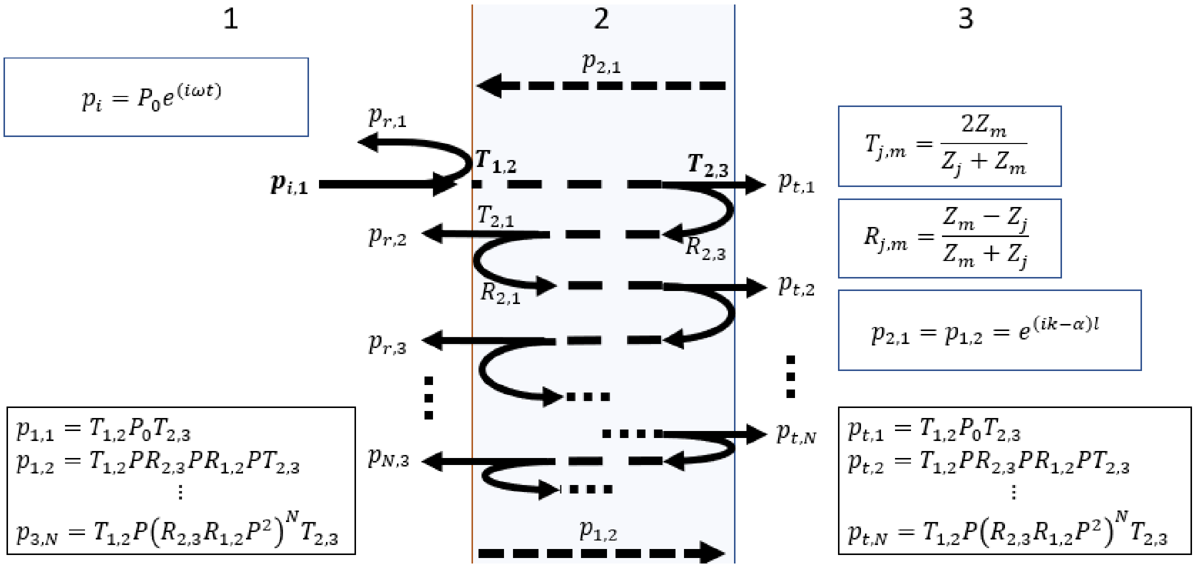

Figure 2-15: Acoustic wave *bounce diagram* for waves propagating through a sandwich layer. $R_{j,m}$ and $T_{j,m}$ are the reflection and transmission coefficients, respectively. $p_{i,k}$, $p_{r,k}$ and $p_{t,k}$ are the pressures of incident, reflected and transmitted waves, respectively. $p_{j,k}$ is the transformation that takes place to the waves as it travels from one boundary to the other. Subscripts j, k, m denote the medium - for variables with two subscripts, the 1st denotes the layer of incidence, and the 2nd denotes the layer post reflection/transmission. k is the wave number, $i = \sqrt{-1}$, l is the layer thickness, and α is the attenuation coefficient.

Considering the case of continuous waves incident into the layer as shown by Figure 2-15, the reflection coefficient of the layer, given $\sum_{n=1}^{N} r^n$, $|r| < 1 = \frac{1}{1-r}$, and $T_{j,m} = 1 + R_{j,m}$, can be shown to be (Leonid Maksimovich Brekhovskikh and Godin, 1990):

$$R_{l_2} = \frac{R_{3,2} + R_{2,1}e^{2i\varphi_2}}{1 + R_{2,1}R_{2,3}e^{2i\varphi_2}}$$

Equation 37

Where $\varphi_2 = k_2 l_2$, $k_2 = \frac{2\pi f}{c_2} + \alpha_2 i$, c_2 is the wave propagation velocity in the sandwiched layer, α_2 is the attenuation coefficient of the layer in Nepers. The transmission coefficient can be shown to be (Leonid Maksimovich Brekhovskikh and Godin, 1990):

$$T_{l_2} = \frac{T_{3,2}T_{2,1}}{e^{-\varphi_2} + R_{3,2}R_{2,1}e^{i\varphi_2}}$$

Equation 38

2.12 Piezoceramic Ultrasonic Transducers

Piezoceramic transducers are ceramic materials that can be used to generate and detect ultrasonic waves. Piezoceramics exhibit both a *piezoelectric* and *reverse piezoelectric* effect. Piezoelectricity is the ability of a material to generate a momentary electric charge on its surface when subjected to mechanical stress. Reverse-piezoelectricity is the ability of a material to deform when subjected to an externally applied electric field.

Piezoceramics initially have net charge neutrality and are polarised by application of an external electric field at temperature just below Curie temperature, T_c and cooled to retain the polarity - it is important to keep the transducers below T_c to retain the polarity. Figure 2-16 shows a crystalline of piezoceramic material before and after being poled. The direction of the applied electrical field can be varied to control the wave mode of piezoceramic transducers, while the thickness of the transducer dictates its frequency range.

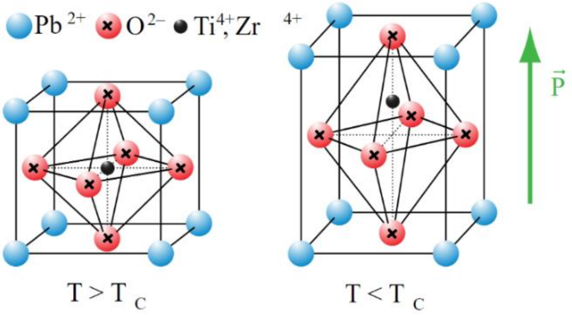

Figure 2-16: A single crystalline of lead zirconate titanate (PZT): (LHS) above Curie temperature and (RHS) polarized cooled to below its Curie temperature.

2.13 Concluding Remarks

The key parameters of a medium which governs the propagation of elastic waves through it has been presented within the chapter.

When using airborne ultrasonic waves, the measurable properties of the medium which affect wave propagation are humidity, temperature, and pressure. While for solids the parameters are temperature and stress. The change in the attributes of an elastic wave is a direct result of these properties.

The attributes of a waveform (the time dependant pressure profile) that form the basis of measurement at present are amplitude/intensity; wavelength/frequency; the phase; and wave propagation velocity.

Ultrasonic waves enable the measurement of the properties of a medium (or various media) by changing in one or multiple attributes, as the wave propagates through it. Similarly, it can also be used to study the properties of an interface between two media by using the concept of reflection and transmission coefficients. Piezoceramic transducers can be used to generate and detect ultrasonic pulses and were utilised for conducting the work presented within this thesis.

While considering the use of measurements of piezoceramic transducers (or any wave generation sources) the effect of diffraction should be considered. The equation to find the nearfield distance can be utilised to ensure measurements are outside this region.

The topics covered in this chapter by no means do justice to the vast topic of ultrasound. However, it is hoped that sufficient knowledge is developed amongst the reader to understand the work carried out within this thesis: design and manufacture of airborne ultrasonic probes, profiling the internal face of a cylinder bore, and understanding the relationship between temperature and wave propagation velocity in a cast iron liner specimen.

3 Experimental Setup and Signal Processing

This chapter describes a generic test setup for distance measurement using ultrasonic waves. The hardware components used in signal generation and detection, and for data acquisition, are presented. The various methods used in processing the acquired signal waveform to obtain distance measurement is also presented. The two experimental rigs that were designed and built to carry out the work are also presented.

3.1 Experimental Apparatus

Figure 3-1 shows the schematic of a commonly used setup for measuring the distance between the ultrasonic probe and target (reflector wall), with the probe working in pulse-echo mode. Here, pulse-echo mode refers to the setup whereby the same transducer is used to emit a pulse (discrete acoustic wave packet) at a set central frequency and detect the reflected echo. The figure depicts all the key components in most ultrasonic measurement systems used in experiments conducted for the thesis.

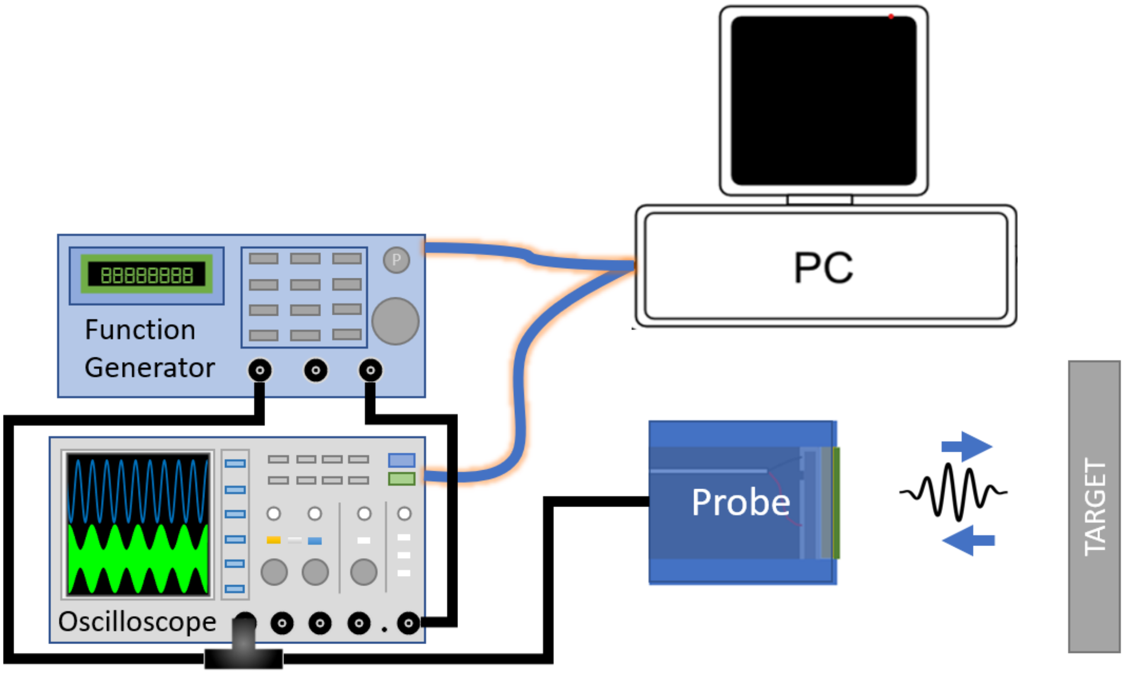

Figure 3-1: Schematic of a generic distance measurement system used for measuring distance between an ultrasonic probe and the target (sound wave reflecting face). The oscilloscope and the function generators are shown connected to the PC, the probe and each other. The function generator and the oscilloscope are synchronised in time by using a trigger signal, generated by either of the two, and to trigger the other, at the start of each measurement.

Figure 3-2 shows a block diagram of a test setup similar to that in Figure 3-1. In addition to Figure 3-1, the block diagram also shows the auxiliary measurement system, consisting of sensors and data acquisition hardware, which are commonly used to obtain information on the environmental condition/reference measurements, e.g. temperature, and reference position of the probe.

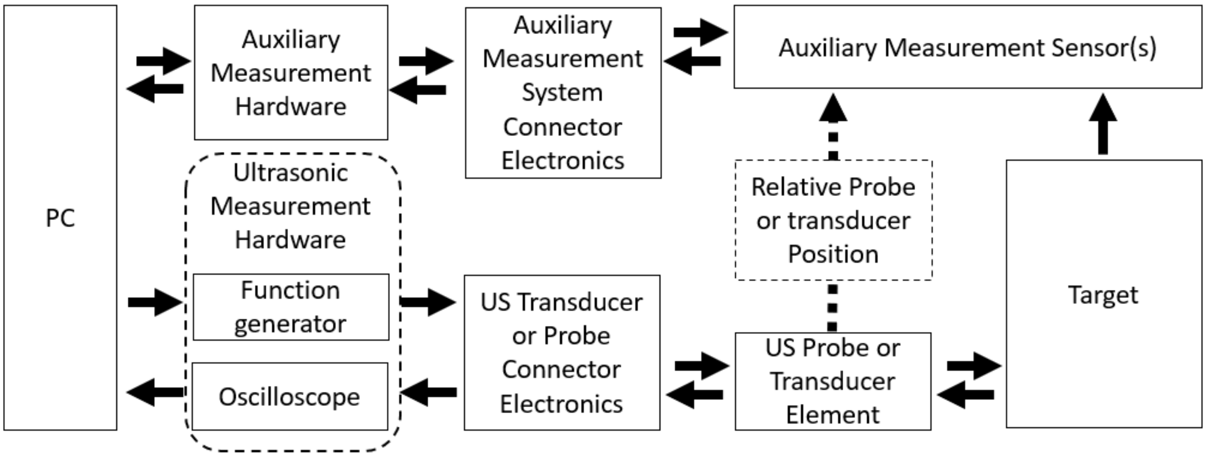

Figure 3-2: Block diagram representing the link between various components used in a typical experiment involving ultrasonic transducers. The target refers to all the components of the environment/test material which impact the ultrasonic measurement. Auxiliary measurement refers to measurements of physical parameters to be used as reference for each ultrasonic reading, e.g. the reference location of the probe as shown in the figure, or properties of the medium such as temperature.

3.1.1 Ultrasonic Transducer

Ultrasonic measurements in solids can be carried out using bare element transducers with or without backing material (used for purposes such as reducing transducer ringing). For the work carried out, the transducers were bonded onto the solid base using 2-part epoxy, M-Bond 600 requiring heat curing. A backing made up of epoxy Duralco was also used in some setups (see Figure 3-3).

Coaxial cable 50 VMTX by NEXANS was used as the lead cable from the transducer. The core of the cable was soldered to the top face terminal of the transducer, while the braid was connected to the bottom face that is bonded to the specimen. The other end of the cable was connected to a 50 Ohms SMB connector RG174/U. The same method and components were used to bond the lead wire onto the air-coupled probe.

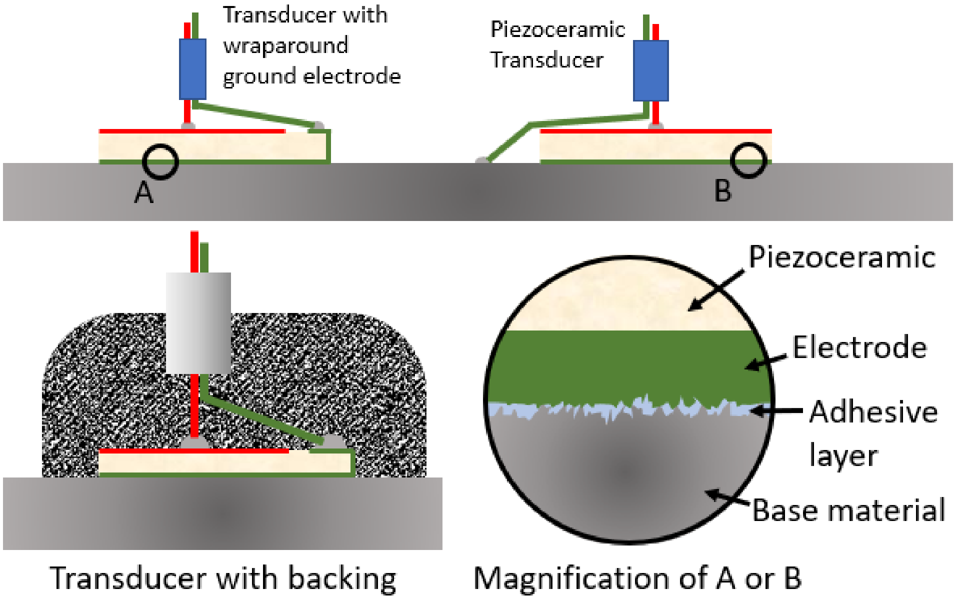

Figure 3-3: Bare piezoceramic element with and with and without wraparound ground electrode, bonded onto a base material using epoxy such as M-Bond 600.

The transducer elements used in this work had their thickness, t, much smaller than their diameter/length, as shown in Figure 3-4.

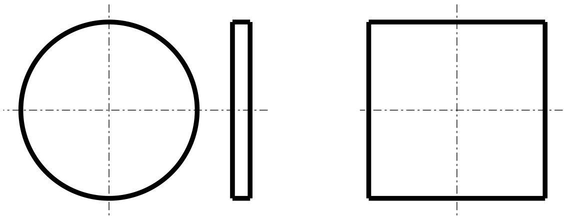

Figure 3-4: Schematic of the circular and a rectangular piezoceramic elements which were used. The thickness of the transducer elements was much smaller than the length/width.

Thus, when selecting the transducer of set resonant frequency, f_r, thickness mode resonance was assumed, and the transducer selected as per the wave propagation velocity through the material and its thickness:

$$f_r = \frac{c}{2t} \qquad \text{Equation 39}$$

The above equation was used to estimate the wave propagation velocity, c if f_r and t were known. If the thickness mode frequency coefficients, N_{TH} was supplied then:

$$f_r = \frac{N_{TH}}{t} \qquad \text{Equation 40}$$

3.1.2 Airborne Ultrasonic Probe

The term *ultrasonic probe* or just *probe* is used here to refer to a sensor which emits/receives ultrasonic waves. The probe used for work presented in the thesis was made up of an active transducer element, backing layers and two front matching layers (see Figure 3-5).

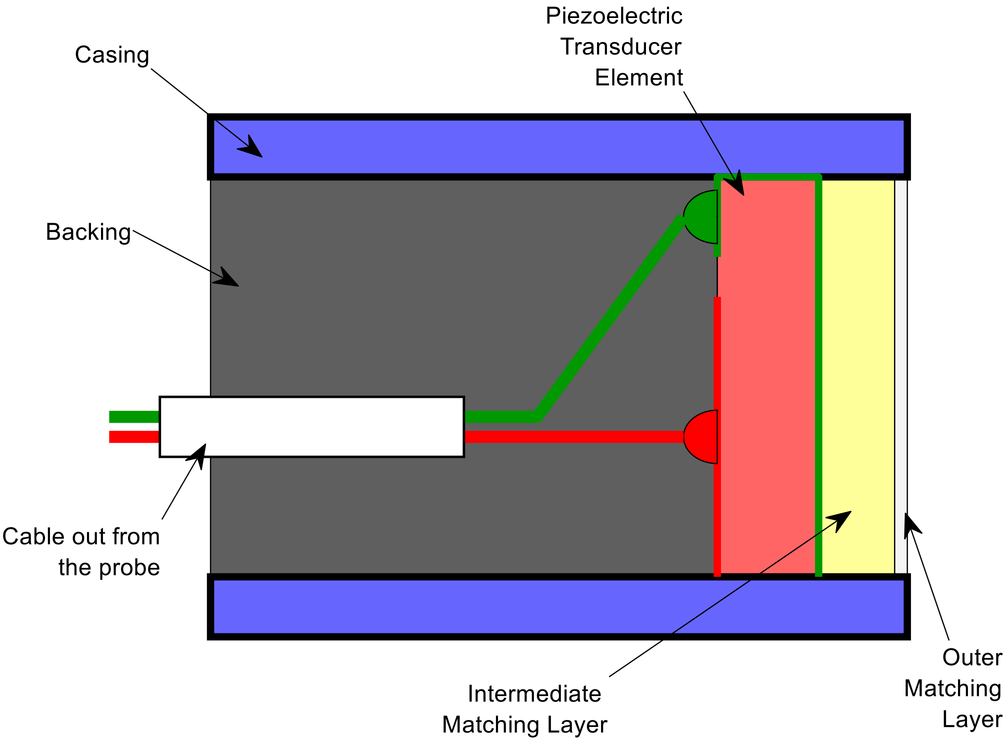

Figure 3-5: Cross-section ultrasonic probe made using circular transducer element, 2 matching layers, and one backing.

The transducer plate emits ultrasonic waves from both faces. Waves are emitted from the back into the backing medium and are assumed to attenuate completely due to the high attenuation of the backing. The waves emitted from the front are assumed to propagate through all the front layers and into the front medium, e.g. air/any other delay line. More details on the probe design are given in Chapter 4 and Chapter 5.

3.1.3 Waveform Generation and Detection Hardware

An arbitrary waveform and function generator (AWG) was used for the generation of the ultrasonic signal, as well as a gate amplifier with synthesizer. A digital oscilloscope was used for acquiring the wave form and transferring the digital signal to the PC for storage and analysis. The waveform generation and detection hardware were as follows:

Picoscope 5442B – Digital Function Generator and Oscilloscope
A Picoscope 5442B from Pico-Technology was used for wave form generation in non-air-coupled applications, and was also used in all the experiments as an oscilloscope. The device consists of AWG and ADC (analogue to digital converter) and was controlled using the LabVIEW® based inhouse software, Triboscope.

Figure 3-6: Picoscope 5442B: digital oscilloscope and arbitrary waveform generator (function generator).

The maximum voltage output of the Picoscope AWG is ±2V, and maximum frequency is 60MHz. The minimum and maximum ranges of the oscilloscope are ±10microVolts and ±20Volts respectively; the maximum sample frequency is 1GHz (1 active channel) or 500MHz (2 or more active channels); the maximum resolution is 16-bits (for 1 active channel) or 12-bits (for 2 or more active channels). To enable its synchronisation in time domain with other hardware, the input and output external trigger channel of the Picoscope was used. The full specification of the Picoscope can be found at www.picotech.com.

RAM-5000 – High Power Function Generator and Amplifier
RAM-5000 by RITEC Inc. was used for generating the waveforms required to drive piezoceramic transducers in air coupled applications. The device worked by gating a continuous waveform generated by a synthesiser, then amplifying it to produce the final output pulse. The built-in analogue, low pass and high pass filter of the RAM-5000 were also used. The device was controlled using a PC with RITEC's own software.

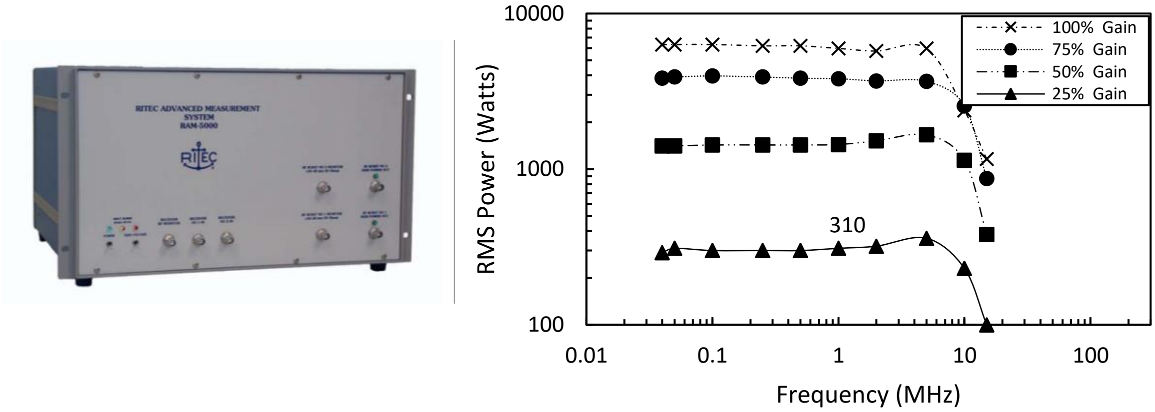

Figure 3-7: RAM-5000 series high-power gated RF amplifier photo and power curve (manufacturer: RITEC Inc) used for sensing oscillating electrical pulse excitation to the transducer, and for amplification and filtering of signal received by the transducer before being transmitted to the Picoscope.

The pulse repetition rate (trigger frequency) of the gated amplifier was limited by the maximum duty cycle of 0.3%, the signal frequency, and the number of cycles in the pulse, given as follows:

$$Trigger\ frequency = \frac{signal\ frequency}{Number\ of\ cycles} \times\ 0.3\% \qquad \text{Equation 41}$$

More information on RAM-5000 series can be found at www.ritecinc.com.

3.1.4 Auxiliary Measurement Systems

Figure 3-8 shows the temperature measurement system (used for work presented in Chapter 8) and the angular position measurement system (used in the bore form measurement rig).

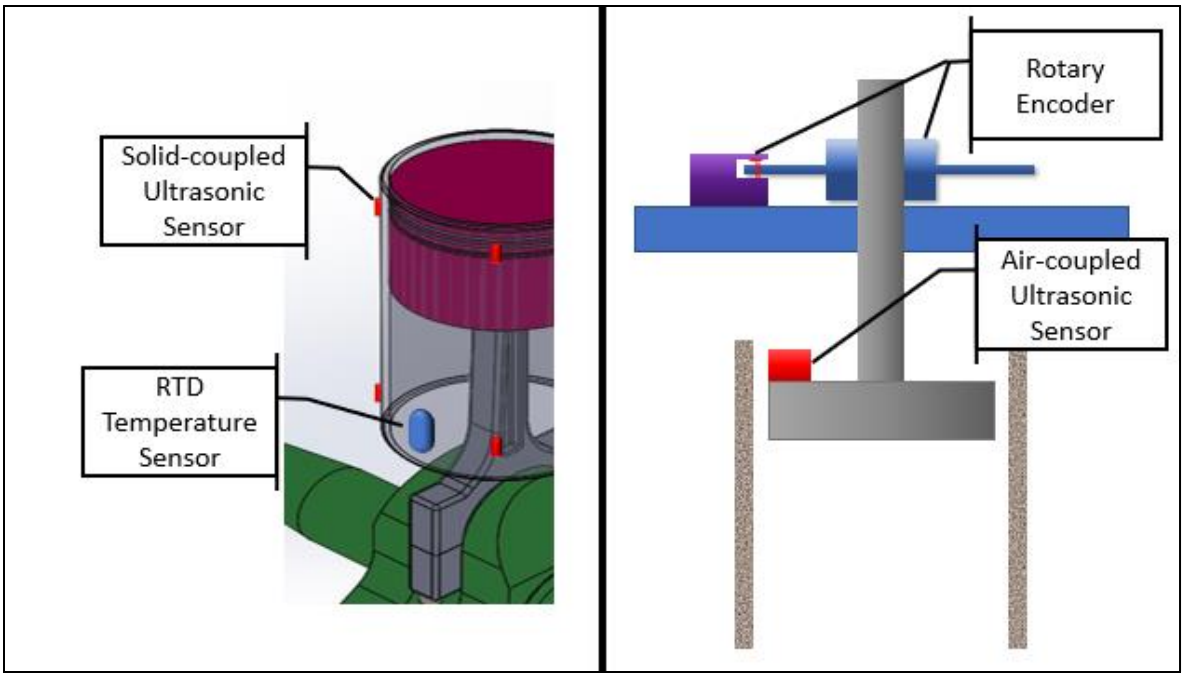

Figure 3-8: Mock-up representations of in-situ ultrasonic measurements with auxiliary measurement systems. (LHS) RTD temperature sensor used to measure reference temperature used to correct wave propagation velocity. (RHS) Optical rotatory encoder used for angular position measurement of the sensor.

3.1.4.1 Temperature Measurement Using RTD Sensor

RTD transducers were used for temperature measurement applications. They work by measuring the change in resistance of a metal resistor with changing temperature. The resistance is measured using an ADC device using a Wheatstone bridge configuration and this is subsequently converted to temperature reading.

PT100 RTD transducers with platinum resistive elements were used. They were bonded using the same method as piezo transducers, as shown in §3.1.1. NI9217 DAQ from National Instruments was used to measure the changing resistance of the RTD. The DAQ was installed into a cDAQ-9171 chassis and connected to the PC where a LabVIEW® programme was used to acquire the temperature measurements. Figure 3-9 shows the wiring diagram of a 4 wire RTD transducer connected to NI-9217 DAQ.

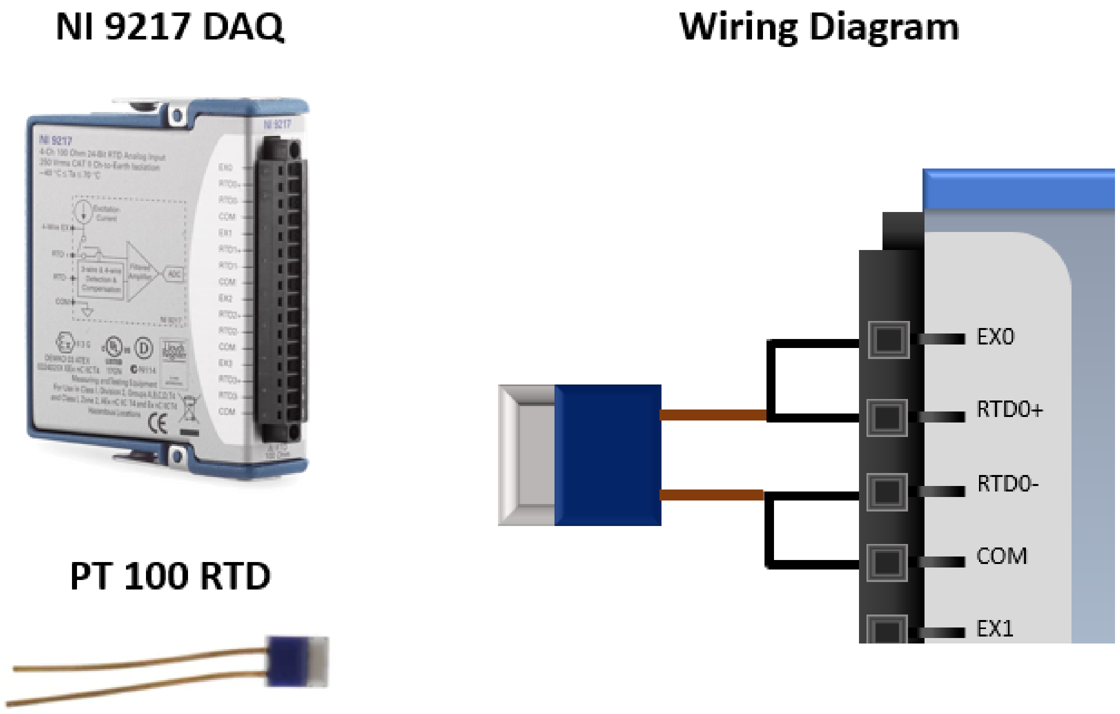

Figure 3-9: PT100 RTD temperature sensor, and NI9217 DAQ for data acquisition from the RTD. DAQ maximum sample rate: 400Hz; DAQ resolution 24 bits; range -200 °C to 850 °C.

Figure 3-10 shows the error in temperature measurement using PT100 Class-A RTD transducer (RS part no. 611-7788), while using the NI9217 DAQ.

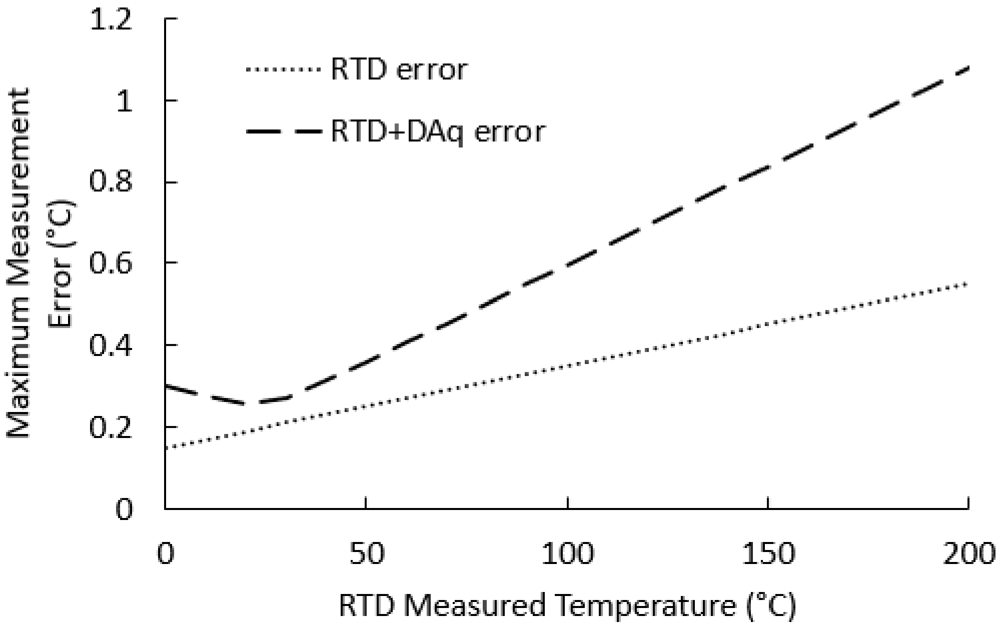

Figure 3-10: Measurement error in temperature value measured using a Class A PT100 RTD and NI DAQ 9217. Value for DAQ error in the plot was obtained from the data sheet of DAQ — based on approximate errors at 25°C and 70°C.

3.1.4.2 Angular Position Measurement Using Rotary Encoders

Figure 3-11: (Left) HEDs-9040-B00 encoder and HEDS-6140-B09 codewheel. (Right) NI USB-6002 DAQ used to power the encoder and obtain count output from each channel using the built in counter of the DAQ.

For angular position measurement of the rotating shaft in §3.1.6, an optical incremental encoder module, HEDs-9040-B00 and HEDS-6140-B09 code wheel were used. The encoder consists of a parallel beam LED light source opposed by an array of photodiode detectors. The integrated circuit of the detector produces a digital waveform which is correlated to the angular position of the wheel. When the code wheel rotates, the pattern on the wheel interrupts the light and this is converted to the angular position measurement of the sensor. Figure 3-11 shows the encoder components and the NI USB-6002 DAQ used for data acquisition from the encoder. Figure 3-12 shows the encoder working principle.

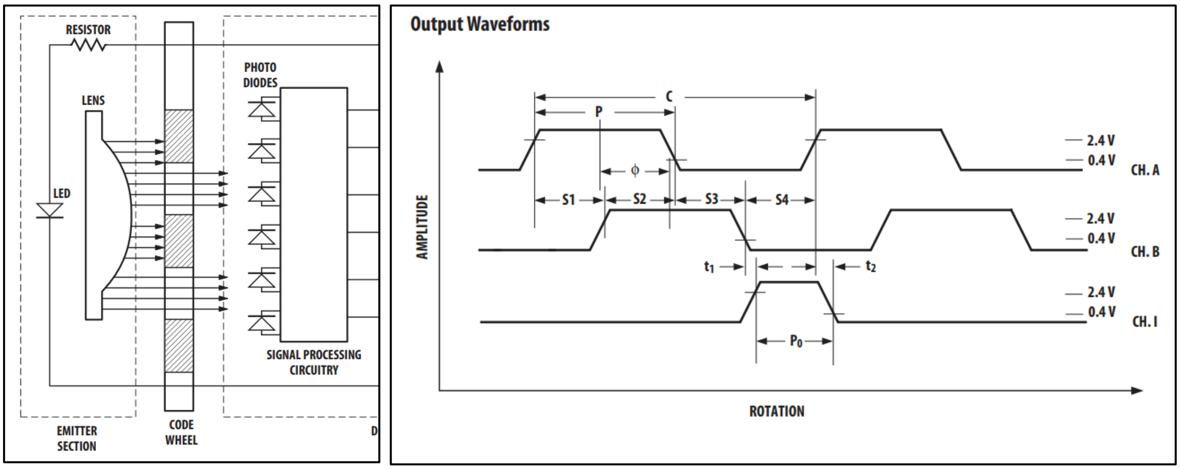

Figure 3-12: Rotary encoder and NI-6002 DAQ. *Figures obtained from the datasheet of HEDs-9040-B00.*

Two USB-6002 DAQ from National Instruments were used to obtain CH. A and CH. I count from the encoder module. This setup limits the rotational measurement to one direction, but serves the required purpose. A LabVIEW based program was used to obtain the angular position of the code wheel, θ_{wheel}, calculated from count output, from CH. A, C_A, as follows:

$$\theta_{wheel} = (N_A/1000) \times 360 \qquad \text{Equation 42}$$

$$N_A = C_A \bmod 1000, \qquad C_A \in \mathbb{N}$$

The count system was set to reset whenever the Index count, from CH. I, N_I, increased by one. Therefore, after each full rotation, the angle was reset to 0 degrees. $Count \bmod 1000$ refers to modular counting.

3.1.5 Air coupled sensor evaluation rig

A benchtop rig was built which was used for the evaluation of air coupled probes. The rig allowed for the swapping of the ultrasonic probe and the reflector target (the component which reflects the ultrasonic waves). The distance of the probe from the reflector target was varied by using the micrometre dial. For the reference distance measurement, the micrometre dial reading and eddy current probe (range 2mm, quoted error 0.25µm) were used. The eddy-current probe reading was found however to vary more than 2/3 microns, and thus a laser displacement sensor was used instead for final calibration; see Chapter 6 for further details. Figure 3-13 shows the rig and its components.

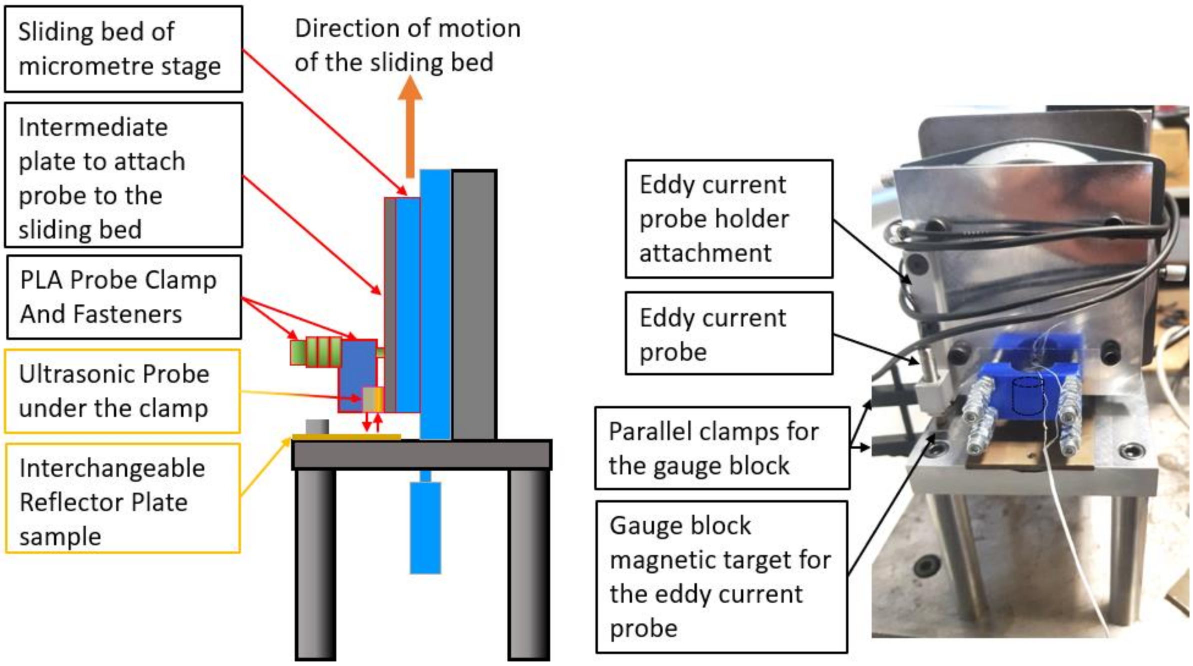

Figure 3-13: Air coupled probe evaluation rig made by adapting a micrometre stage (in light blue). The components which slide are boxed in red in the schematic. The components filled in yellow are the test specimens. (RHS) Photo of the rig with eddy current displacement sensor mounted onto it along with its accessories.

Transducer clamps were designed using 3D printed polylactic acid (PLA) which allowed the placement of 2 probes at an angle to be used in the pitch-catch setup, or one probe to be used in pulse-echo mode. Figure 3-14 shows some angled clamps that were manufactured. The transducer clamp shown in Figure 3-13 is the clamp that was used for pulse-echo mode.

Figure 3-14: Angled clamps made using PLA that were used to clamp the ultrasonic probes onto the two rigs.

Figure 3-15 shows a photograph of the rig while Appendix C shows the assembly drawing of the rig.

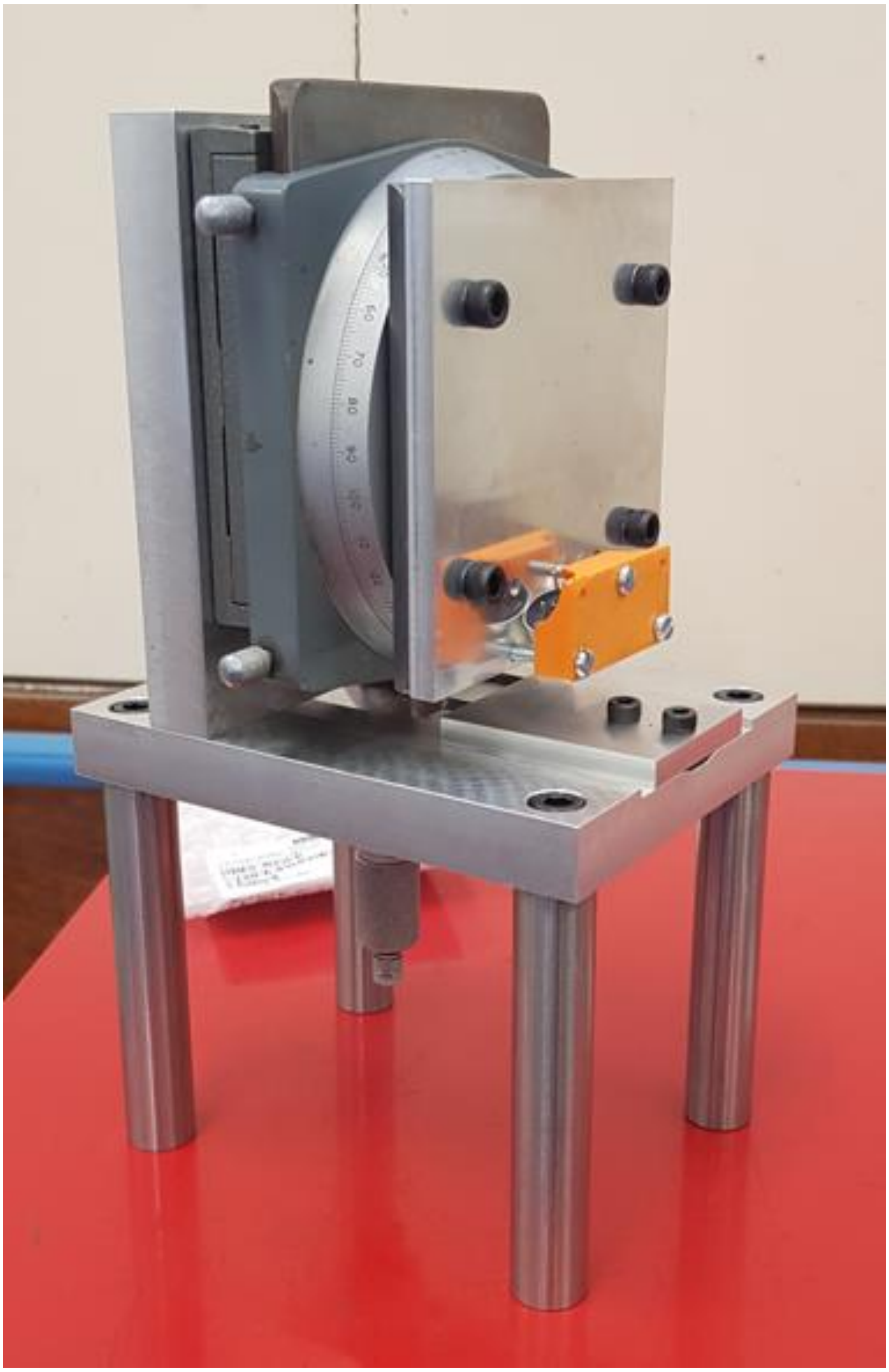

Figure 3-15: The rig setup with the eddy current displacement sensor removed, and with angled transducer clamp to conduct measurements in the pitch catch mode.

3.1.6 Bore form measurement rig

For the in-situ bore form measurement of the cylinder liners using air-coupled probes, a rig was designed and built to mimic the honing environment. Figure 3-16 and Figure 3-17 show a CAD model of a section and a photograph of the rig, respectively, highlighting the key components.

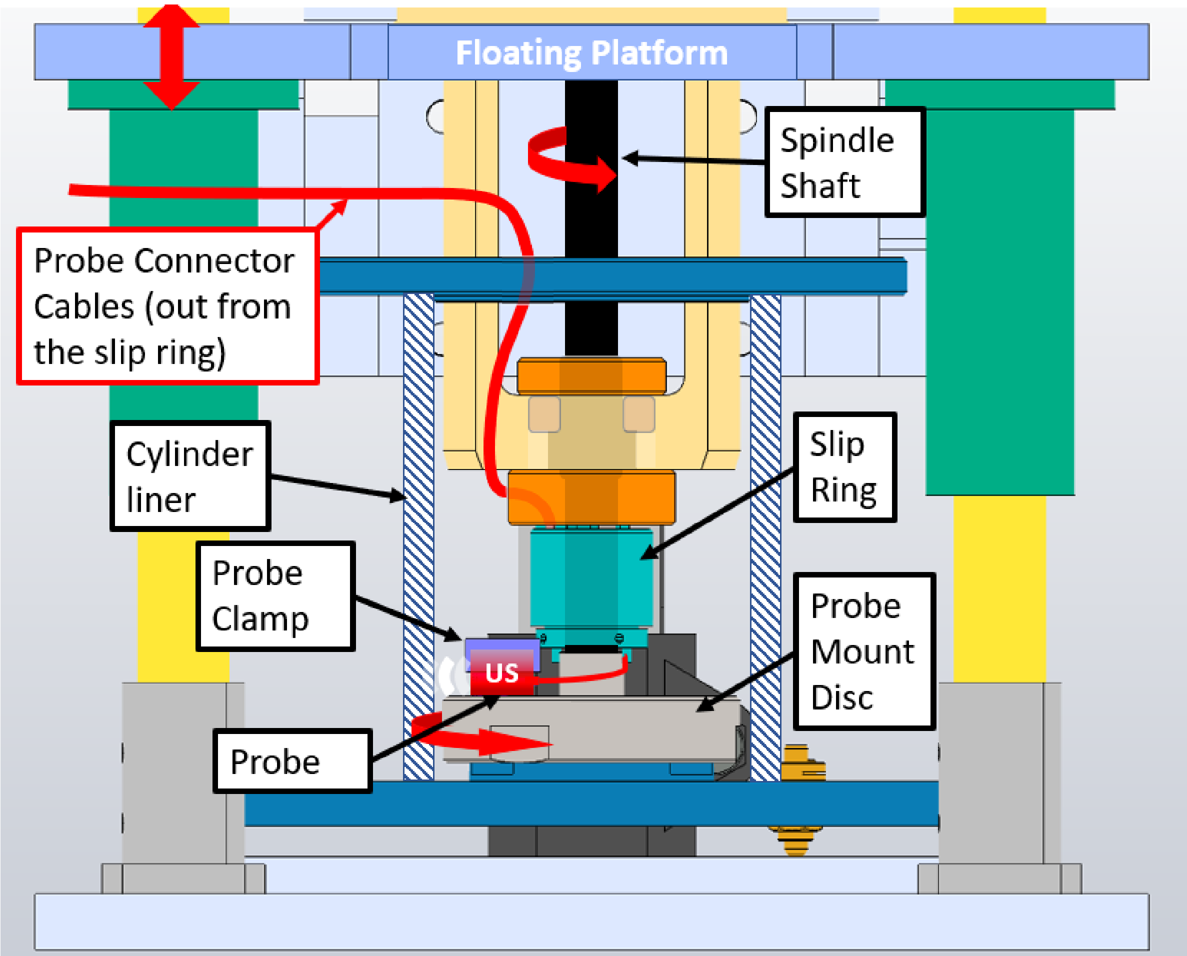

Figure 3-16: CAD model of a section of the bore form measurement rig with components of the rig that were rotating, and the cylinder liner labelled.

The test rig was designed to mimic honing process as this would highlight any measurement error when using an air-coupled ultrasonic sensors for cylinder bore form measurement, in honing machines. The rig design was also influenced by the intention of using it as a demonstration kit.

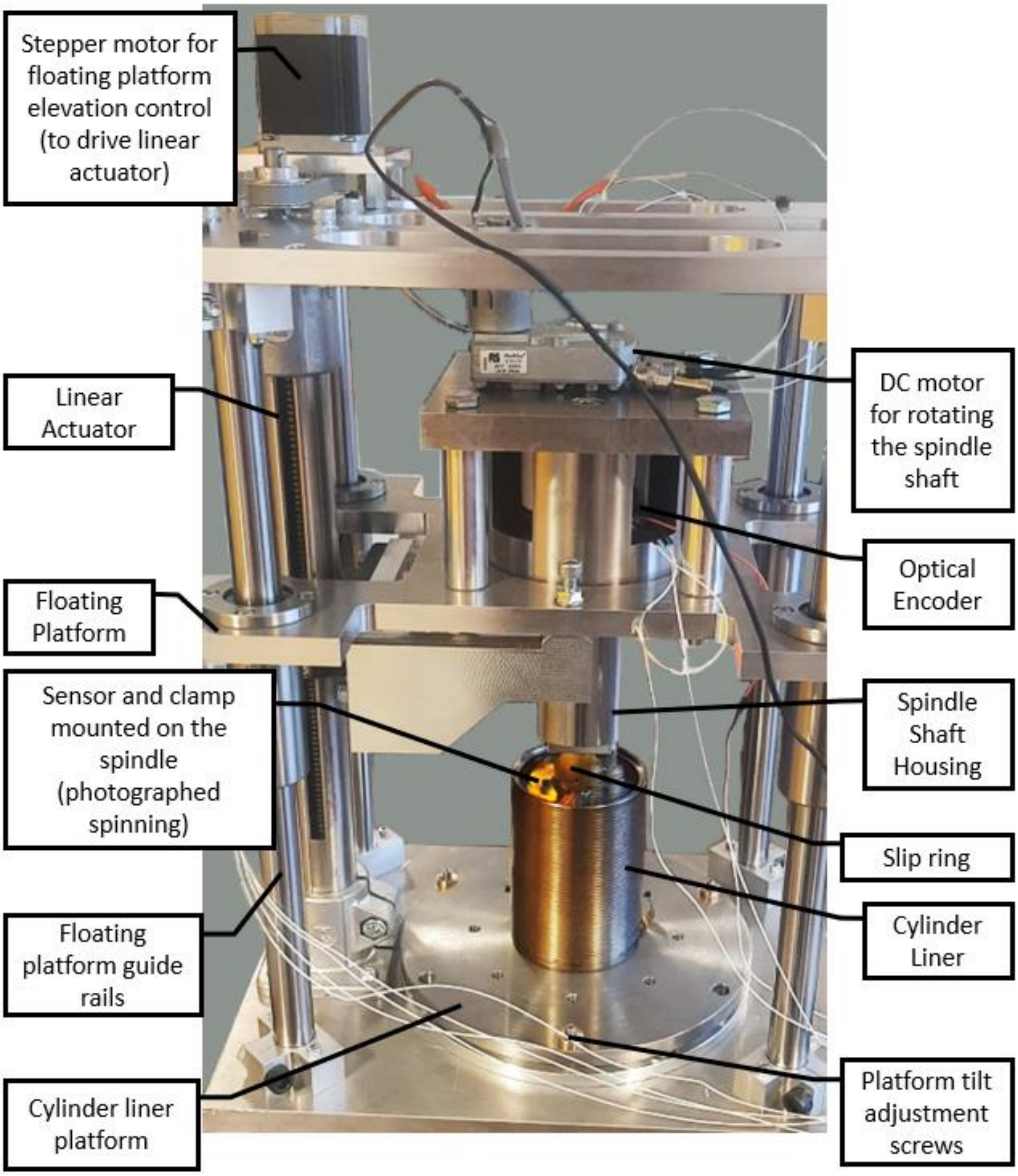

Figure 3-17: A photograph of the in-situ bore form measurement rig. Photographed during operation using long exposure mode of the camera to give the effect of the sensor spinning.

The spindle shaft is connected via a flexible bellow coupling and driven by a 24V 200RPM DC motor. The motor was controlled using ‘Arduino motor shield rev 2’ and an Arduino mega 2560, while the stepper motor was controlled using ‘Stepper Motor Control Shield with IFX9201 & XMC1300’ and the same Arduino. The *CH. I* output from the encoder module was fed to the Picoscope, while *CH. A* and *CH. I* were each connected to NI6002, and subsequently to the PC, to be used for angular position and velocity display of the spindle. Figure 3-18 shows a photograph of the electronic hardware used for controlling the rig, for taking angular position measurements, and for ultrasonic data acquisition.

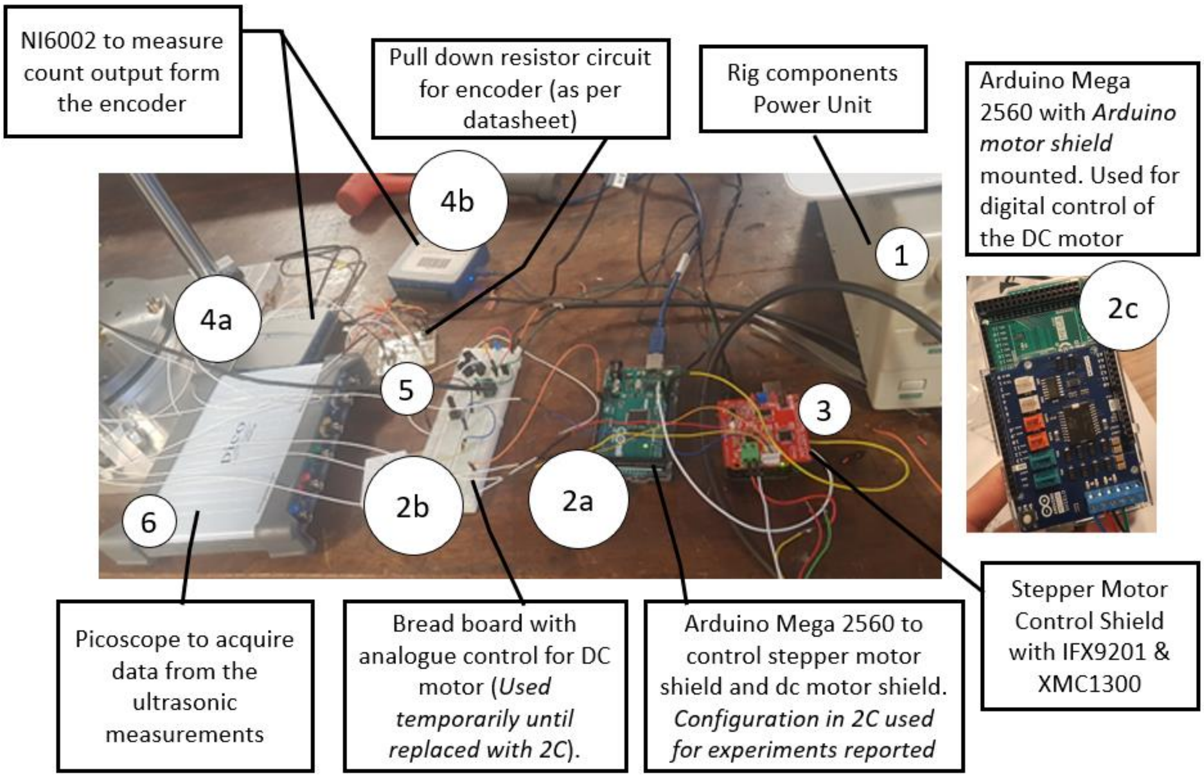

Figure 3-18: Bore form measurement rig electronic hardware. RITEC RAM 5000 gated amplifier used to pulse the probes not shown. A photograph shows a bread board to control the DC motor, however, during the experiments reported in the thesis an Arduino motor mount was used, as shown as per label 2c.

Figure 3-19 shows the front panel of a LabVIEW program used to control the rig.

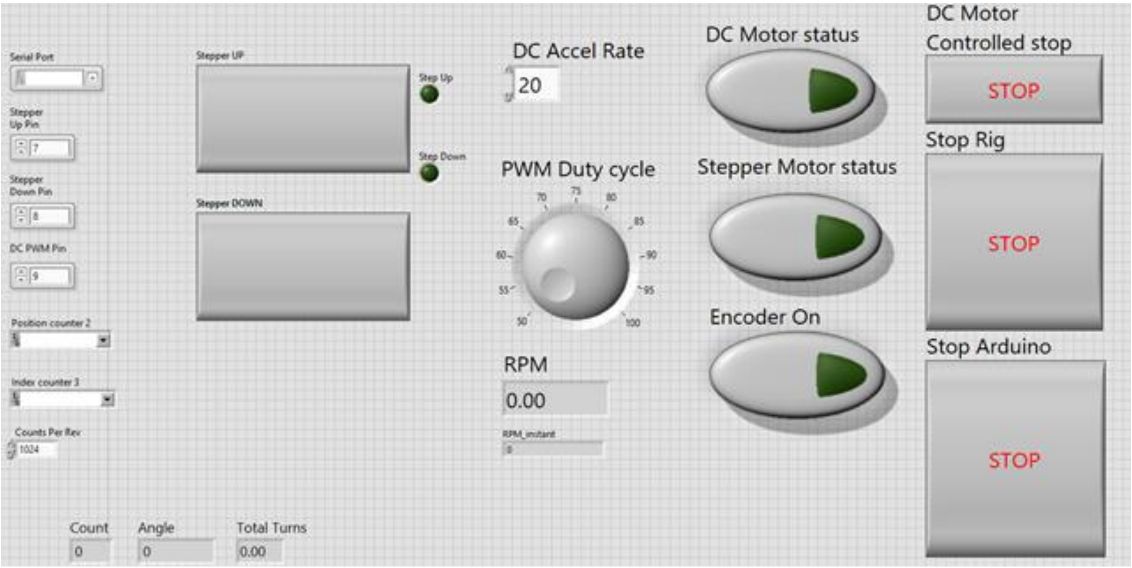

Stepper Up Pin 7

Stepper Down Pin 8

DC PWM Pin 9

Counts Per Rev 1024

DC Accel Rate 20

RPM 0.00

RPM_instant 0

Count 0

Angle 0

Total Turns 0.00

Figure 3-19: Front panel of the bore form measurement rig control program designed in LabVIEW.

Figure 3-20 shows the method used to wire the ultrasonic probes to the slip ring. While the rig was designed to operate up to four sensors at any time, limitation in the pulsing hardware meant only a maximum of two sensors could be utilised. The slip ring accommodates up to 5 if the same ground is shared between the sensors.

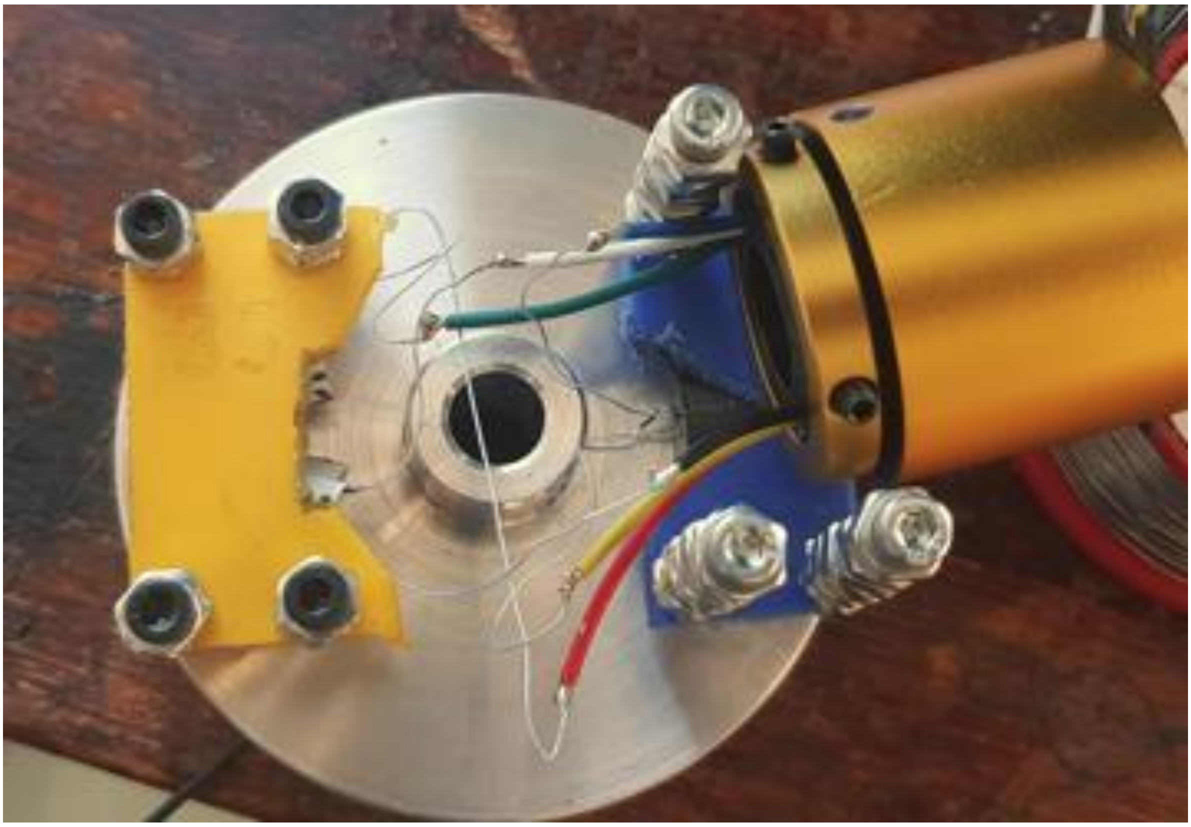

Figure 3-20: Photo showing the wires of the slip ring connected to two probes (to work in pitch-catch mode).

3.1.6.1 Probe Vertical and Rotation Position Precision

The rig measures the bore form at 1000 locations in a complete circle while also traversing axially in the vertical direction to measure the full-bore form. The accuracy of the angular reference location measurement output by the rig is assumed as ±1/1000, degrees accounting for the eventuality that the optical encoder misses a count, or that there may be a problem with triggering.

The vertical position of the platform (where the probe is mounted) was changed using a linear actuator with a screw lead of 4mm (i.e. the platform travelled 4mm vertically per full turn of the actuator screw). The actuator was connected to a driver stepper motor using a timing belt pulley with 2:1 gear ratio. The resulting vertical motion was 800 steps/4mm, and therefore a resolution of 5μm/step.

3.1.6.2 Rig Design Parameters used to Improve Spindle Accuracy

Figure 3-21 shows the cross-section of the rig assembly, highlighting the design used to ensure a concentric rotation of the shaft spindle. Two super precision angular contact bearings (7002A5TRSUL - P3) were used at a distance of 123mm (distance between outer face to outer face) and held in place using the bearing lock nut that was loaded to ensure minimal eccentricity during rotation. Furthermore, the holes for the bearing in the shaft housing were machined to 32mm JS6 (±8μm), while the outer diameter of the shaft to sit on the bearing was machined to 15mm js5 (±4μm).

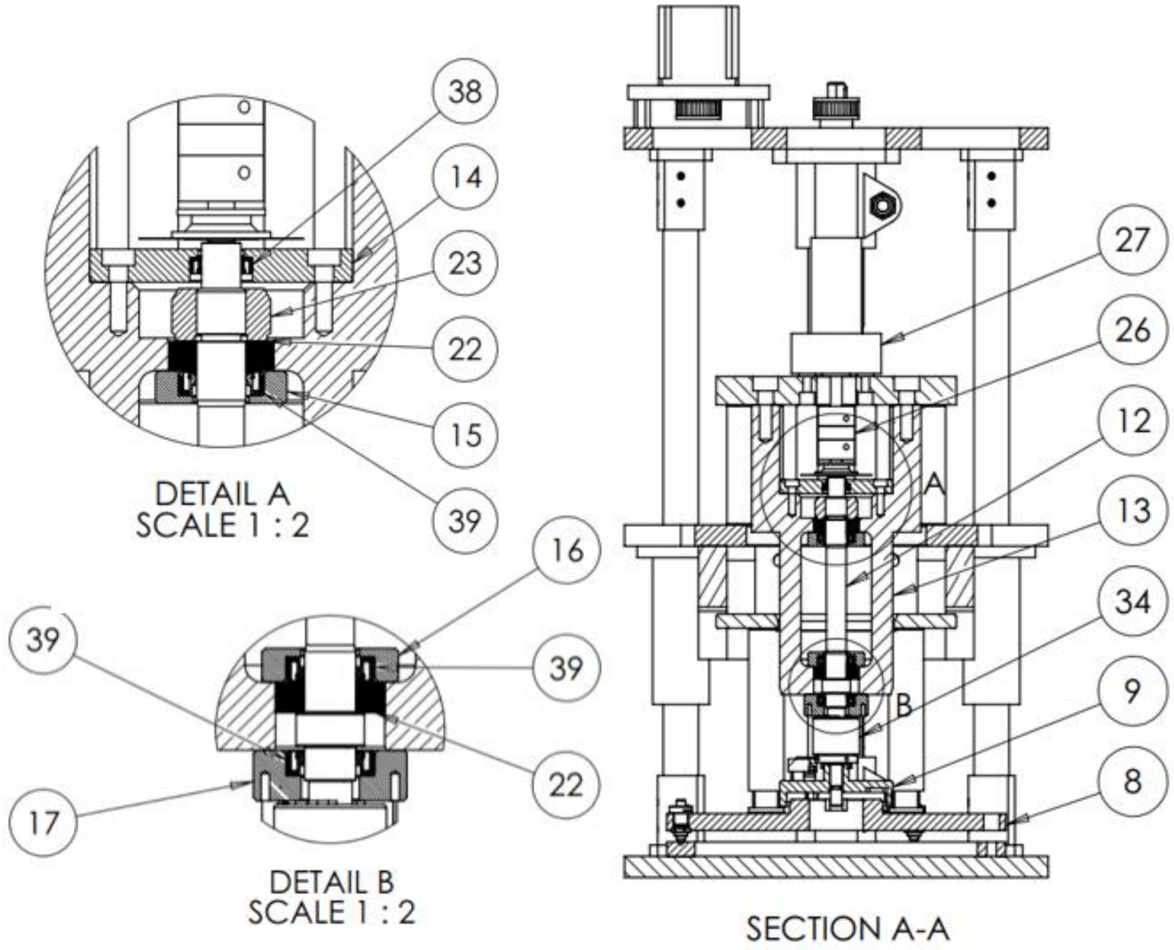

Figure 3-21: Figure showing the shaft mount (part no. 13) which was line bored to machine the hole for bearing housing (bearings part no. 22).

Figure 3-21 also shows the platform where the cylinder is mounted (Item no. 8). To ensure the cylinder liner axis had minimal tilt, the rig was designed to clamp the liner using a lid (see Figure 3-23). The platform had 3 tilt adjustment screws legs (with 100 threads per inch) equally spaced over a diameter of 220mm.

Figure 3-21 also shows the transducer mount plate with a cup and cone fitting to a boss on the liner pedestal. This physical fit setup was chosen to ensure the liner was mounted concentric to the to the spindle. The goal of the adjustment screws was to allow this cup and cone fit to take place, thereby implicitly aligning the probe concentric to the liner.

Figure 3-22 shows the ultrasonic probe mounted onto the spindle.

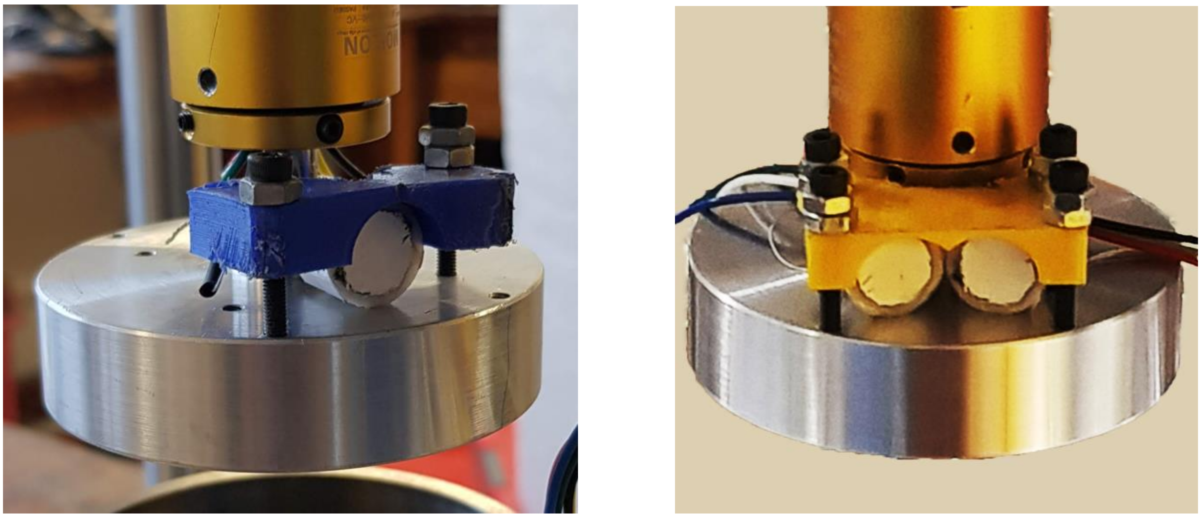

Figure 3-22: Bore form measurement rig spindle disc, with ultrasonic probe mounted onto it using 3D printed PLA clamps. The figure also shows the MOFLON slip ring used to connect the ultrasonic probe to the function generator and oscilloscope devices. The rig is designed to accommodate a total of 4 sensors - 2 sets for pitch-catch mode; when used in pulse-echo mode, only 2 transducers could be used, although spindle disc could be redesigned to allow the use of up-to 5 transducers.

The probes can be seen placed roughly ~10mm away from the edge of the mount plate in pulse-echo mode (using only one single sensor). In pitch-catch mode the angle between the two probes and their exact relative position would need to be considered. Due to the difficulty in knowing the exact location of the two probes in pitch-catch mode, only the results of the pulse-echo mode were used for the bore form measurement, i.e. for the work reported in Chapter 7.

The probes were connected to the RITEC gated amplifier and the Picoscope through a slip ring (MOFLON MT1233-S08-VD).

The final rig assembly is shown in Figure 3-23. Appendix C shows the assembly drawing for the rig.

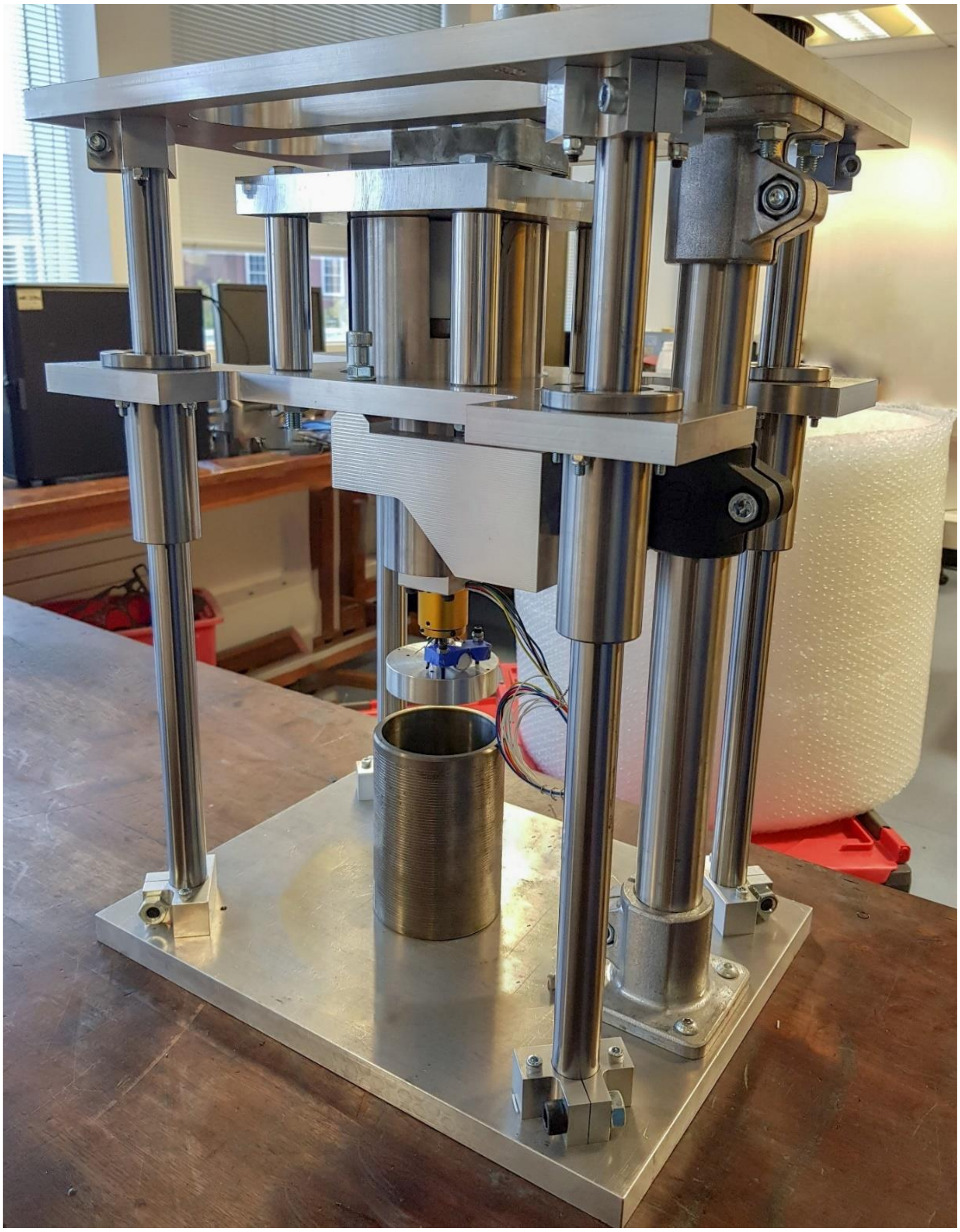

Figure 3-23: Fully assembled bore form measurement rig. In the photograph, the cylinder liner mounting platform and the stepper motor are removed from the assembly.

Due to difficulties in getting the tilt correction mechanism to be fully functional prior to the national lockdown in early 2020 due to COVID-19, it was decided to conduct the experiments and employ a digital method for tilt correction. See Chapter 7.

3.2 Overview of the Data Acquisition Process

Signal acquisition hardware such as the Picoscope 5442B, NI9217 or NI USB-6002 consists of a *digitiser* which carries out the ADC. The ADC process of a digitiser can be conceptualised as *sampling* and *quantisation*, however in reality the two are coupled, and may consist of various steps depending on the digitiser.

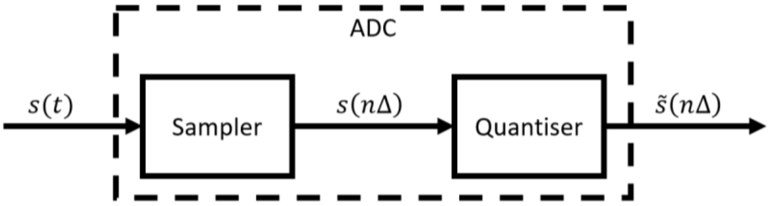

Figure 3-24: Conceptual diagram of the analogue-to-digital conversion (ADC) process.

Figure 3-24 shows the concept of ADC; $s(t)$ is sampled at $t = n\Delta$ (Δ = time increment, also known as the *sample period*, and n = nth sample), i.e. $s(n\Delta) = s(t)$. $s(n\Delta)$ is then quantised to its closest bit representation, $\tilde{s}(n\Delta)$. A finite number of *bits* can be used to represent $\tilde{s}(n\Delta)$. If the maximum possible value of $\tilde{s}(n\Delta)$ is A_{max} and its minimum possible value is A_{min}, then $\tilde{s}(n\Delta)$ is said to have a *range*, $R(= A_{max} - A_{min})$. The possible values of $\tilde{s}(n\Delta)$ are 2^{bit} individual numbers, starting at A_{min} then going up by increments, $I = R/2^{bit}$ up to A_{max}. Values outside the range are *clipped*, i.e. output past the range is set as A_{min} or A_{max}, as follows:

$$\tilde{s}(n\Delta) = \begin{cases} A_{max}, & s(n\Delta) > A_{max} \\ A_{min}, & s(n\Delta) < A_{min} \end{cases}, \qquad \tilde{s}(n\Delta) \in 2^{bit} Rate$$

Figure 3-25 shows the ADC process of digitising an analogue signal with varying number of bits.

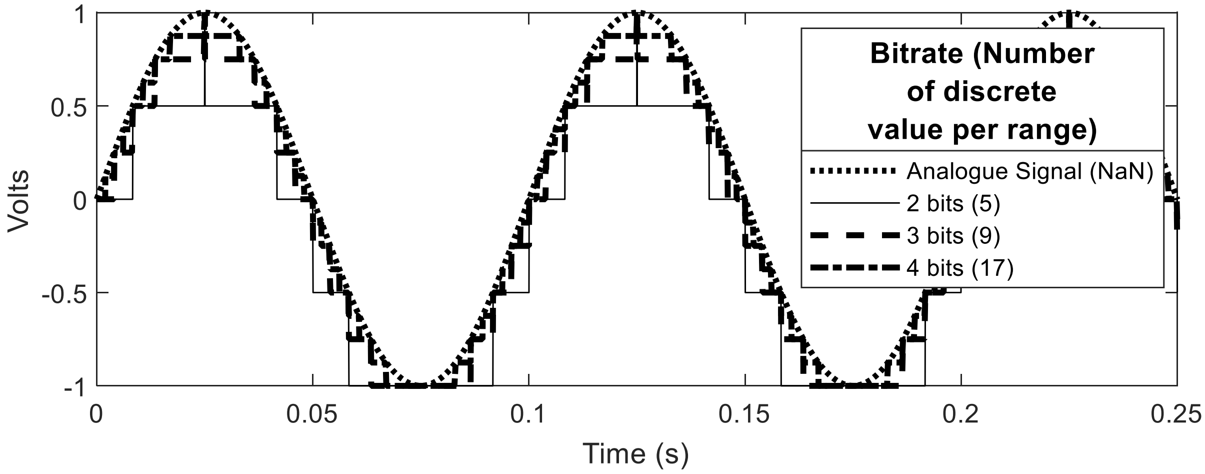

Figure 3-25: Comparison between signal digitised at varying bitrate. The legend shows the number of discrete values for the varying bitrate, respectively, in curly brackets.

The *sample rate* (*sampling frequency*), F_s, is the inverse of the sample period, Δ. There exists a limit to the minimum value of F_s which can be used to digitise any signal defined as:

$$\min[F_s] > 2f_{max} \qquad \text{Equation 43}$$

Where, $f_{max}$is the maximum frequency component of interest off the analogue signal. Sampling below the minimum *sample rate* causes the signal to be aliased and the acquired signal become indistinguishable; see §3.3.3.

3.3 Signal processing

Various digital transformations were applied using their corresponding algorithm, to reduce noise in the acquired waveform and extract measured experimental parameters.

Any acquired signal from a measurement system can be susceptible to having signal noise superimposed onto the signal. Some causes of noise are random, while some can result from external input that is yet to be accounted for. Some processes, such as grain scattering of ultrasonic waves, are not random although they still contribute to noise in measurement. Some other examples of noise in ultrasonic measurements, which were present in the experiments conducted, are the impact of turbulence on ultrasonic measurements in fluids, the impact of temperature fluctuations due to wave propagation, and non-linearity in electronic components.

The ratio between the systematic parameter (signal) and the noise component of the signal is termed signal-to-noise ratio (SNR). SNR is presented as follows:

$$SNR = \frac{Signal\ mean}{Standard\ deviation} \qquad \text{Equation 44}$$

Methods employed to remove the noise component in the acquired signal included taking an average of many individual measurements and/or applying a digital filter.

Both signal averaging and digital filtering can reduce the random noise, which are generally at frequencies close to half of the sampling frequency of the digitiser (of the ADC device). Digital frequency filters however do not take account of the environmental factors, e.g. shaking of the ultrasonic sensor at a rate slower than signal acquisition frequency. Digital filters are also limited in their capability to remove random noise components which are at or near the probe excitation frequency. Signal averaging is limited in removing the impact of low frequency signal distortion, for example due to the electronic circuit. Taking these into consideration, both the tools were utilised to increase SNR. Figure 3-26 shows the impact of signal averaging of 100 acquired waveforms and transforming the signal using a digital filter.

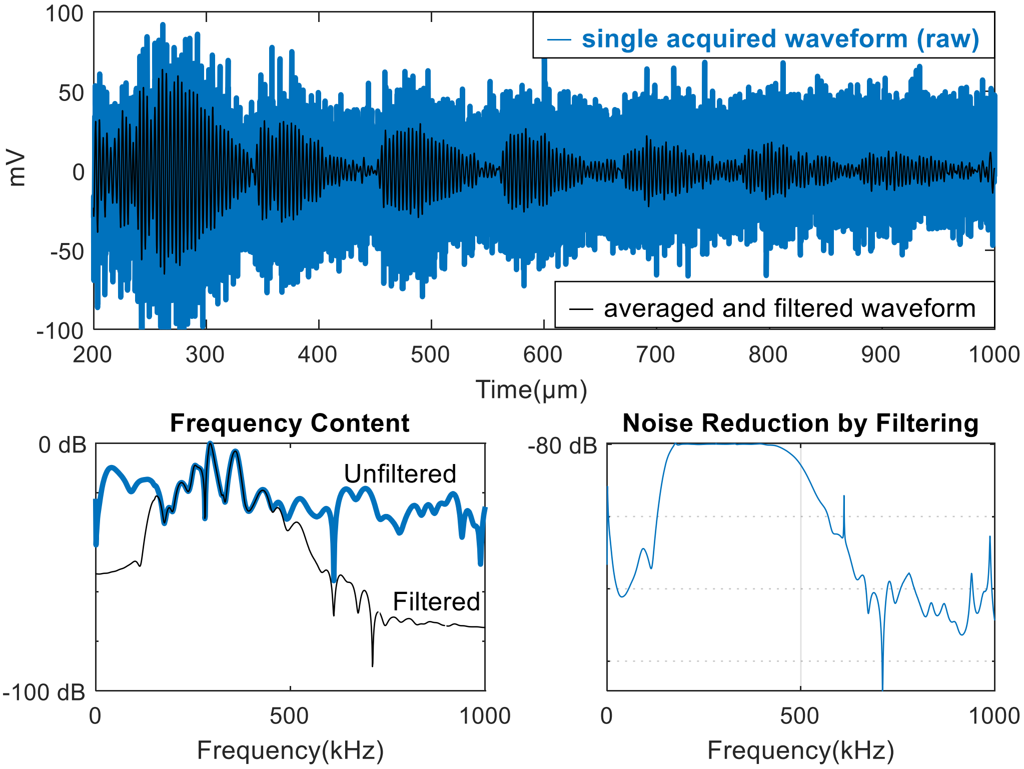

Figure 3-26: Impact of signal digital filtering on acquired signal. (Top) one of 100 raw acquired waveforms and averaged and filtered signal. (Bottom) Frequency domain of the two time domain waveforms on the top figure.

3.3.1 Signal Envelope

Some measurements required the *analytic signal amplitude* instead of the oscillating waveform. The *analytic signal* is a complex signal composed of the acquired signal as the *real* component, while the signal transformed using the Hilbert transform is its *imaginary* component. The absolute value of the instantaneous signal (instantaneous amplitude) was used to obtain measurements for time of flight that relied on identification of the time when the signal crossed a voltage threshold (see Figure 3-28).

The Hilbert transform of a signal, $s(t)$, is the output $\hat{s}(t)$ such that $s(t)$ is convoluted with $h(t) = \frac{1}{\pi t}$, thereby shifting the phase of the input signal by 90°.

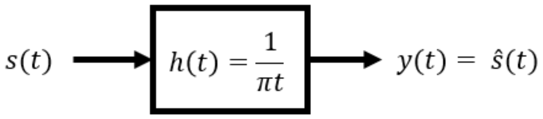

Figure 3-27: Block diagram of the input-output relationship of 90° phase shifted signal.

And the *analytic signal,* $a(t)$ is given as per:

$$a(t) = s(t) + j\hat{s}(t), \qquad j = \sqrt{-1} \qquad \text{Equation 45}$$

The magnitude of $a(t)$ is known as the *instantaneous amplitude,* $A(t) = |a(t)| = \sqrt{s^2(t) + \hat{s}^2(t)}$. *Instantaneous phase,* $\phi(t) = \tan^{-1}\left(\hat{s}(t)/s(t)\right)$; *Instantaneous frequency,* $f(t) = \frac{1}{2\pi}\frac{d\phi(t)}{dt}$.

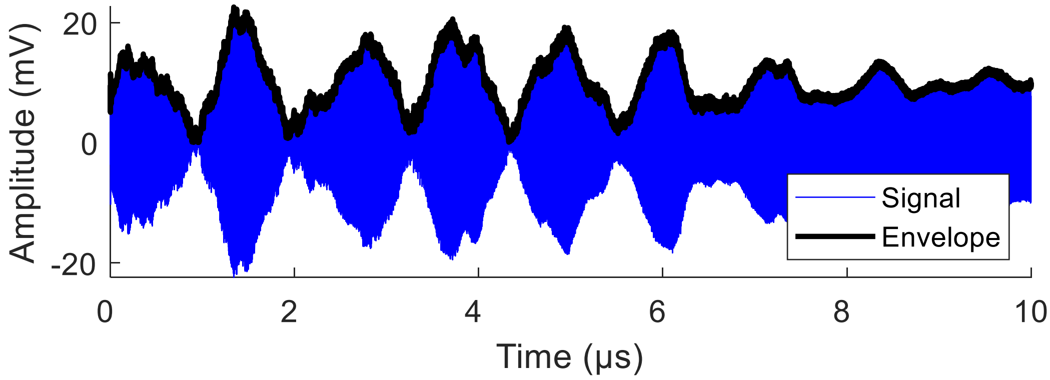

Figure 3-28: Acquired signal and the signal envelope (instantaneous amplitude). Acquired signal corresponds to frequency sweep excitation acquired using 2 transducers in pitch-catch mode and where the medium resonates at various frequencies.

3.3.2 Correlation

The degree of association (correlation) of discrete signal vectors $q(n\Delta)$ and $r(m\Delta)$ is given by:

$$C_{qr}(m\Delta) = \frac{1}{N-m}\sum_{n=0}^{N-m-1}\left(q(n\Delta) - \bar{q}\right).\left(r\left((n+m)\Delta\right) - \bar{r}\right), \qquad 0 \le m \le N-1$$

Where $\bar{q}$ and $\bar{r}$ are the mean value of the signal vectors q and r respectively.

If $q = r$ then correlation, $C_{qr}(m\Delta)$ is a measurement of the self-similarity of the signal at different points in time; this is known as *autocorrelation*. If $q \neq r$ the process is known as *cross-correlation* and the output $C_{qr}(m\Delta)$ is a measurement of the similarity between the two signals at different points in time. The correlation function offers an advantage in minimising the impact of noise. Figure 3-29 shows an example of autocorrelation and signal envelope used to identify the average distance between locations of the maximum amplitude (the peaks) in Figure 3-28.

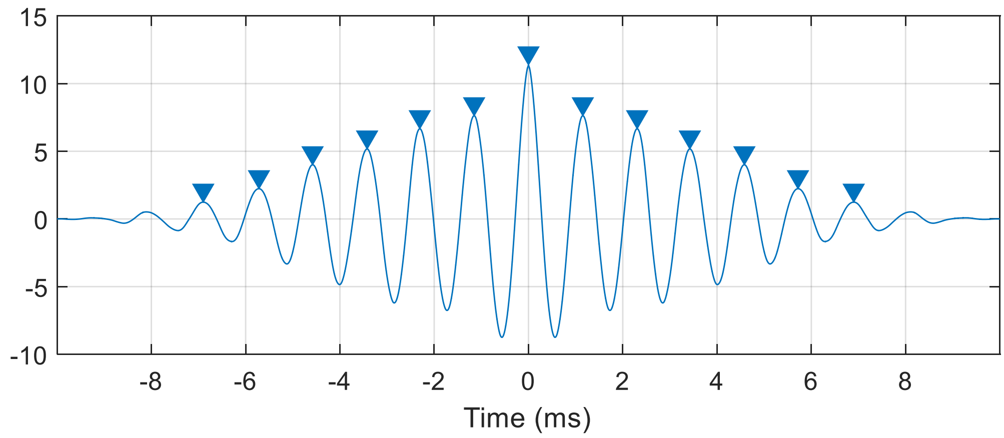

Figure 3-29: *Autocorrelation* used to find the average distance between the locations of maximum amplitude in Figure 3-28. The figure shows only the envelope of the autocorrelated signal and the location of the peaks on the envelope. The same method can be employed to find the average time difference between several reflected echoes, when processing the waveform acquired using pulse-echo mode.

3.3.3 Transformation to Frequency Domain

Analysis of the acquired digital signal vector in the frequency domain is made possible using *Discrete Fourier Transform* (DFT). The application of DFT was carried out by using the fast Fourier transform (FFT) algorithm. DFT allows the computation of the discrete Fourier coefficient vector, C_k (frequency magnitude and phase information) corresponding to a discrete data vector, s_k, with N discrete data points. The forward and the backward transform between $s_k \rightarrow C_k$ and $C_k \rightarrow s_k$ are given as follows:

$$C_k = \sum_{m=0}^{N-1} s_m e^{-i2\pi m\frac{k}{N}} \qquad \text{Equation 46}$$

$$s_k = \left(\sum_{m=0}^{N-1} C_m e^{i2\pi m\frac{k}{N}} \right) \qquad \text{Equation 47}$$

Where, $1 \leq k \leq N$, $k \in \mathbb{N}$. k in the exponent corresponds to the k^{th} fundamental angular frequency, $\omega_{k=}\frac{2\pi i}{N}$, and in terms of fundamental frequency, $f_k = \frac{i}{N}$.

Given the limit in maximum frequency which can be measured by the Nyquist-Shannon critical frequency criterion, the maximum fundamental frequency of a signal attained by transforming it to the frequency domain is,

$$f_{k,max} = \frac{F_s - 1}{2}$$

Where, F_s is the sampling frequency.

3.4 Conversion of a Waveform to Distance Measurement

Once the noise removal processes and the various digital transformations are carried out, the resultant signal can be used to obtain information on the physical parameters. It should be noted that all measurements will have a degree of uncertainty due to the signal to noise ratio and any systematic error that is present in the measurement. Figure 3-30 shows the typical steps in data acquisition and signal processing used to obtain experimental data.

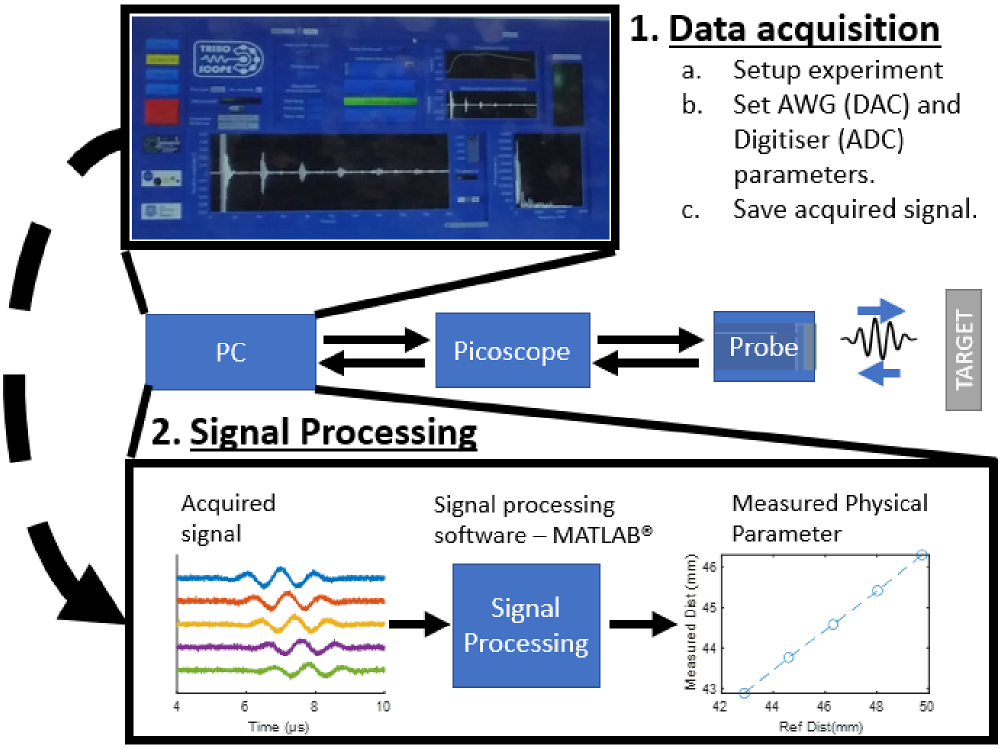

Figure 3-30: Typical process in obtaining distance measurement (or any physical parameter) by analysis of the measured ultrasonic waveforms.

3.4.1 Transit Time Method

The time taken for a pulse to travel from the interface where it is emitted by the emitter transducer to the receiver transducer is known as the time-of-flight, *TOF*. The length of the *delay line*, i.e. the distance travelled by the wave, L, can be found if the wave propagation velocity, c, in the medium is also known, as follows (Krautkrämer and Krautkrämer, 1990a, p. 223):

$$TOF = \frac{L}{c} \qquad \text{Equation 48}$$

When using the *Pulse-Echo* (PE) method as shown in Figure 3-31 (LHS), $L = 2d$. Thus, the distance between the transducer and the reflecting interface is found as follows

$$d = \frac{TOF}{2c} \qquad \text{Equation 49}$$

When using the *Pitch-Catch* (PC) method (Figure 3-31 - RHS), if the two transducers are sufficiently close, then neglecting the angle of wave path does not incur significant errors. Thus, the method used for PE can be used in the case of PC to obtain the distance, d.

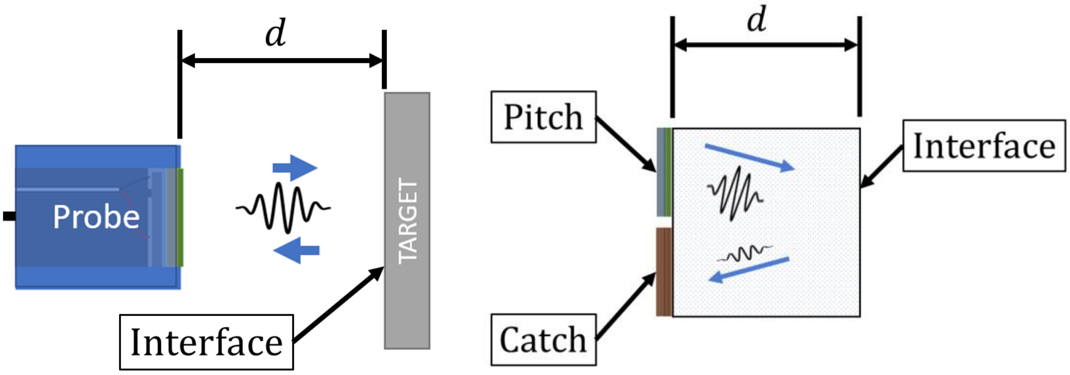

Figure 3-31: Transit time methods used to measure spatial distance, d of the ultrasonic probe/transducers to an interface. (LHS) Typical Pulse-Echo (PE) setup for measuring distance, d to target. (RHS) Typical Pitch-Catch (PC) method for measuring thickness, d of a parallel plate.

Figure 3-32 shows a typical waveform acquired using the PE method, where the distance, d, and its change, Δd were measured.

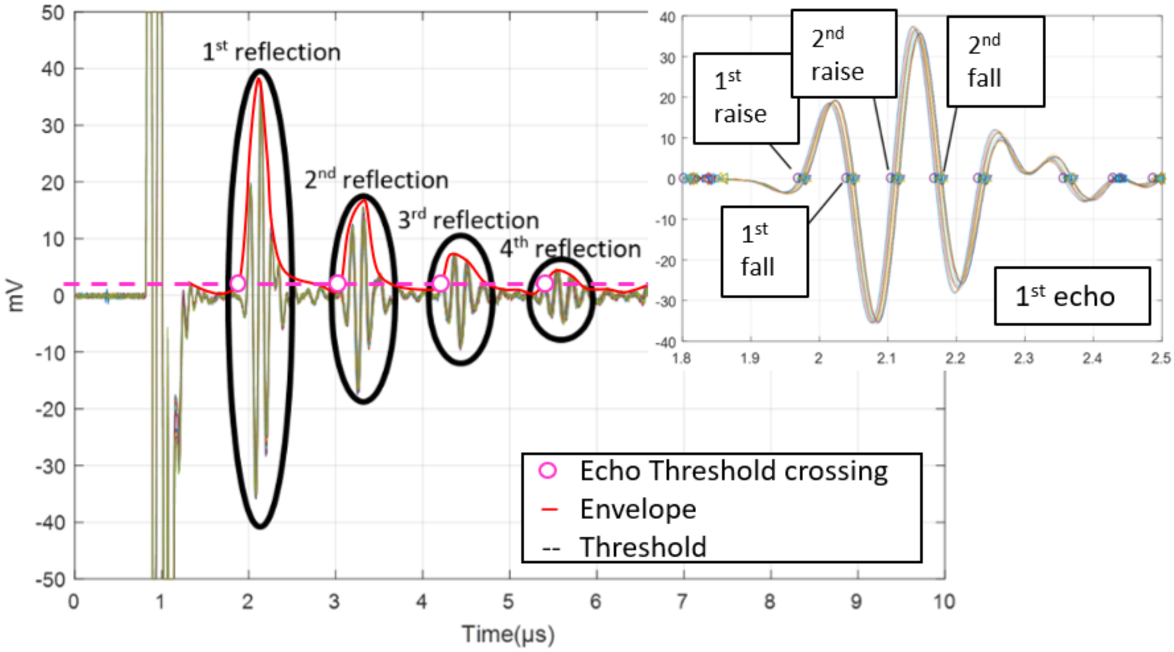

Figure 3-32:Typical pulse-echo measurement of the TOF in an aluminium plate of nominal 3mm thickness. The magnification of the 1st echo distinguishes between 4 *zero-crossings*.

B n n bn

However, the threshold crossing method of obtaining *TOF* is generally susceptible to error, due to effects of noise and wave dispersion. A more accurate measure of *TOF* is the time difference between the same axis crossing (see axis crossings labelled in Figure 3-32) of 2 consecutive echoes (Krautkrämer and Krautkrämer, 1987, pp. 227–230). For example:

$$TOF = T_{2r}^{j+1} - T_{2r}^{j}$$

Where, T_{2r}^{j} and T_{2r}^{j+1} are the axis crossing of 2nd cycle while rising, of the j^{th} and *'j+1'*th reflections.

The correlation function mentioned in §3.3 can also be used to find the *TOF*. For the work reported at present, the waveform within the time window which encompasses 2 consecutive echoes was extracted and its autocorrelation computed; the time of maximum correlation was the *TOF*, provided the two echoes had undergone minimal distortion. Generally, correlation is known to perform better for low SNR (Hull, Kautz and Vary, 1985).

The topic of measurement accuracy of various methods is covered further in Chapter 6 (in §6.2.2).

3.5 Measurement Error Quantification

The probability, $p_{i(x)}$, for an individual measurement, x_n, of the parameter X_i to have an error, $\pm x$ compared to the mean, μ_{X_i} – within n sets of measurements – is given as $p_i(x)$ where:

$$p_i(x) = \frac{1}{\sigma_{X_i}\sqrt{2\pi}} e^{\frac{-\left(x-\mu_{X_i}\right)^2}{2\sigma_{X_i}^2}}$$

Where $\sigma_{X_i}^2$ is the variance of the value X_i, defined as, $\sigma_{X_i}^2 = \frac{1}{N-1}\sum_{n=1}^{N}\left(x_n - \mu_{X_i}\right)^2$; and the mean, $\mu_{X_i} = \frac{1}{N_i}\sum_{n=1}^{N_i} x_n$. While error on X_i is given as the standard deviation, σ_{X_i}, the error on the mean is lower and is quantified by the *standard error of the mean*, $\sigma_{\bar{X}}$:

$$\sigma_{\bar{X}} = \left[\frac{1}{N(N-1)}\sum_{n=1}^{N}(x_n - \mu_X)^2\right]^{1/2}$$

3.5.1 Associated error

If the measured parameter, X_i, with associated error $\pm\Delta X_i$ is the input to a function, *f*, with output, F_i, the associated error in the output, $\pm\Delta F_i$ is approximated as:

$$\Delta F_i \cong \left|\frac{\mathrm{d}f}{\mathrm{d}x}\right| \Delta X_i$$

3.5.2 Error on functions of multiple measurements

If a value, *f*, is a function of several independent measurements, each with their own error, then the error, Δf, in the measurement of *f* is a combination of the independent errors, as per Table 3-1.

Table 3-1: Formulae for error combination

$f = X_1 + X_2$	$(\Delta f)^2 = (\Delta X_1)^2 + (\Delta X_2)^2$
$f = X_1 X_2$	$\left(\frac{\Delta f}{f}\right)^2 = \left(\frac{\Delta X_1}{X_1}\right)^2 + \left(\frac{\Delta X_2}{X_2}\right)^2$
$f = X_1/X_2$	$\left(\frac{\Delta f}{f}\right)^2 = \left(\frac{\Delta X_1}{X_1}\right)^2 + \left(\frac{\Delta X_2}{X_2}\right)^2$

For the quantification of the accuracy of distance measurement, it is appropriate to define the following error parameters on the mean measurement value, X_i, of the parameter X:

- *Linearity error*, $[E_L]_i$ is defined as possible deviation of the measurement from the actual value, during a set of measurements:

$$[E_L]_i = |X - X_i|$$

- *Repeatability error,* $[E_R]_i$ accounts for the variability in measurements of the mean, X_i' and is defined as:

$$X_i' = k(x).X_i \rightarrow [E_R]_i = k(x).[E_L]_i, \qquad k(x) \geq 1$$

The two quantities are generally quoted for distance measurement probes to quantify the error associated with the measurements.

For the work presented in this thesis, the random error is taken as the standard deviation of multiple measurements of a fixed parameter. Linearity error is the deviation of the mean from the reference measurements, for a set of calibration measurements. Repeatability error is as per linearity error, but also accounts for the error when considering multiple calibration measurements.

The reference measurements for distance measurement experiments that are conducted using air-couple probes are obtained using laser displacement sensor with an accuracy of ±0.025µm. The reference bore forms measurements, in Chapter 7, were conducted using a CMM with an accuracy of ±3.5µm. The thickness of the cast iron liner specimen bar, in Chapter 8, was also obtained using the same CMM, at 20°C. The initial distance measurements (at room temperature) between the surface wave transducers bonded on the surface of the cast iron liner specimen, in Chapter 8, was measured using a ruler.

3.6 Conclusions

The chapter covered the various hardware required for taking measurements using ultrasound for solid and fluid coupled media.

The two custom built rigs used for the bore form measurement were presented.

The method of bonding sensors onto a solid test specimen was also shown.

The principles behind the experimental methods and the workings of the relevant hardware used for the work carried out were presented.

The data processing methods and the statistical tools used to quantify the accuracy of measurements were presented.

Where relevant, further information to extend the topics covered is provided within each of the following chapters.

4 Air-coupled Ultrasonic Sensor Development

This chapter presents a method for manufacturing of low-cost air-coupled ultrasonic probes operating in the megahertz (MHz) range. The probe was developed in order to evaluate the capability of ultrasound to measure bore form of cylinder liner, in situ in a honing machine. The motivation for the work was to develop low-cost sensors as opposed to purchasing 1MHz air-coupled ultrasonic probes which generally costs above £2000 each. Probe design and manufacturing methods are presented whereby each probe can be made for under £20.

4.1 Introduction

Air coupled ultrasonic probes in the 100s kHz to MHz range are used in wide variety of applications including non-destructive testing of materials (Chimenti, 2014; Fang *et al.*, 2017), surface roughness measurement (Blessing and Eitzen, 1989; Stor-Pellinen and Luukkala, 1995; Sukmana and Ihara, 2005; Saniman and Ihara, 2014; Saniman *et al.*, 2020), distance gauging/proximity sensing (Hickling and Marin, 1986), meteorological imaging (Blomme, Bulcaen and Declercq, 2002; Gómez-Ullate and De Espinosa, 2004), and many more. Piezoceramic probes seem to be adapted typically where using narrow band probes is sufficient, while CMUT are better for wide band applications (Grandia and Fortunko, 1995; Schindel and Hutchins, 1995; Schindel, Hutchins and Grandia, 1996). Other methods of generating air-coupled ultrasonic waves in the 100s of kHz to MHz range include composite transducers such as a 1-3 connectivity composite (Reilly and Hayward, 1991) (with piezo ceramic and polymer composite mixed in 1-3 ratio), and polymer-piezoelectric transducers made using materials such as PVDF (Takahashi and Ohigashi, 2009).

The application of piezoceramic probes working in the MHz range remains limited due to the significant transmission losses resulting from high acoustic impedance mismatch - transmission coefficient, $T_I = \frac{2Z_{pzt}Z_{air}}{(Z_{air}+Z_{air})^2} = 2.8 \times 10^{-5}$. The use of airborne ultrasound working in the MHz frequency range is generally limited to short distances due to the high values of attenuation that increases with power law, past 1 MHz. Furthermore, the adaptation of MHz frequency sensors has likely been slow due to the high cost of purchasing a single probe; the author obtained a quote for a piezoceramic based probe of 2750 EUR, and for a capacitive micromachined ultrasonic transducer (CMUT) of 4000 EUR.

Piezoceramic based air coupled probes are designed with impedance matching layer(s) to increase the transmitted energy from the transducer element to air. The ones that require wide bandwidth are designed with multiple matching layers. Therefore, the same approach was taken in designing the probe in this work. The construction of the probe included a wrap-around transducer, 2 front matching layers, and a backing material. The working bandwidth of the manufactured probes was from 0.85MHz to greater than 1.5MHz. A detailed manufacturing method that is simple to implement is presented. The probe was designed using material and tools already available in a science laboratory where piezoceramic transducers are used. See Figure 4-1 for the constituents of the probe.

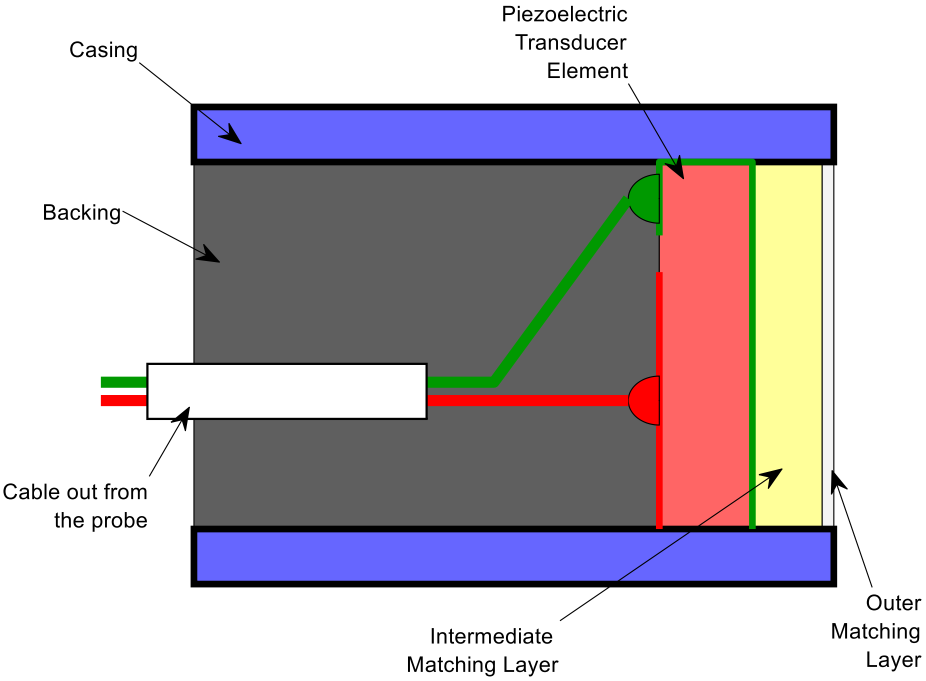

Figure 4-1: Air coupled transducer design.

4.2 Literature Review

Piezoceramics transducers working in the MHz range are seen as challenging to manufacture mostly due to the high impedance mismatch between the transducer (~30MRayls) and air (410Rayls).

Lynnworth (1965) showed the feasibility of using piezoelectric transducers in the megahertz range by using an impedance bridging matching layer, with impedance, $Z_l = \sqrt{Z_a Z_t}$, and its thickness equal to a quarter of the wavelength. Since then, several efforts have been made to improve the transmitted energy by finding a material with impedance close to that of a theoretically ideal matching layer. Some of the matching layer materials included silicone rubber (specific acoustic impedance, z=1MRayls) (Canali *et al.*, 1982; Fox, Khuri-Yakub and Kino, 1983; Khuri-Yakub, Kim and Chou, 1988); silicone loaded with microspheres (z=0.3MRayls) (Tone, Yano and Fukumoto, 1984; Wu *et al.*, 2016); microporous polyolefin (z=0.24MRayls) (Yano, Tone and Fukumoto, 1987); microporous PMMA (z=0.28MRyals) (Gómez *et al.*, 2001) and polystyrene foam (z=0.33MRayls) (Deka, 1987). Improvement in transmission loss from 82dB to up to 30dB is observed when using a single matching layer. Some single matching layers, such as silicon rubber, seem easy to implement but suffered from higher insertion loss and narrow bandwidth. The materials of lower impedance also tend to have slower wave propagation velocities, and high attenuation. The challenge for the designers was finding thin (~100µm), low impedance, low attenuation material. This was generally overcome by using porous material (with low impedance) (Yano, Tone and Fukumoto, 1987). A challenge of using porous materials is bonding them onto the transducer, which usually requires the use of a thin layer of highly viscous epoxy. The adhesive layers can add to the losses, but can be assumed to be minimal (Álvarez-Arenas, 2004). The downside of using a single matching layer method was that the resulting probe had very narrow 6dB bandwidth, usually under 10% for 1MHz. (Fox, Khuri-Yakub and Kino, 1983; Hickling and Marin, 1986; Yano, Tone and Fukumoto, 1987).

The bandwidth of the probe can be widened by employing multiple matching layers (Kossoff, 1966; Goll and Auld, 1975; Tone, Yano and Fukumoto, 1984; Schiller *et al.*, 1990; Gómez *et al.*, 2001). In a two layer system, the *intermediate matching layer* (IML) is generally made up of epoxy with its impedance in the range of 3-6MRyals (Yano, Tone and Fukumoto, 1987), while the outer most matching layer material is similar to single matching layer solutions. Some authors have shown the feasibility of using complex structures with gradual gradient change in impedance (Kelly, Hayward and Gomez, 2001; Kelly, Hayward and Alvarez-Arenas, 2004), and achieved comparably wider bandwidth. However, the process of manufacturing such a probe entails a high degree of complexity, while the transmission loss was similar to other probe designs.

A 2-4 times improvement in the bandwidth of the probe by using multiple matching layers was found. The use of wide bandwidth also led to greater phase linearity, i.e. less ringing and signal distortion (Kossoff, 1966; Goll and Auld, 1975). The ability to produce short bursts without ringing — a quality that is related to the probe having a wide bandwidth — is crucial for range/distance measurement application where the measured distance is relatively short.

Álvarez-Arenas (2004) proposed the use of porous membrane filters as the outermost matching layer material (interface with air on one side). The membrane filters have impedance in the range of 100s of kilorayls, and are manufactured to a high standard, i.e. they are homogeneous and have uniform thickness. A detailed study of several filtration membranes showed probes at 1MHz with 32dB insertion loss and 20% bandwidth. In an earlier work, Álvarez-Arenas (2003) provided useful insight in calculating the materials' acoustic properties. A detailed method to use the resonance spectra of a matching layer material — generally obtained using the *through transmission* method — to obtain the attenuation coefficient of the material, is presented in §5.3.2.

To the author's knowledge, the literature does not outline a cost effective and simple method to manufacture air-coupled probes working in the MHz range. However, the use of a piezoceramic transducer element for liquid or solid coupled applications costs ~15 GBP[1]. There are alternative air-coupled ultrasonic probes available with wider bandwidth, such as CMUT (Schindel, Hutchins and Grandia, 1996), 1-3 piezo-epoxy-composite (Hayward and Gachagan, 1996), and PVDF/TFE (Toda, 2002). However, they have high costs of manufacturing or purchasing of the transducer material.

The present author initially faced difficulty bonding the porous membrane filters as they tended to soak the adhesive. A relatively simple method to use low viscous epoxy is presented.

4.2.1 Backing of the probes

Transducer backing does not generally seem to get much attention for MHz range air-coupled probes. This is likely to maximise the energy output from the probes, as backings increase attenuation. The present author is however of the impression that for close proximity range measurement, it is beneficial to have a probe with higher loss but lower ringing and thus a wide working bandwidth. Therefore, with the intention of adding a suitable backing, a brief review of the relevant literature was conducted.

The use of backing to widen the bandwidth, reduce ringing and improve phase linearity has been shown by various authors (Arm, Lambert and Silverberg, 1962; Kossoff, 1966; Silk, 1984,

---

[1] Calculations based on using a PZT element, from a minimum order of 60, (price quotation date 2019 Q4).

pp. 25–50; Hickling and Marin, 1986). A piezoceramic transducer element has low losses and subsequently rings for a prolonged time if allowed to vibrate freely. Silk (Silk, 1984, pp. 25–50) recommends keeping the amount of trapped energy within the piezo crystal, $E_{trapped}$, — given as per Equation 50 — to under 0.09 for general NDT application.

$$E_{trapped} = W^2 = \left[\left(\frac{Z_P - Z_F}{Z_P + Z_F}\right)\left(\frac{Z_P - Z_B}{Z_P + Z_B}\right)\right]^2 \qquad \text{Equation 50}$$

Where, Z is the respective specific acoustic impedances of its subscript piezoelectric crystal (P), the front matching layers (F), and the backing medium (B).

In general, epoxies such as Araldite filled with tungsten powder have been found to be an effective backing medium. The attenuation characteristics of the epoxy are improved by adding tungsten powder, and found to be in the order of 10^3 dB/m if the filling particle size is comparable to the ultrasound wavelength (Sayers and Tait, 1984; Grewe *et al.*, 1992). However, the volume fraction of tungsten needed to achieve the required impedance is around 60%, and poses a challenge in wetting all the powder without special means.

Using low impedance, high attenuation backing with a $\lambda/4$ thick matching layer in the front, however, ensures the frequency bandwidth is gaussian shaped (only when pulsing at resonant frequency). The Gaussian frequency response ensures a constant time delay across the frequency range (Desilets et al., 1978). Therefore, it seemed beneficial to have a lower impedance, high attenuation backing on air-coupled probes, if the signal distortion can be sufficiently minimised.

4.2.2 Conclusions from Literature Review

The cost and effort of manufacturing air-coupled ultrasonic probes seems to rise with the frequency of the probe. The high cost and effort required have most likely been the drawback in the wider adaption of MHz frequency probes.

The design challenges in manufacturing MHz range air coupled transducers seems to be in limited probe bandwidth and high transmission loss. Use of single or double matching layers seem to result in transmission gains (reduction of transmission loss) of ~40dB. Using single matching layer results in probe bandwidth of around 8-10%, while double matching layer results in probe bandwidth of ~20%.

4.3 Probe design

Probes were designed with two matching layers and a backing to minimise the ringing. For the front outer-most matching layer (OML), 0.45µm pore sized Nylon® 66 membrane filter (thickness 127µm) was used due to its availability in the lab. For the IML, Araldite 2020 was used. The backing also used the same Araldite, but with tungsten powder added to increase its impedance (closer to that of the transducer), and increase its attenuative characteristics. The transducer gauging (connecting to lead cables) is as per the method outlined in §3.1.1. A total of 5 probes were manufactured, three made of soft PZT PIC255[1], and two made of hard PZT PIC181[2]. The transducers had wraparound terminals.

---

[1] Product no: 000014023, PI (Physik Instrumente) Ltd, Bedford, MK430AN.

[2] Product no: PRYY-1128, PI (Physik Instrumente) Ltd, Bedford, MK430AN.

Table 4-1 shows the materials used in the probe, while Figure 4-2 shows the cross-section of a probe. The attenuation for OML may seem high, however the thickness of 127μm means the total loss is ~0.1Np/thickness (0.86dB) (Álvarez-Arenas, 2004).

Table 4-1: Material properties of the passive layers in the probe. OML (outer matching layer); IML (intermediate matching layer); and backing. The range in material properties of the backing is a result of uncertainty in the design.

Material	**Layer**	L **(mm)**	Z **(MRayl)**	c_l **(m/s)**	α' (Np)
Nylon	OML	0.127	0.162	~500	787
Araldite	IML	1.9	2.8867	2554.6	49
Araldite with tungsten filler	Backing	10	~5-10	~1500-2200	~100-1000

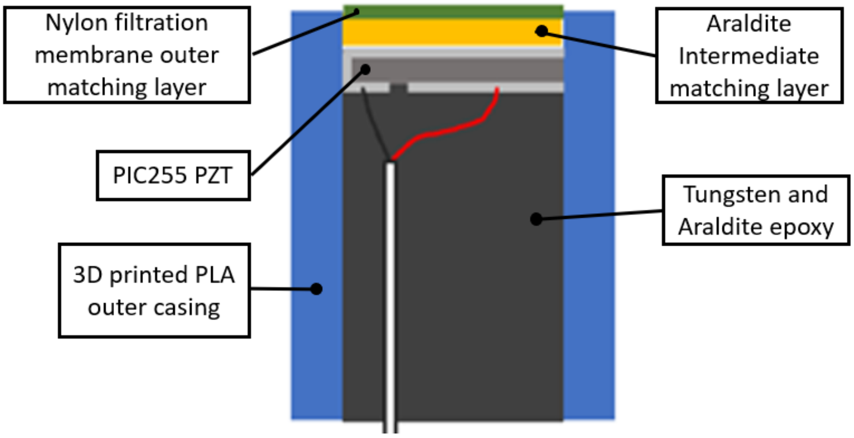

Figure 4-2: 1MHz Air-coupled ultrasonic probe cross-section.

4.3.1 Probe case design

Use of 3D printing has substantially reduced the cost of manufacturing small protype components. Therefore, the method was adapted to manufacture the probe casing and front cap. A cap is used to control the intermediate matching layer thickness. Figure 4-3 shows the casing design used for manufacturing of the probe.

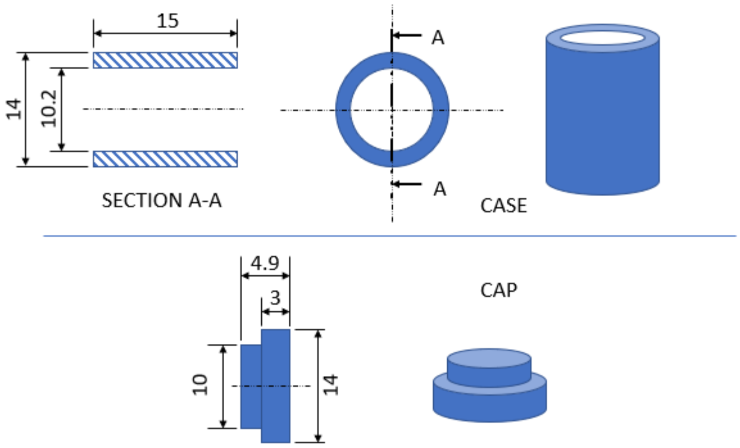

Figure 4-3: Air-coupled probe case, and the front cap design. The cap is used for controlling the matching layer thickness. The cost of printing 10 of the cases and cap – designed as one with breakable link connecting a pair - was quoted as GBP 27.841.

---

[1] Quotation obtained from https://craftcloud3d.com. Date of access: 16/07/2021.

The cap had a stepped boss of 1.91mm±0.1mm in length. This was based on the 2nd quarter wave resonant mode in the Araldite layer (with the quarter wavelength at 1MHz, $\lambda_{1\mathrm{MHz}}/4$ =0.639mm).

4.4 Probe Manufacture

The process used to manufacture the probe is laid out below in Table 4-2 and Figure 4-4. It was found to be easier to have the backing material prepared prior to starting the process. The backing was made by mixing the 2-part Araldite 2020 as per manufacturer's instructions, then mixing it with tungsten powder with weight ratio of 1:8 Araldite to tungsten.

Table 4-2: Steps of manufacturing the air-coupled probe.

Step No.	**Description**
1	Clean the transducers using relevant solvent and air dry.
2	Stick the front face (non-terminal face) onto the cap of the casing using double sided tape, as shown in the figure.
3	Solder ~50mm long coaxial cables onto the terminals of the piezo ceramic. The present author found it easier to use 2 separate micro coaxial cables (42AWG PFA, 50 OHM, Molex/Temp-Flex: 100065-0023), one for each terminal.
4	Attach the case and the cap, with the cable passing through the casing.
5	Fill the casing with prepared backing. Cure the backing as per epoxy manufacturer's instructions. NB: if using the oven, ensure the temperature is low enough so as not to deform the casing and cap material.
6	Remove the cap from the cap-case assembly and discard. Clean the transducer exposed in the front with a fibre glass pen to remove any adhesive from the double-sided tape. Then fill the front with Araldite 2020 to the brim.
7	Heat the epoxy at 50°C in the oven for 1 hr so it partially sets. After the hour, check if the epoxy has started solidifying by dipping a tiny piece of filtration paper every 5 minutes. Once the filtration paper visibly stops absorbing the epoxy, remove the probe from the oven. The epoxy should look set but feel sticky when touching it with filtration paper.
8	Stick the filtration paper onto the front face of the transducer. Apply light pressure with folded tissue or folded cloth to stick the paper initially. Leave the transducer for 24 hours to allow the epoxy to set properly.

While the probe was manufactured without a connector, in hindsight it would have been preferable to connect the coax leads from the probe to an SMB connector (see §3.1.1) and curing the connector embedded in the backing epoxy. This can avoid cable detachment at a later stage, which would render the probe useless. Thus, steps 4 and 5 would need additional steps to be added in between for such a scenario.

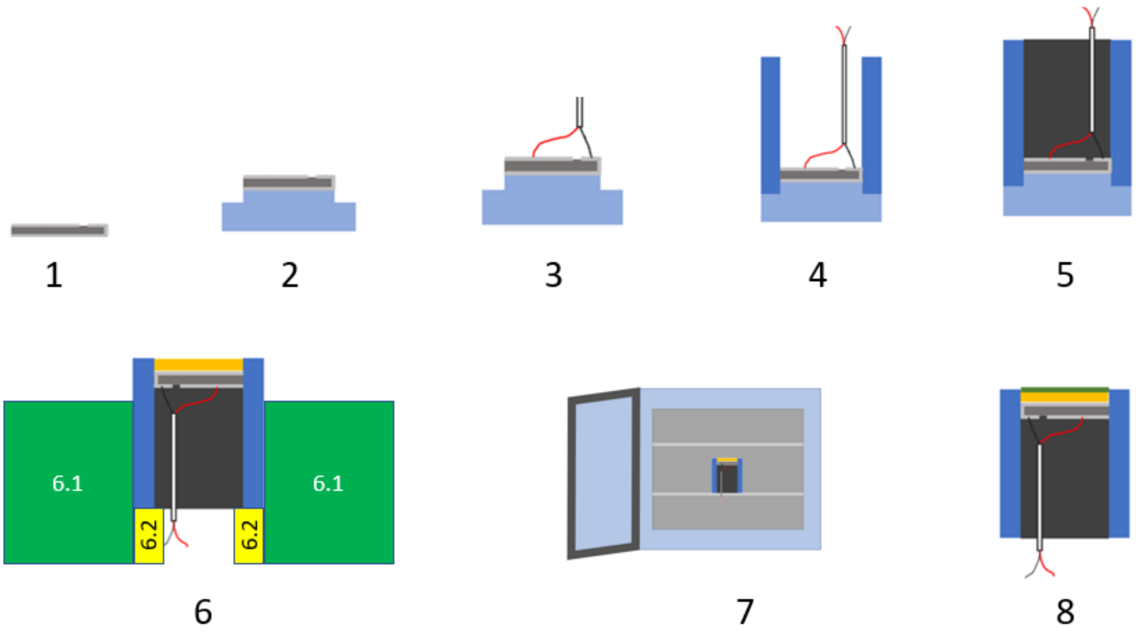

Figure 4-4: Figures corresponding to the steps in probe manufacture. 6.1 and 6.2 are parallel clamps and 3mm gauge blocks, respectively, used to keep the probe fixed upright in the oven.

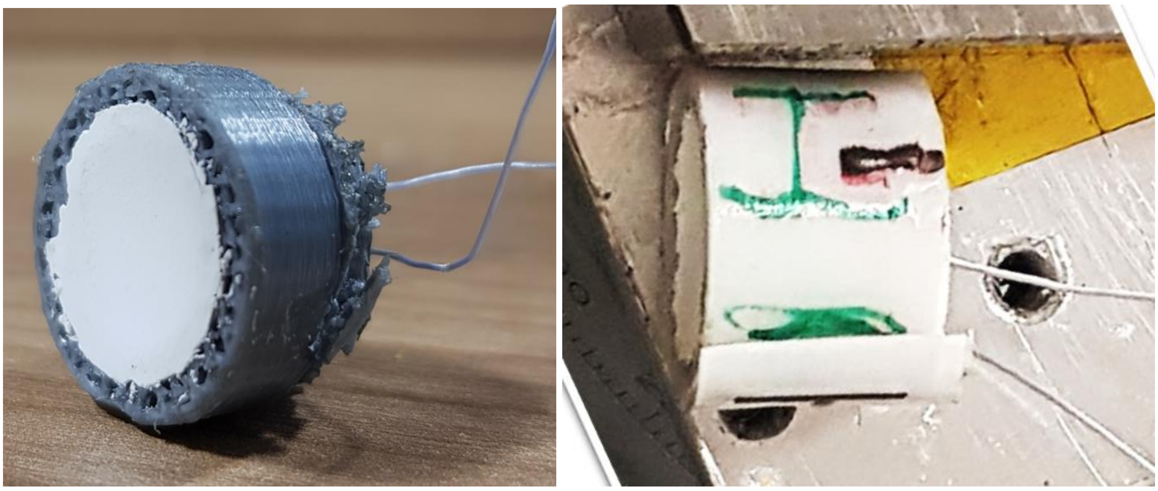

Figure 4-5: 1-1.5MHz air-coupled ultrasonic probe. (Left) probe manufactured using PIC255. (Right) Probe manufactured using PIC181 (harder PZT material of the 2).

Out of the 5 manufactured, 4 were found to work. One made of PIC255 showed no response when connected to the test circuit, most likely due to detachment of one of the cables soldered onto transducer terminals.

4.5 Experimental setup

The setup as shown in Figure 4-6 was used to study the response of the probes. The probes were evaluated in pulse-echo mode using the air-coupled sensor evaluation rig (see §3.1.5 for further detail on the rig).

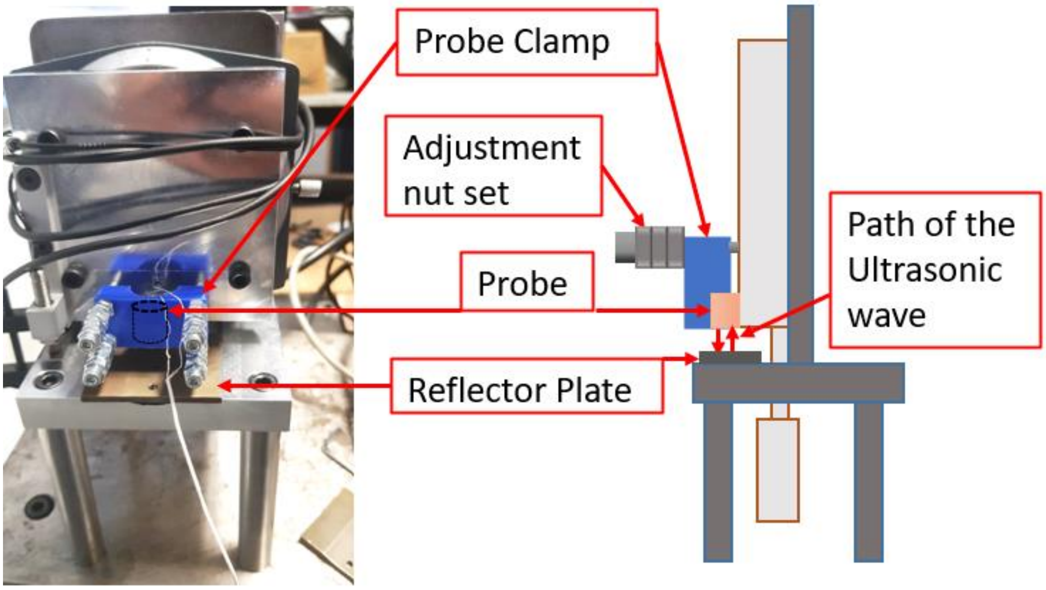

Figure 4-6: Rig setup used to measure the waveform and the frequency bandwidth of the probes in pulse-echo mode.

The probes were also evaluated in pitch-catch mode. Figure 4-7 shows the probes setup in pitch-catch and through transmission modes. Through transmission test was conducted using parallel clamps to ensure the probes were aligned facing each other. A gauge block was used to set the distance between the two probes. Pitch-catch mode was conducted by resting the side of the probes onto an angle gauge block as shown in the figure.

The tests used the probe made of PIC181 to transmit and the probe made of PIC255 to receive. This was because the hard PZT are known to be able to withstand higher pulsing power input.

Figure 4-7: Test setup used to measure the waveform and the frequency bandwidth of the probes in the pitch-catch mode (LHS) and through-transmission mode (RHS). In the through transmission test, the probes were separated using a gauge block while clamped with parallel clamps to them hold steady.

Figure 4-8 shows the schematic of the probe evaluation experiment conducted in pulse-echo mode. Similar setup is applicable when 2 probes were used.

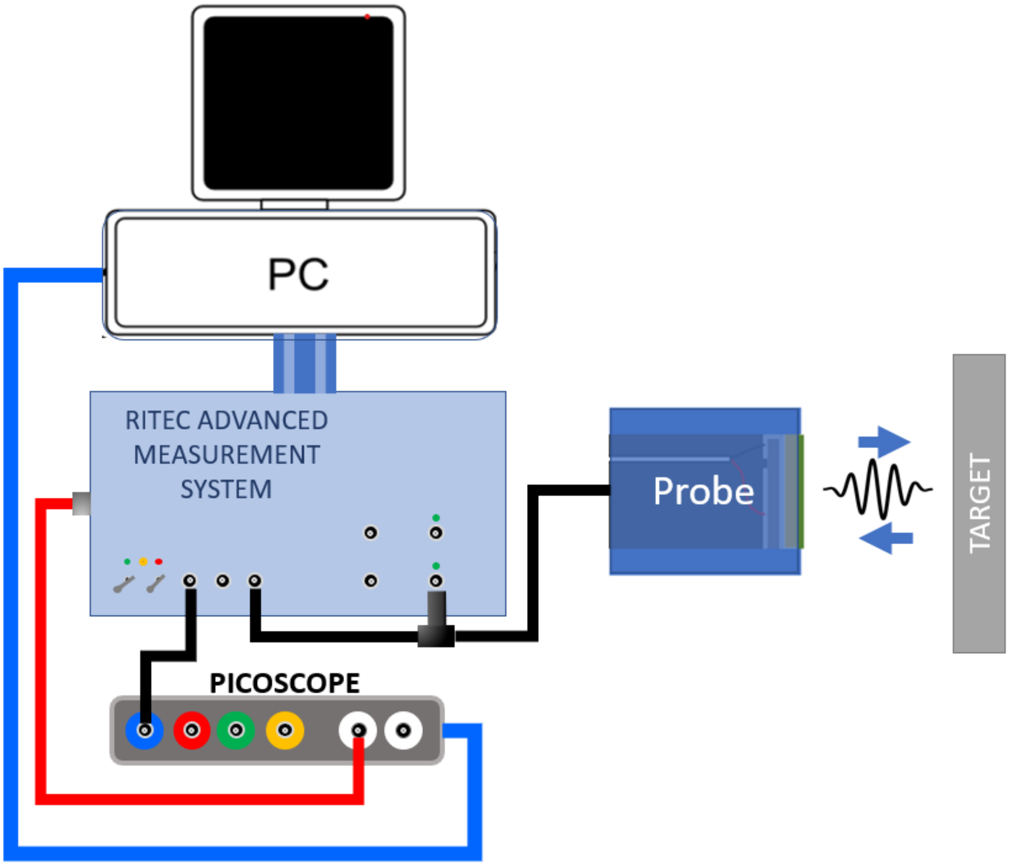

Figure 4-8: Schematic of the setup used for the probe bandwidth study.

The excitation signals of 350 Volts peak-to-peak (p2p) sine wave of 5 to 10 cycles were generated using a RITEC RAM5000 function generator at a pulsing rate of 200 Hertz. This was coupled directly to the probe terminals, using the core of a 50 Ohms coaxial cable as the live connection, and the outer braid shield of the coaxial cable coupled to the ground terminal. The reflected pulse was detected by the same probe in pulse-echo configuration, or a separate probe in pitch-catch configuration. The detected signal was put through a bandpass filter (passband: 50kHz to 5MHz) and the built-in amplifier in RITEC RAM5000 (gain: 32dB), before transmitting to the Picoscope 5442B. The Picoscope was used to digitise the signal with ADC settings as follows: range of ±1Volts, resolution of 12bits, digitisation rate (sampling frequency) of 250MHz. The digitised signal was transferred to the PC where an inhouse LabVIEW program, Triboscope, was used to acquire and save it. The saved waveforms were processed using MATLAB®.

For pitch-catch and through-transmission modes, the lead cable from the receiver was connected to the input port of the RITEC unit (third connector from RHS), while the lead cable of the emitter was connected to the output terminal. For pulse-echo mode, the same probe was connected to both the input and output terminals. The emitter port did not require a splitter as shown in the pitch-catch configuration. The probe excitation signal for the through transmission mode was 1000V p2p, while the sine wave used was of 3 cycles.

Table 4-3 shows the experiments conducted to evaluate the probe performances. Due to high losses only one of the hard piezoceramic probes (PIC181) was evaluated.

Table 4-3: Experiments conducted to evaluate the probes manufactured.

Description	Probe(s) used	Distance	Excitation Frequency (Cycles of sine wave)
Pulse-Echo	PIC255a	12 mm	0.5 MHz – 1.5 MHz, (5)
Pulse-Echo	PIC255b	12 mm	0.5 MHz – 1.5 MHz, (10)
Pulse-Echo	PIC181	12 mm	0.5 MHz – 1.5 MHz, (10)
Pitch-Catch	Transmitter: PIC181 Receiver: PIC255	~25mm from reflector	1MHz, (3)
Through transmission	Transmitter: PIC181 Receiver: PIC255	50mm from each other	1MHz, (3)

An average of 100 recordings was used to obtain the final waveform. This waveform was filtered using a band pass filter set between 0.25MHz and 3.5MHz. The FFT algorithm of MATLAB was used to present the frequency content of the signal after the processing. See §3.3 for further information on digital signal processing.

Figure 4-9 shows the attenuation of sound waves within air, which must be considered for comparison of probes if they are used with varying frequency. For the analysis at present, the signals in the frequency domain were multiplied by the inverse of the total loss for the respective airgap (length of wave path) and frequency.

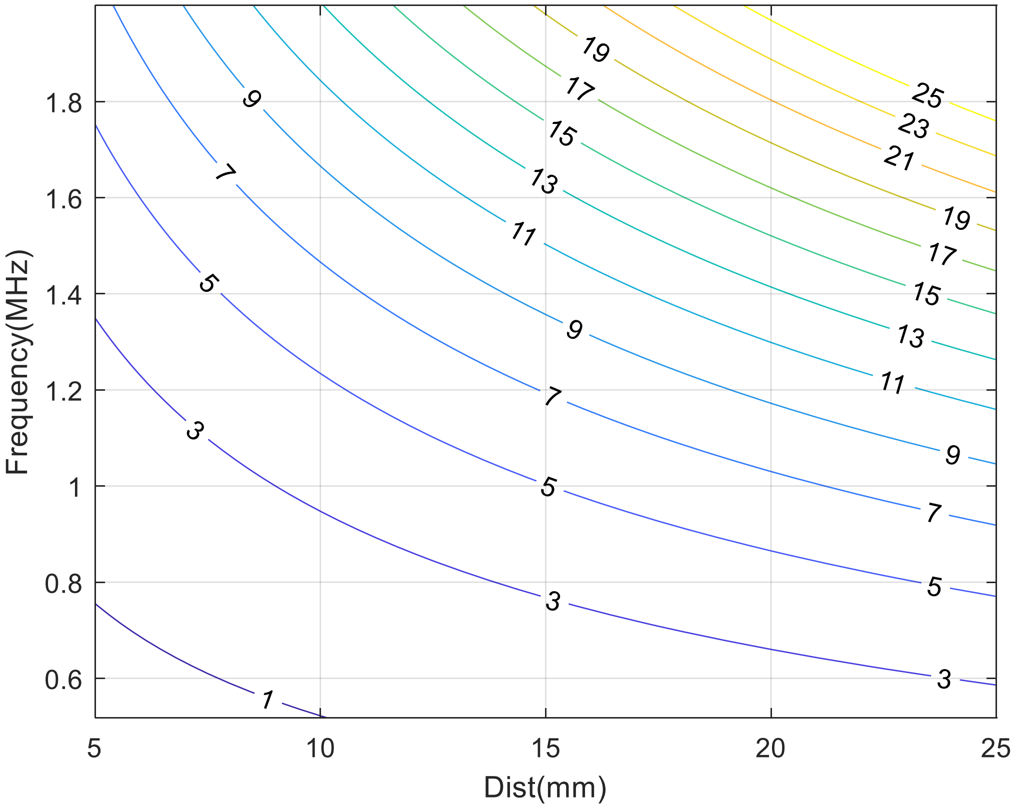

Figure 4-9: Attenuation in air (in dB) with varying distance between the probe and the reflector target at different frequencies. The reflection loss at interface can be assumed negligible due to significant impedance differences.

4.6 Results and Discussion

Table 4-4 shows the outcome of the central frequency, bandwidth and transmission loss tests conducted using the probes. Transmission loss is calculated as per Equation 22, by comparing the voltage of the received signal with that which was induced.

Table 4-4: Experimental outcome of the probe analysis.

Probe(s) used	Central Frequency	Bandwidth	Transmission Loss
PIC255a	~1.40 MHz	>20%	87.48
PIC255b	~1.00 MHz	20%	74.74
PIC181	~0.85 MHz	10%	77.03

The unfiltered probe responses, while not shown, were greater than that reported in Table 4-4. However, due to significant signal distortion, possibly due to the use of a high-powered excitation signal from the gated amplifier, the analogue filter built in the amplifier was used to filter the raw waveform and obtain the final waveform (acquired by the oscilloscope (Picoscope)).

Figure 4-10 and Figure 4-11 show the performance of 2 separate probes designed using PIC255 soft piezo, while Figure 4-12 is that of a probe made using hard piezo, PIC181.

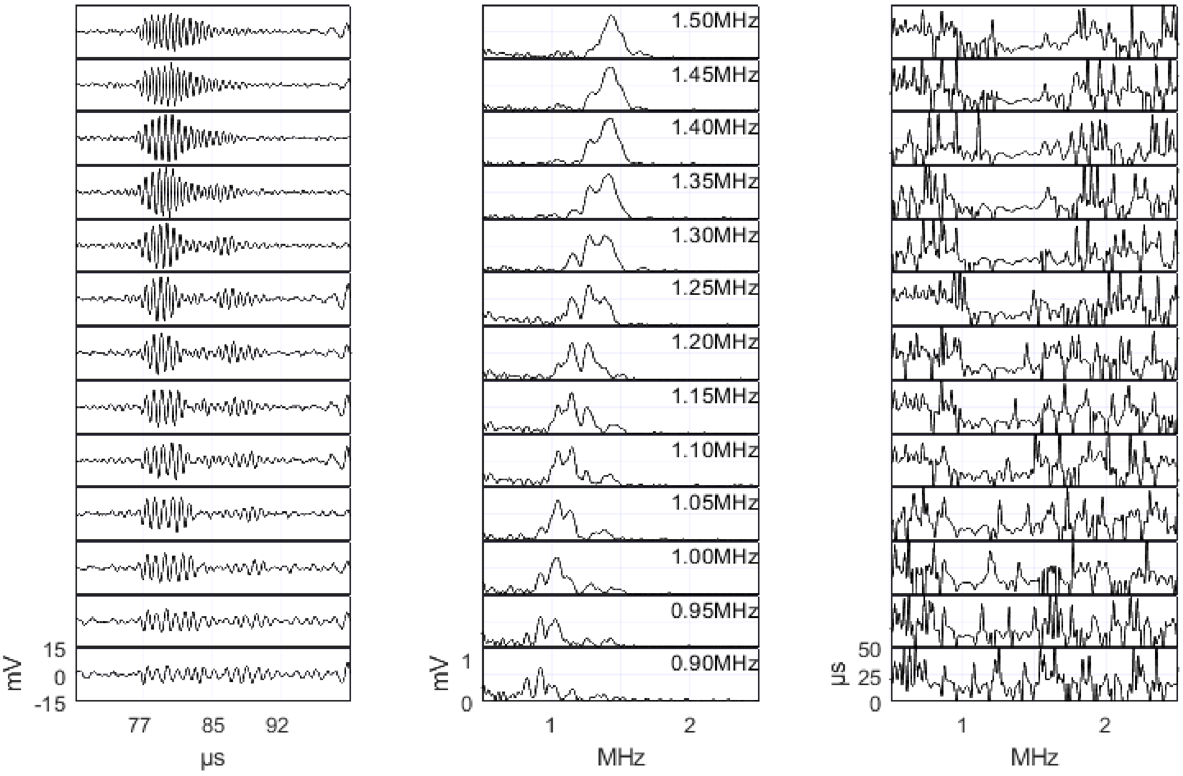

Figure 4-10: Plots acquired using probe made up of PIC225a transducer excited at varying frequencies. (Left) Time domain waveform, (centre) frequency domain (right) group delay of the signal.

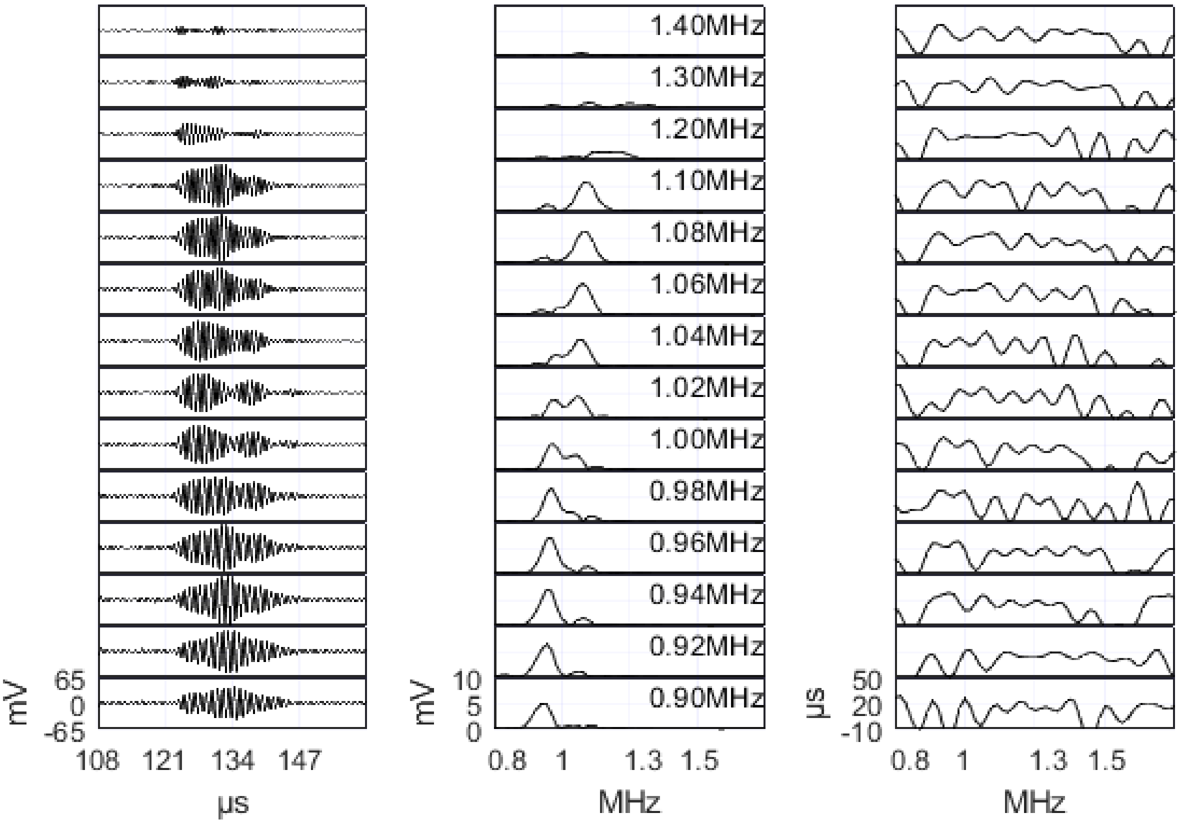

Figure 4-11: Plots acquired using probe made up of PIC225b transducer excited at varying frequencies. (left) Time domain waveform, (centre) frequency domain (right) group delay of the signal.

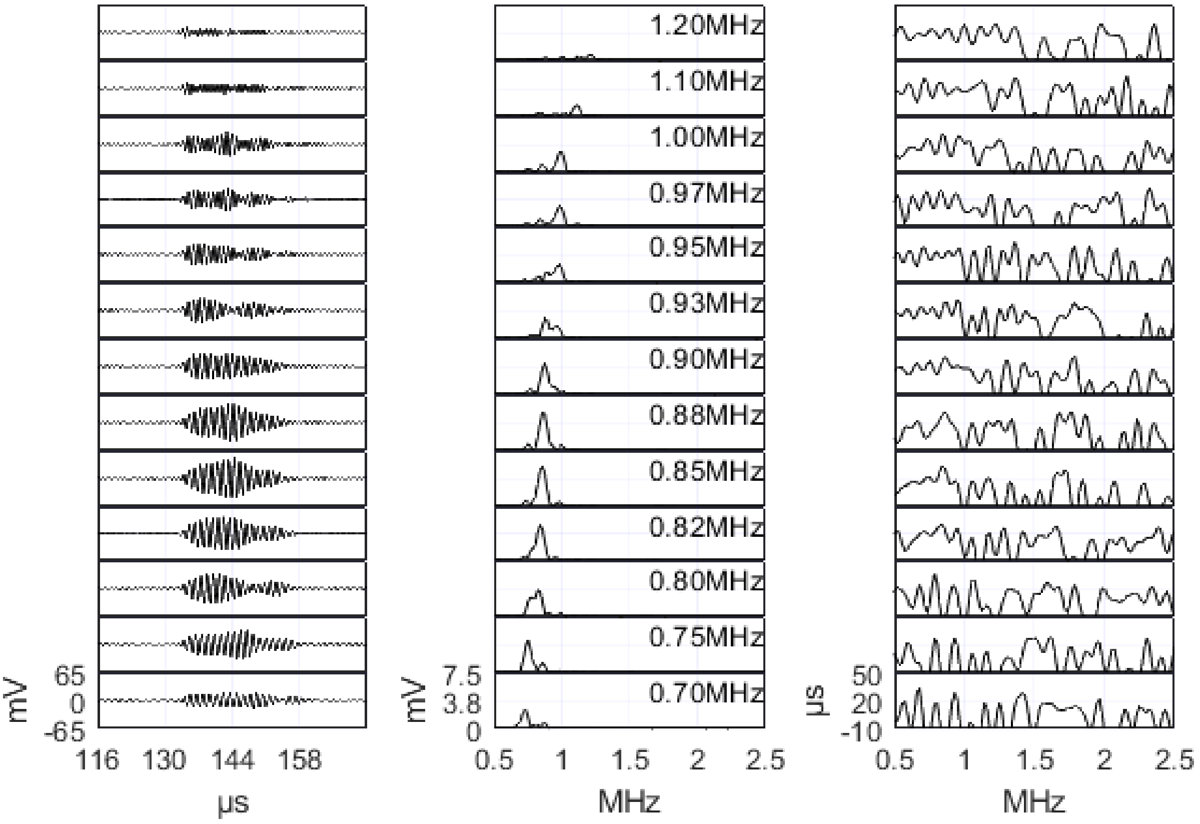

Figure 4-12: Plots acquired using probe made up of PIC181 transducer excited at varying frequencies. (left) Time domain waveform, (centre) frequency domain (right) group delay of the signal.

Variability in the resonance spectra of the probes can be observed even in probes manufactured with the same piezoceramic (c.f. results for PIC255a and PIC255b). Whilst all design parameters which dictate the probe resonance spectra were kept relatively constant, the one parameter which could vary significantly was the thickness of the IML. Therefore, the probable variability in the IML thickness, which would mean different *quarter wavelength* resonant frequency, was likely the most significant cause for variation in frequency response between the different probes. Other factors such as lead cable length and amount of soldering would have also affected the probe resonance characteristics but likely not to the same degree as IML thickness. The difference in the resonance characteristics would also have resulted in the observed low ring response of PIC255a when compared to that of PIC255b.

The values for transmission loss of all the probes were much greater than those of the probes reported in the literature (e.g. 32-48dB (Álvarez-Arenas, 2004)). The higher transmission loss was expected due to the manufactured probes having a backing material. However, it is likely that the lack of IML thickness control also affected the transmission loss; the further the thickness deviated from λ/4 of the resonant frequency, the lower the resulting transmitted energy (higher transmission loss).

It should be noted however that a proper comparison of the transmission loss to probes in literature was not possible. This is because the values reported in literature likely correspond to experiments where the probes were excited with waveforms of several 10s of cycles in length, as this would be required to get the probe response to reach a steady state. A similar method of analysis was not possible for the tests carried out, due to limitations in pulsing rate of the gated amplifier; see §3.1.3. However, given the application requirement of the probe, i.e. its intended use as close-proximity range measurement sensor, the evaluation using 5-10 cycles with the observed SNR was seen as sufficient.

The response of PIC181 had narrower frequency bandwidth when compared to the softer piezoceramic material excited by same number of cycles (PIC255b). This can be explained by the higher attenuation of the softer piezo resulting in lower Q-factor and therefore a wider frequency bandwidth. See §5.3.2 for more information on Q-factor and attenuation.

The difference in resonant frequency of IML, OML and the piezoceramic transducer element would contribute to signal distortion; due to each layer amplifying different frequency content of the waveform. The lack of thickness control of the IML thus also likely contributed to the observed signal distortion (seen as amplitude modulation of the time domain waveform or the greater degree of change in group delay plots) because its λ/4 resonant frequency would vary from that of the transducer and OML.

The frequency domain response of probes in literature such as Álvarez-Arenas (2004) show a similar pattern to the one observed, i.e. three peaks in frequency response. The author proposes that it is beneficial to have the OML quarter wave resonant frequency in between two of IML quarter wave resonances, as this results in a probe with wider bandwidth. For applications requiring a short duration pulse, it may instead be better to have a Gaussian shape frequency spectrum (when excited at its operating frequency), as this would result in minimum waveform distortion and a constant group delay. Lower amplitude modulation would likely lead to a greater accuracy in distance measurement applications.

Figure 4-13 shows the outcome of through transmission setup, while Figure 4-14 shows the outcome of pitch-catch setup.

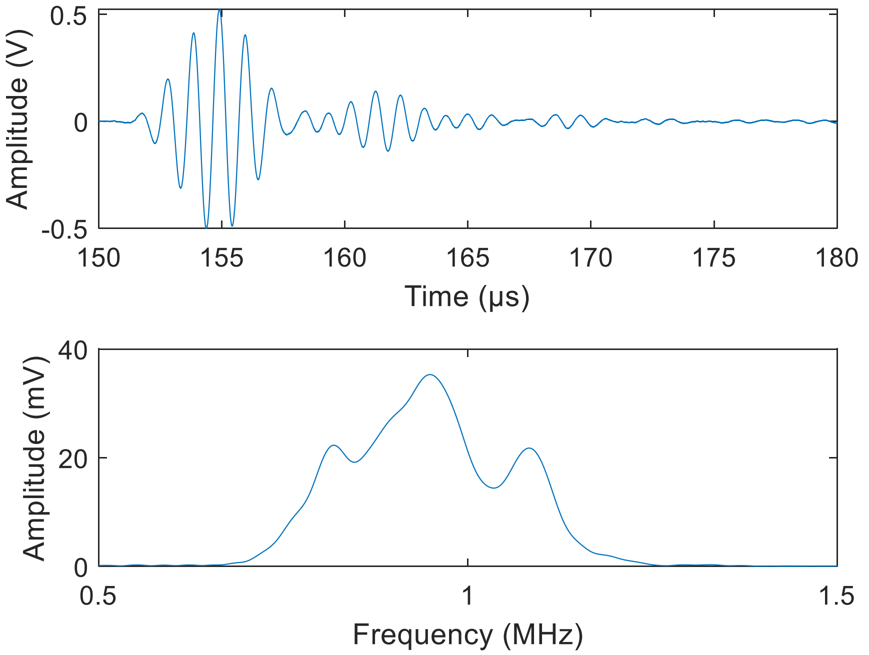

Figure 4-13: 2 Manufactured probes used in through transmission setup with the two facing each other 50mm apart. The frequency domain of the signal is obtained using the first portion of the pulse, i.e. around 6 cycles after pulse arrival.

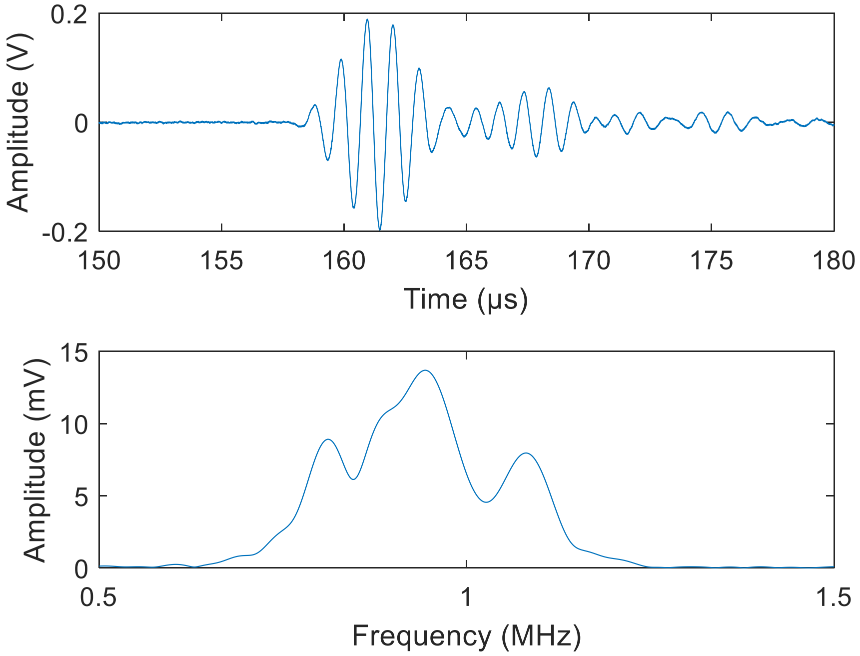

Figure 4-14: 2 Manufactured probes used in pitch-catch setup with the two facing the reflector plate at an angle, while being roughly 25mm away from the reflector plate. The frequency domain of the signal is obtained using the first portion of the pulse, i.e. around 6 cycles after pulse arrival.

Using separate emitter and receiver probes, the received signal can be seen to consist of lower probe ringing. The higher ringing observed in pulse-echo mode was likely due to the interaction of the high voltage input signal with the various electrical components, such as the cable, amplifier, and the probe itself. Using separate probes for emission and detection meant the receiver probe was isolated from the impact of the high voltage input signal.

The requirement to pass the received signal through an analogue filter when using the pulse-echo configuration, as well as the low signal distortion in the raw waveform acquired in the pitch-catch/through-transmission configurations, highlights the need to use electronic components in the probe to act as a bandpass filter. Further information on the use of electronic circuit components to filter the probe response (e.g. by using various configurations of inductors, capacitors and resistors) can be found in Silk (1984) and Desilets et al. (1978).

The waveforms of the PIC255a probe offered low ringing characteristics, while also giving a high signal-to-noise ratio (SNR) output for 5-cycle excitation. Therefore, the sensor was selected for bore form measurement application, the details of which are presented in subsequent chapters.

A more cost-effective design could also have been the use of a material such as a Polyestersulfone membrane filter as the OML. To make the thickness of the intermediate matching layer more uniform, material such as off-the-shelf polypropylene plastic film of 0.45mm thickness[1] (quarter wave resonant frequency of 1.167MHz @ v=2100m/s) could be used. Araldite 2020 could likely be used to bond the outer layer to the intermediate layer, using a similar curing method to the one presented to ensure the filtration membrane does not absorb the epoxy.

4.7 Conclusions

Three low-cost air-coupled ultrasonic probes for application of near proximity range measurement were successfully designed and manufactured. The probes consisted of 2 front matching layers (intermediate layer as Araldite 2020 and outer layer as nylon membrane filter) and tungsten powder in Araldite as backing.

It was shown that by using materials available within the lab and purchasing some relatively cheap components, it is possible to manufacture an air-coupled probe working at 0.85-1.5MHz for around ~17.83GBP. This is around 130 times cheaper than purchasing such a probe. Assuming only 3 in 5 probes work properly, this would still be at a fraction of the cost.

In pulse-echo mode, the soft piezoceramic (PIC255) probes resulted in lower distortion in the acquired waveform and a wider frequency bandwidth, and were therefore more suitable than hard piezoceramics (PIC181). However, for pitch-catch application, using hard piezoceramic as the emitter probe resulted in clearer SNR due to its ability to withstand greater excitation voltage in comparison to soft piezoceramics. Thus, for pitch-catch application, hard piezoceramic seems more applicable as the pulser — if high power pulsing instruments are available to excite the probe.

The 2-way insertion loss of the transducers was found to be 74dB to 87dB, while the working bandwidth of the probes varied from 10% to 20%. Due to the short burst probe excitation method employed, the transmission loss calculated at present is likely higher than reality, i.e. if excitation waveform of several 10s of cycles were used. However, the SNR of PIC255a was found to be satisfactory to use, as the prospective bore form measurement sensor.

---

[1] Such as part number:RS775-7797 from https://uk.rs-online.com/

5 Sensor Optimisation Using Transmission Line Model.

Effort in ultrasonic probe design has generally included the use of transmission line models to predict the frequency domain and time domain probe response. This chapter presents the outcome of using one such model, namely the KLM model, to evaluate the probe design that was used in the previous chapter. The probe model is evaluated with varying thicknesses, impedance, and attenuation coefficients of the intermediate matching layer (IML). The motivation behind the work presented was to find the most suitable design parameters of the IML for any future probe designs.

5.1 Introduction

Transmission line models were first used by Mason (1948) to simplify the problem of coupling of electrical and mechanical systems in components such as piezoelectric transducers. The model allowed tuning parameters such as impedance and thickness of matching layers to achieve a probe design based on application requirements. The model was used to study varying impedance, attenuation, and thickness of intermediate layers. Figure 5-1 shows the physical composition of the air coupled ultrasonic probe investigated within this section.

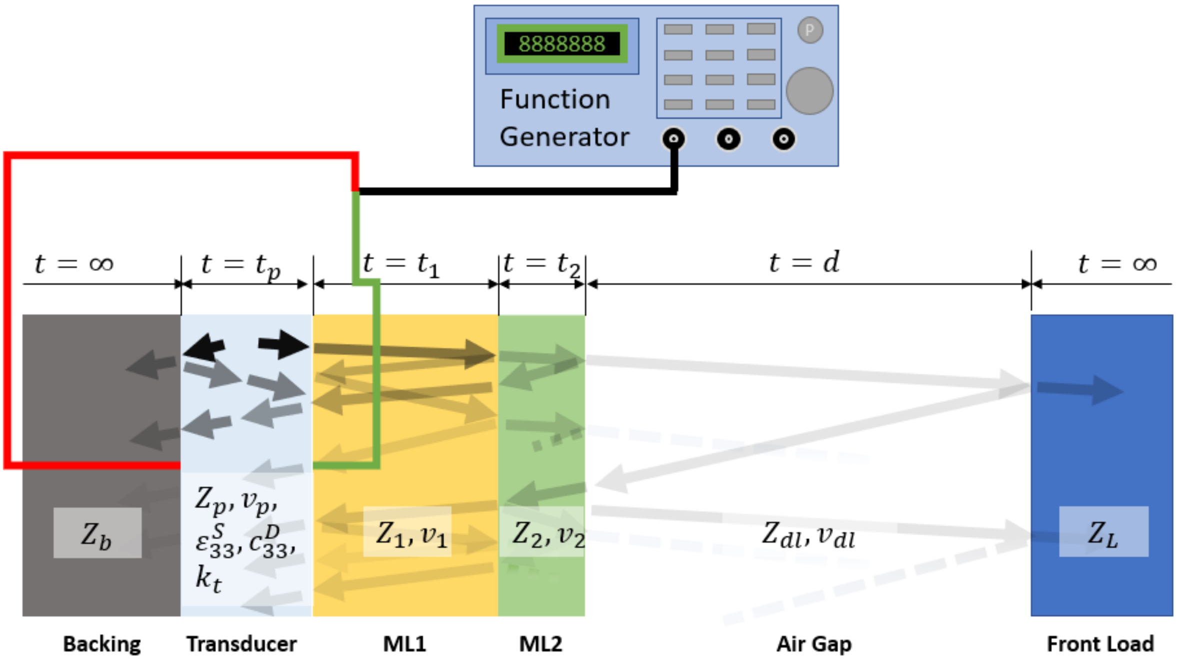

Figure 5-1: Configurations of a 1-D multi-layer analytical model studied using transmission line model. The model has two front matching layers, one backing and a piezoceramic transducer. The air gap to be measured and the wave reflecting plate are also shown – names of the layers are given below the layers. *ML1* and *ML2* are matching layer 1 and 2, respectively. Thickness, t, the impedance, Z and the velocity, v of the layers are the design parameters to be set; for piezoceramic transducer, additional parameters include the permittivity, ε_{33}^S, stiffness, C_{33}^D and the electromechanical coupling factor, k_t. The backing and the front are treated as semi-infinite layers. The changing opacity arrows represent changing intensity of the waves bouncing around within the various layers.

5.2 Literature Survey

Since its first adaptation by Mason (1948, pp. 230–238), the transmission line model of circuits with piezoceramic materials, in particular those of transducers used in ultrasonic measurements, has been utilised a great deal, and is the recommended method for designing ultrasonic probes using piezo crystals (EN50324-2, 2002).

The mechanical layers, which includes the piezoceramic, the backing material, the front matching layers, and the material into which the transducer is coupled to at the front (known as the front load), are converted into equivalent electrical components of an electrical transmission line. Each front matching layer, and the piezoceramic transducer are assigned an impedance value depending on their thickness, characteristic acoustic impedance, and velocity; the characteristic impedance of the front and backing are also included in the model. The mechanical layers are coupled to the electrical components of the circuit at the piezoceramic transducer terminal, treating the transducer as a perfect transformer, with a transformer coupling coefficient that is dependant on the electromechanical coupling coefficient of the piezoceramic.

Authors such as Kossoff et al. (1966) and Arms (1962) have used the model to investigate the effect of backing and front matching layers, of ultrasonic probes. The authors show that group delay can be kept constant within a frequency bandwidth by using a backing material with acoustic impedance similar to the transducer. This is also shown to be possible by using front or back quarter wave-matching layers with their impedance similar to the geometric mean of the transducer and the load impedances; see Equation 36. Desilets et al. (1978) show the frequency bandwidth of the probe is Gaussian shaped when using quarter wave matching layers, and this results in constant group delay — when the probe is pulsed at the layer's resonant frequency. A linearly varying group delay means there is no phase distortion in the waveform. For more on group delay, readers are referred to Young (1962).

The Mason model is found to be effective, but only practical for a small number of layers. An alternative was proposed by Krimholtz, Leedom and Matthaei (1970), which is commonly known as the KLM model. The authors uncoupled the electrical and mechanical components from the preceding models and represented the impedances of each elastic layer as one acoustic transmission line component (compare Mason model in Figure 5-7 to KLM model Figure 5-8). However, both the Mason and KLM models can lead to an overestimation due to using piezoelectric deformation coefficient h_{33} (Silk, 1984, p. 6). The more realistic coupling coefficients are the electromechanical coupling efficiencies, k_r and k_t, for the radial and the transverse modes, respectively, and related to each other as follows (Silk, 1984, p. 6):

$$(1 - k_{33}^2) \approx (1 - k_r^2)(1 - k_t^2) \qquad \text{Equation 51}$$

Desilets et al. (1978) propose a modified KLM model where the effective piezoelectric coupling coefficient, k_t replaces the piezoelectric deformation coefficient, h_{33}. The authors also give valuable recommendations for the design of probe with regard to backing and matching layer materials’ parameter selection.

Sherrit et al. (1999) had shown that by using complex versions of elastic and electromagnetic coefficients which account for the wave dispersion, the initially proposed Mason and KLM models obtain identical results that agree with the experimental data (see Figure 5-11). The method presented by the author is simple in obtaining the probe impedances, however obtaining the time domain response is not possible.

To simplify the calculations scheme van Kervel and Thijssen (1983) proposed using a 2 port network on the KLM model in Desilets *et al.* (1978); formulating transference matrices of each layer, the authors proposed a method that enables the use of linear algebra to find the frequency domain transfer function. The transfer function obtained can be convolved with the input signal to attain the response of the ultrasonic probe; by use of inverse Fourier transform, the time domain response of the probe is attainable. Further work exists on the improvement of the transmission line model. A calculation scheme such as that used by Castillo, Acevedo and Moreno (2003) included loss within each layer. The authors recommend using complex forms the coefficients similar to Sherrit et al. (1999), to include the losses of each layer, and the piezoceramic. However, the authors recommend using non-complex forms of the transformer coupling constant, k_t, and the variable capacitance — the results shown in Figure 5-12 shows that all coefficients should be left in their complex forms to obtain the same input impedance as that obtained using the method proposed by Sherrit et al. (1999). More recently Geonwoo et al. (2019, 2020) find the behaviour of through transmission pitch-catch systems and response of the probe to electrical tuning. All the proposed KLM models show a reasonable accuracy in predicting both the time and frequency domain probe responses of piezoceramic transducers, when compared to the experimental data.

The designed probes presented in Chapter 4 used hard and soft PZT. Given that the dielectric losses within these materials vary, and also because of the relative ease of using the method, the method by Sherrit and Mukherjee (2007) (the same as the one presented by Sherrit (1999)), and that by van Kervel and Thijssen (1983) were used in this work. The methods used to convert the material constants of the elastic layers to complex constants is given by McSkimin (1964, pp. 273–276) and Toda (2015), of whom the latter applies it to air-coupled probes. The method used to convert the coefficients of piezoceramics provided in the datasheets for others that were missing can be found in Berlincourt et al. (1964), Jaffe et al. (1971), ('ANSI/IEEE Standard on Piezoelectricity', 1988), Sherrit (1999), Dahiya and Valle (2014, p. 214), and Sherrit and Mukherjee (2007).

Readers are referred to the following references for further information on transmission line models utilised within the chapter; Berlincourt el al. (1964), van Kervel and Thijssen (1983),Silk (1984), Sherrit and Mukherjee (2007).

5.3 Theory

5.3.1 Input Impedance

The concept of *input impedance* is generally adapted for design evaluation of multiple layers (Brekhovskikh and Godin, 1990). Given the similarity in the analogy of the mechanical to electrical impedance, the idea is adapted for coupling multiple elastic layers in the electrical transmission line models of ultrasonic transducers (Silk, 1984, pp. 25–50).

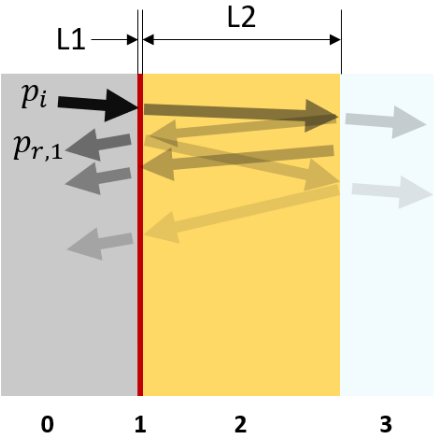

Figure 5-2: Composite of several matching layers with each layer of varying impedance.

The expression for input impedance at the boundary of a j^{th} layer (with thickness l) is given by (Leonid Maksimovich Brekhovskikh and Godin, 1990):

$$z_{in,j} = z_l \frac{z_{j+1} + iz_l \tan(\varphi_j)}{z_j + iz_{j+1} \tan(\varphi_j)} \qquad \text{Equation 52}$$

Where, $\varphi_j = i(k - i\alpha)l$; k is the wave number, α is the attenuation per unit length; z_{j+1} is the input impedance of the layer in front, z_l is the characteristic impedance of the j layer, and $i = \sqrt{-1}$. To find the input impedance of the layer 'L1' in Figure 5-2 one would start with the input impedance at the surface of the half space, given by the characteristic impedance given by Equation 27. This, along with the characteristic impedance of layer 2, is substituted into Equation 52 to find the input impedance at boundary 1-2. In the same manner the input impedance at the boundary 0-1 can be found. This is the total "complex resistance" the waves entering the 'composite layers' have to "overcome".

Finding the effective reflection coefficient incident to the first layer from LHS is given by Equation 34, where z_2 is the input impedance of the composite layers calculated as mentioned. Figure 5-3 shows the reflection and transmission coefficients, and the input impedance at the boundary between medium 0 and 1, for a wave incident to medium 1.

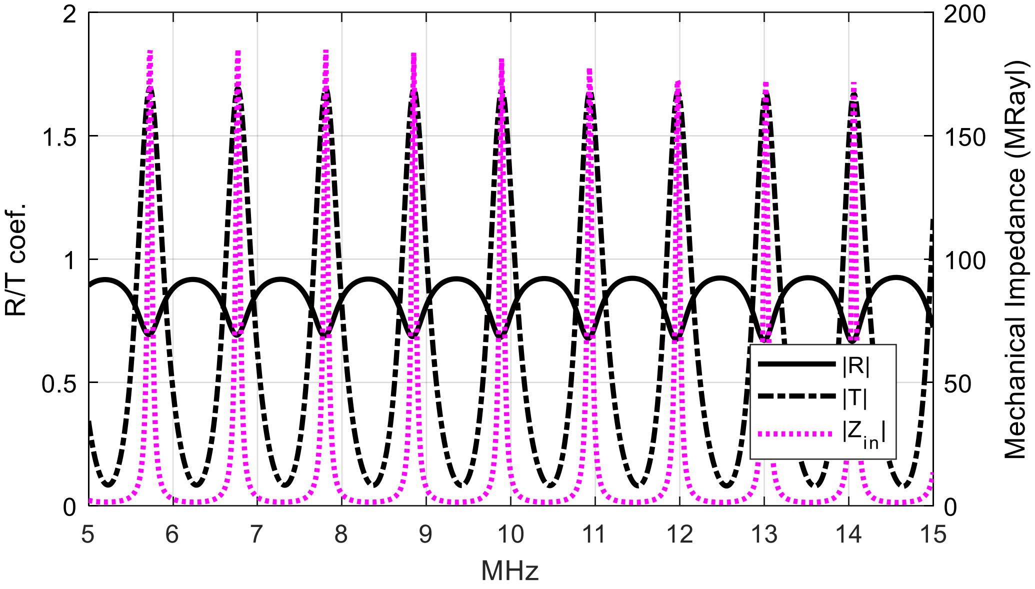

Figure 5-3: Input impedance, and reflection and transmission "coefficients" for wave incident to layer 1 from medium 0 in Figure 5-2, as functions of frequency. The media and their properties are (0) z=30MRayl, c=4000m/s; (1) z=3.5MRyal, c=1410m/s, t=0.01mm; (2) z=17.4MRyal, c=6320, t=3.2mm; and (3) air.

The composite of the two layers is found to transmit or reflect acoustic energy depending on the thickness and wave propagation velocity of layers one and two, as well as the characteristic impedances of the two layers and of the transducer (*layer 0*) and of air. The "*hedgehog spikes*" in Figure 5-3 is due to *layer 2*, showing that it resonates every ~1.025MHz. Higher input impedance results in higher loss in energy of the incident wave, thus the composite of layers and the transducer layer (from where wave is incident into the composite of layers), behave as if they are connected in series in an electrical circuit.

5.3.2 Complex Coefficients

In this work, to include the effect of wave dispersion and attenuation in the elastic layers and the piezoceramic transducers, complex coefficients were introduced, as recommended by

Sherrit and Mukherjee (2007). For the elastic layers, the velocity and impedance were substituted with their complex counterpart. For the lead zirconate titanate (PZT) piezoceramic transducer, the dielectric, elastic and electromechanical-coupling coefficients were converted to their complex counterpart. PZT are polycrystalline piezoceramics that have a crystallographic symmetry class of C_{6mm} ($= C_{6v}$) (Sherrit and Mukherjee, 2007). Therefore, the missing PZT parameters in the datasheet can be obtained from the ones supplied using equations relevant to the C_{6mm} class.

5.3.2.1 Elastic passive materials

The complex coefficients for the passive layers were derived by first obtaining the complex stiffness modulus, E^* from the attenuation coefficient of the materials as shown in Berlincourt et al. (1964, pp. 233–256) as follows:

$$E'' = \frac{\frac{2\rho V^2 AV}{\omega}}{\left(1 + \frac{A^2V^2}{\omega^2}\right)^2} \qquad \text{Equation 53}$$

$$E' = \frac{2\rho V^2\left(1 - \frac{A^2V^2}{\omega^2}\right)}{\left(1 + \frac{A^2V^2}{\omega^2}\right)^2} \qquad \text{Equation 54}$$

Where, the complex Young's modulus, $E^* = E' + jE''$; A is the attenuation coefficient; V is the phase velocity; ρ is the density; and ω is the angular frequency. The complex velocity, V^* and complex impedance, Z^* were derived as follows:

$$V^* = \sqrt{E^*/\rho} \qquad \text{Equation 55}$$

$$Z^* = \rho V^* \qquad \text{Equation 56}$$

Where the attenuation, A was not available but a frequency spectrum of resonance of a layer of the material was available — as was the case for the OML — the mechanical loss factor Q was found from the 3dB bandwidth, Δf and used to find A:

$$Q \cong \frac{f_r}{\Delta f}, \qquad \text{for } Q \geq 10 \qquad \text{Equation 57}$$

$$A \cong \frac{B}{2Q} \qquad \text{Equation 58}$$

Where $B = \omega/V$. The 3dB band, Δf is the frequency band where the frequency spectrum of the amplitude is above $\frac{I_{max}}{\sqrt{2}}$, with I_{max} being the maximum resonance amplitude at resonant frequency, f_r.

5.3.2.2 Piezoceramic material

Complex coefficients of the piezoceramic were calculated from the loss tangents as follows (Dahiya and Valle, 2014, p. 214):

$$C_{33}^{D^*} = C_{33}^{D}(1 + j\tan\delta_m) \qquad \text{Equation 59}$$

$$\varepsilon_{33}^{S^*} = \varepsilon_{33}^{S}(1 - j\tan\delta_e) \qquad \text{Equation 60}$$

Where $\tan\delta_m$ is mechanical loss tangent (the inverse of the often-quoted mechanical loss factor, Q_m (aka mechanical Q)); and $\tan\delta_m$ is the dielectric loss tangent. The calculated material coefficients were: $C_{33}^{D^*}$ = free complex stiffness, $\varepsilon_{33}^{S^*}$ = clamped complex permittivity. The complex electromechanical coupling factor, k_t^*, was found following Sherrit (1999):

$$e_{33}^* = k_t \sqrt{\left|C_{33}^{D^*}\right|\left|\varepsilon_{33}^{S^*}\right|} \exp\left(\frac{j \tan\delta_m + j\tan\delta_e}{2}\right)$$

$$h_{33}^* = \left|\frac{e_{33}^*}{\varepsilon_{33}^{S^*}}\right| \exp\left(\frac{j \tan\delta_m - j\tan\delta_e}{2}\right)$$

$$k_t^* = h_{33}^* \sqrt{\frac{\varepsilon_{33}^{S^*}}{C_{33}^{D^*}}} \qquad \text{Equation 61}$$

Where, $\tan\delta_m$ and $\tan\delta_e$ are the mechanical and electromechanical loss tangents. It should be noted that the data available in datasheets of the transducers were only approximations, and experimental methods would have been required to establish the transducer parameters if higher accuracy modelling was desired. Appendix A shows the MATLAB code used for the purpose of obtaining the transducer material parameters.

5.3.3 Transmission Line Transducer Model

The propagation of plane waves through 1D media can be solved using the network theory (Berlincourt, Curran and Jaffe, 1964) — using the method first proposed by Mason (1948, pp. 230–238). The solution to the wave equation for a purely mechanical layer of thickness, L, presented as equivalent components of a transmission line circuit, is shown in Figure 5-4 (Sherrit and Mukherjee, 2007).

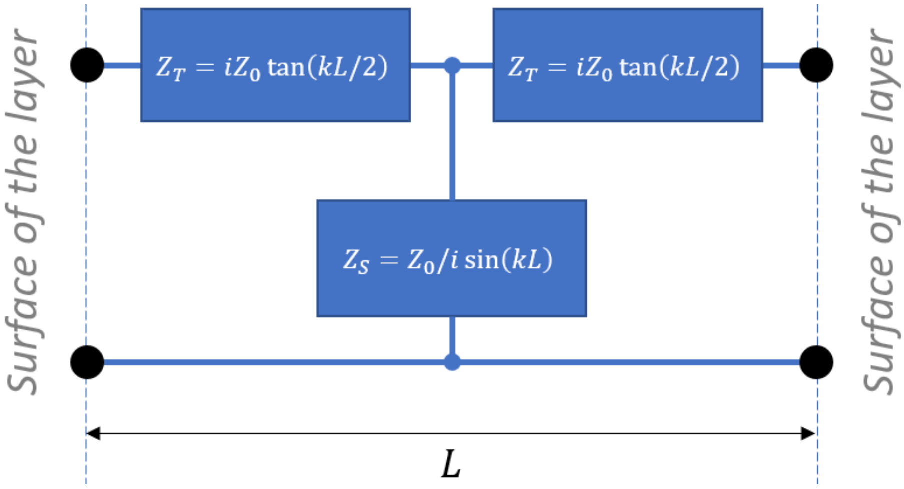

Figure 5-4: A layer of thickness L presented in its equivalent circuit form to be used in an electrical network model. Z_0 is the characteristic acoustic impedance of the layer, k is the wave number. The filled black circles represent the acoustic terminals - 2 layers are connected by their RHS or LHS terminals.

In the model Ohm's law, $V = IZ$, in the electrical circuit, has the analogue $p = vz_c$ in the "elastic circuit". V and I are the voltage and current, respectively; p, v and z_c are the pressure, wave propagation velocity and characteristic acoustic impedance of the layer, respectively.

Figure 5-5 shows the physical layer represented as a component that is part of a two-port transmission line network. Such representation is typical for the KLM model.

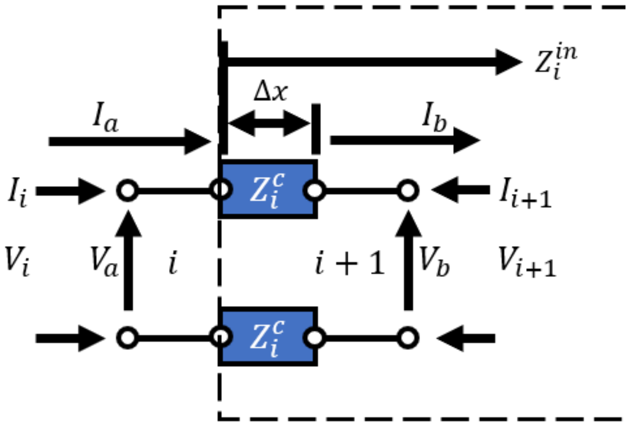

Figure 5-5: i^{th} Physical layer represented as a component of a two-port network transmission line. The impedance of the layer is Z_i^c, the voltages (represented by V) are analogous to mechanical force, and the current (represented by I) is analogous to particle velocity.

Each layer can be cascaded as per the method outlined above in §5.3.1 or represented as transfer matrices corresponding to the two-port network analogy. The Mason model and the two forms of KLM models are explored further below.

5.3.3.1 Mason model

The Mason model for a piezoelectric transducer element and the method of finding the input impedance is given in Figure 5-6.

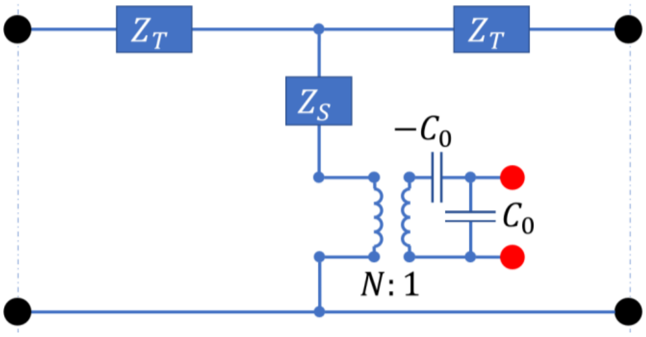

Figure 5-6: Mason's equivalent circuit model for 1D flat plate transducer element. The filled black circles represent the acoustic terminals while the red filled circles represent the electrical terminal. Z_T and Z_S are the mechanical circuit parameters for the transducer as shown in Figure 5-4; $C_0(= \varepsilon_{33}^S A/L)$ is the electrical capacitance of the transducer element — its corresponding impedance is $Z_{C_0}(= [i\omega C_0]^{-1})$; a perfect transformer with winding ratio of $N(= C_0 h_{33})$ is used to represent the electromechanical transformation — if the input impedance at the mechanical side of the transformer is Z_m, then this transforms to the electrical side as $Z_{me}(= Z_m/N^2)$. The input impedance at the electrical ports is given as $Z_{in} = \frac{BC_0}{[B+C_0]}$, where, $B = Z_{me} - Z_{C_0}$.

Combining the transducer (Figure 5-6) and the physical layers (Figure 5-4), it is possible to find the network circuit equivalent to an ultrasonic probe. The front and the backing media can be treated as purely resistive elements — assuming the waves that enters the "layers" are not reflected back towards the transducer. Figure 5-7 shows a circuit for an ultrasonic probe with a piezoceramic transducer element, one front layer and a backing. The backing is treated as non-resonant layer, similar to the purely resistive element (also known as the load) at the front.

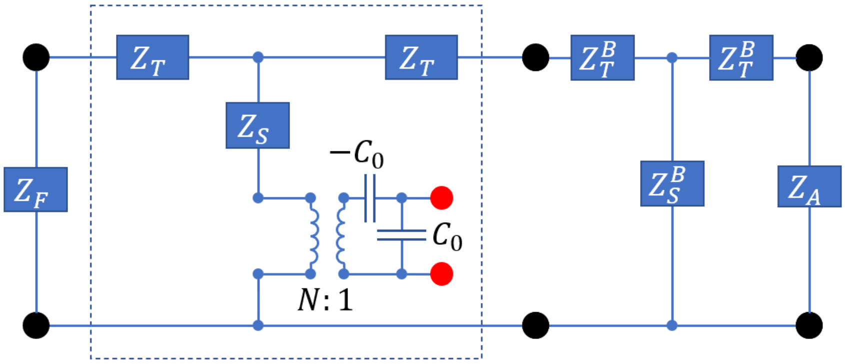

Figure 5-7: Equivalent circuit, as per the Mason model, of an ultrasonic probe with a resonant backing layer (with components of the t-section as per Figure 5-4), coupled to non-resonant backing material (Z_A) and a front matching layer (Z_F).

5.3.3.2 KLM Model

The equivalent of Figure 5-7 is shown in Figure 5-8 but as per the KLM model. The electrical and mechanical counterparts are placed on either side of the transformer in the KLM model. Each physical layer is presented as one impedance component rather than the 3 used in the Mason model. The approach is similar to that used to represent electrical transmission lines. The input impedance of the whole probe is arrived at by cascading the input impedance through all the elastic layers, starting from the outermost, as per the method outlined in §5.3. This results in a circuit with two input impedances Z'_{TL} and Z'_{TR} (different to Z_{TL} and Z_{TR}) on the elastic side. The resultant reduced circuit is solved using standard methods of circuit analysis, as with the Mason model.

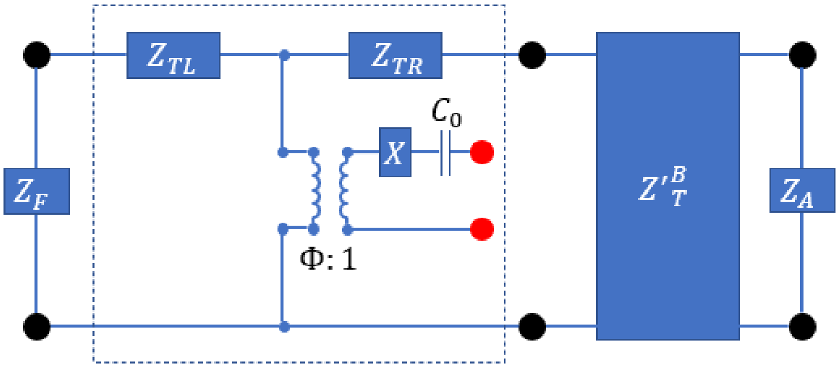

Figure 5-8: KLM equivalent circuit model of probe in Figure 5-7. The dashed lined box shows the piezoelectric element. The elastic layers are treated as a segment of an electrical transmission line. Impedance at the electrical port: $Z_{in} = Z'_{me} + X + Z_{C_0}$; where $Z'_{me} = Z'_m/\phi^2$, $Z'_m = Z'_{TR}Z'_{TL}/(Z'_{TR} + Z'_{TL})$, and $Z_{C_0} = [i\omega C_0]^{-1}$. Z'_{TR} and Z'_{TL} are obtained by cascading the input impedances. Variables: $\phi = [2M\sin(kt/2)]^{-1}$; $X = iZ_0M^2\sin(kt)$; $M = \frac{h_{33}}{\omega Z_0}$; $C_0 = \varepsilon_{33}^S A/L$.

5.3.3.3 Two-Port Network Representation of KLM model

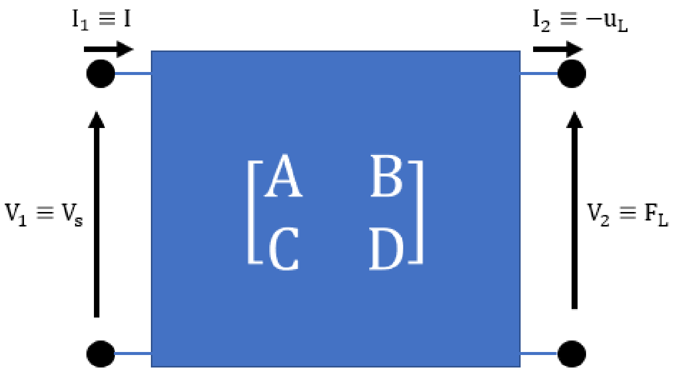

Figure 5-9: Two-Port network representation of a transducer model which related the electrical and mechanical variables at the terminal by the ABCD matrix.

Figure 5-9 shows a commonly used method where the KLM transducer model is represented as two-port network, and the electrical input is related to the mechanical output and vice versa (van Kervel and Thijssen, 1983). Table 5-1 shows the transfer matrix of components within a circuit, including the mechanical layer in the transmission line.

Table 5-1: ABCD-matrix coefficients of elements in a circuit (San Emeterio and Ramos, 2004). l and c are the thickness of and the wave propagation velocity through the mechanical layer, respectively.

Series Impedance, Z_s	Parallel Impedance, Z_p	Mechanical Transmission Line
$\begin{bmatrix} 1 & Z_s \\ 0 & 1 \end{bmatrix}$	$\begin{bmatrix} 1 & 0 \\ 1/Z_p & 1 \end{bmatrix}$	$\begin{bmatrix} \cosh\left(\frac{i\omega l}{c}\right) & -Z_l \sinh\left(\frac{i\omega l}{c}\right) \\ -\frac{1}{Z_l}\sinh\left(\frac{i\omega l}{c}\right) & \cosh\left(\frac{i\omega l}{c}\right) \end{bmatrix}$

The transducer is represented by two matrices, one modelling the capacitances:

$$N_2 = \begin{bmatrix} 1 & \frac{C_0 + X}{p\, C_0\, X} \\ 0 & 1 \end{bmatrix} \qquad \text{Equation 62}$$

Another models the transformer in the KLM model, providing the coupling between the electrical and the mechanical side of the circuit:

$$N_3 = \begin{bmatrix} \frac{1}{\phi} & 0 \\ 0 & \phi \end{bmatrix} \qquad \text{Equation 63}$$

The backing layer, with impedance Z_0, is transformed via the back half of the transducer to yield the following transfer matrix:

$$N_4 = \begin{bmatrix} 1 & 0 \\ -1/Z_l & 1 \end{bmatrix} \qquad \text{Equation 64}$$

Where,

$$Z_l = Z_c \frac{\mathrm{Z_b} + iZ_0 \tan(\varphi_j)}{Z_0 + i\mathrm{Z_b} \tan(\varphi_j)} \qquad \text{Equation 65}$$

The front acoustic port of the transducer is represented as per the transfer matrix of a mechanical transmission line, given in Table 5-1. The front layers include the half layer of the transducer and any other front layers.

The ABCD matrix of each layer is multiplied to arrive at the final ABCD matrix, N_t. For a transducer with a total of n transfer matrices, N_t is a product of all the matrices, given as follows:

$$N_t = \prod_{j=1}^{n} N_{n-j+1} \qquad \text{Equation 66}$$

The overall impedance of the transducer is:

$$Z_e(\omega) = \frac{D\,Z_l - B}{A - C\,Z_l} \qquad \text{Equation 67}$$

The voltage transfer function of transmission is:

$$H_t(\omega) = \frac{2Z_l}{(-Z_e Z_l\,C + Z_e\,A - C + Z_l\,D)} \qquad \text{Equation 68}$$

The voltage transfer function of reception is:

$$H_r(\omega) = \frac{2Z_e}{(-Z_e Z_l\,C + Z_e\,A - C + Z_l\,D)} \qquad \text{Equation 69}$$

The round-trip or through transmission transfer function is given by multiplying the transfer functions for transmission and reception:

$$H_{tr}(\omega) = H_t H_r = \frac{4Z_e Z_l}{(Z_e Z_l\,C - Z_e\,A + C - Z_l\,D)^2} \qquad \text{Equation 70}$$

Figure 5-10 shows the flow chart highlighting the process of obtaining complex material properties of a Piezoceramic transducer.

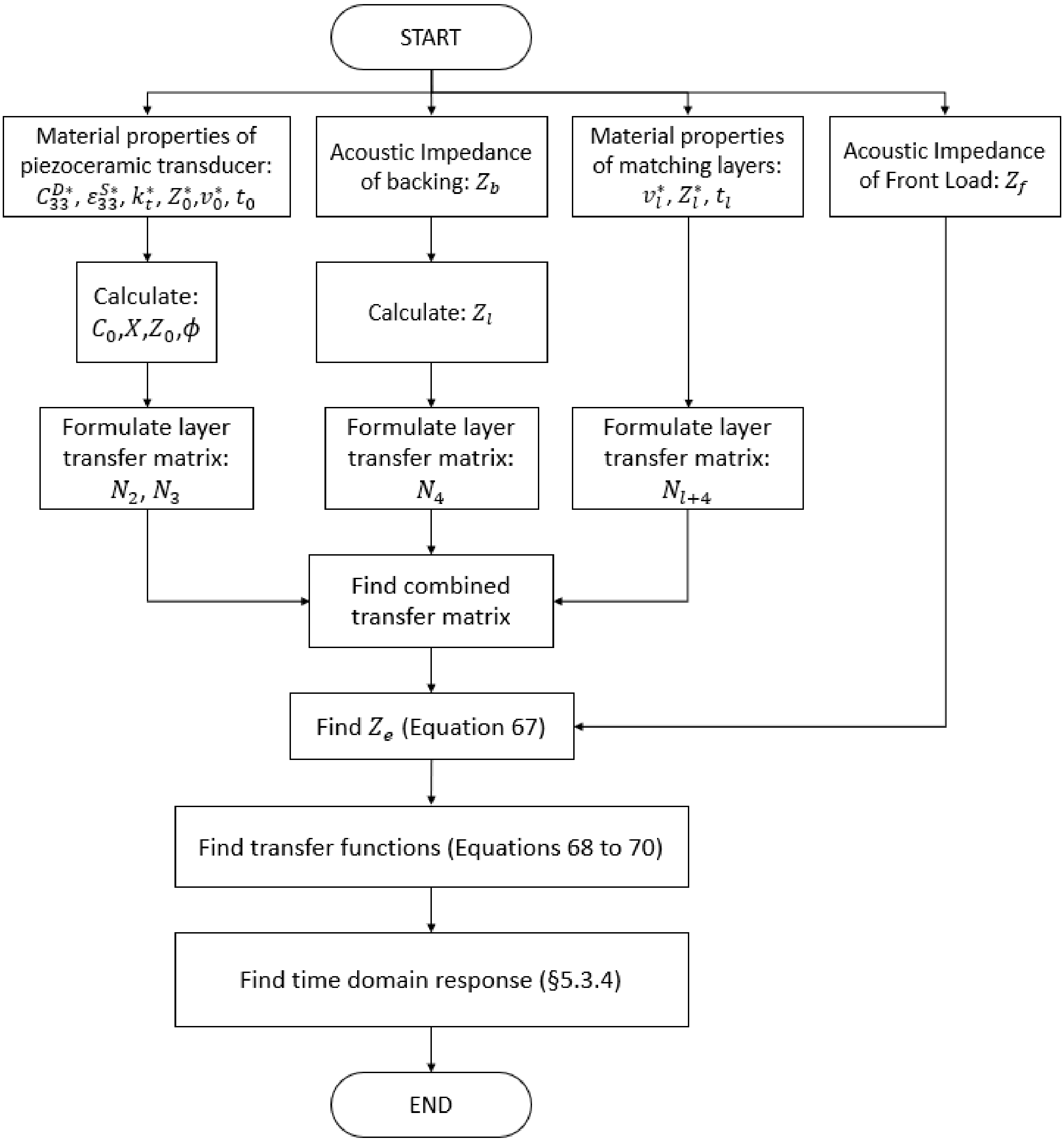

Figure 5-10: Flow chart of the process highlighting the steps in solving the KLM model to obtain the probe impedance and its time domain response. The material properties of all the resonant layers (excluding the front load and the backing) are given in their complex form; The complex coefficients of the piezoceramic transducer and the matching layers are obtained following the steps shown in §5.3.2. Flow charts to obtain the complex versions of the material properties are given in Appendix B.

5.3.3.4 Model Comparison

Figure 5-11 shows the response of probe in Figure 5-8/Figure 5-7 obtained using the Mason and the KLM model. Figure 5-12 shows that the results of the two-port network method and the method to cascade the impedance layer by layer, as per §5.3.1 (and Figure 5-8) are the same.

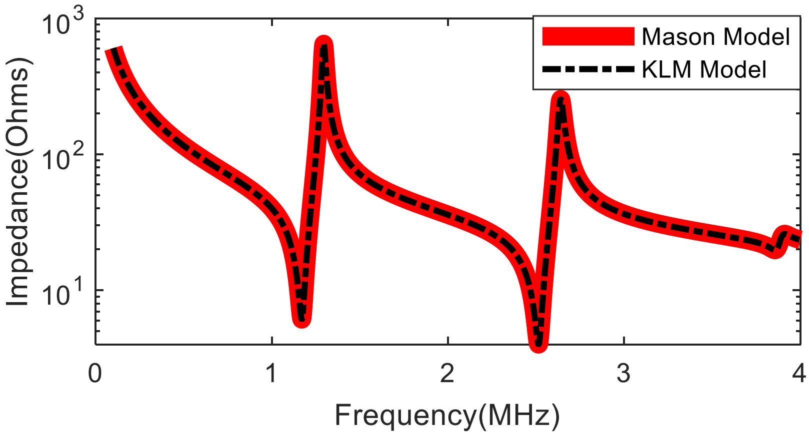

Figure 5-11: Impedance of piezoceramic transducer with a stainless-steel backing. The layer parameters are as per Sherrit et al. (1999); the figure is reproduced from the reference to validate the model used for the current work.

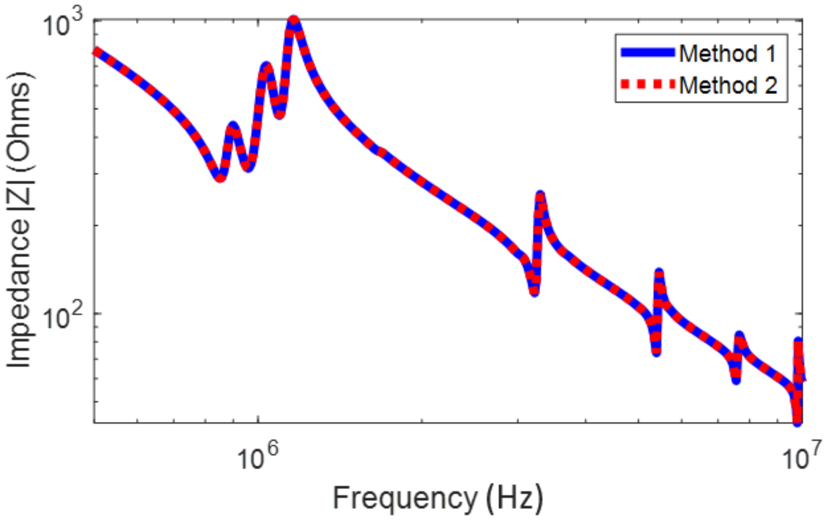

Figure 5-12: Comparison of the probe impedances obtained using the KLM model and method in Figure 5-8 (Method 1), similar to Figure 5-11 and the two port network method in §5.3.3.3 (Method 2). The figure is produced to validate the two-port network method.

5.3.4 Time Domain Response

The time domain response for a discrete input waveform vector is obtained from the transfer functions (calculated in the frequency domain) given above, as follows:

1. Obtain a symmetric transfer function vector, H' from the calculated transfer function, H:
   a. Find the complex conjugate, $\overline{H}$, of the transfer function, H.
   b. Restructure $\overline{H}$ such that it is symmetric about its first element to obtain $\overline{H}'$ — the present author "flipped" the vector.
   c. Concatenate the unaltered transfer function vector, H to the vector obtained from step b, $\overline{H}'$. The new vector, H' is symmetric in magnitude and asymmetric in phase about the midpoint.
2. Find the inverse discrete Fourier transform of H' to obtain the impulse response.
3. Convolute the impulse response with the time domain excitation signal.

The method was obtained during a video interview (J. Davidson, 2021, personal communication, July 27).

5.4 Probe Design for Analysis using the Transmission Line Model

The two port KLM model was used to predict the time and frequency domain response of the probe with varying design parameters of the intermediate layer. Figure 5-13 shows the configuration of the probe model studied. The model included a semi-infinite (non-resonant) backing layer, an electromechanical piezoceramic layer, elastic intermediate matching layer (IML), elastic outer matching layer (OML), elastic layer of air, and elastic cast iron layer that is purely resistive. Table 5-2 shows the material properties of components in the model, along with the parameters that were varied to study their impact on the model response.

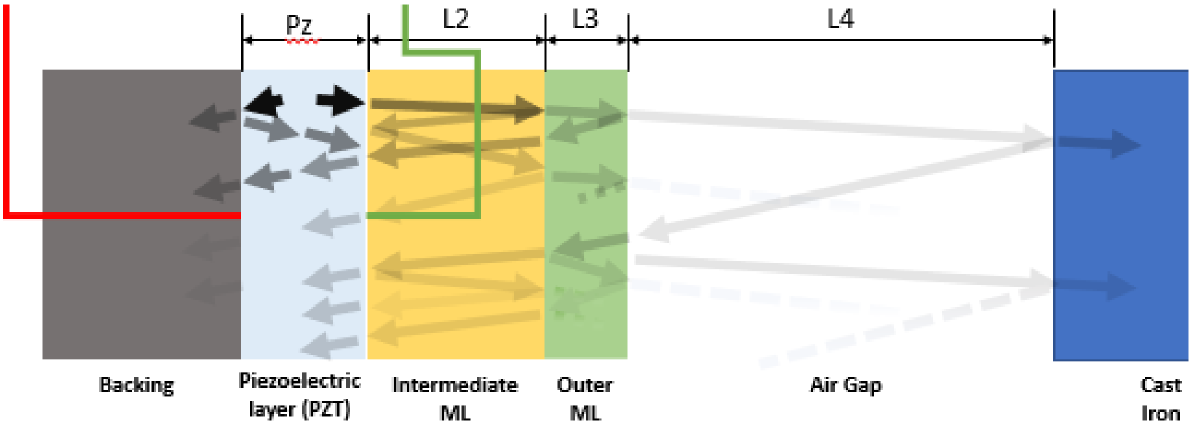

Figure 5-13: Configurations of a 1-D multi-layer analytical model used to study the response of various matching layer materials of the 1MHz ultrasonic probe. The green and blue wires represent the electrical leads while the arrows represent various waves bouncing within the layers.

Table 5-2: Material properties of the layers used in the model. Values with † were varied in the model.

Material	Specific Impedance (MRayls)	Wave propagation velocity (m/s)	Attenuation (Nepers/m) [per layer thickness (γ)]	Thickness
Backing	5	1500	1000	Inf
IML	2.88†	2554.6†	50 [0.06] †	638.5µm†
OML	0.16	500	787 [0.1]	127µm
Air	410e-6	330	17	10mm
Cast Iron	33	4250	33	Inf

Initially, properties of PZ4 and PZ5H, similar in properties to those of PIC181 and PIC255 from the catalogue of PI[1], respectively, were used to validate the model by comparing to experimental outcome in § 4.6 to the model. Subsequently a probe model with transducer properties of PIC255 was studied. Complex velocity and specific impedance for the elastic layers, and complex forms of free stiffness and clamped permittivity of the piezoelectric transducer, were obtained as shown in §5.3.2. The solution to the model was obtained for excitation signals (10 cycle waveform of unit amplitude) of 0.7MHz – 1.5MHz. The MATLAB codes used are given in Appendix A. A flow chart to show the method followed in solving the KLM model is given in Figure 5-10.

---

[1] Obtained from https://www.piceramic.com/en/service/downloads/catalogs-brochures-certificates/

5.5 Results and Discussion

5.5.1 Probe Response

Figure 5-14 shows the outcome of using two probes' models — a probe with hard PZT (PZ-4) was used to emit, while a probe with soft PZT (PZ-5H) was used to receive. Alternative transducer elements were used due to all the piezoceramic variables available for PZ-4 and PZ-5H (Berlincourt, Curran and Jaffe, 1964, pp. 202–203), while the datasheet of PI does not provide variables like C_{33}^{D} of PIC255.

The model is obtained from multiplying the through transmission transfer function of using the two probes, as per Equation 70, with the through transmission through layer of air of 52mm thickness, as per Equation 38.

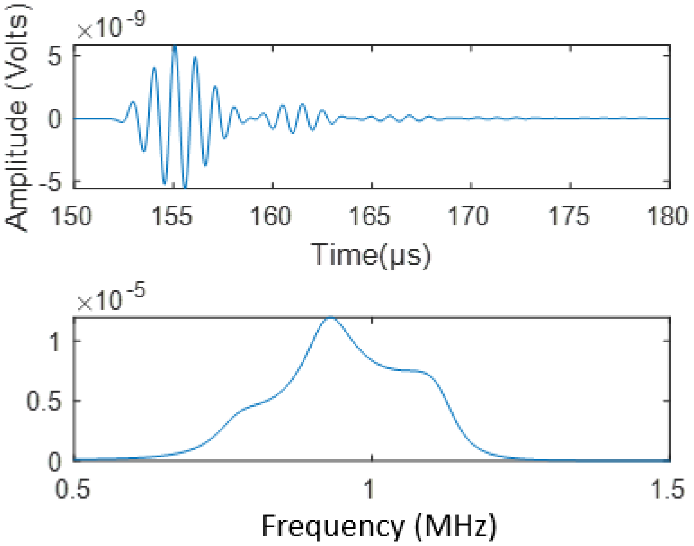

Figure 5-14: Recreation of pulse echo experiment using soft air coupled probe with active transducer element PZ4 (similar to PIC181) as pulser and PZ5H (similar to PIC255) as receiver, to measure a gap of 52mm. The model is recreated using the KLM model, using the MATLAB code in Appendix A. (Top) Impulse response of the probe. (Bottom) Frequency domain response of the probe. Alternative transducer elements were used due to all the data available for PZ4 and PZ 5H, while the datasheet of PI does not provide variables like C_{33}^{D} of PIC255.

When comparing the frequency domain of the model to that of the experimental outcome (the lower plots of Figure 4-13 and Figure 5-14) it can be seen that the frequency domain response is captured to a reasonable accurately. The discrepancy in the model is likely due the transducers not being exactly the same, and also the model is also just 1D. The model also did not accurately account for the impedance of the transmitter and receiver electronic equipment as well as the impedance of the backing. Another reason could be that the model assumes the layers to have a constant thickness, while this would not be the case for the manufactured probe, where the thickness would vary through the cross-section. Finally, the model neglects the impact of reflection of the 3D non-flat surface which would result in different superposition of waves compared to a flat 3D surface.

The probe model is seen to give a reasonable approximation of the experimental behaviour and thus is seen sufficient to use when designing future probes.

5.5.2 Probe Design Evaluation

The design parameter of the probe with varying intermediate layer properties (as shown in Table 5-2) was evaluated using the KLM model, the results of which are presented below.

When the IML resonates or has lower attenuation, the KLM model (results shown in the plots below) shows higher energy transmission out from the probe and back into the probe – when the wave completes one round trip. Thus, the amplitude of the wave reflected in the plots below show the effectiveness of the IML.

Varying Thickness of IML

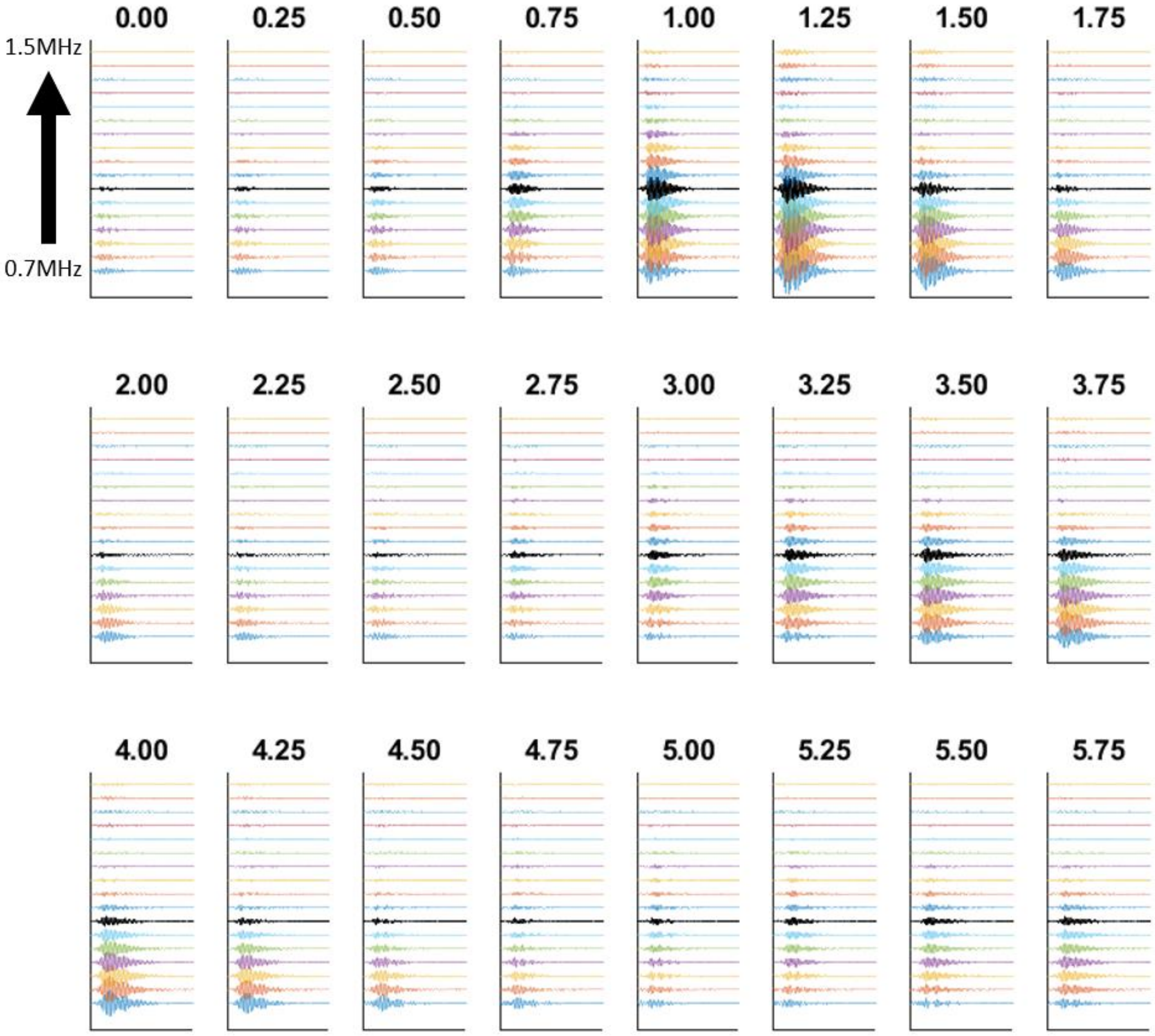

Figure 5-15: Waveform of the probe in Table 5-2 with varying IL thickness, obtained using the KLM model. *Lowest plot is 700kHz, going up in 50kHz to 1.5MHz at the top. The black line is 1MHz. All the cells are to the same scale.*

Figure 5-15 shows the results of varying thickness, t of the IML. As expected, the model shows that the thickness impacts the resonant characteristics. The probe models are shown to resonate when pulsed at frequencies equal to the quarter wave resonant frequency of the IML, i.e. the thickness of the IML, $t = \lambda(2n - 1)/4$. The IML thickness can therefore be assumed as one of the critical parameters of the probe. The resonant characteristics from Figure 5-15 is summarised in Figure 5-16.

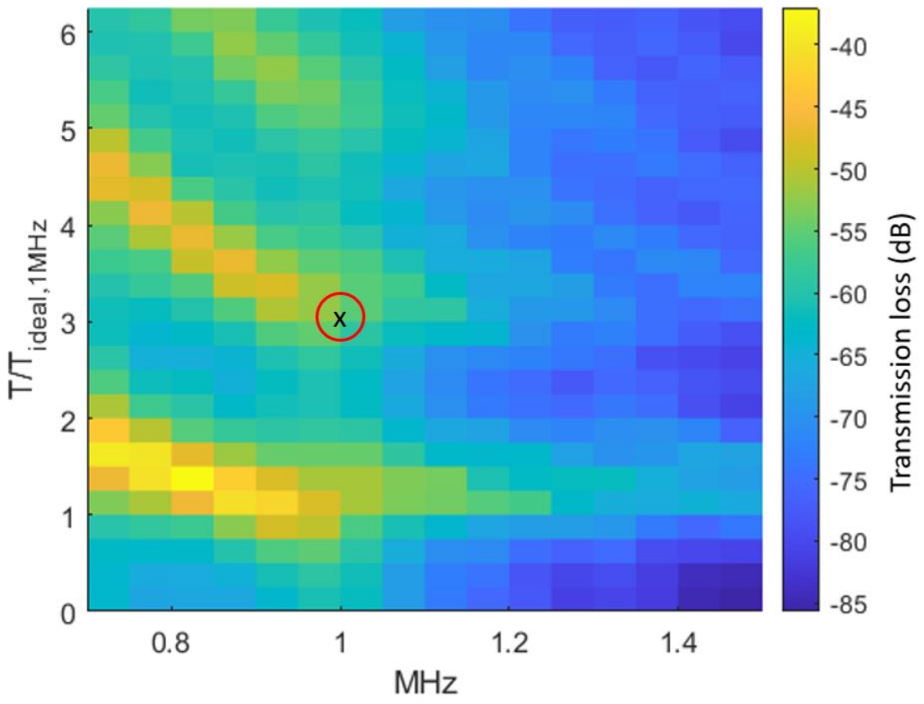

Figure 5-16: Transmission loss as function of IML thickness and excitation frequency. The thickness axis is normalised by the thickness of a perfect ¼ wave resonant layer. The black cross inside the red circle marks the intended design thickness of the IML of the probes manufactured, see Chapter 4.

Varying Impedance

The impedance of the IML was varied on the assumption that the relationship between density and velocity are roughly linear for materials to be used as intermediate matching layers; see Figure 5-17. Based on this and assuming a constant mechanical quality factor, Q_m, the complex impedance and velocities of IML material to be used in the model were derived. The velocity was used to find the thickness of IML such that its 1st quarter wave resonance was at 1MHz.

The method kept the ratio $\frac{\alpha f}{4V}$ constant, consequently $\frac{f}{4V} = \lambda$. Therefore, it was possible to find the value for complex velocity and impedances, that only studies the impact of varying impedance. The total attenuation within the layer for one round trip was kept constant.

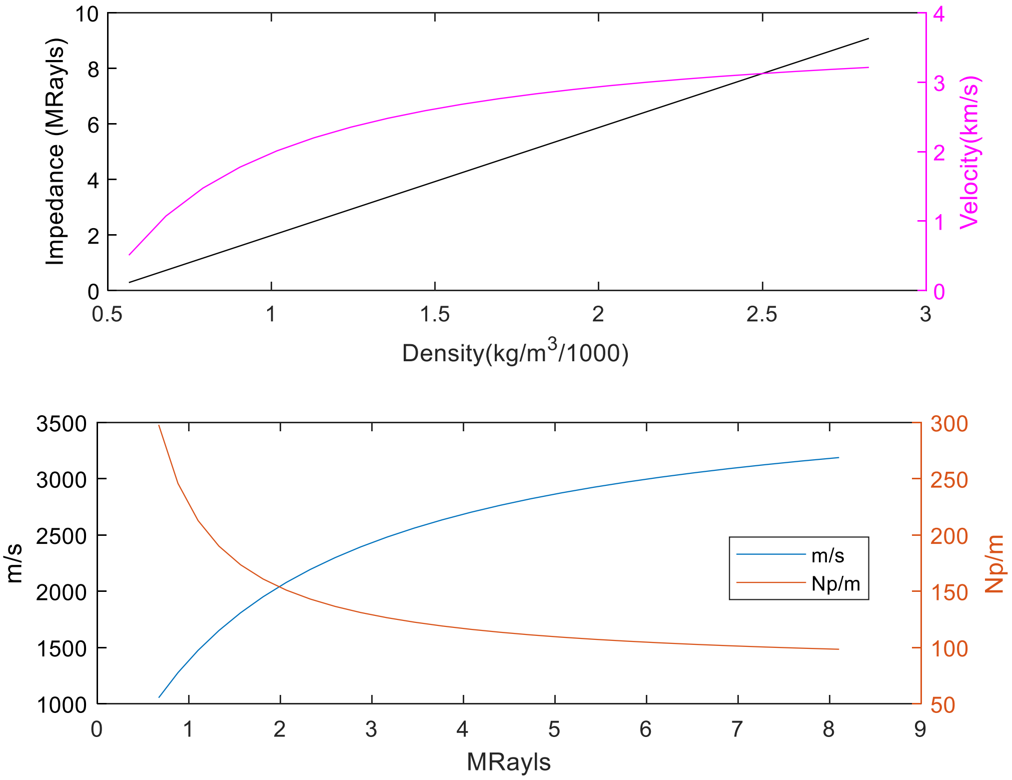

Figure 5-17: (Top) Linear least square fit to the density and impedance of common materials, data used to obtain the density and velocity relationship which was subsequently used to derive theoretical IML with varying impedance but constant attenuation per thickness. (Bottom) Attenuation, Velocity, and Impedance of the IML used for the simulation.

Figure 5-19 and Figure 5-18 show the solution to the model with changing IML impedance. It is seen that probe response at 1MHz does not vary much with changing impedance, while the attenuation of other frequencies is affected to a greater magnitude. This is similar to what was highlighted by Desilets et al. (1978). If the IML thickness is matched to the λ/4 resonant frequency, then the "impedance bandwidth" for possible IML material seems to be wider.

Different impedance matching schemes are recommended for probes with composite matching layers in the literature (Desilets et al., 1978). However, they result in impractical material (unrealistically low acoustic impedance) for the case at present; and the analysis was limited to realistic material, with specific acoustic impedance greater than 0.67 MRayls.

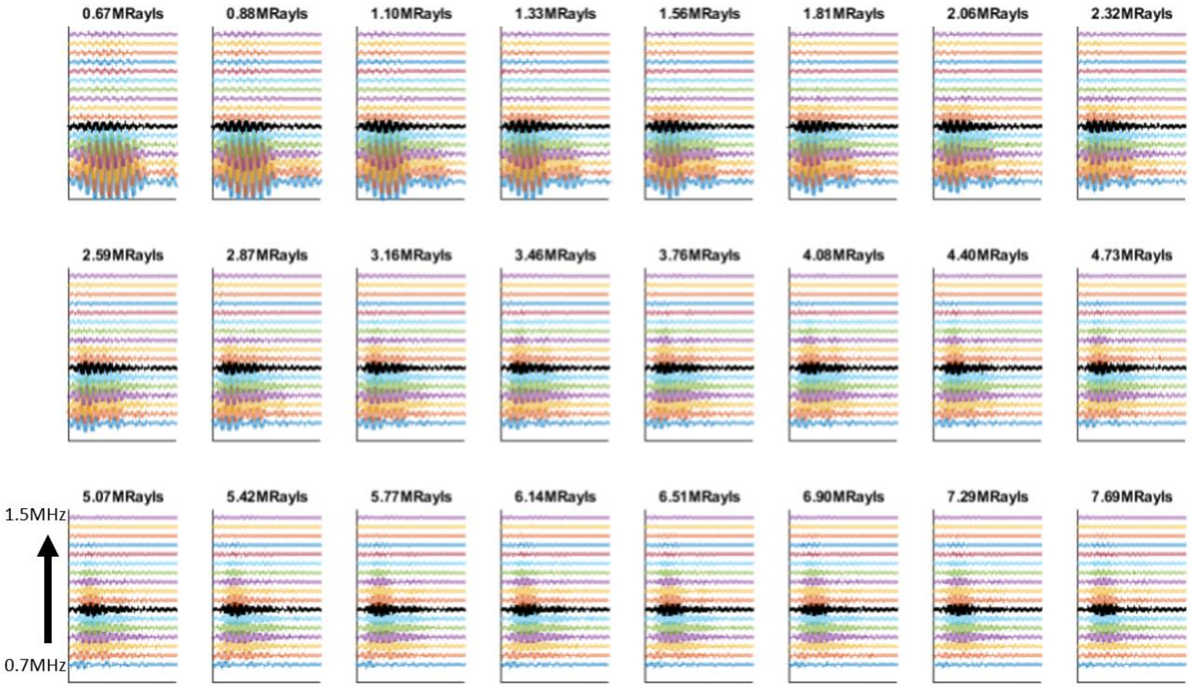

Figure 5-18: Impact of varying the impedance of the intermediate matching layer on the time domain response of the probe, obtained using the KLM model. 7th waveform from the bottom is the 1MHz excitation. *Lowest plot is 700kHz, going up in 50kHz to 1.5MHz at the top. The black line is 1MHz. All the cells are to the same scale.*

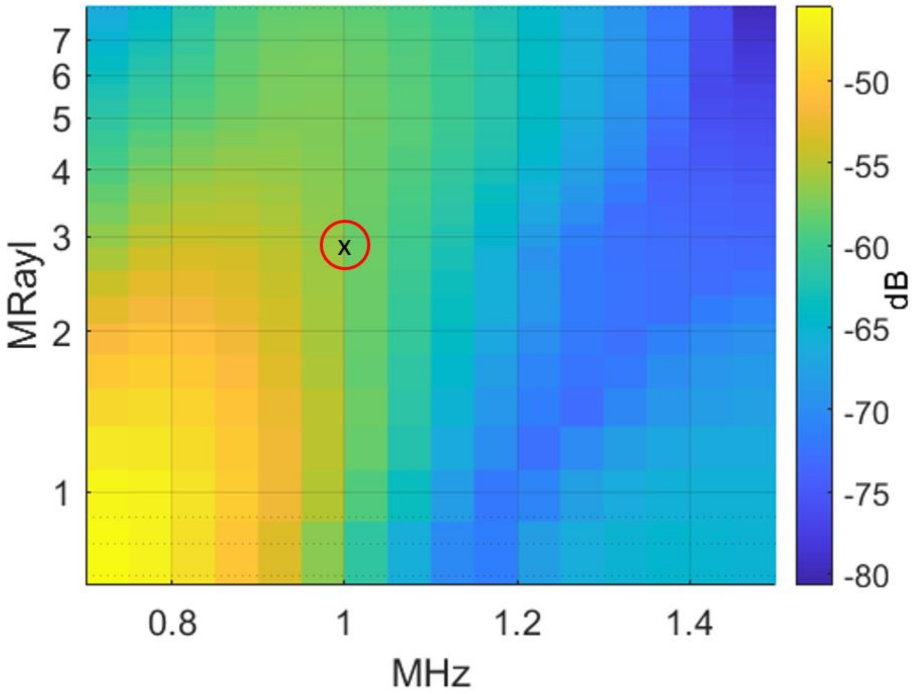

Figure 5-19: Changing impedance versus excitation frequency of the probe. Box in top RHS highlights the resonant characteristics of the probe changing with increasing impedance. The black cross inside the red circle marks the impedance of the IML of the probes manufactured, see Chapter 4.

Similarly, a solution is obtained by only varying the total attenuation within IML, results of which are presented in Figure 5-21 and Figure 5-20.

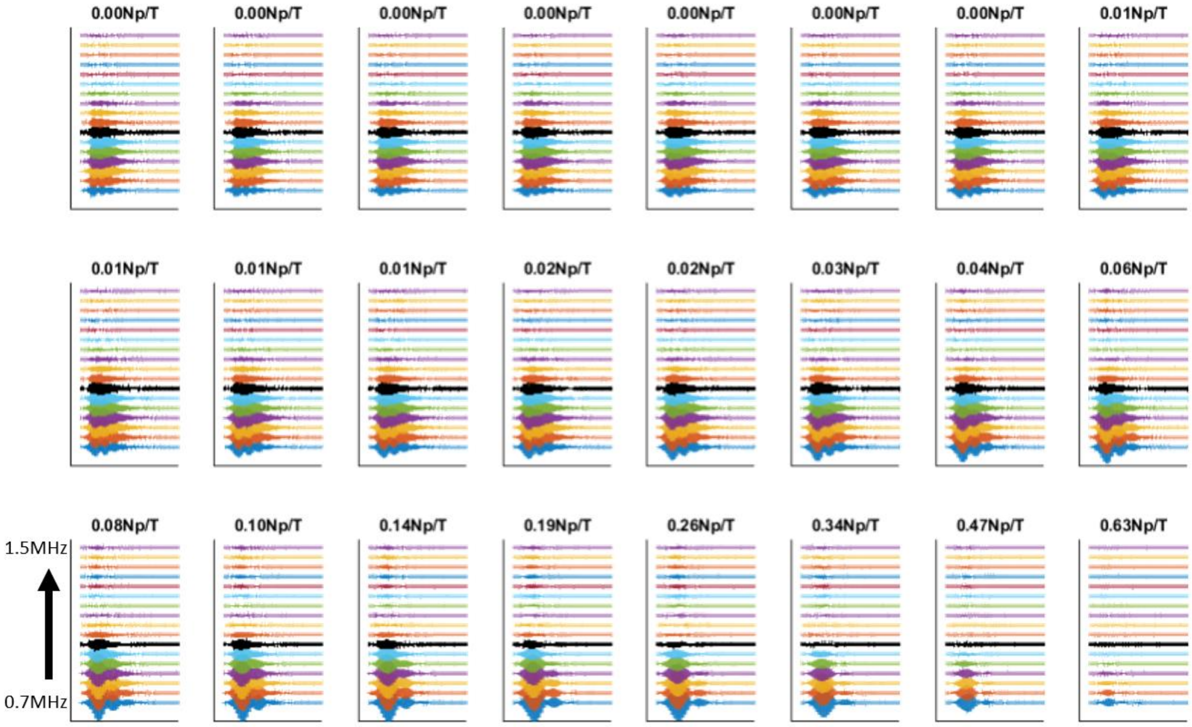

Figure 5-20: Waveform of the response of the probe model with changing attenuation while other parameters are kept constant, obtained using the KLM model. Np/T is the total loss as the wave travels the distance of the layer thickness. *Lowest plot is 700kHz, going up in 50kHz to 1.5MHz at the top. The black line is 1MHz. All the cells are to the same scale.*

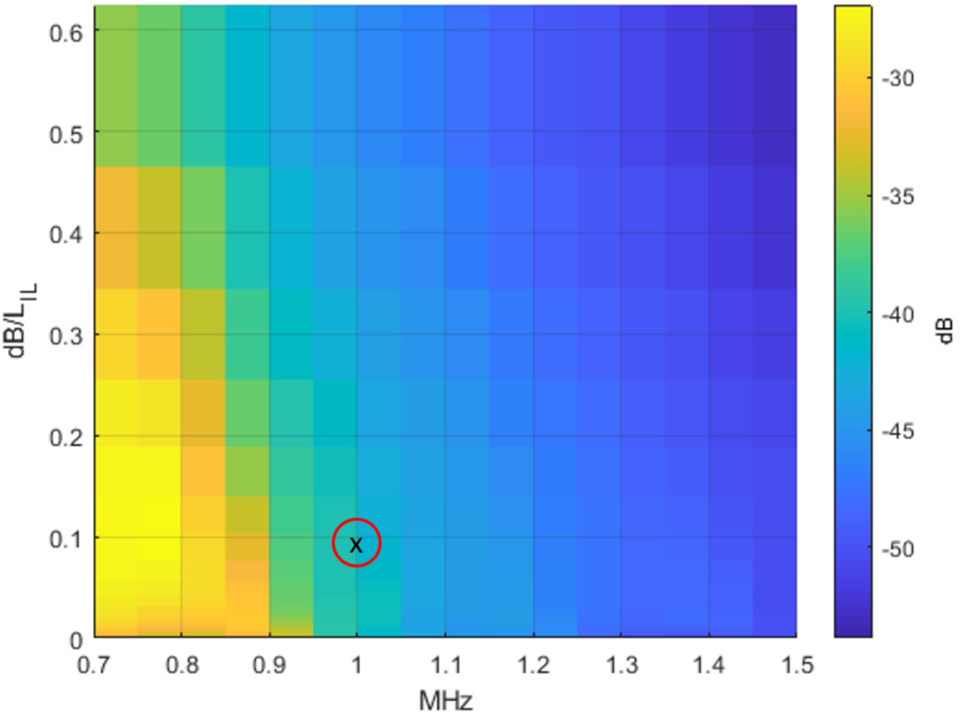

Figure 5-21: Effect of varying the attenuation of the intermediate matching layer on the resonant characteristics of the probe. The IL thickness is kept constant to correspond to a quarter wave resonant frequency. The black cross inside the red circle marks the attenuation per thickness of the IML of the probes manufactured, see Chapter 4.

Using the lowest attenuation, the possible attenuation coefficient does not seem to improve transmission. This is likely because the primary mode of energy loss is that which escapes the layer at the interfaces, as a portion of the wave is reflected while a portion is transmitted. There seems to be a region (around ~0.14Np per thickness of the IML) where the attenuation losses become more significant and the wave attenuates rapidly with changing attenuation past this point; this observation is similar to that mentioned by Álvarez-Arenas(2004).

The simulations showed a clear need for the probe to be designed with better control of the thickness of the intermediate layer. This was unfortunately not possible for the probe that was designed and manufactured (shown in Chapter 4).

It was found that the impedance of the intermediate layer was not as restrictive. Therefore, for future probe designs use of an IML material with higher acoustic impedance but with better thickness control would be recommended.

Finally, the attenuation of the intermediate layer was found to have significant impact only when it was increased past a certain amount. Therefore, using the model developed in this section could identify the highest value of attenuation coefficient possible for an IML material.

5.6 Conclusions

A two-port network KLM model was developed to analyse several IML material parameters of an air coupled ultrasonic probe consisting of two passive front matching layers, a passive backing, and an active piezoceramic transducer. The outcome of the model can be summarised as follows:

1. The thickness of the IML is a critical parameter and probes with IML thickness that is unmatched can result in significant transmission losses.
2. Matching the thickness of the intermediate layer to a quarter wave thickness allows the impedance of the layer to be varied, i.e. giving the designers a "wider impedance bandwidth".
3. Consideration of the attenuation coefficient of the layer seems to depend on the primary mode in which the trapped energy within the layer is lost. If the primary mode is transmission at the boundary, then attenuation does not seem to impact transmission loss. However, if the attenuation becomes the primary mode, then using material with a higher attenuation coefficient seems to lead to increase in transmission loss.
4. There is a threshold where the attenuation coefficient of the IML becomes the primary mode of transmission loss.

6 Sensor Evaluation

This chapter describes the method for high accuracy (micro meter level) distance measurement and potential sources of measurement errors. The resolution and accuracy of the distance measurement made by a manufactured ultrasonic probe described in Chapter 4 (1.4MHz) to flat and curved surface reflector targets were analysed and are reported in the chapter.

The work serves as calibration of the air-coupled probe that was used for bore-form measurement of cylinder liners in Chapter 7.

6.1 Introduction

Figure 6-1 shows a typical setup using an air coupled probe to measure the distance to a reflector target and the associated waveform that is captured. The waveform was processed as per the generic method presented in Chapter 3 (§3.4) to find the distance measurement.

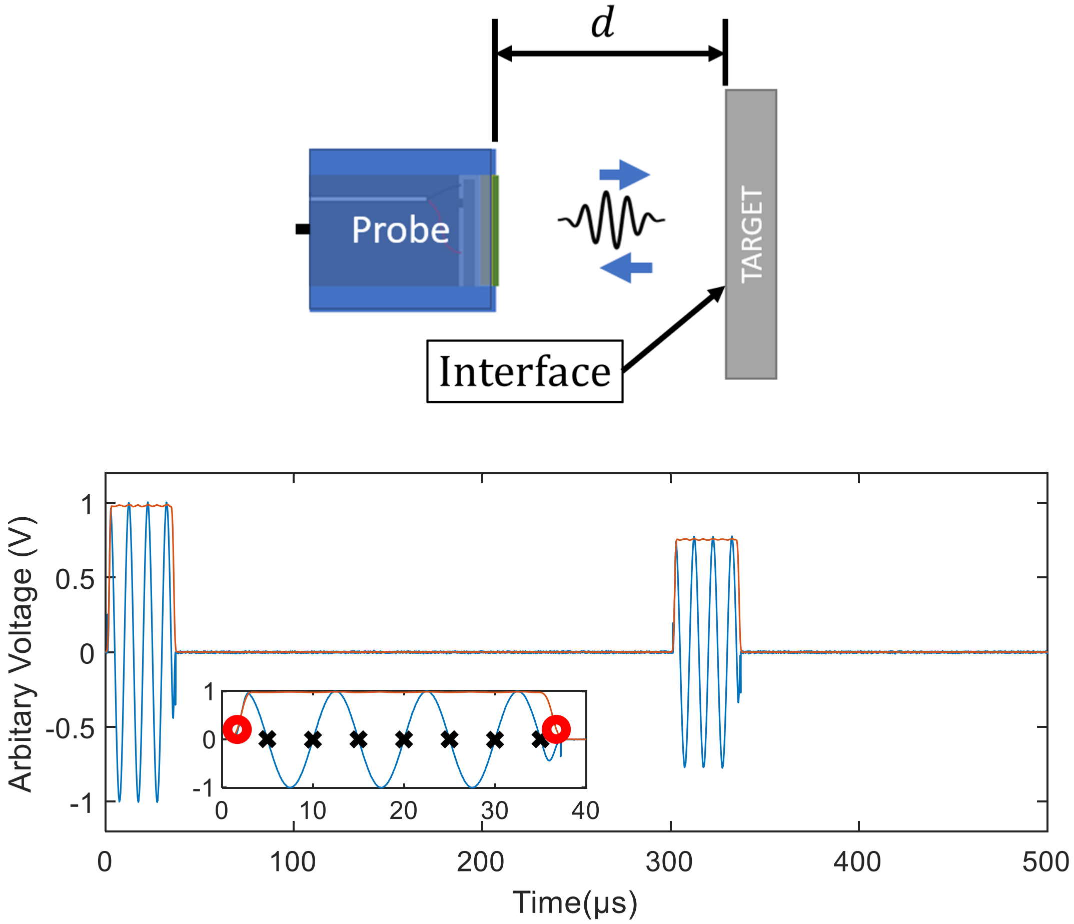

Figure 6-1: (Top) Schematic of an ultrasonic probe used to measure distance between itself and the target. (Bottom): Typical waveform gathered (by an oscilloscope) for the setup in top figure.

Commercially available ultrasound-based distance measurement sensors (generally in the form of proximity sensors) have a quoted accuracy of around ~±0.5mm. In the literature the quoted accuracy of similar probes is around ±0.1mm (Hickling and Marin, 1986). However, both the distance measurement accuracies correspond to systems which involve measurement to targets that are up to 200mm and in some instances up to few metres away. While the measurement accuracies of the probes in literature were sufficient for their applications requirements, for the work presented within this thesis, it was important to measure the ability of the probes to measure to an accuracy that is within a few microns.

The commercial air-coupled probes generally tend to be limited to few 100s kilohertz. The application of higher frequency ultrasonic waves, in the megahertz range, has however shown promising results in the literature and is of interest at present.

6.2 Literature review

Air coupled transducers have been used as distance sensor or proximity sensor for several decades. The advantages of using ultrasound have been that of the large measurement range and its ability to work against any type of reflecting surface (also known as *target*), offered at a reasonable cost. The use of ultrasonic proximity sensors at present can be found in automotive (Canali *et al.*, 1982), manufacturing (Hickling and Marin, 1986), ranging (Hill, Bury and Gray, 1994), linear and angular position control (Marioli, Sardini and Taroni, 1988), and surface metrology (Robertson *et al.*, 2002; Gómez-Ullate and De Espinosa, 2004), to more recent applications being investigated into tactile sensation for pain distraction (Karafotias *et al.*, 2018), and material differentiation in robotics (Fang *et al.*, 2019).

Typical air-coupled ultrasound probes for range measurement applications operate between a few 10s of kilohertz to a low 100 kilohertz range. The accuracies of early proximity detectors in the 100s kHz range were reported to have an accuracy of around 0.1mm-1mm and offered measurement of 100cm for 250kHz (Canali *et al.*, 1982), 30cm for 400kHz and 1m at 200kHz (Hickling and Marin, 1986; Magori and Walker, 1987), while more recent work has reported higher accuracy using various pulse excitation and signal processing techniques, although the requirement for signal averaging is evident (Sasaki *et al.*, 2009).

For velocity of 343m/s (of 1MHz - value obtained from Fang et al. (2019)) the change in 1µm would give a change in time of flight of 5.83ns (in pulse echo mode). However, in close proximal distance sensing of say 10mm, the TOF is only 0.583µs, therefore the short time required to take a reading allows for signal averaging of various readings - provided high frequency (relative to the target motion) triggering methods are available – subsequently improving the accuracy. Shorter distance to the target also means lower variations in velocity thereby leading to lower error.

Various literature on amplitude-based methods to conduct accurate depth change measurement was reviewed. Focused probes operating at 600kHz were used by Robertson et al. (2002) to measure depth change due to placement of gauge blocks in between a granite table and the probe. A depth resolution of around 2-5µm is reported, although the authors point out potential improvement on the measurement by employing a phase change method, provided a phase tracking method is employed. Similar work was carried out by Gómez-Ullate and De Espinosa (2004) using a probe of 1-4MHz. The authors show it is possible to detect depth change of printed ink of 10µm on substrate. While the depth change is evident, the measurement data seem to suggest the measured change could have been due to the sudden impedance change of the reflector — something Blomme et al. (2002) take advantage of to measure the etching on PCB boards.

The literature suggests depth change measurement by monitoring phase change of the wave is more robust than measuring amplitude change. Amplitude based method are also susceptible to dispersion due to change in surface roughness, as various authors have shown in the use of air coupled probes for such applications (Blessing and Eitzen, 1989; Oh *et al.*, 1995; Stor-Pellinen and Luukkala, 1995).

More promising applications of in depth measurement is presented by Takahashi et al. (Takahashi and Ohigashi, 2009) who successfully scan the printed image of 2000-yen bill, subsequently reporting a depth resolution in the sub-micron range , using probe with PVDF as the active transducer material. Another application sees the use of a 1MHz focused probe in the fingertips of a robotic arm (Fang *et al.*, 2019), to detect proximity to objects the hand is about to grab; the accuracy is reported but only to under 0.1mm.

6.2.1 Impacts due to Environmental Factors

Attenuation of acoustic waves can impact the accuracy of measurement by affecting signal-to-noise-ratio (SNR), as has been pointed out by authors such as Grandia and Fortunko (1995). Attenuation in air as a function of frequency, relative humidity and temperature is calculated using the method presented in references (Zuckerwar, 1990; Bass *et al.*, 1995) and is presented in Figure 6-2. The calculation scheme used to produce the figure is presented in Appendix A.

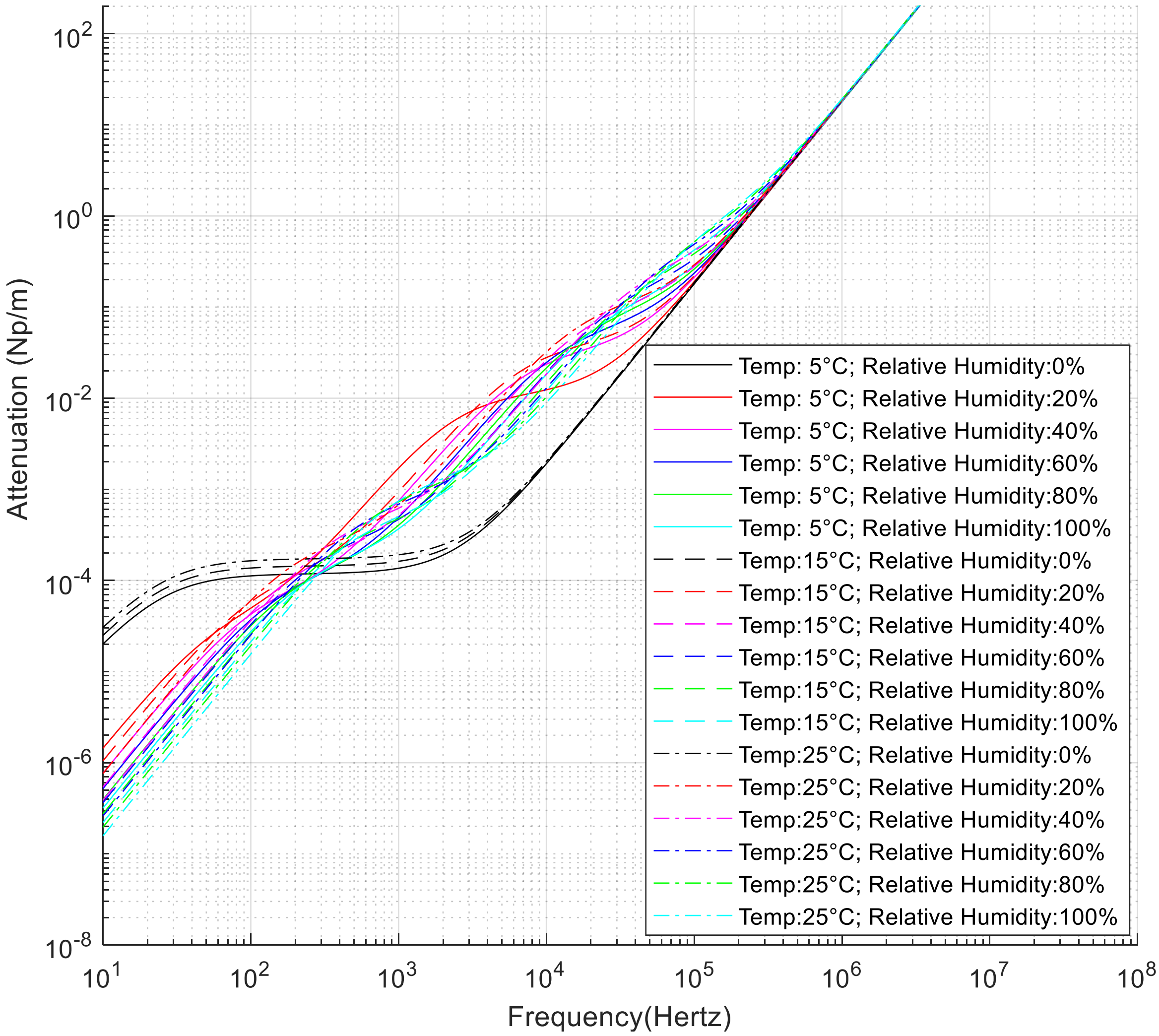

Figure 6-2: Sound attenuation in air at 1ATM, as a function of frequency, with varying temperature and relative humidity (RH). The *colour scheme* of the plots differentiates RH, while the *line style* differentiates temperature.

The attenuation in the MHz range is seen to be almost solely a function of the frequency, i.e. the impact of temperature and relative humidity does not appear to matter. However, as was highlighted above, the varying acoustic impedance (Blomme, Bulcaen and Declercq, 2002) and surface roughness (Blessing and Eitzen, 1989) will impact distance measurements.

The variation in acoustic wave propagation velocity in air due to humidity, air pressure, CO_2 concentration, and air temperature is presented by Cramer (1993). Using the authors' method, the impact of varying humidity and temperature on wave velocity is shown in Figure 6-3. It can be seen that temperature could be the most likely source of measurement error, while the effect of humidity is relatively small, c.f. top and bottom plots.

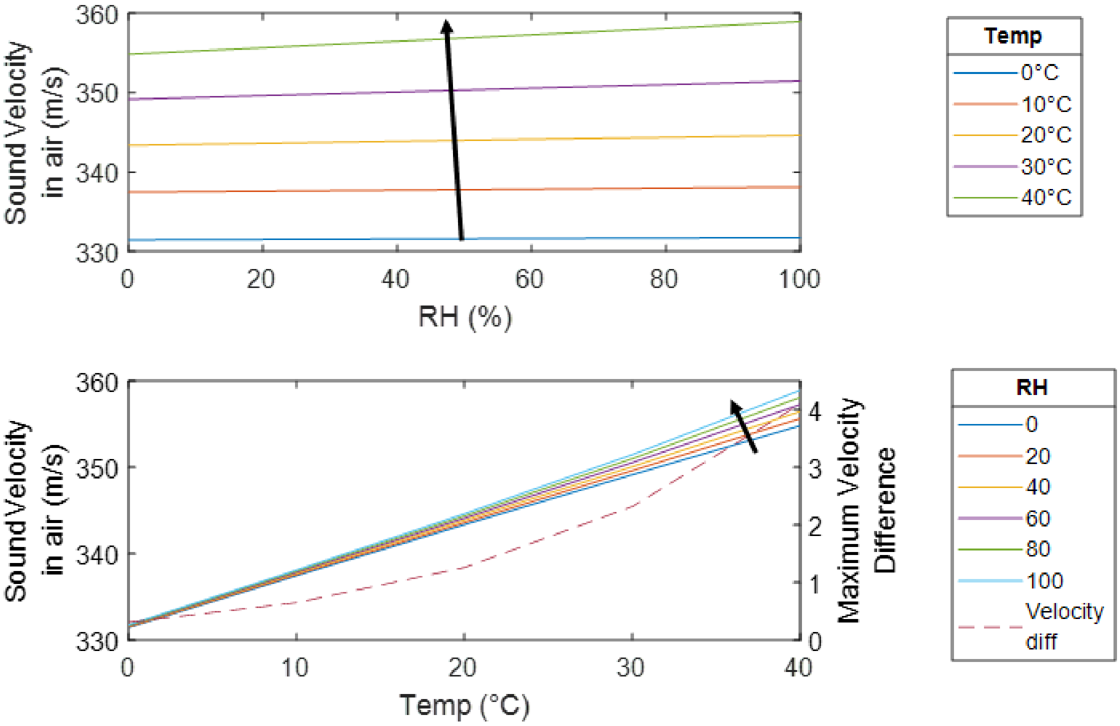

Figure 6-3: Impact of relative humidity (RH) and temperature on wave propagation velocity in air. (Top) Velocity vs RH – plot as presented by Cramer (1993). (Bottom) Velocity vs Temp – plot as presented by van Schaik et al. (2010). Arrows in top and bottom plots point in the direction of increasing temperature and relative humidity, respectively.

The work by Hickling and Marin (1986) to study the impact of environmental factors on ultrasonic range (distance) measurement using 215kHz airborne waves was of particular interest. The authors find the measurement error of ~0.1mm with varying distance, varying air temperature (temperature range 14<T<26 °C), and for turbulent air stream (of velocity ~7.5m/s). However, highest errors of ~±0.2mm are found when varying the surface temperature of the reflector, which was 140mm away from the probe (only results from a target surface temperature between 25 to 120 °C is reiterated).

The errors just due to environmental factors in the work of Hickling and Marin (1986) is re-evaluated here. The authors report the measured temperature difference, ΔT over a set time period, at distance d=0mm, 100mm and 200mm. ΔT =0.05°C at d=0, ΔT=0.15°C at d=100mm, and ΔT=0.25°C at 200mm. Using the equation for sound velocity in air provided by the authors (Equation 71), Figure 6-4 shows the extrapolated error in measuring a gap of 10mm without accounting for temperature variations.

$$c = 331.31 \times \sqrt{\frac{T + 273.16}{273.16}} \qquad \text{Equation 71}$$

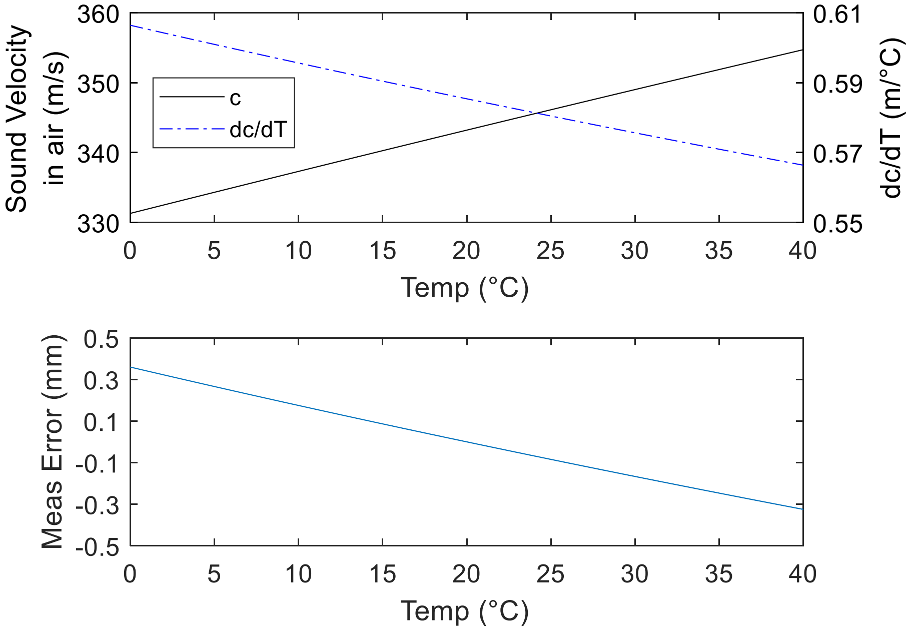

Figure 6-4: (Top) Variations in acoustic wave propagation velocity, *c* in air, with changing temperature, *T*; and the rate of change in velocity with changing temperature. (Bottom) Theoretical error in distance measurement, of a 10mm gap, if the velocity, *c* is assumed to be constant at all temperatures.

The measurement Error, e_m in Figure 6-4 is obtained as follows:

$$e_m = \mathrm{d} \times \left(\frac{c_{T_{\mathrm{ref}}}}{c} - 1\right) \qquad \text{Equation 72}$$

The work of Hickling and Marin (1986) and Cramer (1993) highlight the need to correct the velocity for varying temperature when conducting measurements in air.

Canali et al. (1982) used an oxide thermistor in the electronic circuit of an ultrasonic proximity detector to compensate for the measurement error bought on by variations in temperature. The final probe is quoted as having ±1% error for the measurement range of up to 1m and temperature range of -20°C to 110°C.

Work by Hickling and Marin (1986), when evaluated in the light of the temperature correction of wave propagation velocity presented by Canali et al. (1982), seems to suggest that for a short range distance measurement, knowing the air temperature would substantially reduce the measurement error in distance measurement.

6.2.2 Methods to Improve Measurement Accuracy

Literature which addresses the issue of measurement error from narrow bandwidth probes by introducing innovative pulsing and signal processing methods was reviewed. Sasaki et al (2009) use a pulsing method that relies on sudden phase inversion to give a more Gaussian shaped pulse and reduce the impact of unwanted ringing. Their reported accuracy of 15μm however is questionable given the system used a sampling frequency of 1MHz (each sample corresponds to distance step of $\frac{1}{1e6} \times 343 = 343\mu\text{m}$).

Saad et al. (2011) used cross-correlation followed by a minimum variance search algorithm to find the phase shift from a stepped frequency modulated signal. Queirós et al. (2015) used a similar method, while differing from Saad et al. (2011) in the sequence of the frequency steps. The use of long-time duration pulse was not possible for measuring distance to target ~10mm. Nevertheless, the two studies highlighted the power of using correlation methods in improving measurement accuracy.

Concerning air-coupled probes in the MHz range, Yano et al. (1987) reported an accuracy of 0.1mm using a 1MHz probe and simple pulse echo methods. Fox et al. (1983) used a method similar to the aforementioned frequency stepping, while using an automatic phase comparison in electronic circuitry to find the range to the target. The authors show the possibility of reducing the measurement error to <10μm for distance measurement of 1-40cm. However, the authors corrected their reported error to account for the temperature variations and reported a more modest value of ±0.5mm.

6.2.3 General environmental temperature variations

(Melikov *et al.*, 1997) studied the temperature fluctuations in a room with a mechanical exhaust ventilation system. Measurements were conducted at varying distance from the ventilation system and at varying elevations above the floor. A PT100 thermometer (type S1220) with calibrated maximum instantaneous error of 0.15°C was used. The authors found that in a 10-minute duration, at an elevation of 0.6m and distance of 0.8m from the ventilation system, the standard deviations in measured temperature was 0.42°C, while further away from the ventilation, the deviations were <0.10°C. At a distance of 3.4m from the ventilation, the deviation was ≤0.34°C for all elevation.

From the study it can thus be seen that when considering air-coupled measurement to attain highest possible accuracy, relative positioning of the measurement system needs to be considered as well. It is likely however that the measurements that are conducted in the laboratory environment, with stable air flow and controlled temperatures, are within 0.10°C.

6.2.4 Conclusions from Literature Review

The findings from the literature can be summarised as follows:

1. The errors in ultrasonic range measurements in air are mainly attributed to environmental factors. Temperature variations could result in high measurement error if the change in air temperature is unaccounted for. Atmospheric conditions such as turbulence and target surface temperatures could result in significant enough measurement error.
2. High resolution imaging is possible with air-coupled probes, provided the environmental factors are sufficiently stable. It also seems necessary to employ some method of averaging to minimise error.
3. The standard room condition maintains air temperature to within 0.4°C, while in an environment with minimal air circulation, the temperature is likely maintained within 0.1°C.

Given the velocity of sound in air, a high sampling rate of the signal is also required to improve the measurement accuracy. Factors such as target surface temperature may pose a challenge. The work presented within the chapter is limited to a fixed target temperature (the same as the environment).

6.3 Experimental Setup

Following the manufacturing of the probe, its accuracy was calibrated against a laser displacement sensor with measurement accuracy of ±0.025µm. The air-coupled sensor evaluation rig presented in §3.1.5 was used. The calibration rig was placed on a flat anti-vibration bed. The micrometre dial on the rig was used to change the relative distance of the probe from the reflector face (see Figure 6-5). Separate analysis was also carried out using an eddy current sensor as a reference measurement. The reference measurement made by the eddy current sensor was found to have an error in the range of ~0.67µm. Figure 3-13 shows the rig with eddy current probe.

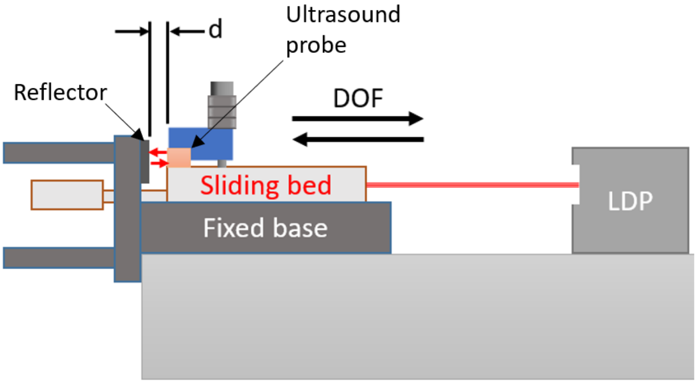

Figure 6-5: Setup used for the evaluation of the ultrasonic range measurement, using a 1.4MHz probe. The distance, *d* between the probe and the reflector was measured using the ultrasonic probe (the two red arrows represent the wave travelling back and forth between the probe and the reflector plates). The probe was mounted on the sliding platform (bed) of the *air-coupled sensor evaluation rig* presented in §3.1.5, as shown in the figure. The probe motion was constrained to degree of freedom, DOF, as shown; this was used to change the gap between the probe and the reflector.

The initial distance between the probe and the reflector was set at a nominal gap of 10 mm. The accuracy of measuring to flat surface reflector and curved surface reflectors were evaluated. Figure 6-6 shows a photo of the reflector plates used.

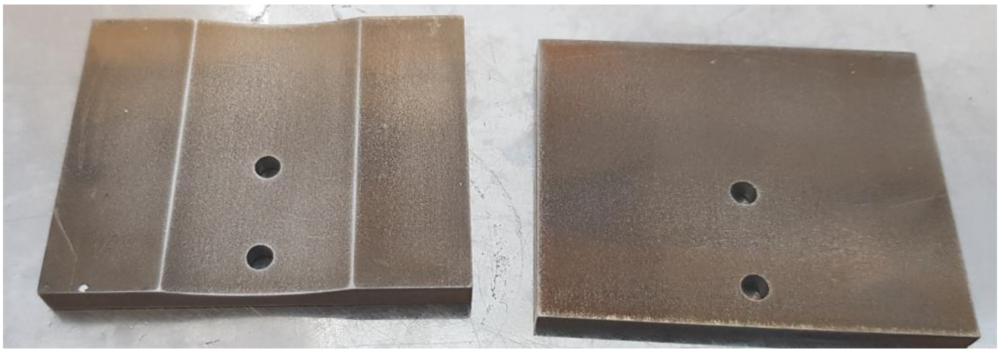

Figure 6-6: Cast-iron samples used as reflectors. The curved reflector (LHS) has a diameter of 83mm.

Figure 6-6 shows a schematic of the equipment used for the experimental work reported within the chapter.

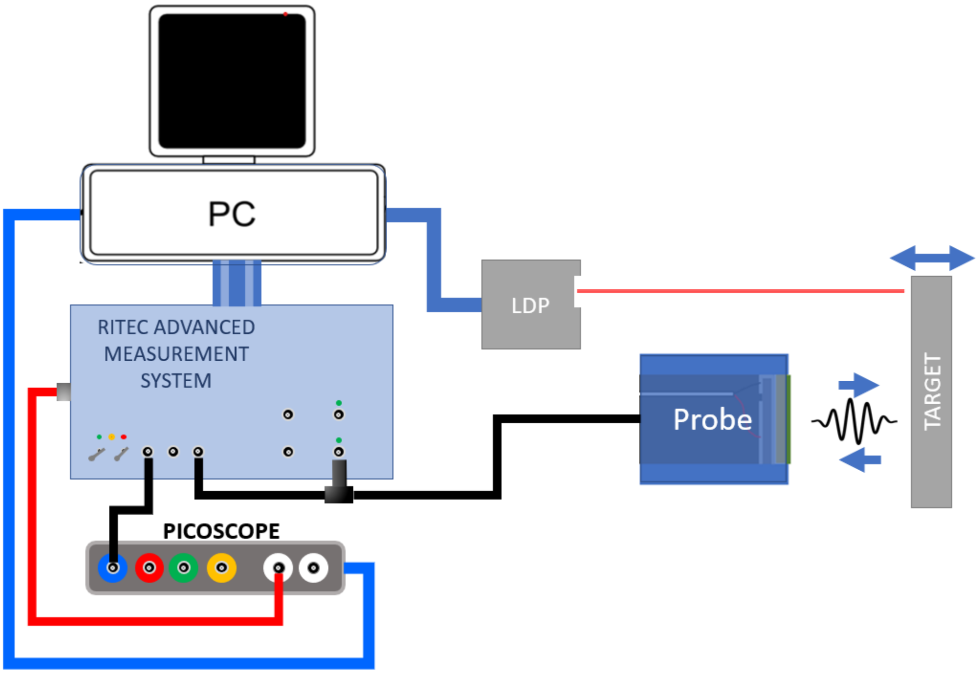

Figure 6-7: Experimental setup of the probe accuracy evaluation experiment. The components labelled *LDP, Probe* and *target*, is a simplified representation of the setup depicted by the schematic in Figure 6-5; for the *target* reflectors, cast iron samples shown in Figure 6-6 were used – the specimen with curved surface (with a diameter of 83mm) was used to mimic the surface of cylinder liner, with same diameter.

A PC was used to control the RITEC RAM5000, Picoscope and LDP sensor, with each hardware controlled using their respective software. An excitation signal of 5 cycles at 1.4MHz was generated using the RITEC RAM5000 function generator. The excitation signal was coupled directly to the probe terminals. The reflected pulse was detected by the same transducer and transmitted to the RITEC amplifier. The acquired signal was put through a bandpass filter (passband: 50kHz to 5MHz) and amplified 32dB using the built-in amplifier. The amplified signal was transferred to an input channel of Picoscope 5442B. The Picoscope was used to digitise the signal with ADC settings as follows: range: ±1Volts, resolution: 12bits, digitisation rate (sampling frequency): 250MHz. Finally, the digitised signal was transferred to the PC where an inhouse LabVIEW programme, Triboscope, was used to acquire and save it. The saved waveforms were processed using MATLAB®.

The measurements from the laser displacement probe were acquired by the same PC. Each set of ultrasound measurements had a corresponding 4000 individual reference distance measurements taken by the laser; the average value of the reference distance was used. It is assumed the relative error in reference measurements was negligible.

However, it was only possible at present to compare against a relative change in distance due to the setup of the laser displacement sensor. The accuracy of the reference system is only valid as a relative distance measurement, and therefore the ultrasonic readings are compared as a relative change measurement. Results of the test however gives a good indication of the measurement system which will be calibrated. It is likely the probe would be calibrated prior to its use in the manufacturing setting.

6.4 Results

The probe with the least ringing and widest bandwidth from Chapter 4 was used for the measurement application. Figure 6-8 shows the plot of the frequency bandwidth of the PIC255a probe that was used. The operational frequency band of the probe was found to be 1.1MHz to 1.5MHz, and it also exhibited a stable group delay within the region (see §4.6, Figure 4-10).

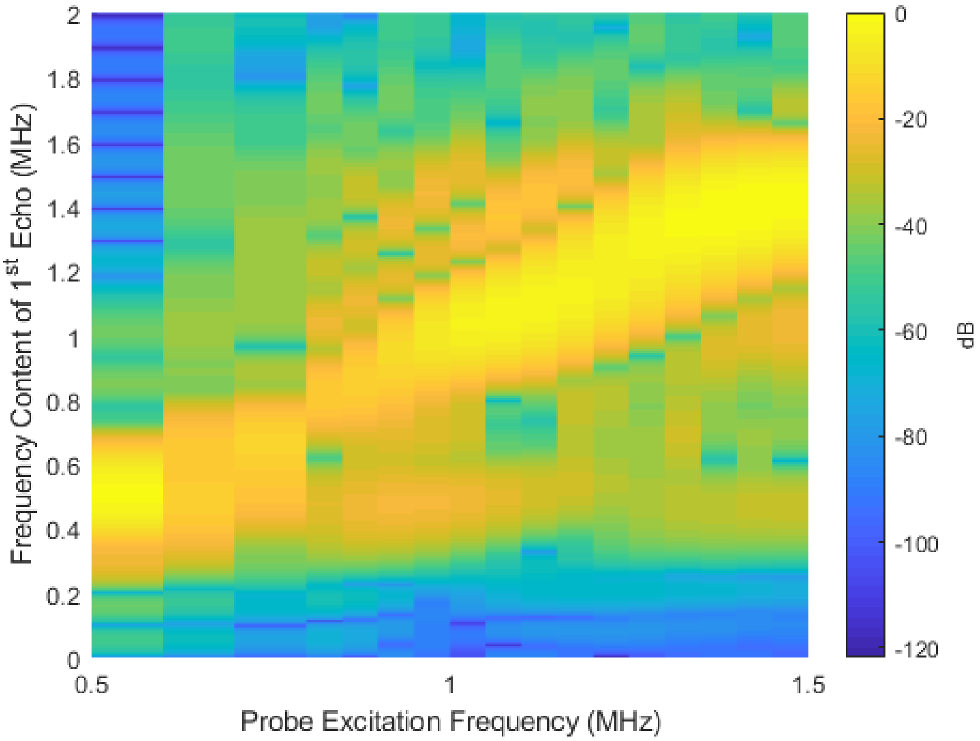

Figure 6-8: Frequency domain response of the ultrasonic probe used for the range measurement experiment. The figure represents the result of several experiments, where in each, a different excitation frequency was used to excite the ultrasonic probe. The amplitude values are normalised against a maximum.

6.4.1 Waveform to TOF

Table 6-1 shows various steps followed to obtain the TOF measurement from the acquired waveform. The various methods followed were such that the time-of-flight reading could be obtained automatically from the recorded waveform. The reference measurements for this set of experiments were obtained using an eddy current probe.

Table 6-1: Methods and steps in obtaining TOF.

Method	Step 1	Step 2	TOF
A	Find the signal envelope.	Set threshold amplitude which when the envelope crosses on its raise indicates arrival of an echo.	The time difference between two threshold crossing points.
B	Find the auto correlation of the waveform and its envelope.	Find the time corresponding to the location at the peaks of the envelope.	The time difference between the two maximums of self-correlated data.
C	Locate start of first echo as per Method A.	Find set of 10 axis crossings for both the echoes.	The time between the 1st and the 2nd set.
D	Locate start of second echo, by adding the TOF obtained from Method B.	Find the time difference between the axis crossing.	Mean is the TOF and SDV is the measurement uncertainty.

Figure 6-9 shows the waveform of 6 distance steps measured by the probe.

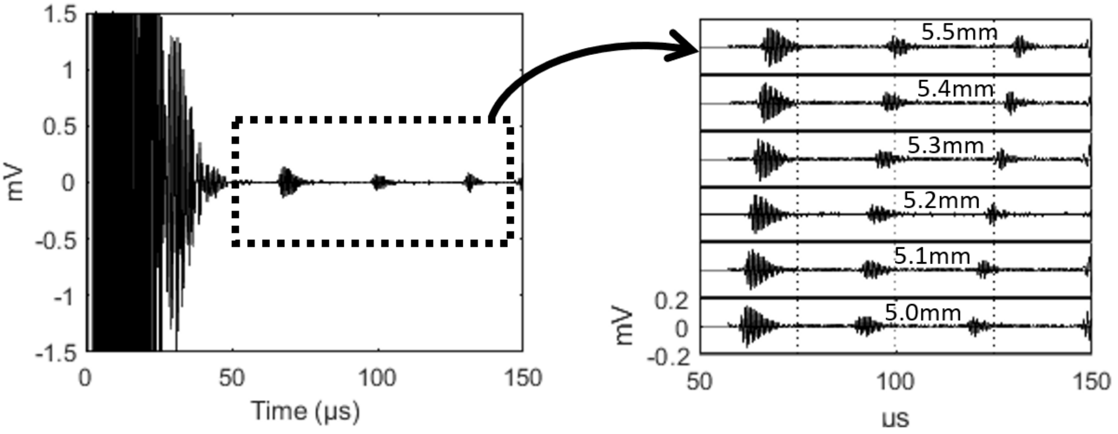

Figure 6-9: Waveform acquired form range measurement experiments, measuring the changing distance between the probe and the target reflector. Initially the distance between the probe and the reflector was set to a nominal value of 5mm; this was then increased in steps of 0.1mm. The LHS plot shows a single waveform acquired from one experiment, while the RHS plots show a selected time window corresponding to varying distances (as shown).

Figure 6-10 – Figure 6-13 correspond to the 4 methods shown in Table 6-1.

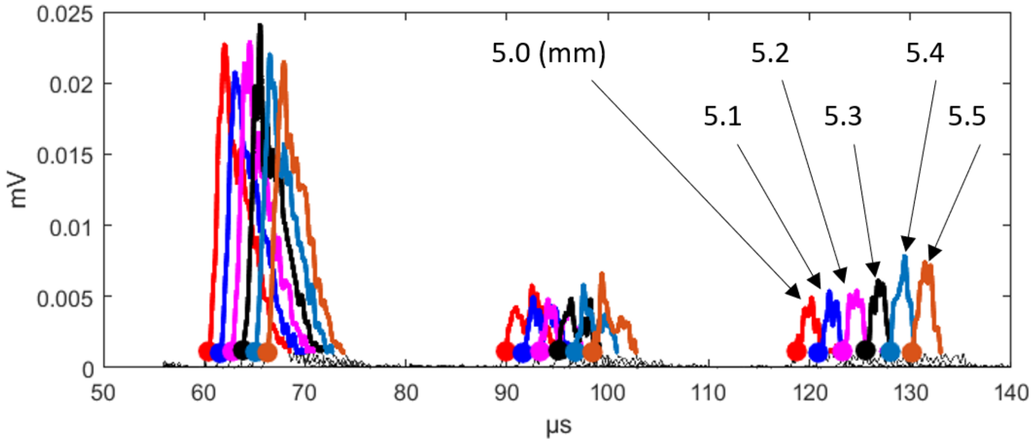

Figure 6-10: Plots of envelope function, (see §3.3.1) applied to the time domain waveforms in Figure 6-9. The filled circles show the time where the waveform intensities cross a threshold value (selected as 0.001mV); the calculated TOF is the time difference between 2 consecutive circles of same colours, i.e., corresponding to consecutive echoes. The figure is a depiction of Method A in Table 6-1.

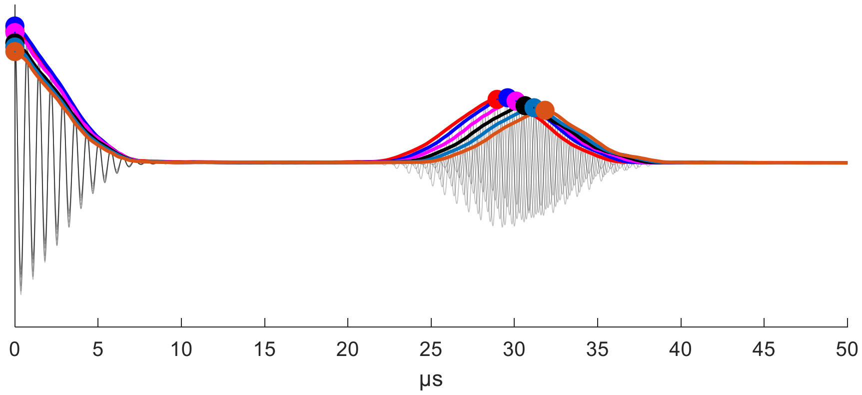

Figure 6-11: Auto-correlation method used to find the TOF, depicting Method B in Table 6-1. The coloured lines are envelopes of auto-correlation of waveforms in Figure 6-9, while the circles are the local peaks of the envelopes. The second peak (on RHS) of the correlation function are the TOFs.

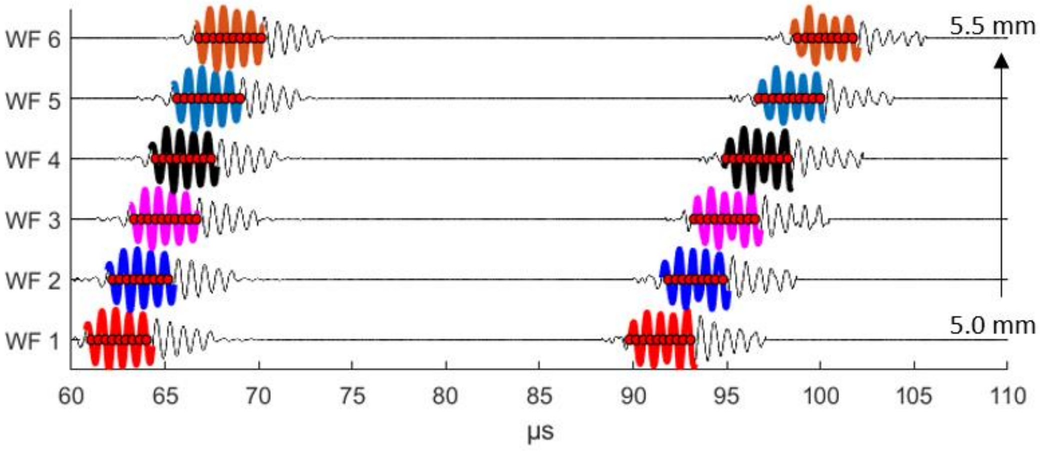

Figure 6-12: Time window of Figure 6-9, containing the portion of the waveforms with axis-crossings used to find the TOF; the figure is a depiction of Method C, in Table 6-1. Circles mark the axis crossing time. The average time difference between the axis crossing of two consecutive echoes (show in the plots above) are the corresponding TOF.

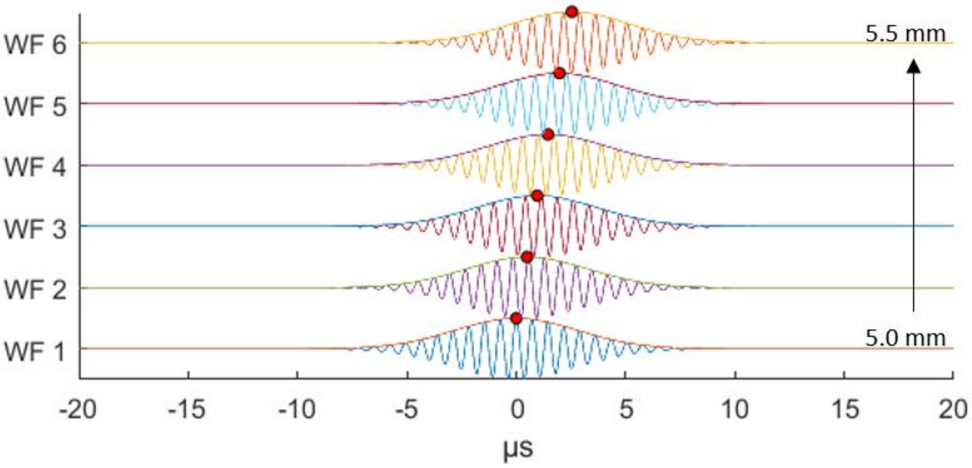

Figure 6-13: Plots of cross-correlation function applied to two auto-correlation vectors that are plotted in Figure 6-11; the figure is a depiction of Method D, in Table 6-1. Each of the auto-correlation vector is correlated with that of 5.0mm.

Using autocorrelation followed by cross-correlation (Method D) or just cross correlation (Method B) on its own were found to perform the best, giving a linearity error of ~7μm for an automated system. From the comparison between the various methods shown in Figure 6-14, it is evident the axis crossing method (Method C) performs the best. However, a semi-automatic method was required unless the step change in displacement was lower than half the signal wavelength.

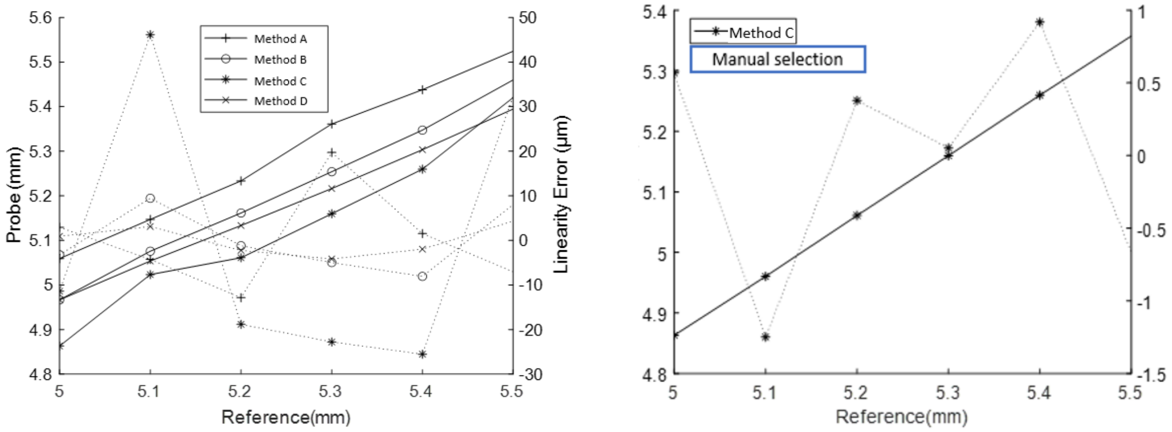

Figure 6-14: (LHS) Comparison of measurement error in distance measurements obtained using methods in Table 6-1. (RHS) Modified Methods C, where the axis crossing locations were manually selected, as opposed to this being automated in Method C; this method can be automated if change in the distance between two subsequent measurements are less than half the wavelength. Dotted lines show error, and correspond to y-axis on RHS.

6.4.2 High Resolution Distance Measurement

Table 6-2 shows the various experiments that were conducted to analyse the resolution and accuracy of the probe. Each measurement corresponds to an average of 100 readings taken.

Table 6-2: Experiments conducted to evaluate the probes manufactured for resolution and accuracy of range measurement for small changes in distance.

Exp.	Reflector Surface	Probe(s)	Distance	Excitation Frequency
A	Flat	PIC255A	12mm (Nominal) Increments of 10µm - 100µm	1.4 MHz
B	Curved (radius 41.5mm)			

Figure 6-15 shows the signal acquired for the evaluation of range measurement to flat plate reflector. Figure 6-16 shows the results for a curved surface reflector. It was found that the flat plate reflector was impacted by some diffraction effects on the 2nd echo. Similar was not the observed for the curved surface reflector, likely due to the focusing of the beam by the curved surface.

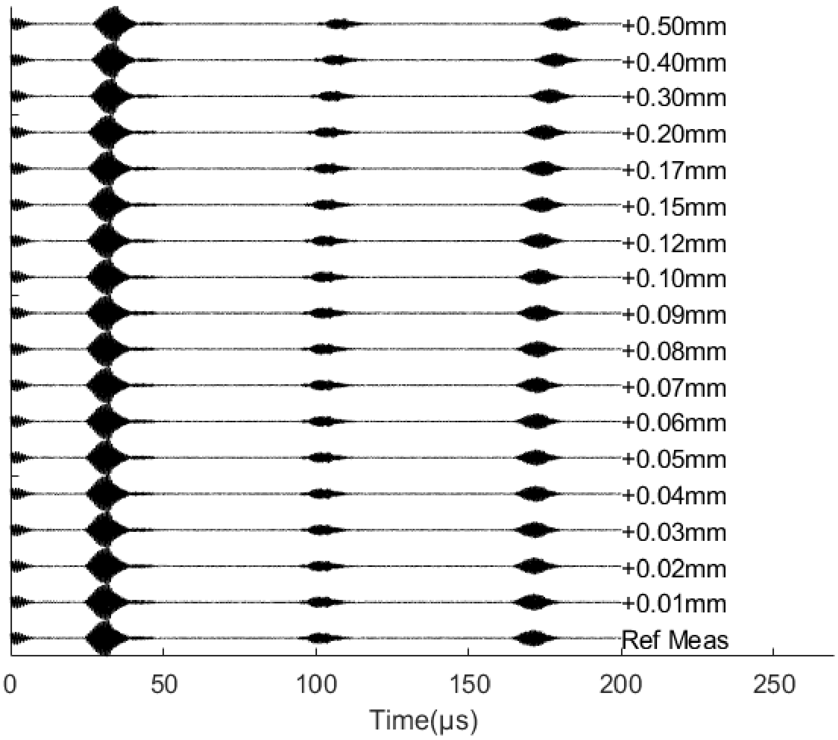

Figure 6-15: Ultrasonic waveforms acquired from the set of range measurement experiments, carried out using the 1.4MHz transducer and a flat plate reflector; experiment set A in Table 6-2.

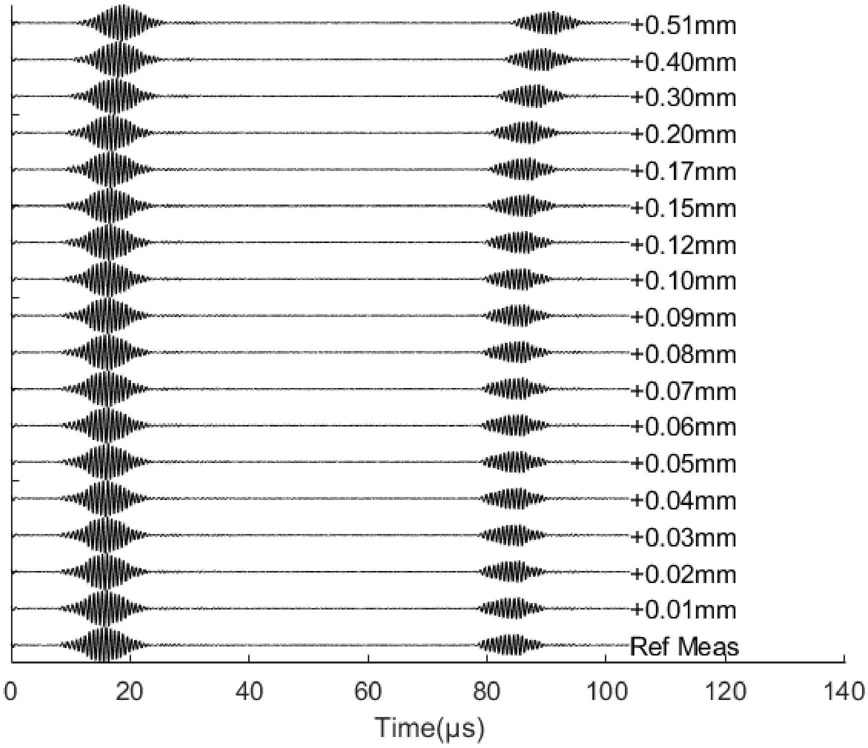

Figure 6-16: Ultrasonic waveforms acquired from the set of range measurement experiments, carried out using the 1.4MHz transducer and a curved surface reflector, with a radius of 41.5mm; experiment set B in Table 6-2.

The acquired waveforms were evaluated using the axis crossing method presented in Table 6-1 (Method C). Figure 6-17 shows the results for range measurement using the flat plate reflector as the reflecting face.

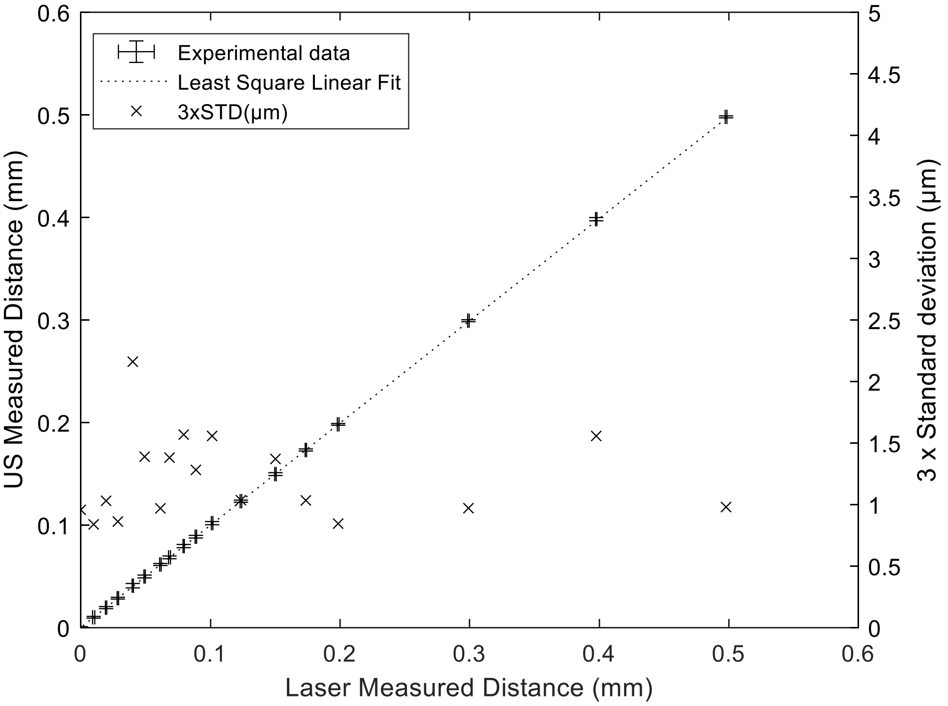

Figure 6-17: Distance measurements between the 1.4MHz transducer and a flat plate reflector; corresponding to acquired waveform presented in Figure 6-15. Cross markers correspond to RHS vertical axis.

The error in measurement was found to be $\sigma_{3SDV} = 2.2\mu m$ ($\sigma_{1SDV} = \pm 0.73\mu m$) when a flat plate reflector was used. Figure 6-18 shows the results for a curved surface reflector.

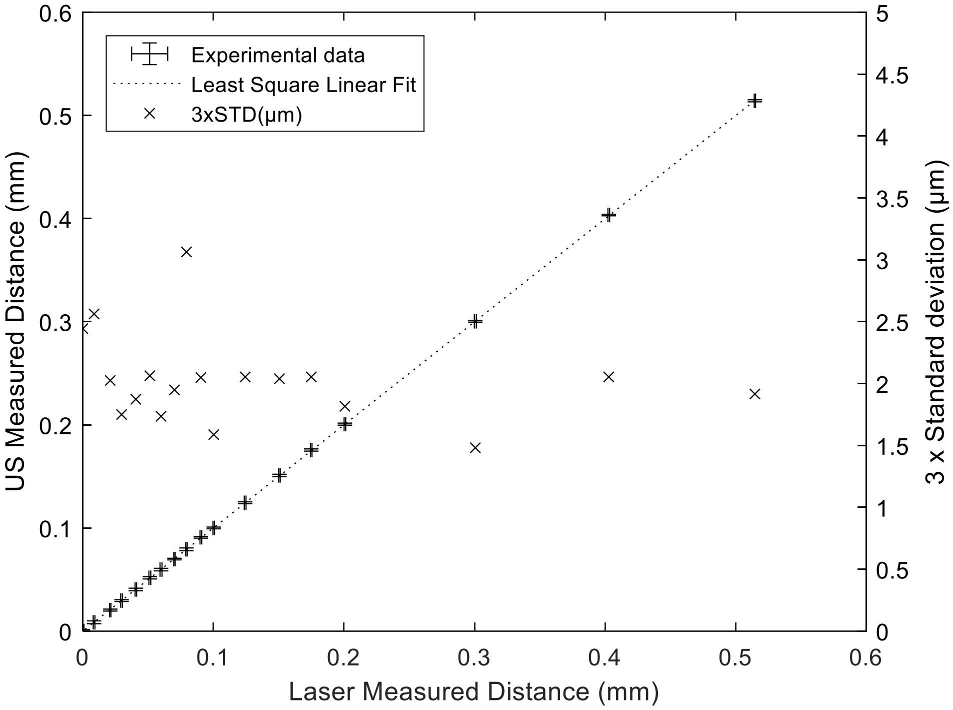

Figure 6-18: Distance measurements between the 1.4MHz transducer and a 41.5mm radius curved surface reflector; corresponding to acquired waveform presented in Figure 6-16. Cross markers correspond to RHS vertical axis.

The error is found to be greater for the curved surface reflector, but still within ±3.2μm. The errors in temperature measurement of ±0.15°C are presented in Figure 6-19.

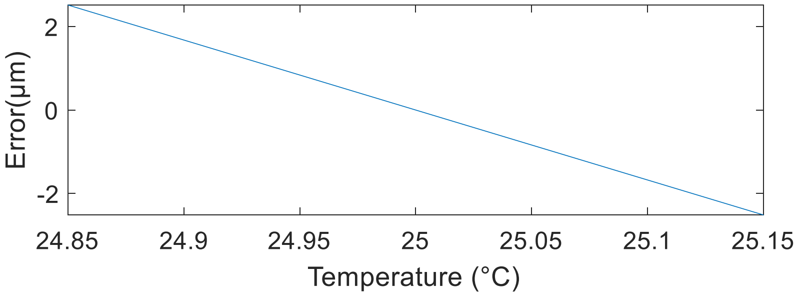

Figure 6-19: Measurement error on range measurement of 10mm distance, at 25°C nominal temperature, if the wave propagation velocity is corrected for by using an air temperature measurement probe with measurement uncertainty of ±0.15°C. The maximum error in distance measurement, due to the ±0.15°C uncertainty in the temperature measurement, is ±2.52µm.

Adding the value of 2.52µm to the measurement error by finding the root mean squared error of the two, the final measurement uncertainty for a curved surface reflector is ± 4.07µm for a curved surface reflector of radius 41.5mm, and ± 3.35µm for a flat surface reflector.

6.5 Conclusions

An ultrasonic range measurement probe was analysed for its ability to perform distance variation measurement in the order of 10±0.025µm, with the probe 10mm from the reflector target. Methods for data processing of the range measurement results were investigated.

The most suitable method for processing of the waveform to achieve distance measurement was found to be an axis-crossing method, provided the phase change between subsequent measurements was less than 1/2 wavelengths. For change greater than this, autocorrelation was found to be the more suitable method.

The accuracy of the probe in measuring the distance to a curved surface reflector of radius of 41.5mm was found to be within ±3.2µm, and the measurement of distance to a flat surface reflector was found to be within ±2.2µm. Accounting for temperature variations of 0.15°C the corresponding values were ±4.07µm and ±3.35µm respectively.

The error of ±3.2µm in distance measurement between the ultrasonic probe and a curved surface reflector shows ultrasound could potentially be used to conduct bore form measurements in honing machines, with higher measurement accuracy than currently available in the honing machines (of ±10µm). This specific application is explored further in the next chapter.

7 Cylinder Bore Form Measurement

The surface profile of the cylinder liner bore (or block bore) is achieved by the bore honing machining process. Current methods in measuring the bore surface profile during honing, in an automotive production plant, at present only serve to give an indication of the various parameters.

This chapter presents the application of an air coupled probe in measuring the bore form of a cylinder liner in-situ to a higher accuracy than currently available. The probe used for the measurement is one that was developed and evaluated in the previous two chapters. The motivation for the work is directly linked to the requirement of such a method at the JLR production plant in the UK which the current author was made aware of.

7.1 Introduction

Honing is one of the final machining processes to get a bore application ready. A common trend in the automotive industry at present has been in using a rough honing tool which uses air gauges for in process sizing. While the process gives a rough estimate, the bores still require additional post gauging to ensure accuracies of the bore size, roundness and taper (Zhmud and Chobany, 2020). Figure 7-1 shows a depiction of a rough honing tool.

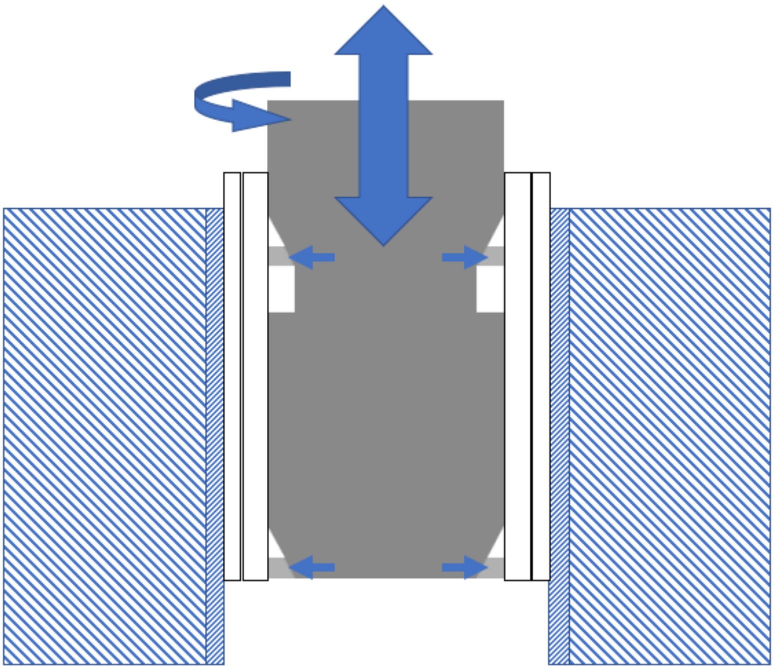

Figure 7-1: Schematic depicting the working of a bore honing process. The tool works by expanding outwards while moving up and down to control parameters such as cross hatching pattern on liner face.

In the event the bore is out of tolerance, further machining is required to make corrections. The features and parameters which a bore honing process is used to control include (Tolinski and SME Media, 2008):

- Diameter control of the bore.
- Macroscopic bore geometry, i.e. the cylindricity, roundness, straightness, etc.
- Microscopic surface characteristics, including surface roughness parameters and cross-hatch pattern.

Figure 7-2 shows a depiction of the air proximity gauges embedded between a pair of honing stones.

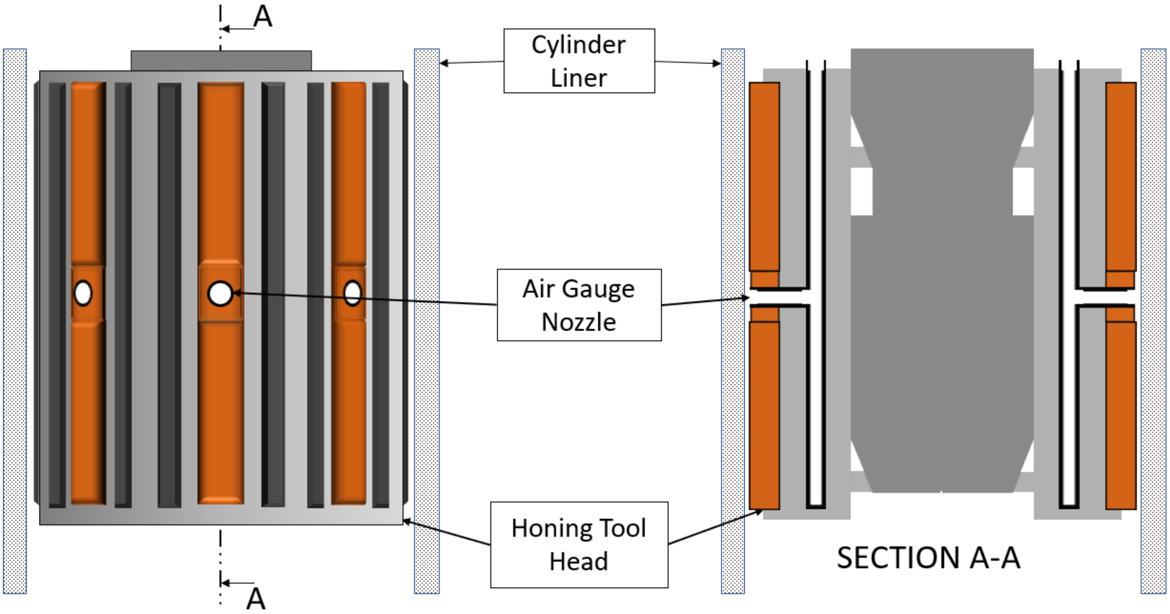

Figure 7-2: A schematic showing the honing tool head inside a cylinder liner during the honing process. Cylinder is already fitted inside the engine block at this stage (engine block not shown). RHS is a cross-section of the LHS about line A-A. Only the cylinder liner cross section is shown in the LHS figure.

The air proximity gauge provides a mean bore radius measurement of ~10µm (personal communication, Littlefair B. 2018). It is therefore of interest to investigate the potential for using an in-situ measurement tool, such as ultrasound, which could provide information on the bore profile measurement and subsequently improve the quality management of the honing of cylinder bores. To the author's knowledge, the measurement of the bore form in a manufacturing production line using air coupled ultrasound working at MHz frequency has never been studied before.

7.2 Background

The amount of material removed in a bore honing of cylinder liners can vary and may typically be in the range of 100µms per step in automotive applications (Tolinski and SME Media, 2008). The process is typically carried out in separate cycles of coarse/lower precision finish, and fine/higher precision finish, with additional steps necessary for structured honing if implemented (Dahlmann and Denkena, 2017; Zhmud and Chobany, 2020). The typical rotational speed of the tool head in the range of 100RPM to 200RPM for 80mm nominal diameter bore. Typical material removal rate varies from 0.57mm^3/s to 1.83mm^3/s, with slower speeds corresponding to lower removal rates (Goeldel *et al.*, 2013).

Large-scale manufacturing plants are mainly concerned with the speed of the manufacturing process as well as the quality of the finished product. Therefore, a common objective in automotive bore honing is to remove as little material as possible to achieve the required bore profile parameters (Tolinski and SME Media, 2008). The manufacturing speed is limited by the tolerances and surface quality required of the finished bores. A slower process of manufacturing during honing increases the cost of manufacturing the engines. The tolerances to be met by the honing operation of cylinder liners in an automotive application is given in Table 7-1.

Table 7-1: Typical tolerances to be met by bore honing process of a thermal stray coated bore. Table obtained from Zhmud and Chobany (2020).

Parameter	**Typical tolerance**
Rectangularity	± 50µm
Position	± 100µm
Cylindricity	10µm
Diameter	± 10µm
Rpk	0.25µm
Rz	5µm

There are various sensors installed on the honing machines to control the machining process. ASM Machining Handbook (Davis, Lampman and Zorc, 1989) on grinding outlines 5 different gauges used in typical honing machines to automatically control the bore diameter – air gauges, ring gauge, expanding gauge, plug gauge and bar gauges; see Table 7-2 for a summary.

Table 7-2: Automatic bore size control mechanisms in honing machines as quoted in the ASM Machining Handbook (Davis, Lampman and Zorc, 1989). † The accuracy of the air gauge quoted in the table can be higher (~±10µm) if incremental calibration procedure is used.

Gauge	Accuracy (Adjustment Range)	Bore size Range	Method of operation (used to terminate the honing cycle)
Air gauge	75µm† (100µm)	-	Pneumatic pressure transducer output compared against reference value.
Ring gauge	7.6µm (13µm)	3.05mm-100mm	Contact between honing stone cut diameter and ring of predetermined size.
Expanding gauge	7.5µm (250µm)	>19mm	Gauging sleeve compared against inner diameter of the bore at the bottom of down stroke.
Plug gauge	5µm (-)	-	Plug of predetermined size attempts to enter the bore from opposite side to the honing tool.
Bar gauge	7.5µm (1mm)	>50mm	Two bars mounted on a split ring spring loaded by the ring against the bore results in contact of two points on split ring when set bars pass a certain threshold.

The use of a capacitive displacement sensor to give a positional reference measurement of the tool head is reported by the authors in the design of a hybrid tool for honing and structuring (Dahlmann and Denkena, 2017). However, distance measurement using capacitive sensors have limitations in the bore honing environment, as is pointed out by the authors. The presence of fluid or moisture and machined particles in the gap between the sensor and the target would alter the dielectric property of the gap and impact the reading (Nihtianov, 2014). Other considerations for a capacitance sensor would be the shape and tilt of the target (Smith, 2003). Similarly, other methods available such as eddy current - which is more robust than the capacitive sensor - have limitations in use against a cast iron target for high accuracy range measurement.

Use of air-coupled ultrasonic waves for range measurement have been reported to offer an accuracy of below 1µm (Takahashi and Ohigashi, 2009). As reported in Chapter 6, airborne ultrasound was found to offer measurement accuracies of ±3.2µm (±6.04µm is assuming error in temperature measurement of ±0.15°C) for a curved surface of 41.5mm in radius.

The amplitude of the reflected ultrasonic waves have also been used for the purposes of surface roughness parameter R_q as well as non-Gaussian parameters, skewness R_{sk} and kurtosis R_{ku}

(Blessing and Eitzen, 1989; Sukmana and Ihara, 2005, 2007; Arunachalam, Anand Kumar and Ramamoorthy, 2011; Saniman *et al.*, 2020), all of which are key design parameters of the engine bores.

The effect of surface temperature on the measurement error have not been evaluated at present, and such investigations are left for future work.

7.3 Experimental Method

A cylinder liner had its bore profile measured using a CMM machine at the height of 5mm below one of its side faces. Subsequently, this measurement was repeated using the *PIC255a* probe in the bore form measurement rig, with the probe working in the pulse-echo mode. The outcome of the probe calibration is found in Chapter 6. Figure 7-3 shows a schematic of the rig as it was set up for the experiment, and a corresponding photograph of the rig with liner.

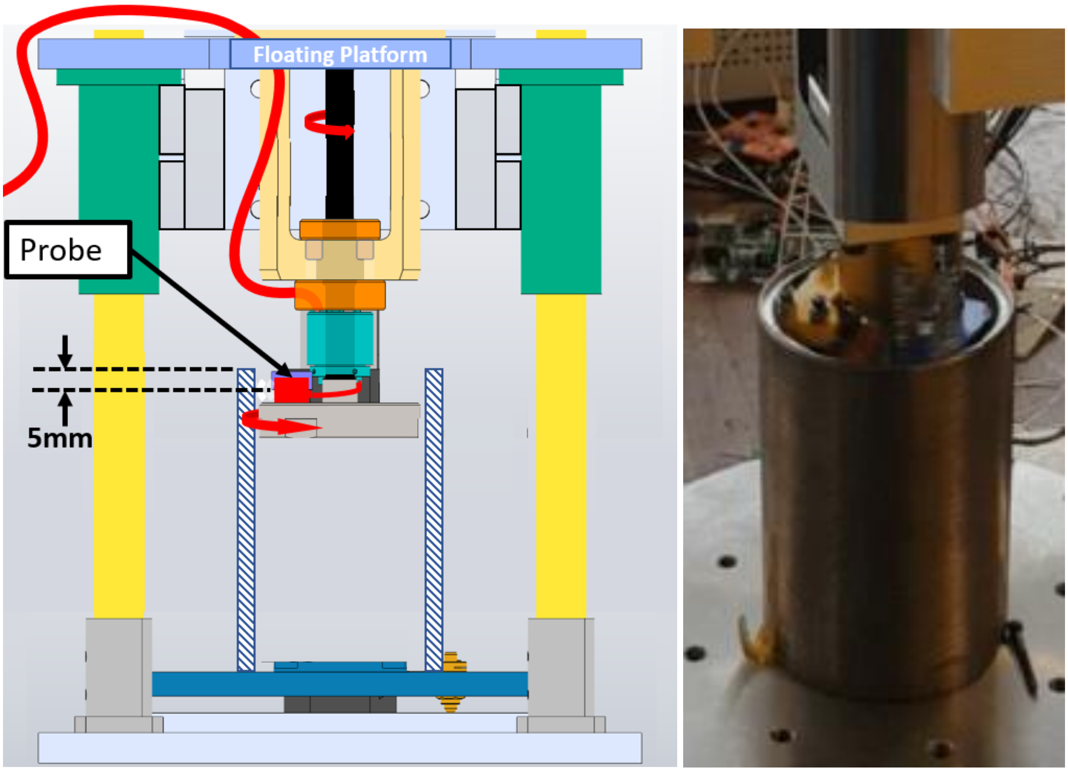

Figure 7-3: Bore form measurement rig set up to take the bore form measurement of a cylinder liner, at a height of 5mm down from the top of the liner. (LHS) Schematic showing the lower half of the rig as it was set up; (RHS) Photograph of the liner and the probe set up prior to starting the measurement experiment.

Figure 7-4 shows the profile of a cast iron cylinder liner measured using the CMM machine. The liner was a sample taken out from the batch of liners before being installed in the engine block, therefore prior to being honed.

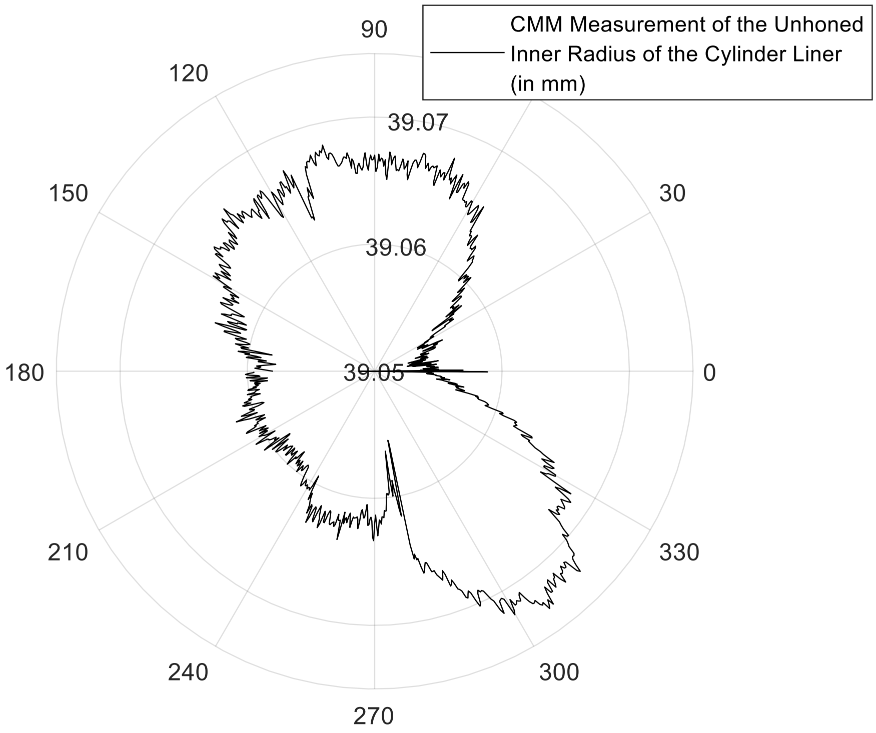

Figure 7-4: CMM measurement of inner radial profile of the un-honed cylinder liner.

7.3.1 Signal pathway

Figure 7-5 shows a schematic of the setup used for the bore form measurement test. The measurement was started by starting the DC motor. The turning of the motor caused the encoder channels to output accordingly. The index pulse from the encoder was fed to Picoscope Channel B, and this waveform was used to find the 0 degrees angular position of the probe. The count output from the encoder was split to the PC and RITEC RAM5000 gated amplifier. The signal to the PC was used to monitor the spindle rotational speed. The signal to the RITEC was used to trigger the amplifier. The amplifier, on receiving the trigger signal, output an excitation signal to the probe and a trigger signal to the Picoscope, telling the Picoscope to start recording from the connected terminals. Meanwhile, the signal from the amplifier was passed through the MOFLON MT1233-S08-VD slip ring to excite the probe. The ultrasonic waveform detected by the probe is directed to the receiver terminal of the RITEC amplifier back though the slipring. The signal is amplified by the amplifier (gain: 32dB), filtered (filter passband: 50kHz to 5MHz), then transferred to the Picoscope. The Picoscope digitised the signal (sampling frequency of 250MHz) and transferred to the PC where it was processed to find the measured range.

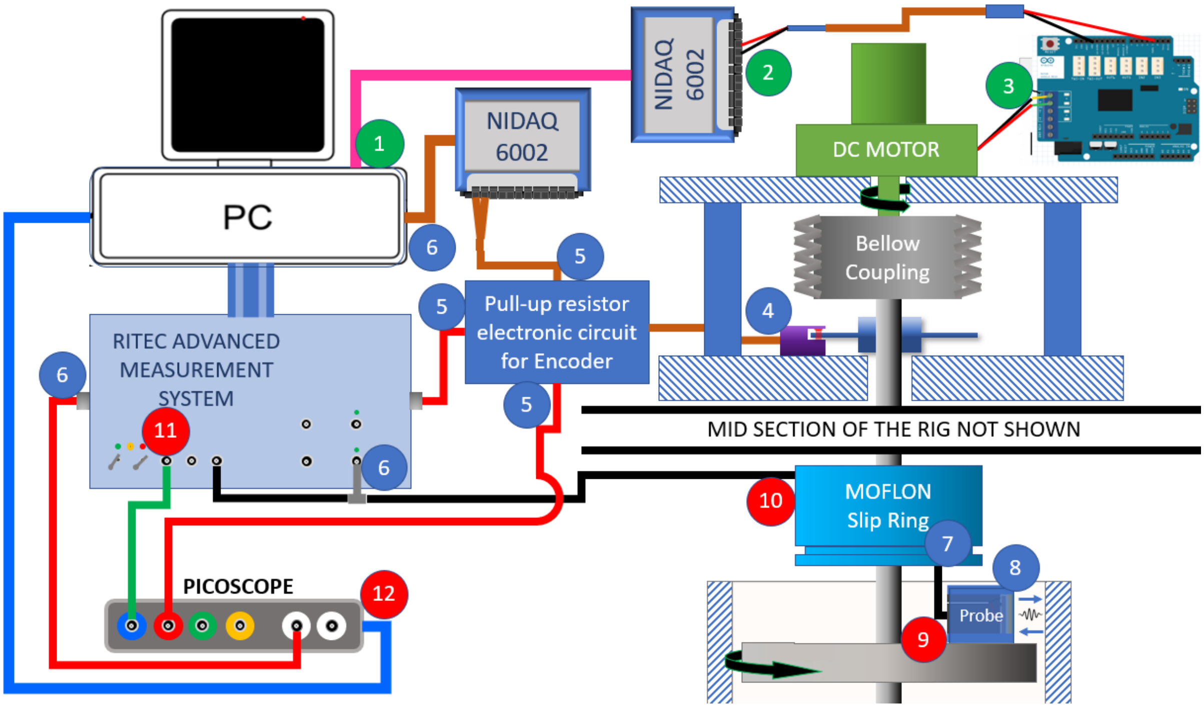

Figure 7-5: Schematic of the setup used for the bore form measurement using the bore form measurement rig. Numbers in coloured circles represent the order in the signal pathway. Green filled circles are related to the motor control, the blue ones show the pulse excitation pathway, while the red ones are in the pulse detection pathway. The numbers are shown where there is an output.

7.4 Results

Figure 7-6 shows one measured waveform from the rig.

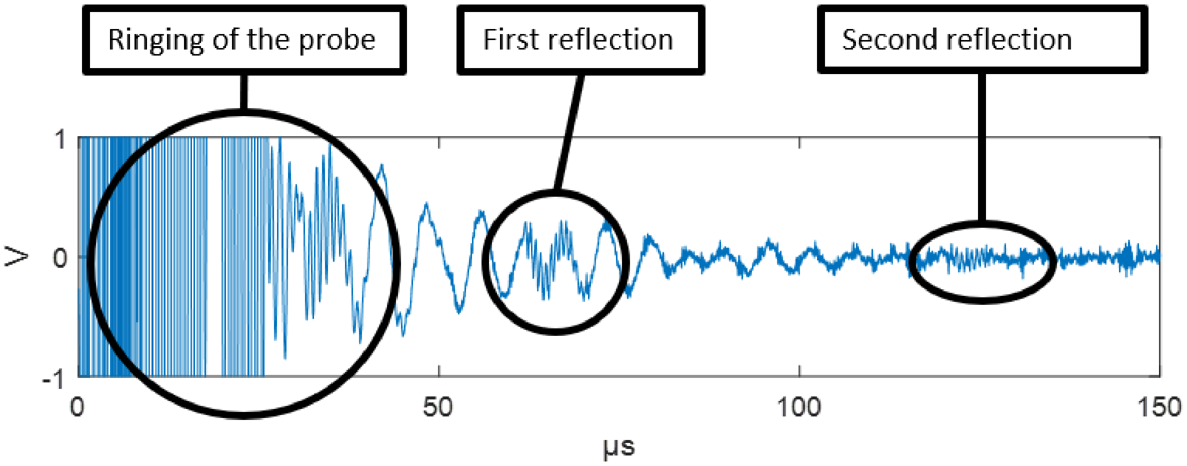

Figure 7-6: Waveform of the signal acquired from the bore form measurement rig. The low frequency waveform superimposed is likely due to the impedance of the cables and the pulser and receiver electronic components.

The signal is found to have a noise component in the region on 100kHz, most likely due to the impedance of various components used in the signal pathway coupled with the impedance of the transducer. Given the requirement to use an individual waveform without averaging, the signal was smoothed using a Savitzky–Golay smoothing filter with window length of 10 elements (80ns). This was followed by applying a bandpass filter with a pass band between 1.25MHz and 2MHz. See Figure 7-7.

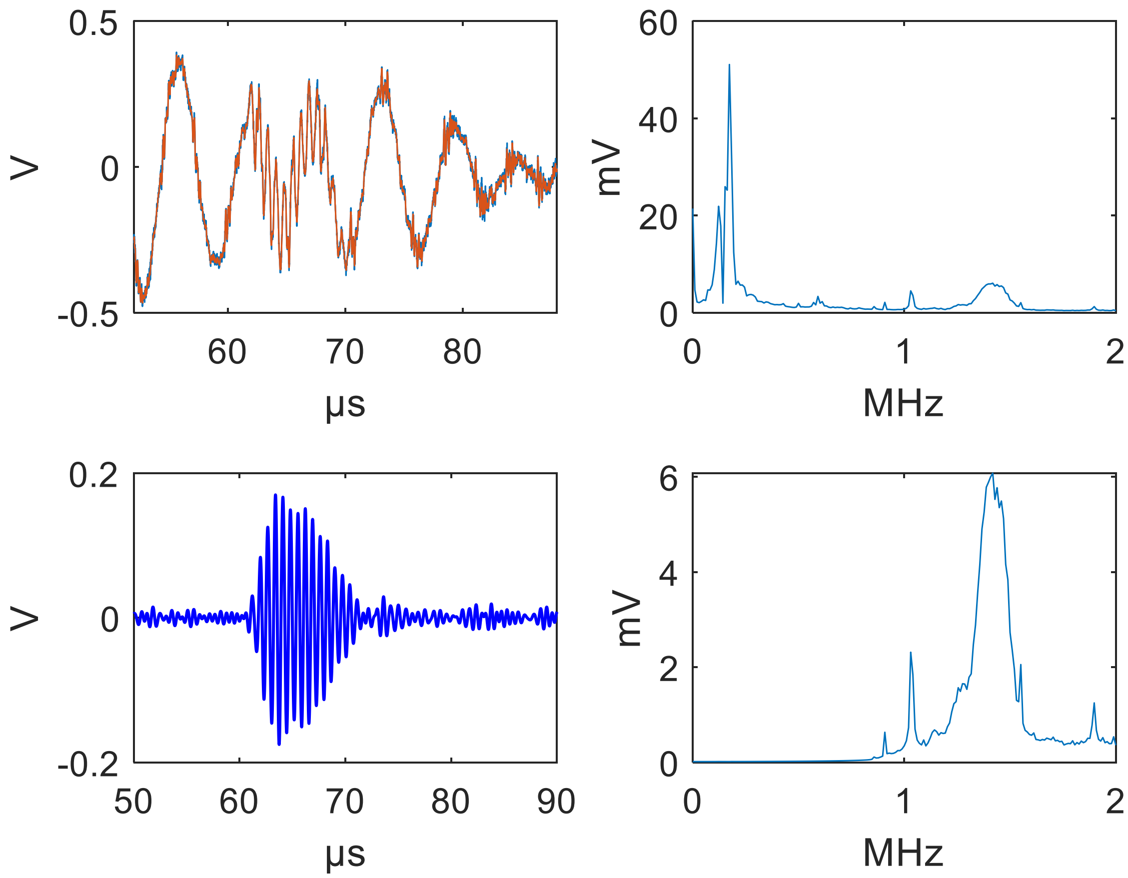

Figure 7-7: Digital signal processing of experimentally acquired signal from the bore form rig (shown in Figure 7-6) to remove low and high frequency noise. (Top pair) Raw signal acquired form the rig in time and frequency domain. (Bottom pair) Time and frequency domain of the acquired signal after digital filtering.

7.4.1 Automated Axis Crossing Tracker

Following the processing of the signal to remove noise, a method was developed to automatically track the shift in axis-crossing. Figure 7-8 shows the process followed as per Method 3 in Table 6-1.

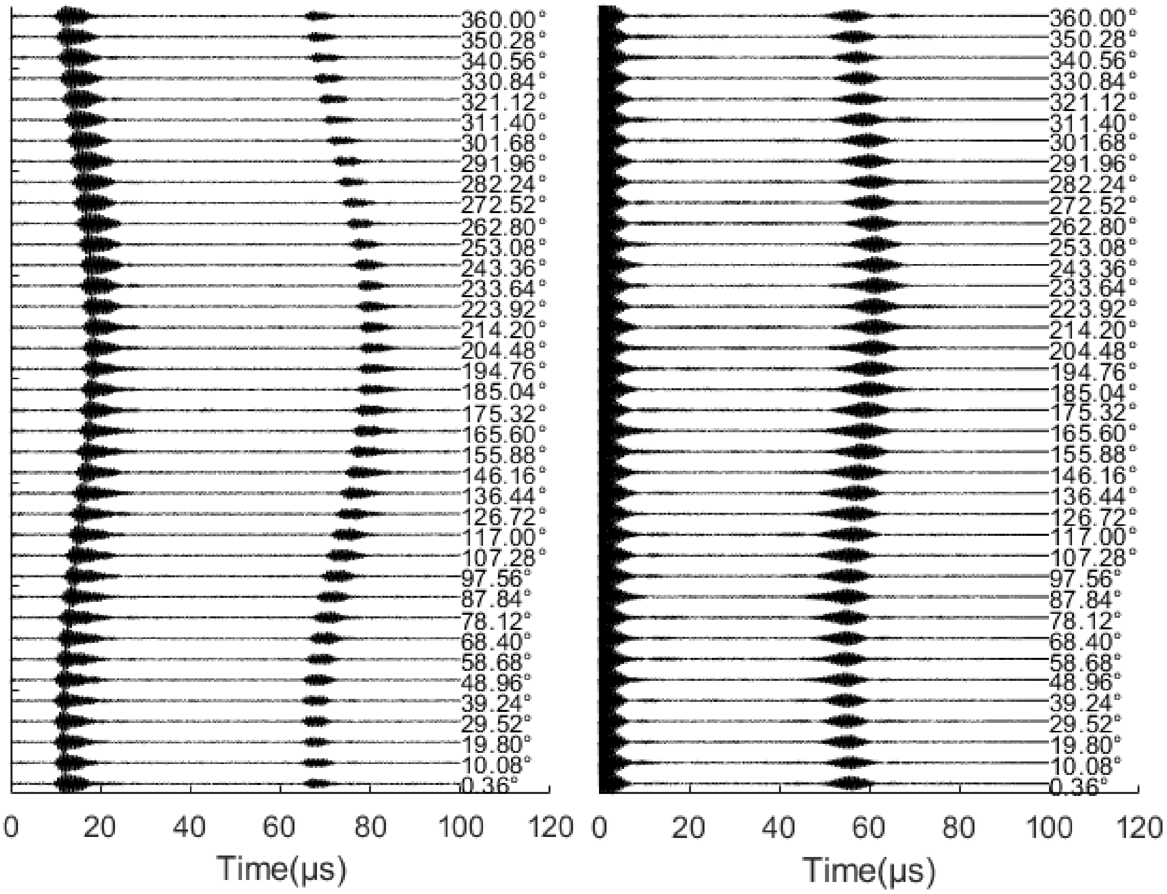

Figure 7-8: (LHS) Acquired waveform. (RHS) Auto-correlation of the acquired signal.

All the axis crossings were detected by multiplying the signal vector from the first point to the second last point in the vector with the second point to the last point:

$$x = s[N-1]\ .\ s[2-N]$$

All the points where $x < 0$ correspond to axis-crossings. The tracking of the axis crossing in one waveform to the next was possible by:

1. Selection of a single crossing point.
2. Setting the search window to 1/2 wavelength.
3. If there is a crossing within the window, then start again at step 1 to find the same crossing on the next waveform.

The result of the axis crossing tracker is presented in Figure 7-9, showing how the method was used to track several crossings of the auto-correlation, with the output as the mean value of these.

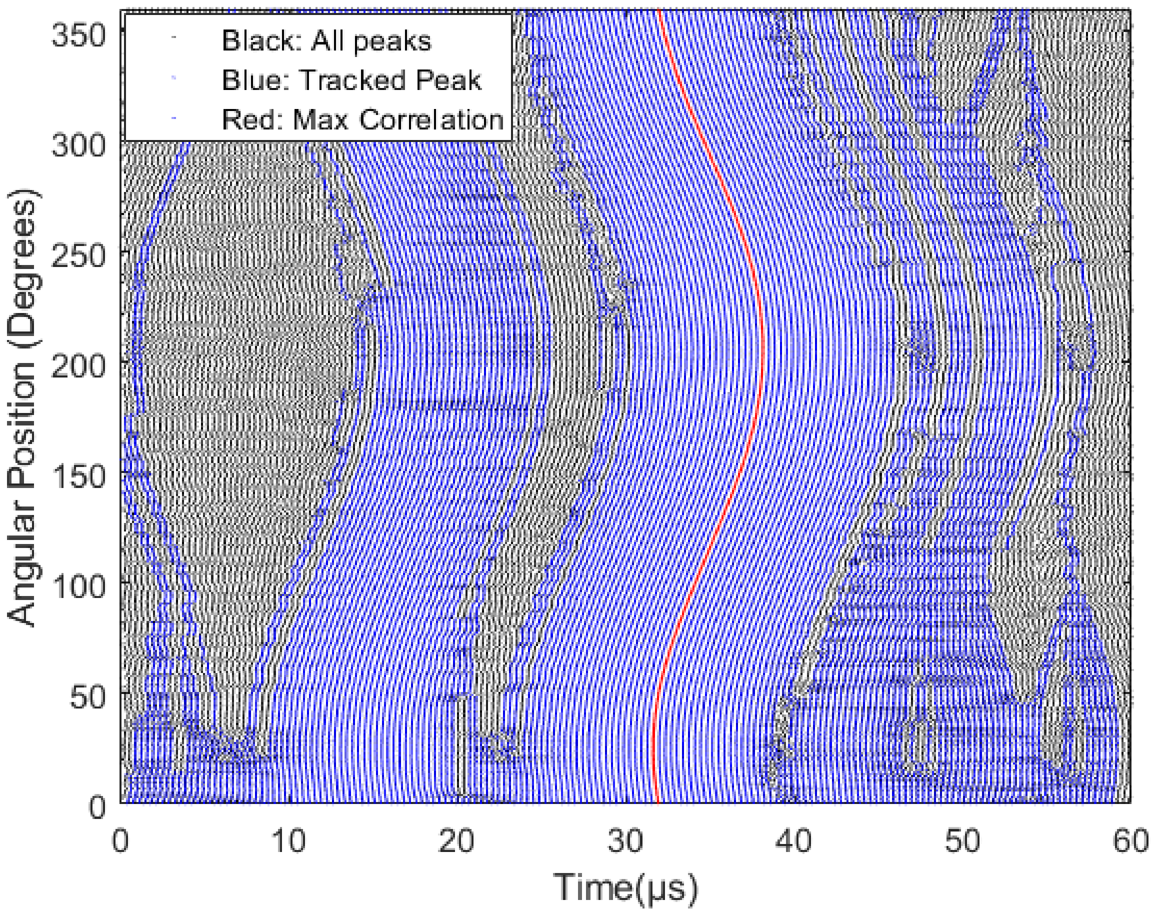

Figure 7-9: The black points represent all the axis crossings from the waveform. The blue points correspond to all the tracked axis crossing points. The red line shows the location of maximum correlation.

Figure 7-9 shows all the axis crossing points of each waveform acquired at each incremental angular step around the bore, using the bore form rig. The location of maximum correlation is tracked to find the TOF, and the tracked crossing is shown in red. A large change in the TOF of around 6μs is observed, which corresponds to ~1mm axial misalignment of the axes of the bore to the rotational axis of the spindle the sensor is mounted on.

7.4.2 Form Measurement: Centroid Alignment

Figure 7-10 shows the absolute distance measurement from the sensor to the cylinder liner face.

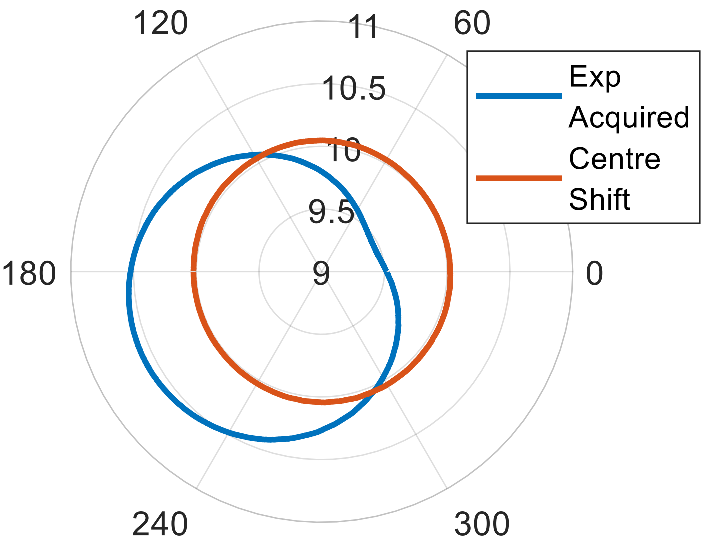

Figure 7-10: Distance measurement obtained from the bore form rig showing axial misalignment between the cylinder bore axis and the rotational axis of the spindle the sensor is mounted on. The figure also shows the plot of the form measurement with shift digitally removed in post processing.

From the figure, the axial misalignment between the cylinder bore and the rotational axis of the sensor is observable; the linear was off by ~0.5mm. This resulted in an eccentric shift of the measured data. This was removed by first finding the centroid of the circle in polar coordinates, then shifting the centroid such that it aligned with the origin.

7.4.3 Form Measurement: Tilt Removal

Figure 7-11 shows the measurement attained once the mean centre was shifted to the origin. The distance measurement was observed to be greater in one plane when compared to the plane orthogonal to it, i.e. one plane had higher radius measurements, as shown by the characteristic 2 lobes in the polar plot. Furthermore, small amplitude sine-wave-like patterns were observed in the measurement, potentially due to unnoticeable stick slip motion of the spindle or vibration of the spindle head.

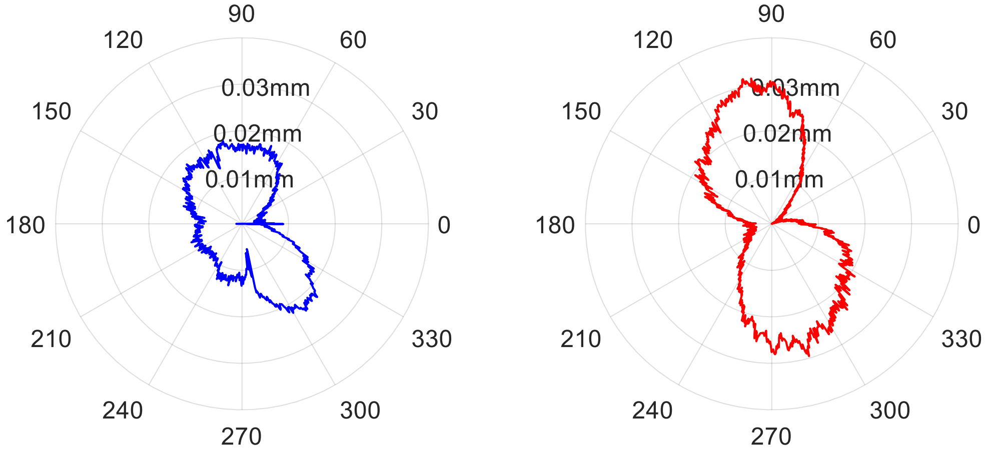

Figure 7-11: Relative change in radius measured using CMM (LHS/Blue) VS Ultrasound (RHS/Red).

The reason for the lobes is the relative tilt of the spindle axis and the axis of the bore. Thus, the tilt was removed from the measured data – by removing a second order distortion from the measured shape; see Figure 7-12.

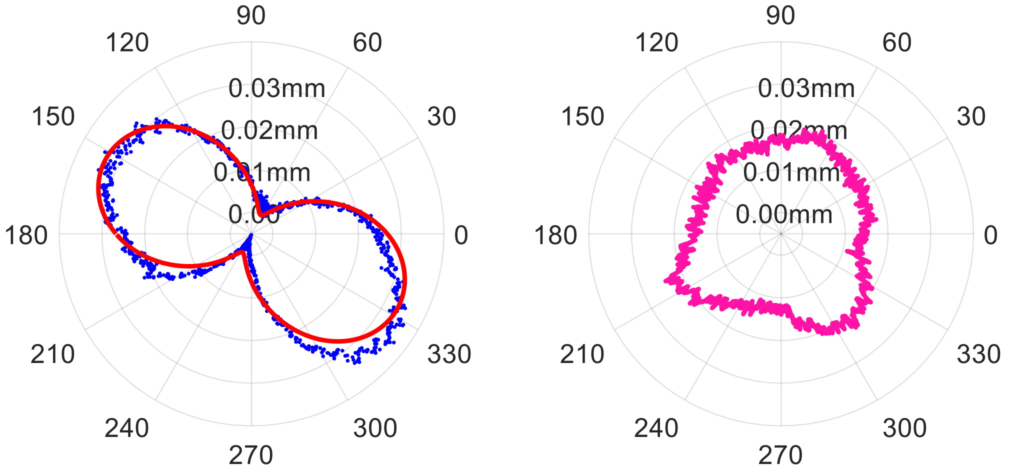

Figure 7-12: (LHS) Experimental data (blue points), and 2nd order fit (red line) that was to be subtracted from the experimental data. (RHS) Experimental data with 2nd order distortion subtracted.

7.4.4 Form Measurement: Angular Alignment

On comparing the experimental data with that obtained from a CMM machine, the ultrasound measured data were found to be off alignment in the polar axis. Therefore, the two measurements were correlated to find the angular shift, and the shift removed. Figure 7-13 shows the measurement prior to the angular alignment and after the alignment of the CMM measurement to the measurement obtained from the bore form rig.

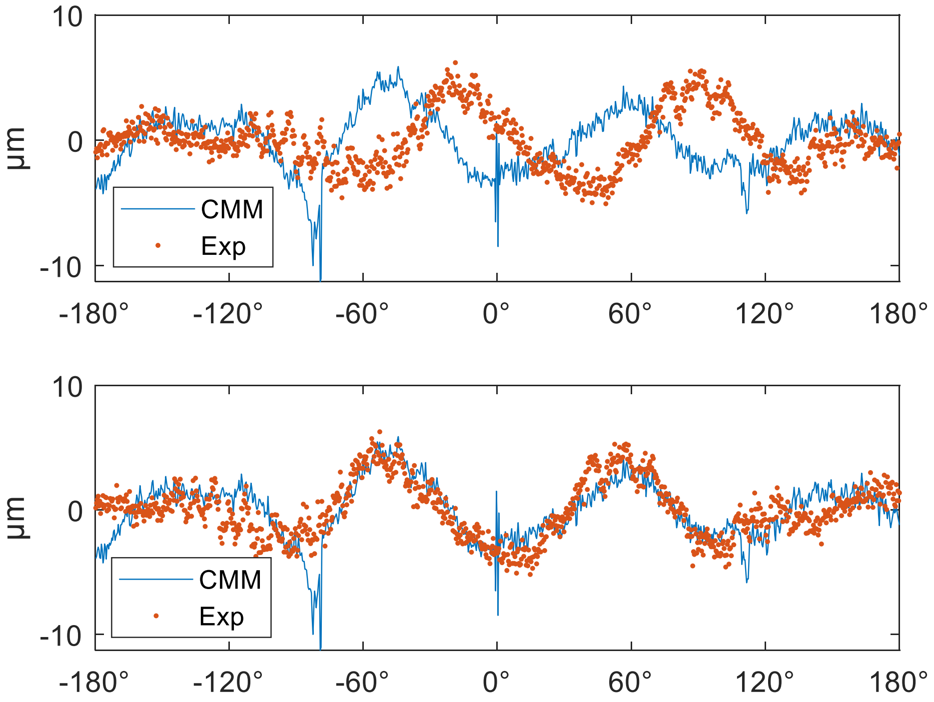

Figure 7-13: (Top) CMM vs Exp, Sensor Tilt Removed. (Bottom) Exp relative angular position corrected.

7.4.5 Feature Detection

To determine whether a step change in the bore could be detected, a step of 70µm thickness was created using a Kapton masking tape. Figure 7-14 shows the setup of the experiment.

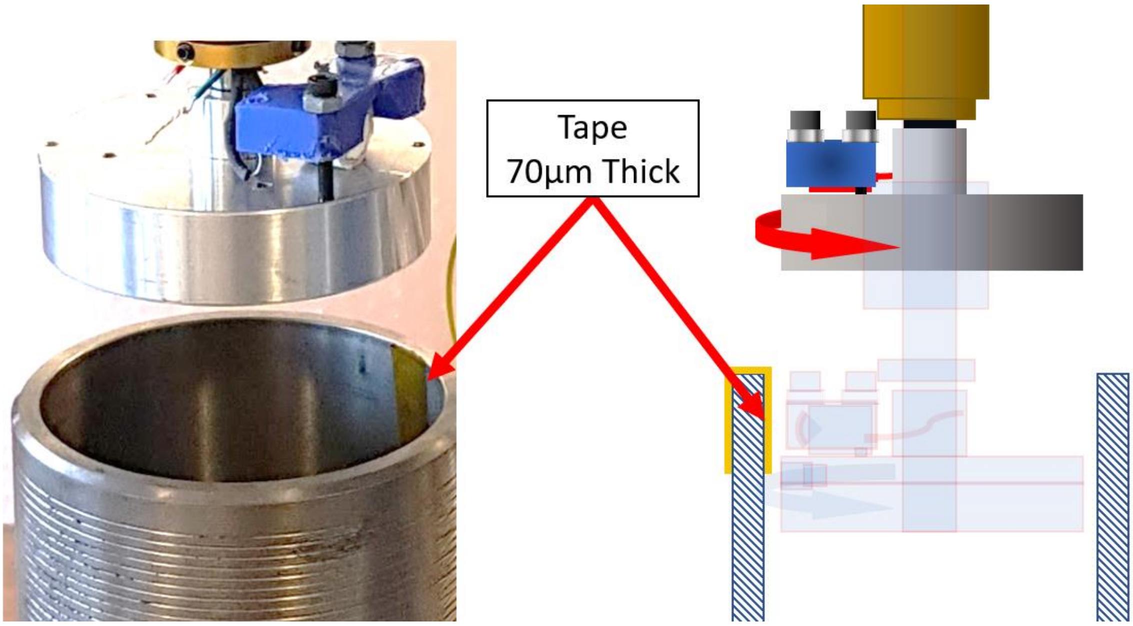

Figure 7-14: Step change measurement experiment with Kapton masking tape (RS:436-2762) of 0.07mm thickness (the step).

Figure 7-15 shows the axis crossing plot (similar to Figure 7-9) obtained from the experiment which clearly shows a step change at around 0.5 radians.

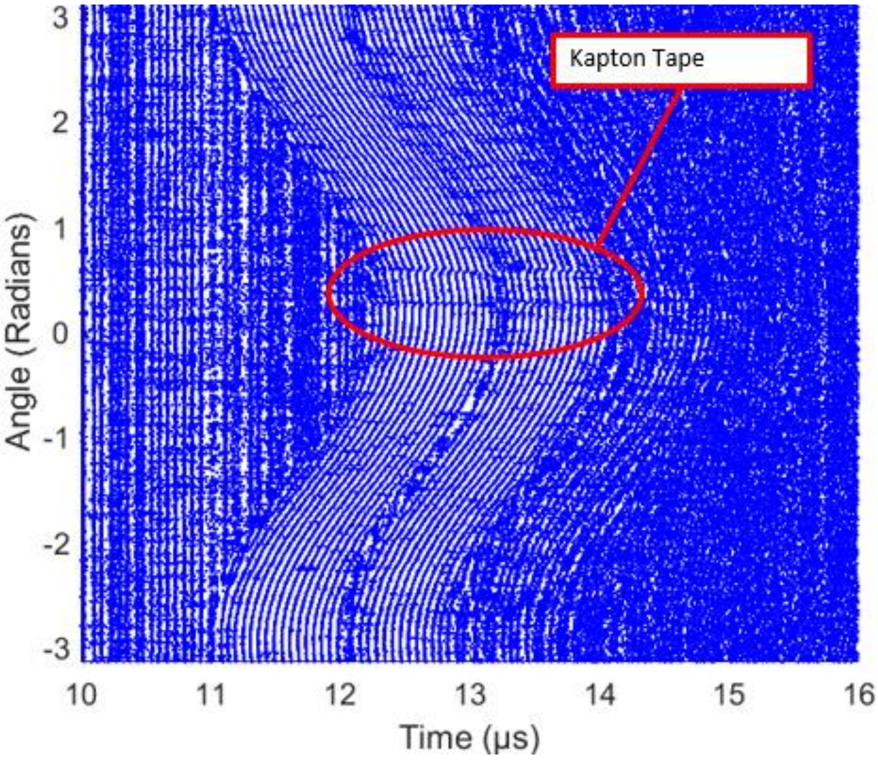

Figure 7-15: Step change in bore measurement with the rig running at 34RPM.

The sudden change in axis crossing points is observed in the plot when the sensor passes over the Kapton tape (labelled in the figure). Figure 7-16 shows a plot of the tracked line in Figure 7-15.

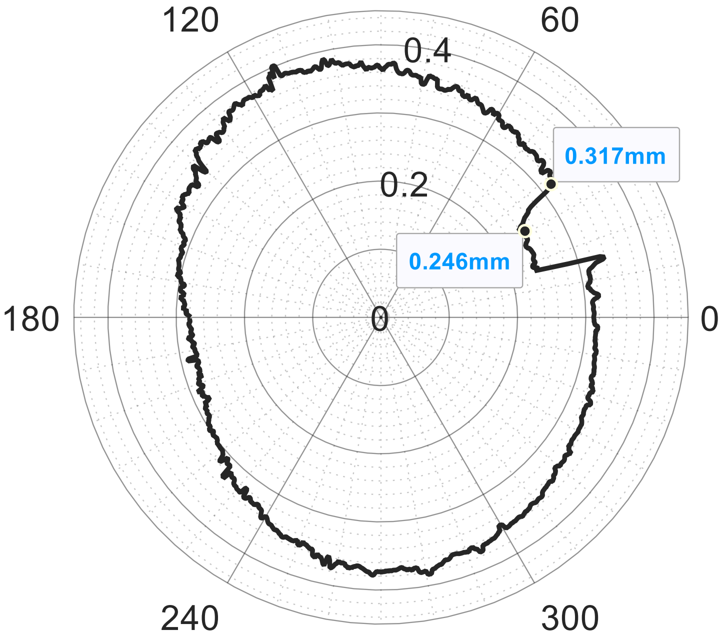

Figure 7-16: Plot of relative distance measurement between the air-coupled sensor and the internal face of the bore, with Kapton tape stuck on the bore. Step change in distance to the bore internal face — due to the tape stuck on the bore — is clearly observable. The circumferential resolution is 0.36 degrees.

The step change in the measured distance to the internal face of the bore is used to infer the thickness of the Kapton masking tape. The manufactured thickness of the tape is 70µm, while the measured thickness was 71±6µm. The measurement is carried out to a reasonable degree of accuracy. The measurement likely contains higher error due to regions of the uneven bond thickness.

7.4.6 Form Measurement: Ultrasound vs. CMM

Following the investigation into various method of processing the measurement data to obtain the bore form, the rig was run at 2 different speeds to measure the bore form at those speeds.

Figure 7-17 shows the results when the machine was running at 65 RPM, while Figure 7-18 shows the results for the rig running at 200RPM.

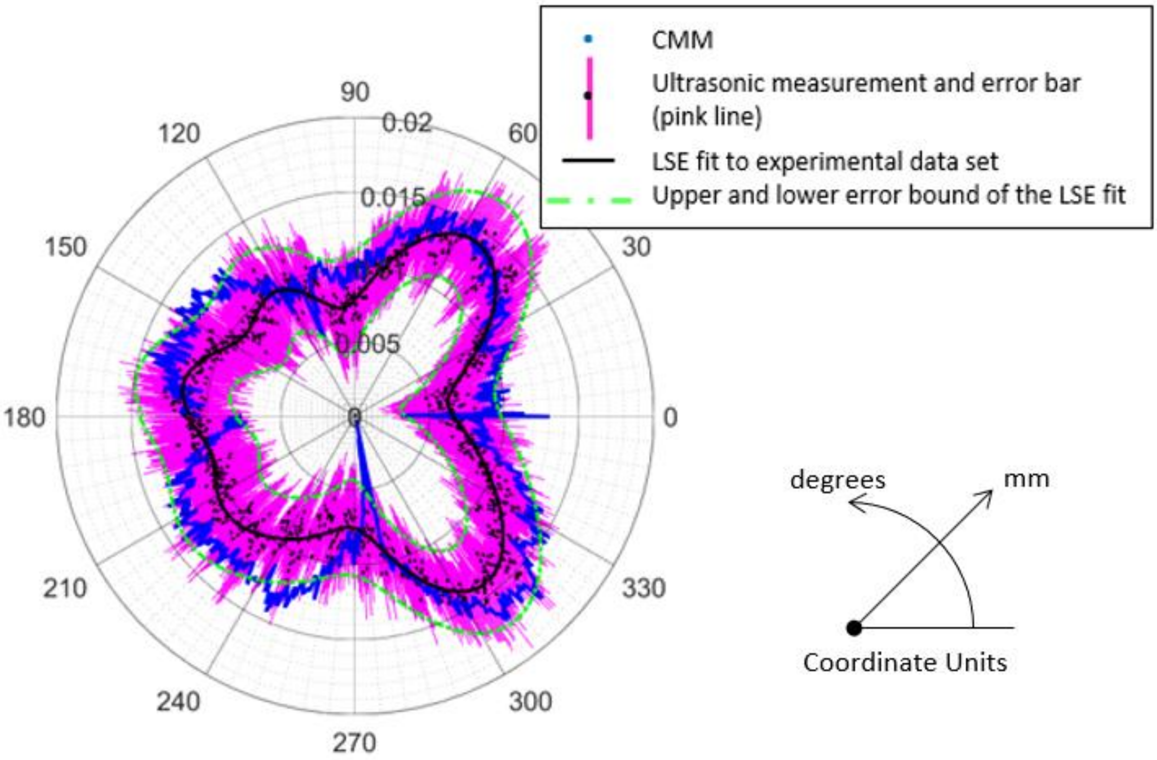

Figure 7-17: CMM vs Ultrasound, Spindle Speed 65RPM. Blue Line - CMM reference measurement; Black Dots - Experimentally measures points with magenta lines as error bar; Black Line - fit to experimental data; Green dashed lines - lower and upper error bound of the fit.

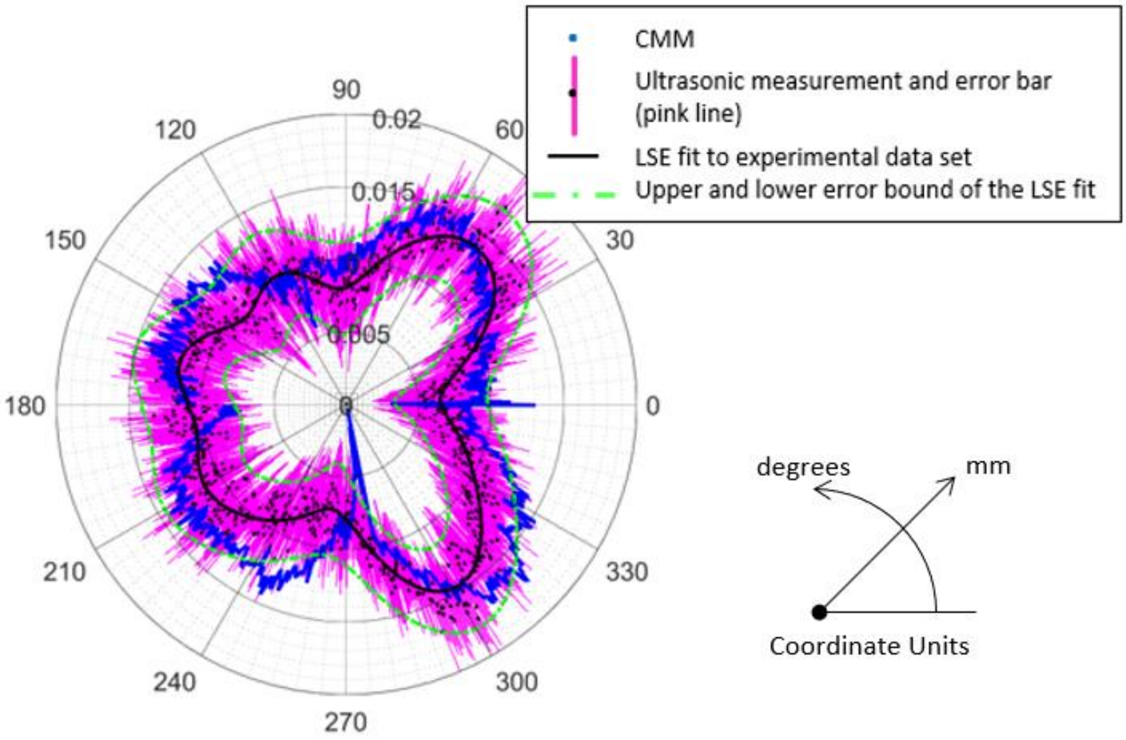

Figure 7-18: CMM vs Ultrasound, Spindle Speed 200RPM. *Plot legend as per Figure 7-18.*

When compared to the reference measurement from CMM, the bore form measurement at 65RPM was found to have an additional error (on top of the value attained for the probe presented in §6.4.2) of $\sigma_{3SDV} = 1.38\mu m$, thus the total measurement error of $\sigma'_{3SDV} = \sqrt{3.20^2 + 1.38^2} = 3.48\ \mu m$. Similarly, for measurement at the speed of 200RPM, $\sigma_{3SDV} = 2.04\mu m$, and the total measurement error, $\sigma'_{3SDV} = \sqrt{3.20^2 + 2.04^2} = 3.79\mu m$.

The higher measurement error for the faster rotational speed was most likely due to the higher noise in the electronic equipment such as the slip ring, or alternatively it was due to the dynamic effects causing the spindle and the sensor to both shake more.

The results of bore form measurement using an ultrasonic method when compared to the reported measurement accuracy of air gauges (around 10μm) currently installed on the bore honing machine was thus found to be better. However, the effects of varying surface temperature and the presence of contaminants on the bore surface are yet to be explored. While the ultrasound system can be affected by contaminants on the liner surface, a key advantage of using an air gauge is that the high air pressure used for the measurement blows the contaminants off the liner surface and therefore the measurement is not affected by contaminants.

7.5 Conclusions

Bore form measurement of a 78mm internal diameter cylinder was conducted using the bore form measurement rig presented in §3.1.6, and the ultrasonic probe designed as per §4.3 – with the outcome of its calibration presented in §6.4.2.

The measurements acquired were corrected for centroid shift, tilt correction, and angular misalignment, with the methods used presented.

The findings of the chapter can be summarised as follows:

1. A measurement of a step change in the bore was performed using Kapton masking tape stuck to the inside of the liner. The step change was measured to 71±6μm, while the thickness of the tape was 70μm.
2. The bore form measured using air coupled probes were found to match those obtained using the CMM machine within ±3.48μm while the rig was running at 60RPM and ±3.79μm while the rig was running to 200RPM.
3. Accounting for setups where there could be errors in measurement due to uncertainty in measuring the temperature, and assuming this uncertainty is within 0.15°C, the corrected measurement uncertainty of the bore form measurement is ±4.30μm for 60RPM and ±4.55μm for 200RPM.

Therefore, it was shown that using an air coupled ultrasonic probe (manufactured using methods as outlined in §4.4) could present a viable means of measuring the bore diameter to within the tolerance of ±10μm (see Table 7-1).

It should be noted however that the effect of surface temperature and temperature change in the measurement accuracy in general have been left for future work. Equally, it would be worth exploring the use of capacitive micromachined ultrasonic transducers (CMUT) with much wider bandwidth and lower power requirement may outperform the air coupled probe. This assumes the cost implication of such a probe would not be a limitation to selecting it for use in the honing machine.

Some alternative means of using air-coupled ultrasonic probes to perform bore form measurements are presented in Chapter 10 (§10.3).

8 Bore Distortion Measurement using Ultrasound

Ultrasound is used as a tool in NDT to measure various tribological parameters of an engine, in-situ. However, until now it has not been used to measure bore distortion. The main challenge in using ultrasound is that the dynamic variations in the through thickness temperature and stresses make it difficult to know the wave propagation velocity accurately. The chapter describes the impact of changes in temperature on bulk and surface wave methods that can be used to measure bore distortion.

8.1 Introduction

The combustion chamber inside an automotive engine is sealed by gasket seals and by the piston rings. The pressure required for the activation of the gasket seal is provided by the engine head bolts - typically either 4 or 6 bolts are used. The pressure required for the activation of the sealing mechanism by the piston ring is the combustion pressure itself. Figure 8-1 shows a cross-section of an engine liner and other components which can be tuned to minimise bore distortion.

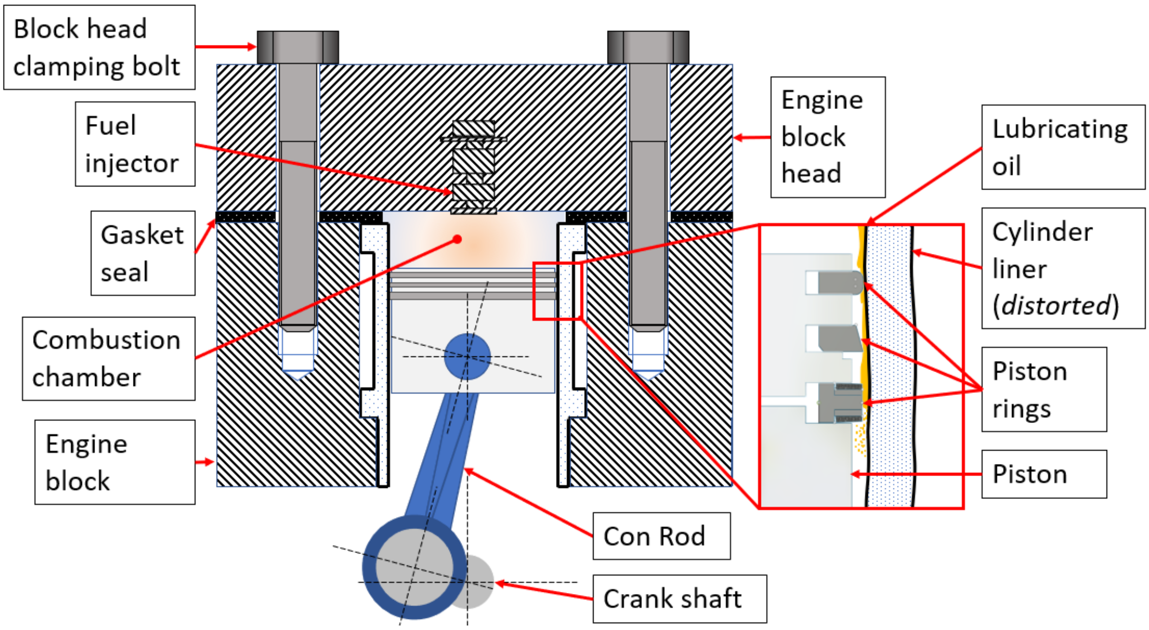

Figure 8-1: Schematic of an engine liner inside an engine, showing the components that affect bore distortion.

During operation, the combustion chamber can reach pressures in the range of 10-18MPa while the combustion temperature can be in the range of 2000°C. The temperature of the liner inner wall can reach around 150°C, while varying in the axial and radial directions. The temperature also varies through the wall thickness, and varies with locations, axially and radially. The liner is subjected to additional loading by piston slap side-to-side during the cycle. The cyclic nature of all the thermal-elastic and mechanical forces results in bore distortion that can vary through the cycle. The problem increases in complexity as the forces change with engine load, speed, and other environmental factors. Figure 8-2 shows the resultant shape of a deformed bore.

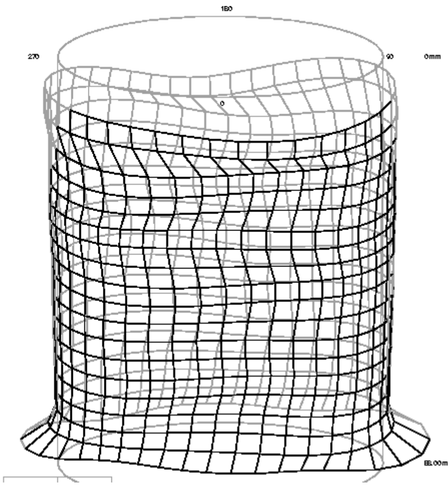

Figure 8-2: Bore distortion observed by Bird and Gartside (2002). Figure obtained from the referenced article.

The thickness measurement of the cylinder liner, using ultrasound, at various locations around the bore, could allow for the measurement of true bore distortion.

The research challenge is in quantifying and managing the errors in predictability of the wave propagation velocity as a function of temperature and stress, such that the TOF reading can be converted to distance with measurement uncertainty that is less than the measured quantity itself. The chapter looks into velocity calibration for temperature for bulk and surface waves. Following this, a technique to measure bore distortion that accounts for the temperature variation is presented.

8.2 Literature review

Issues in conformability between the bore and piston rings lead to problems such as increased friction, lubrication oil consumption (LOC), and blow-by (escaping of combustion pressure). These can lead to lower efficiency/power losses, increased noise-vibration-harshness (NVH), increased unwanted emission products, and reduced component life, etc. Bore distortion is a major proponent of the lack of piston ring conformability (Andersson, Tamminen and Sandström, 2002).

The shape of the bore is generally defined in terms of the decomposed Fourier coefficients (Chittenden and Priest, 1993). The level of distortion in the radius, ∂R is described by:

$$\partial R = \sum_{n=0}^{N} (A_n \cos n\theta + B_n \sin n\theta) \tag{Equation 73}$$

Where, A_n and B_n are the Fourier coefficients of the n^{th} mode, N is the total number of modes considered to describe the shape, and θ is the angle around the bore. Usually, the actual final shape of the bore is a superposition of these different shapes at varying magnitudes; see Figure 8-3.

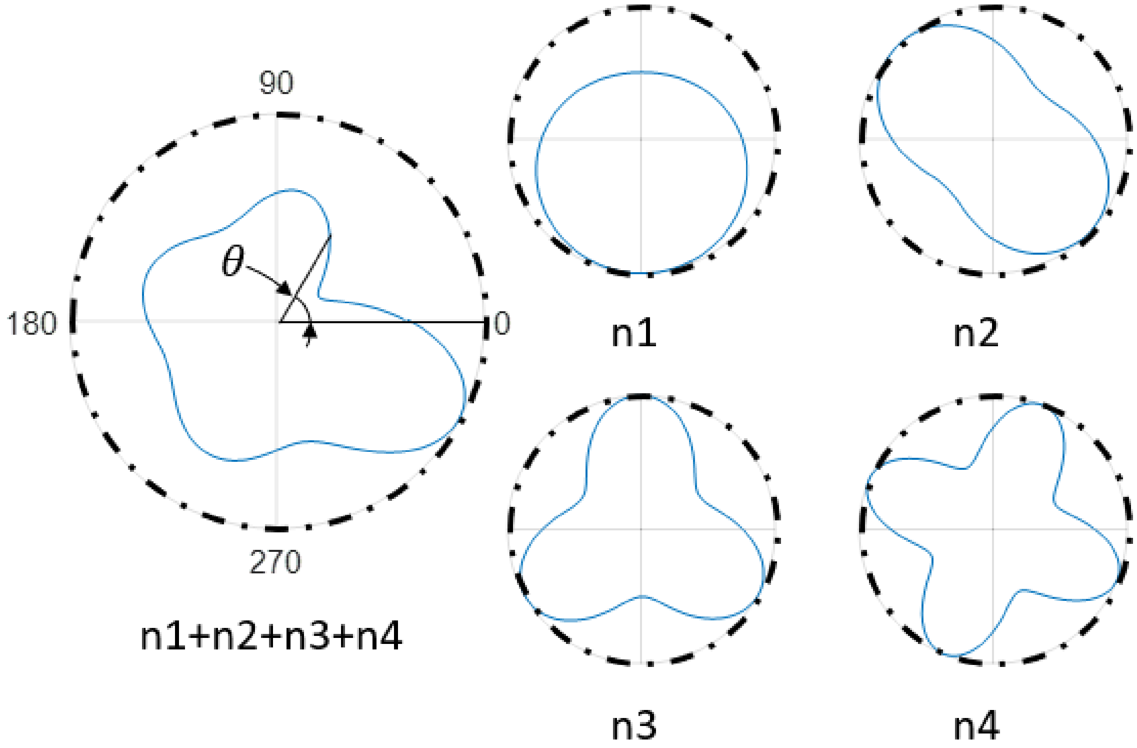

Figure 8-3: (LHS) Shape of a distorted bore accounting for the 1st 4 modes. (4 on RHS) 1st to 4th orders of bore distortion decoupled from the final shape. Dash-dot lines represent an undeformed bore. *Modes shown as shrinking of original round shape, while in reality there can be expansions as well.*

The conformability of the rings and the liner is dependent on various factors, such as the various forces on the ring to the magnitude of bore distortion. Considering bore distortion, the contact pressure distribution on the ring-contact becomes uneven with higher orders of distortion, an issue which is more profound at lower loads, i.e. when the back pressures on the rings are lower (Andersson, Tamminen and Sandström, 2002; Söderfjäll *et al.*, 2014). The issue of confirmability is thus greater for higher orders of distortion, although the magnitude of distortion of higher orders are generally lower.

The maximum acceptable bore distortion values (i.e. which do not affect the function of the ring package) as per an empirical formula based on observation, are given as follows (Knaus, 2017):

$$U_{i,max} = C_i \,.\, D \,.\, 10^{-4} \qquad \text{Equation 74}$$

Where, $U_{i,max}$ is the deformation of the order i, D is the bore diameter, and C_i is the empirical factor given as per Table 8-1.

Table 8-1: Values for Empirical Factor, C_i

Order	2	3	4	5	6	8
C_i	2.5	1.6	1.2	0.6	0.4	0.3

Using the empirical formula, the values of maximum acceptable bore distortion attributed to various orders for cylinder of various sizes are presented in Table 8-2.

Table 8-2: Typical value of bore distortion below which the functioning of the piston package is affected, calculated as per Equation 74.

	Distortion Order (distortion values in µm)					
Bore diameter (mm)	2	3	4	5	6	8
60	15	9.6	7.2	3.6	2.4	1.8
70	17.5	11.2	8.4	4.2	2.8	2.1
80	20	12.8	9.6	4.8	3.2	2.4
90	22.5	14.4	10.8	5.4	3.6	2.7

Table 8-3 shows the maximum bore distortion magnitudes of a 4-cylinder engine with cylinder bore of 80mm.

Table 8-3: Typical values of maximum bore distortion of 80mm bore in an engine of a typical family car (B. Littlefair 2020, personal communication).

Order	2nd	3rd	≥4th
Magnitude (µm)	50µm	30µm	20µm

8.2.1 Bore distortion measurement

Bore distortion measurements have been performed on static or live running engines. The static ones seem to be focused on identifying the effects of thermal and static loads and are generally used to study the effect isolated parameters. The dynamic ones meanwhile attempt to find the exact bore deformation with all running conditions considered.

Several attempts to conduct bore deformation measurements been made using inductive based sensors mounted on the ring land (Fujimoto *et al.*, 1991; Chittenden and Priest, 1993; Koch, Fahl and Haas, 1995; Maassen *et al.*, 2001; Bird and Gartside, 2002; Ghasemi, 2012). (Fujimoto *et al.*, 1991) use a single sensor on the second ring land, while using a geared mechanism to turn the position of the sensor and to obtain the measurement of the inner face. Being one of the first to attempt the measurement, the significant modifications required of the block were found to change the bore deformation characteristics. The method was improved upon by Koch, Fahl and Haas (1995). Quantifying the distortions as per Equation 73 had allowed the authors to measure up to a given n^{th} order by having 2n+1 number of sensors, that are equi-spaced — i.e. dictated as per Nyquist–Shannon sampling theorem. However, Koch, Fahl and Haas (1995) seem not to have accounted for this. Maassen et al. (2001) repeat the work with varied engine parameters, however the measurement is again performed with 8 sensors. Bird and Gartside (2002), use 10 sensors in light of the aforementioned criterion. The authors validated accuracy of the sensors comparing it to a PAT inclinometer, by measuring static bores, and found the two methods to be within 1.6µm. Figure 8-4 shows the sensors fixed onto their mount plate and then into the piston, as shown by Bird and Gartside (2002).

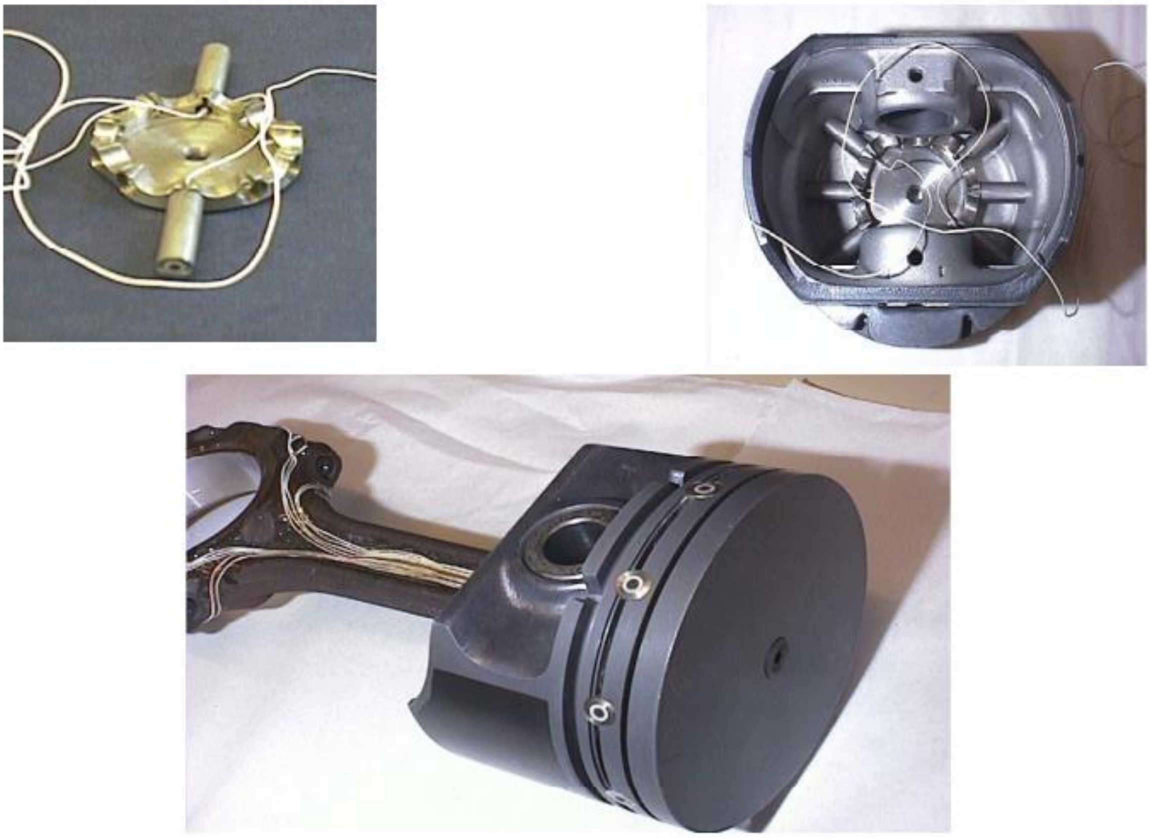

Figure 8-4: Piston with eddy current sensors mounted radially around the 2nd ring land of the piston, as shown by Bird and Gartside (2002).

A key consideration which has not been accounted for in the previous attempts to measure bore distortion of live running engines seems to be quantification of measurement errors of the methods that were used.

Inductive sensors give out a non-linear response to displacement and usually require calibration, specific to the target to attain high accuracies (Nihtianov, 2014). Factors which impact the accuracy of inductive sensors include tilt of the sensor relative to the target. Another factor could potentially be the impact of external forces on the assembly of the sensor components, i.e. the flexing of the sensor may change the sensor makeup.

However, a more significant source seems to be not knowing accurately the position of the piston where the sensors are mounted. The authors have generally used models to predict the piston tilt (rotation about wrist pin axis) and lateral displacements to estimate the reference location of the sensor. The following paragraphs present a brief review of the literature on piston secondary motion with the aim of validating the existence of potential measurement errors.

McClure and Tian (2008) use a numerical model to predict piston secondary motion of a heavy-duty diesel engine of nominal 130mm cylinder bore and piston diameter and with piston-liner clearance in cold state of 65μm. Lateral motion of the piston is predicted to around 80μm, while the tilt is predicted to 0.097°. Littlefair et al. (2014) have measured the piston lateral displacement of a Honda CRF engine with bore and piston nominal size of 96mm and measure the lateral displacements as ~100μm and piston tilt as ~0.17º. The work also reports piston skirt deformation in the region of 40μm. Dolatabadi et al. (2015) measure the piston slap force in the Honda CRF engine using sound recording — the frequency of the sound is related to the force by assuming the impedance relationship analogous to Equation 25, and therefore higher load is assumed to result in faster lateral velocity of the cylinder wall and piston combined. The experimental results seem to show some level of periodicity in the piston slap; however the result shows higher transient behaviour (i.e. there is less of a periodic pattern) for higher engine speed. Tan and Ripin (2013) have measured the piston motion using a laser for a motor driven piston, and have shown its motion to be chaotic for fast speeds. For any piston crank system, the piston lateral position and angular tilt seems to transition from periodic behaviour for slower speeds, to chaotic (oscillations with no precise pattern) behaviour at faster speeds (Farahanchi and Shaw, 1994). With increased engine load, higher temperatures and consequent thermal expansion seems to allow more space for the piston to move and result in greater nonlinearity in the lateral motion, i.e. moving towards a transient and possibly chaotic region.

The review of the literature in piston secondary motion, albeit brief, seems to show that measuring bore distortion using sensor mounted on the piston ring land has potential for significant measurement errors. This assumption is made based on the following:

- Impact of piston deformation may be significant enough to deform the distort the housing of the sensors inside the piston ring land.
- On impact, the force of the piston slap on the sensor itself seems difficult to measure.
- A method which predicts the piston tilt and lateral motion, when the piston secondary motions are comparable in magnitude to bore distortion (much greater in magnitude than the higher order distortions), will likely consist of higher measurement errors. This error will likely be greater when the piston secondary motion starts to exhibit greater non-linearity.

Bore distortion measurements conducted at slower speeds when piston motion is in the periodic region, which rely on predicting piston lateral motion/tilt however likely has some credibility. However, it is likely such engine test parameters will not cover the full operating range.

8.2.2 Numerical Models to Predict Bore Distortion

With growing computation power, various studies using FEA to test engine parameters have become a common occurrence. Ghasemi (2012) calculated the bore distortion using linear FEA, including distortions due to the effects of thermal load, clamping loads and combustion pressure. Kagnici and Akalin (2014) studied the combined effect of cylinder bore and piston distortion on various lubricant oil consumption mechanisms. Mohammed et al. (2015) studied the effect of variation in gasket thickness, liner thickness, number of cylinder head bolts and bolt preload on bore distortion of a cylinder in a direct injection diesel engine. While a range of literature exists that has utilised numerical analysis to study bore distortion, Barbieri et al. (2019) note that finite element models fundamentally rely on real test data which are limited by current methods. Therefore, numerical models seem to have a limitation when compared to real test data.

8.2.3 Ultrasonic Measurements of the Liner

Works by various authors have shown the feasibility of using an ultrasonic transducer for the measurement of engine parameters such as wear as well as oil film thickness (OFT) (Birring and Kwun, 1989; Dwyer-Joyce *et al.*, 2006; Avan, Mills and Dwyer-Joyce, 2010; Mills, Avan and Dwyer-Joyce, 2012; Mills and Dwyer-Joyce, 2014). The schematics depicting the measurement configurations used by Birring and Kwun (1989) for wear measurement, and by Avan et al. (2010) for OFT measurement, are shown in Figure 8-5.

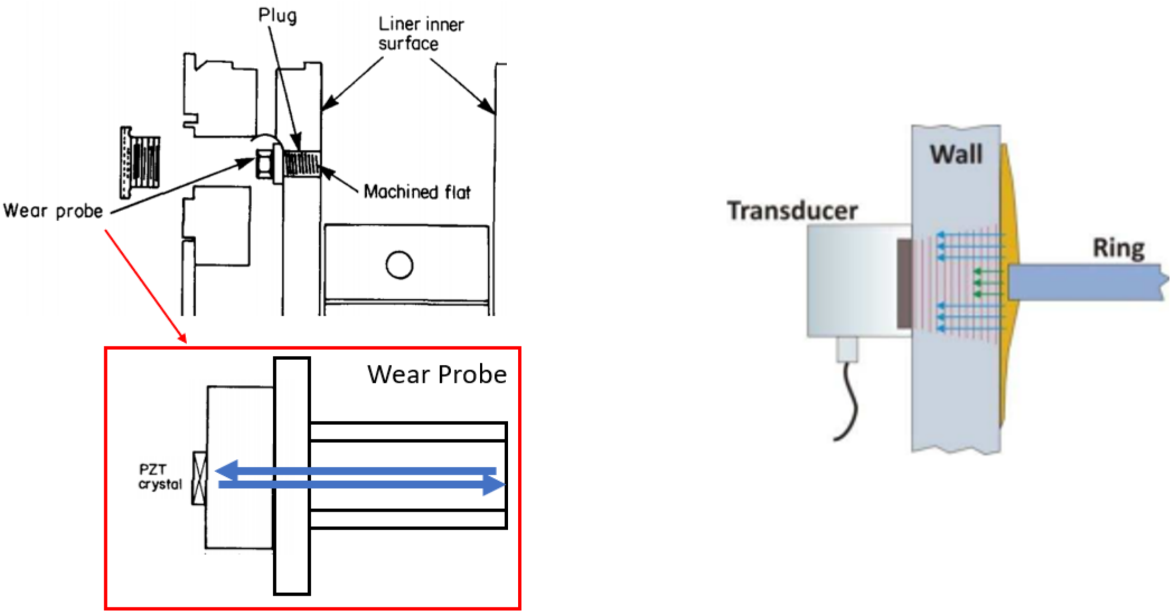

Figure 8-5: (LHS) Schematic of ultrasonic sensor (PZT crystal) used by Birring and Kwun (1989) to measure wear of an engine; (RHS) Schematic showing the method used by Avan, Mills and Dwyer-Joyce (2010) for oil film thickness measurement. *Both figures have been taken from the corresponding authors' articles; figure on the LHS has been modified to highlight the probe.*

The authors have shown the feasibility of using an ultrasonic method as an effective measurement instrument in the engine environment. In the case of OFT measurements, this is also minimally invasive. Studies such as this give credence to a study which investigates the use of ultrasonic sensors to measure bore distortion. There are however some challenges which need to be considered at present.

Ultrasonic OFT measurements rely primarily on the amplitude comparison method. The amplitude of a reflected ultrasonic waveform is measured at a reference, i.e. when the piston rings are not opposite to the transducer. This is compared to when the rings pass the axial locations of the transducer, as depicted in Figure 8-5 (LHS). Here the engine liner effectively acts as a delay line medium and also provides the reference measurement to account for all the temperature and stress effects. When the liner itself is the subject of interest, e.g. in the case of bore distortion measurement, the effects of temperature and stress on the measurements would be significant.

The temperature effects on the wave propagation velocity are highlighted in work by Birring and Kwun (1989) along with the subsequent errors in measurement. The authors suggest taking ultrasonic TOF measurements from before heating the liner to after the experiment has been completed and the liner has returned back to a steady state temperature throughout its thickness. The authors report an accuracy of ~1μm in thickness measurement.

8.2.4 Temperature distribution in a Liner

The average temperature and heat flux of cast iron liners as presented by Heywood (1988) shows that the TDC of the liner is subjected to high heat transfer from combustion gases, frictional heat between liner and piston rings, and conductive heat transfer from its surroundings. Closer to BDC, the effect seems solely reliant on the conductive heat transfer and friction with the piston ring. The steady state temperature variations between the inner surface (the bore) and outer surface of a cast iron liner at BDC can be in the range 10-15°C while at the location of TDC this can be in the range of ~50C°.

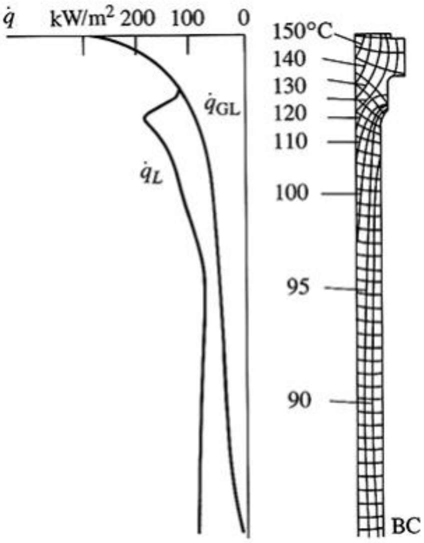

Figure 8-6: Temperature variations in a liner. Figure adapted from Heywood (1988).

8.2.5 Conclusions from the literature review

The topic of ring and liner conformability is vast, ranging from piston ring wear, ring dynamics, piston distortion and secondary motions, to contact lubrications engineering that is used to account for the different lubrication regimes. Most of the topics are required to assume that bore distortion is one of the existing issues to mitigate against, therefore being able to reduce the distortions or control it would offer significant advantages in efficient engine designs.

Current in situ bore distortion methods rely on installing inductive sensors within the piston. Such methods of measuring bore distortion in live engines seem to rely on predicting the lateral position of the piston. This is limited in accuracy due to high error in knowing the relative position of the sensors to a known reference in a fired engine. Whist inline piston location could probably be measured using tools such as laser displacement sensors, thus minimising the error in knowing the piston location, such applications would most likely be limited to non-fired conditions. In addition, the methods also seem to be laborious, requiring substantial engine modification. Thus, the need for a new measurement system which gives the actual bore distortion seems ever more important.

The direction of future liner designs seems to be taking the shape of non-circular cold geometries, such that they become round in operation; for example conical liners or initially deformed liners achieved by method such as hot honing (McCormick and Meara, 2002; Alshwawra *et al.*, 2020, 2021). Methods such as surface texturing introduced by means of honing (Dahlmann and Denkena, 2017) are also being investigated. It becomes ever more important to study how these modifications will impact piston ring-liner conformability of a live running engine at all engine parameters if possible.

The ability to measure bore distortion is of key interest because various methods of controlling the bore distortions could directly be investigated. Ultrasonic methods in studying other parameters within an engine seem to be a promising candidate for the new bore distortion measurement tool. Ultrasound would offer a non-invasive method for the measurement which would be a significant leap when compared to existing methods.

However, the wave propagation velocity, which the ultrasonic method relies on, is affected by temperature and stress. Therefore, a clear need to understand the effect of these parameters on measurement accuracy is highlighted.

8.3 Measurement Error

The factors which could add to the measurement error were those of working in the nearfield as shown in §2.8, the error due to the phase shift of the wave reflected at the bond interface, the phase distortion due to diffraction, and sources of such as quantisation error in the ADC process as discussed in Chapter 3.

The phase change, γ in radians of the wave reflected at the bond interface – which is resultant due to the input impedance at the interface – per reflection, can be presented as follows (Papadakis, 1976, pp. 290–295):

$$\gamma = \tan^{-1}\frac{2Z_eZ_s}{(Z_e^2 - Z_s^2)} \qquad \text{Equation 75}$$

Where,

$$Z_e = Z_1\left[\frac{(Z_1/Z_2)\ \tan B_1l_1 + \tan B_2l_2}{(Z_1/Z_2) - \tan B_1l_1 \tan B_2l_2}\right] \qquad \text{Equation 76}$$

Where, Z_s is the impedance of the specimen, and Z_e is the input impedance of the adhesive and the transducer, as seen by the specimen.

The pressure field due to diffraction for a circular piston transducer can be calculated as Equation 23. Figure 8-7 shows the acoustic pressure field along the transducer axis of a 5x2x0.4mm PZ27 that was used for the through thickness measurement application.

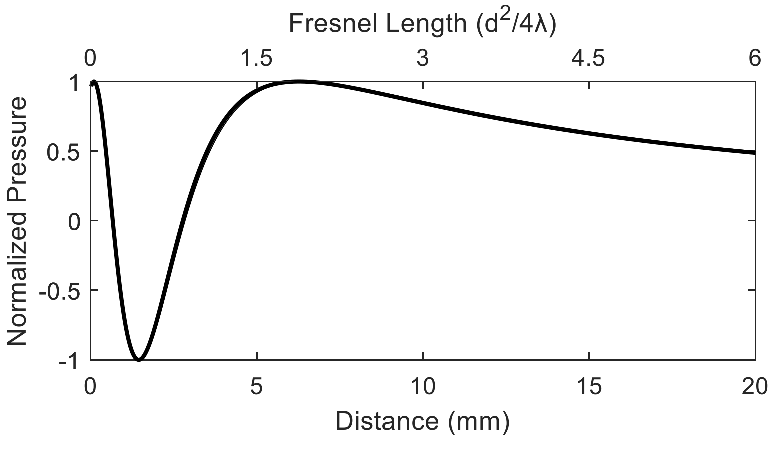

Figure 8-7: Pressure magnitude along the transducer axis.

Whilst the thickness of the specimen resulted in the probe working outside the theoretical nearfield region, Papadakis (1976, pp. 319–323) suggests λ/40 as a reasonable value of error to attribute to diffraction when it has been accounted for. Neglecting the error due to noise, Figure 8-8 shows the error magnitude of the various components for a 5x2x0.4mm PZ27 transducer bonded onto cast iron test specimen.

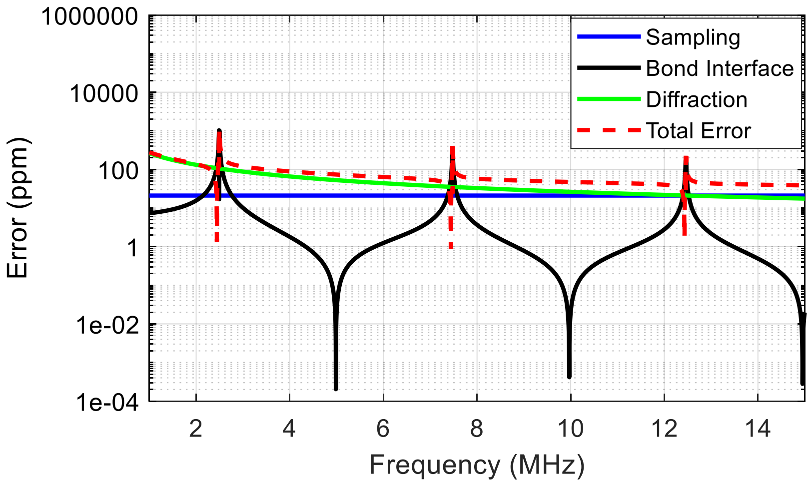

Figure 8-8: Sources of error and their contribution to the thickness measurement of a 5mm thick cast iron specimen by ultrasonic wave using a transducer of 5mm diameter. Bond thickness of 10µm; specimen thickness of 3mm; transducer thickness of 0.4mm. Calculated as per Papadakis (1976, pp. 319–323).

Various signal processing methods have been proposed to minimize error TOF measurement. Hull, Kautz and Vary (1985) show the use of correlation methods was most suitable when the signal consists of low SNR (high noise), while for high SNR (low noise) correlation or pulse-overlap was found suitable. Thus, a similar approach is taken in this work.

8.4 Experimental Methods

When the cylinder liner distorts, the thickness of the liner changes. With various orders of distortion, some region will expand while others will shrink. Where the liner expands, its wall thickness reduces, and where it contracts, the thickness increases. Similarly, the distance between two points on the outer surface of the liner will change accordingly. Figure 8-9 shows how bulk acoustic wave, and surface acoustic waves can be used to measure bore distortion.

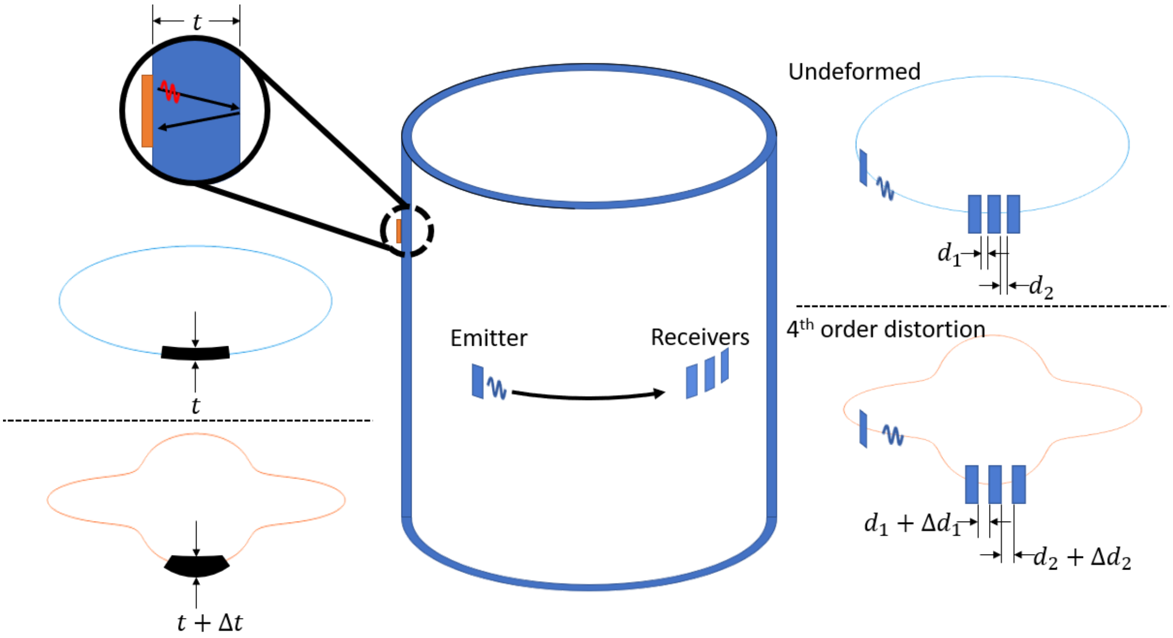

Figure 8-9: Schematic showing the concepts behind through thickness, bulk acoustic wave (on LHS) and surface acoustic wave (on RHS), that were studied for application in measuring cylinder liner bore distortion. Undistorted circle and 4th order distorted shape shown, show how thickness and distance between points on the surface chances due to distortion. t= liner thickness, $d_{1,2}$ = distance between transducers, Δ = change due to distortion.

Experiments were conducted to study a possible method/configuration through which ultrasound transducers could be used to measure bore distortion, as shown in Figure 8-9. A bar specimen that was machined from a sample cast iron cylinder liner was used for the study. The various studies which were conducted are outlined in Table 8-4.

Table 8-4: Experiments conducted to evaluate the probes manufactured.

ID	Study	Description
1	Temperature calibration of BAW.	TOF readings were taken while heating the specimen inside an oven, and while allowed to cool.
2	Temperature calibration of SAW.	As above but for surface wave.
3	Impact of surface temperature variation on measurement using SAW	Specimen was heated inside the oven then removed and "quenched" on one end (by placing into water). Measurement taken during "quenching".
4	1 pitch 3 catch setup using SAW to mitigate temperature effects.	A set of receiving transducers were placed at 39.5mm away from a pulsing transducer. A RTD temperature sensor was bonded locally to receiving transducer set. Experiment was conducted as outlined above.

8.4.1 Transducer configuration

Figure 8-10 shows a schematic of the liner specimen with surface acoustic wave (SAW) and bulk acoustic wave (BAW) transducer, and RTD temperature transducer bonded. Figure 8-11 shows a corresponding photograph. The process used to bond the piezoceramic and RTD transducers was as outlined in §3.1.1.

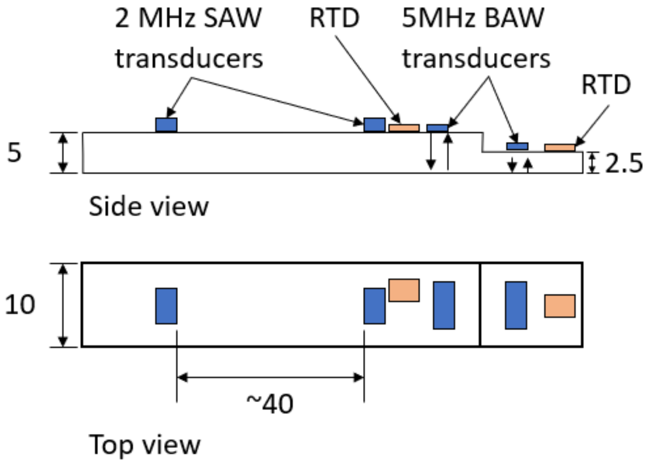

Figure 8-10: Schematic showing cast iron liner specimen with surface acoustic wave (SAW) and bulk acoustic wave (BAW) transducers and RTD temperature sensors. *Some transducers are not shown on the schematic.*

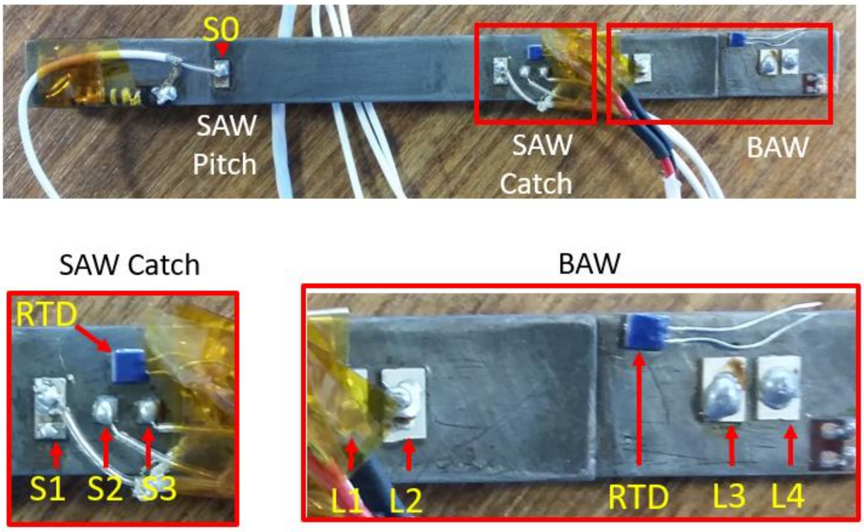

Figure 8-11: Photograph of the cast iron liner specimen with transducers and RTD. Transducer label: {S0, S1, S2, S3} = PZT PZ27 used in their radial resonance mode; {L1, L2, L3, L4} = DL10 (Del Piezo Specialties, LLC, 350 Tall Pines Road, Suite H & I, West Palm Beach, FL 33413), used in their thickness resonance mode. The receiver transducers are 39.75mm, 43.87mm and 46.7mm away from the emitter transducers, respectively.

8.4.2 Experimental setup

Figure 8-12 shows a typical configuration used, highlighting the order of events during each measurement conducted. The general working principle of the electronic equipment used is outlined in §3.1.

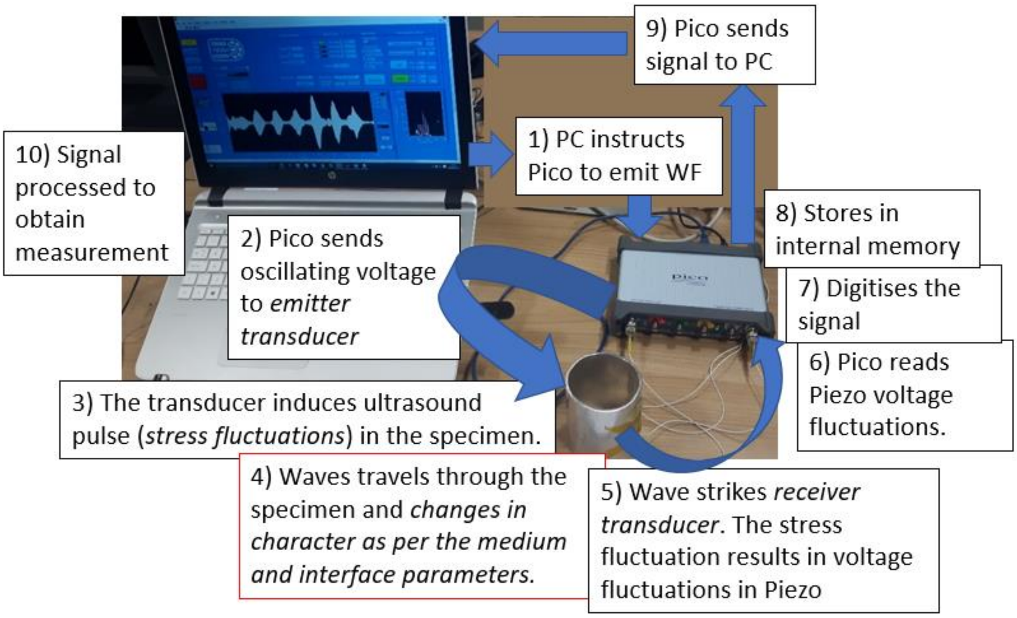

Figure 8-12: Photographs of the cast iron liner specimen used for surface wave velocity calibration as a function of the temperature.

8.4.2.1 Temperature Calibration of Velocity

A Memmert UF55Plus programmable oven or Gallenkamp hotbox oven were used to heat the specimen in the experiments where required. A PT100 RTD (class A) was used to measure the temperature from the specimen, while a NI-9217 DAQ was used to supply the input voltage and measure the resistance change within the RTD, resultant of temperature change. Temperature readings at the time of each ultrasonic measurement were taken. Figure 8-13 shows a photograph of a temperature calibration experiment with the equipment used for the experiment shown.

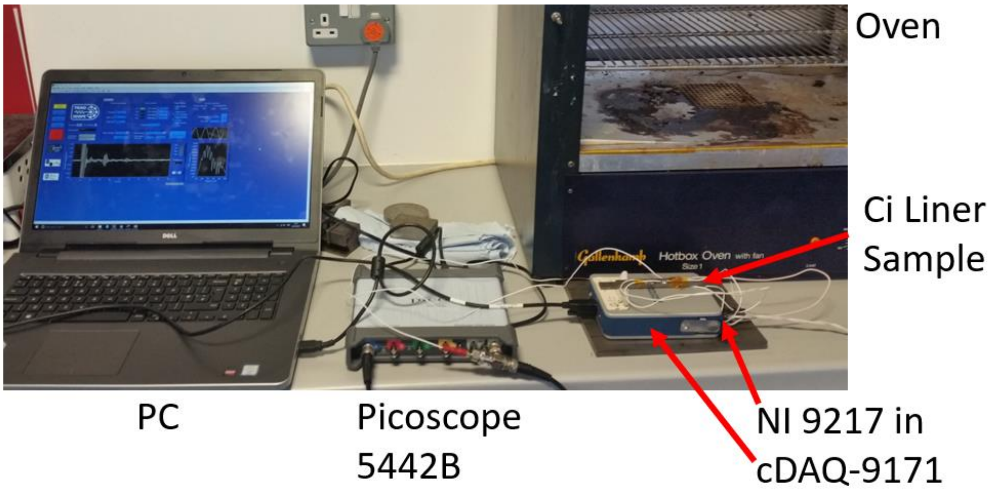

Figure 8-13: Photograph of a typical temperature calibration experiment with the key components shown.

8.4.2.2 Impact of Temperature Variation

The impact of varying temperature along the wave path of surface wave and its impact on measured distance and change in distance were investigated. Experiments were conducted with the specimen (configuration as shown in Figure 8-10) heated inside an oven to around 150°C, then taken out and one of its ends dipped inside the water (to act as heat sink) at 20°C. See Figure 8-14.

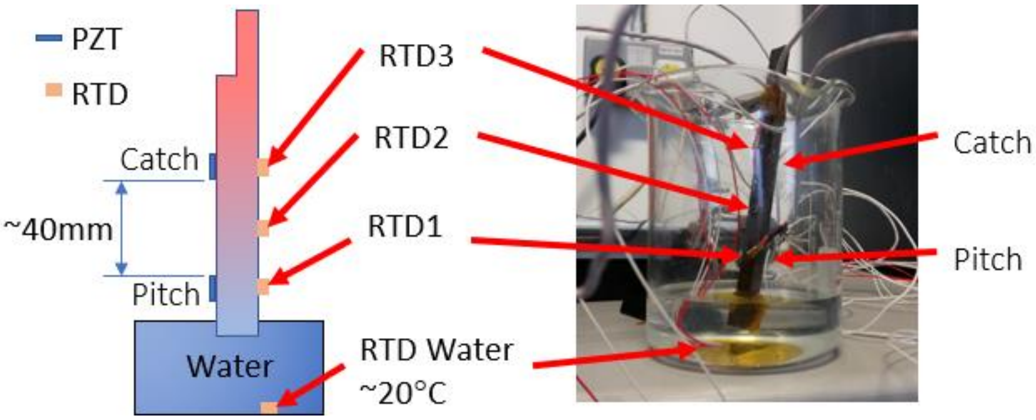

Figure 8-14: Experimental schematic (LHS) and a photograph (RHS), showing the CILS dipped in water at one end and held standing by crocodile clip at the other end, after just being heated in an oven to 150°C. Setup used to study the impact of varying temperature along the path of surface wave on the distance it measures.

8.5 Methods for Obtaining Measurement from Acquired Waveform

8.5.1 Bulk waves

Figure 8-15 shows waveform acquired from temperature calibration of the BAW - longitudinal mode, for 25°C and for 180°C.

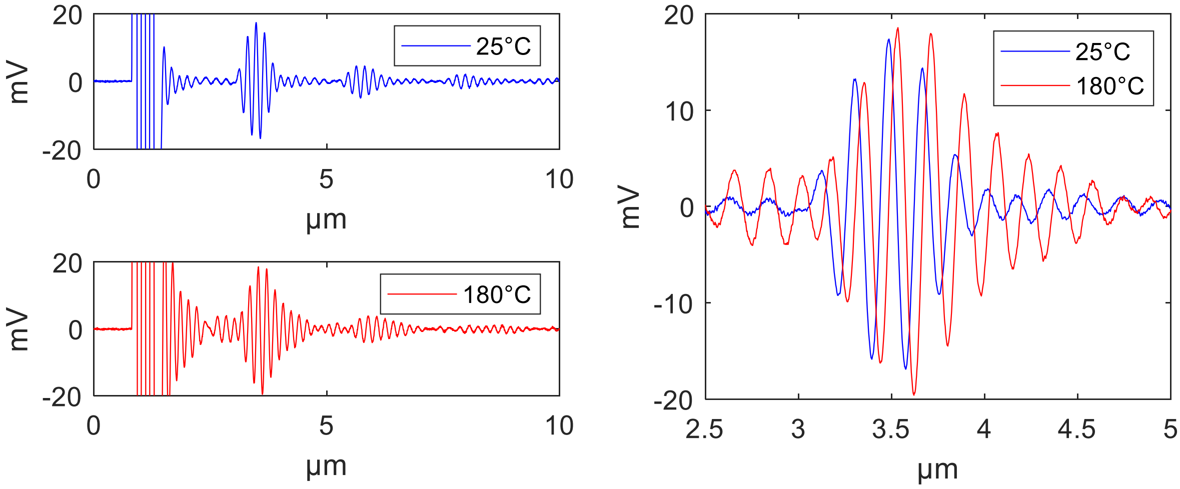

Figure 8-15: Typical waveform acquired form experiments where bulk waves (through thickness wave modes) were used to study the impact of either the temperature or stress variations.

The waveform contains a greater amount of ringing with increase in temperature, most likely due to the change in wave velocity, impedances, bond layer and thickness of the piezoceramic, the solder used to bond the cable terminals (Tanaka *et al.*, 2005), which all determines the input impedance as seen by the cast iron sample, see Equation 75 and Equation 76.

Thus, to minimise the impact of wave distortion, only the time window containing the first two echoes were correlated to find the TOF. See §7.4.1.

8.5.2 Surface waves

The PZ27 transducer used for generating surface waves also generated various other wave modes, thus it was first necessary to identify the surface wave component to use for measurement. The method of identification included pressing down on the surface along the wave path with a thumb and studying the impact of the loading on the waveform in the oscilloscope (i.e. Picoscope acquired signal displayed in the PC). The impact of loading is shown in Figure 8-16.

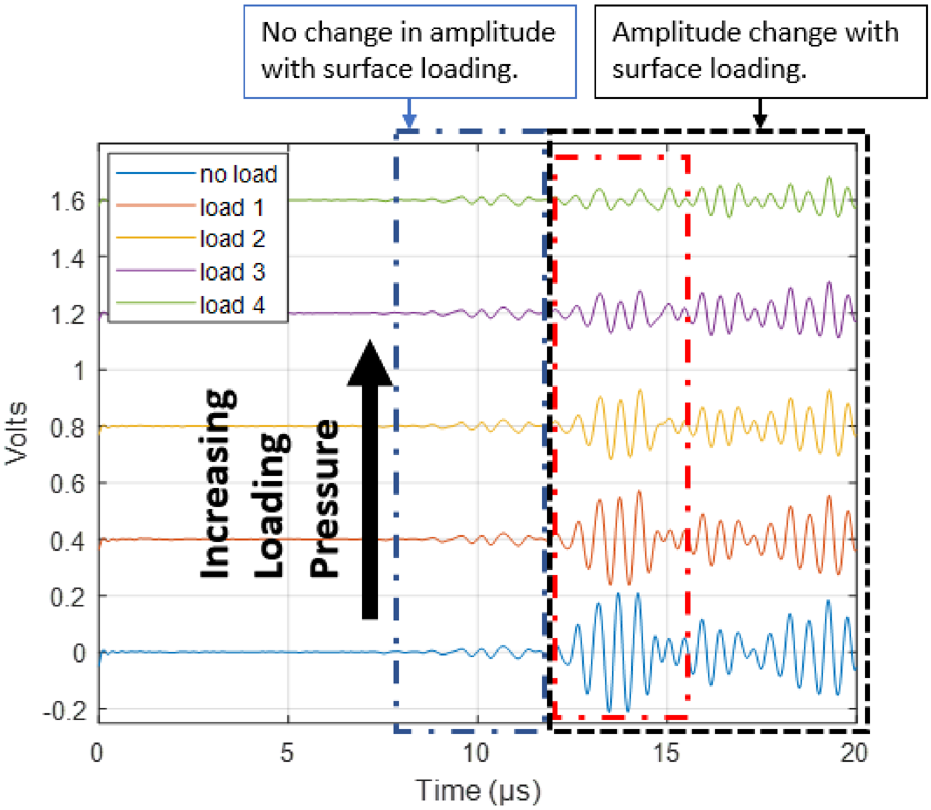

Figure 8-16: Identification of guided wave packet to use for measurement. Portion in red box corresponds to the first arrival whilst others correspond to various reflections of the edges.

Once the region corresponding to the surface wave was identified, it was seen necessary to identify the exact time of wave arrival (also known as the TOF). For the first experiment the TOF wave was obtained by correlating the acquired waveform with itself. See Figure 8-17.

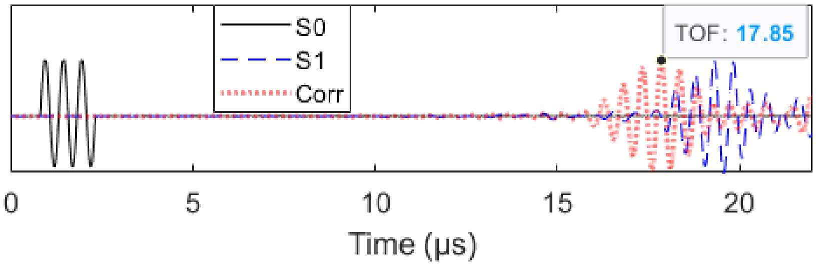

Figure 8-17: Correlation method used for finding the time of flight between the emitter transducer (S0) to receiver transducer (S1).

The TOF for the subsequent waveforms were obtained by employing an axis tracking algorithm, thus were relative change with reference to the first TOF. This was found to give lower standard deviation in the measured TOF when compared to a linear fit.

8.5.3 TOF to Velocity

The coefficient of thermal expansion (CTE) of the cast iron liner specimen was experimentally measured by studying the expansion of a 10mm nominal thickness cast iron liner specimen, using a Differential Mechanical Analyser[1] (DMA). Figure 8-18 shows the results from the DMA and the theoretical thickness of a 5mm section while being heated from 25°C to 180°C.

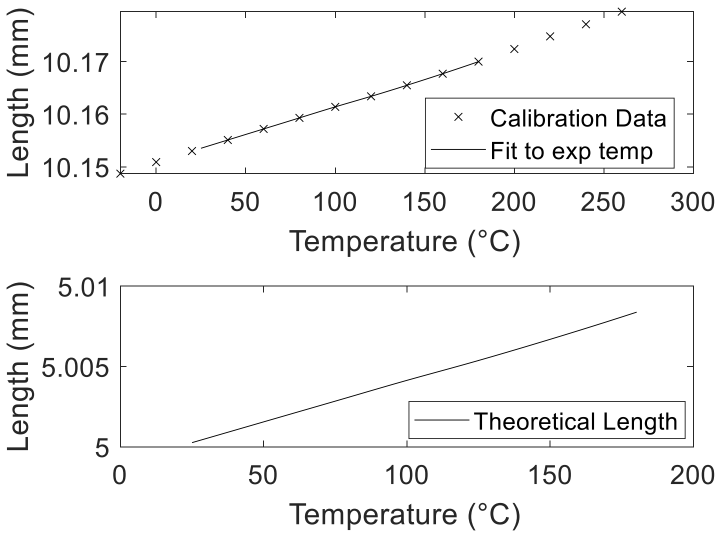

Figure 8-18: Theoretical thickness of the cast iron liner specimen as a function of the measured temperature. (Top) Curve fitting of calibration data to experimentally recorded temperature. (Bottom) Fitted curve rescaled to obtain theoretical thickness.

The temperature, T_i reading from the RTD, the TOF_i measurement from ultrasound, and the length, $L_i(T_i)$ of the wave path (predicted form DMA calibration as a function of RTD *local temperature*) were used to find the wave propagation velocities. Figure 8-19 shows the concept. The aim of the method was to calibrate for the velocity.

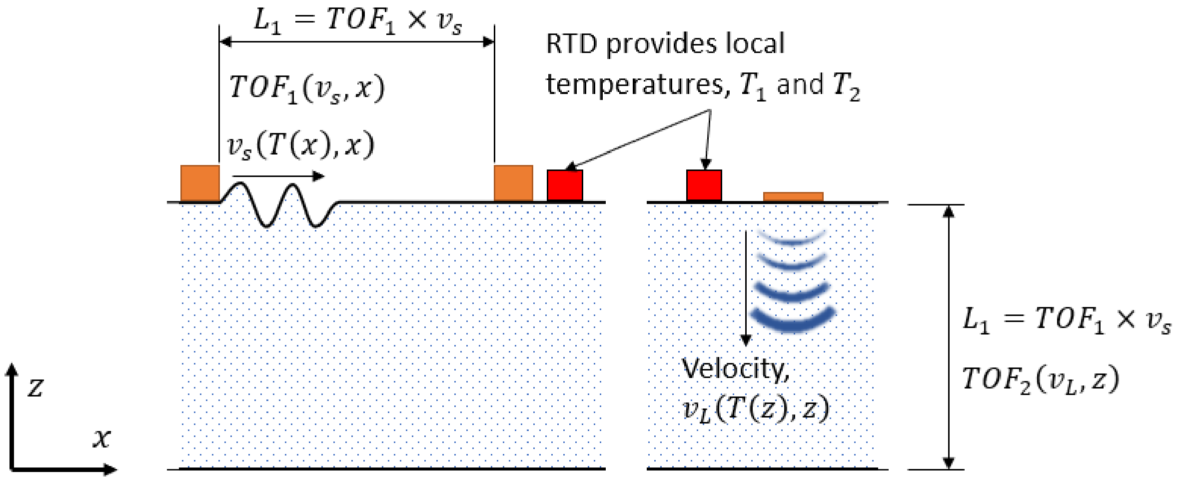

Figure 8-19: Through thickness temperature variation study. While the temperatures are presented as scaler value at the wave path, they are functions of heat diffusion in *all* directions.

8.5.4 Measurement of the Length of Wave Path

The results from the velocity calibration, the temperature reading and the TOF can be used to find the length of the wave path.

---

[1] Calibration performed by Jaguar & Land Rover Materials Engineering Gaydon Laboratory, and data supplied to the author.

8.6 Results

The impact of through thickness temperature variation was evident during the study intended for velocity temperature calibration. The test was conducted using bulk longitudinal wave, however given the only varying parameter is the temperature, similar is expected for shear waves. Figure 8-20 shows the outcome of velocity measurements as a function of the temperature and the theoretical length.

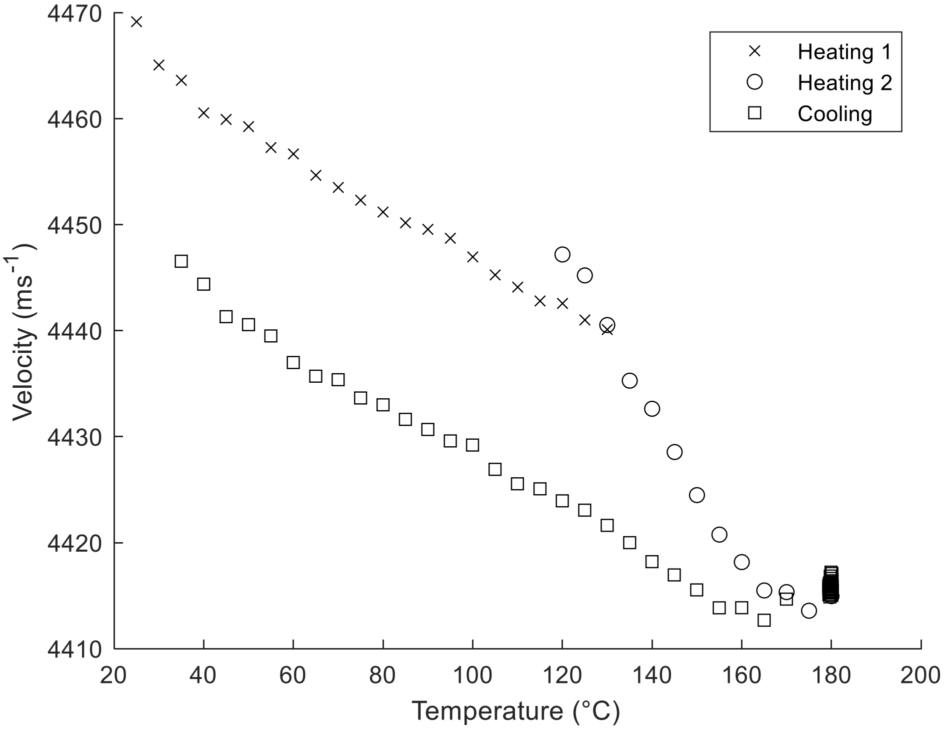

Figure 8-20: Predicted longitudinal wave velocity assuming the temperature distribution is constant along the 5mm cross-section. *Heating 1* corresponds to slower rate of temperature rise in comparison to *Heating 2*.

A difference of around $20ms^{-1}$is observed, which would lead to errors in the range of 0.4-0.5% of total thickness. The error is mainly attributed to the assumption that through thickness temperature profile is constant, which unfortunately is not the case. Other sources of error were most likely due to varying rate of attenuation of different frequency content, other sources such as phase distortions as discussed in §8.3, and changes in phase distortions as outlined in §8.5.1. Figure 8-21 show a plot of measured velocity difference between the heating and the cooling cycles.

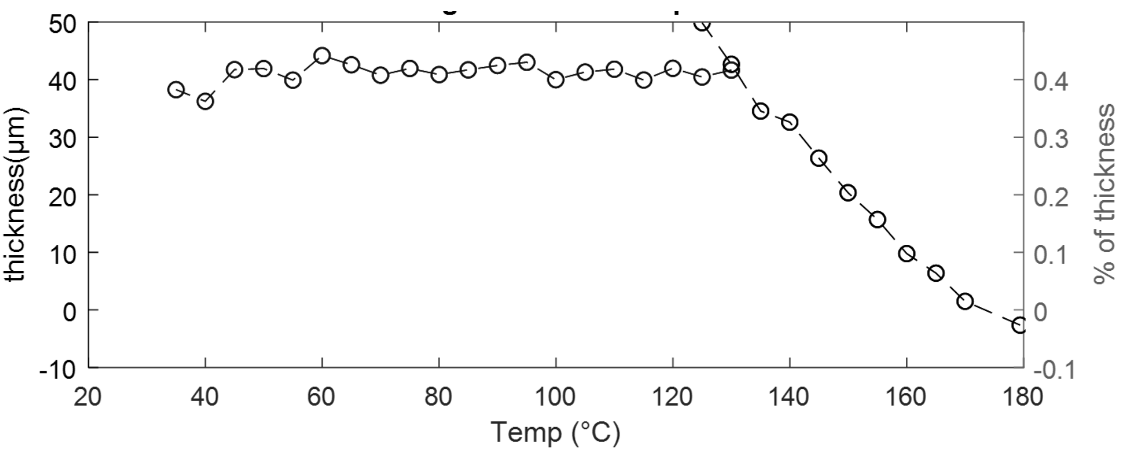

Figure 8-21: Error in thickness measurement if the through thickness temperature distribution were assumed to be uniform.

Therefore, the outcome of the experiment suggests that measuring the temperature on the surface alone would most likely result in significant measurement uncertainties, if only one mode of bulk acoustic wave is used for studying bore distortion as a function of changing thickness.

There is however literature on the use of ultrasonic waves to study the 2D internal temperature distribution within isotropic component. Wadley et al. (1986) have used a tomography type setup to perform temperature distribution measurement of cylindrical and square cross-sectioned metal blocks, up to ~700°C±20°C (reference temperature measured using thermocouple). The authors solve the nonlinear regression problem (least square error minimisation) between measured and predicted TOF. The convergence of the problem is based on knowing accurately the wave propagation velocity as a function of the temperature; the velocity is assumed as being independent of the frequency; and it is assumed the rate of change of the temperature profile through the wave path is relatively slow, such that the prediction of one-time step is valid for the next. Similarly, Ihara and Takahashi (2007), Takahashi and Ihara (2008b, 2008a) measure a 1D temperature distribution using one ultrasonic probe. More recently Wei et al. (2020) have shown an accurate measurement of the internal temperature distribution within a metal specimen is possible by employing multiple transducers measuring the change in the magnitude and direction (changing refractive index with through thickness temperature variation) of the wave velocity. However, the impact of stress variation and distortion due to thermal expansion have not been considered. The present author has found the impact of temperature variations on the wave propagation velocity of longitudinal bulk wave to be ~56ppm, while the coefficient of thermal expansion results in change of thickness of ~10ppm, i.e. ~1/6th.

8.6.1 Temperature Calibration of Surface Wave Velocity

Figure 8-22 shows the outcome of a velocity calibration experimental set. Comparing this to the longitudinal wave in Figure 8-20 it can be seen the measurement error is lower between heating up and cooling. Figure 8-23 shows the results of 8 experiments. The mean value for 3 standard deviations, $\sigma_{3SDV} = 2.776\text{ms}^{-1}$. The equation shown in Figure 8-23 can be used to find the velocity of surface waves.

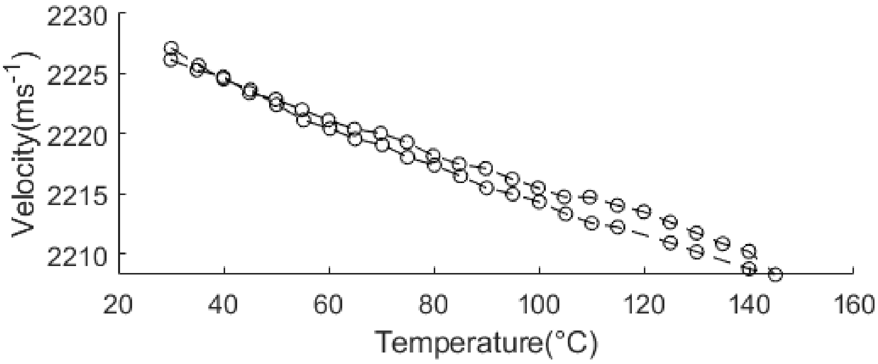

Figure 8-22: Surface wave velocity calibration from one experiment.

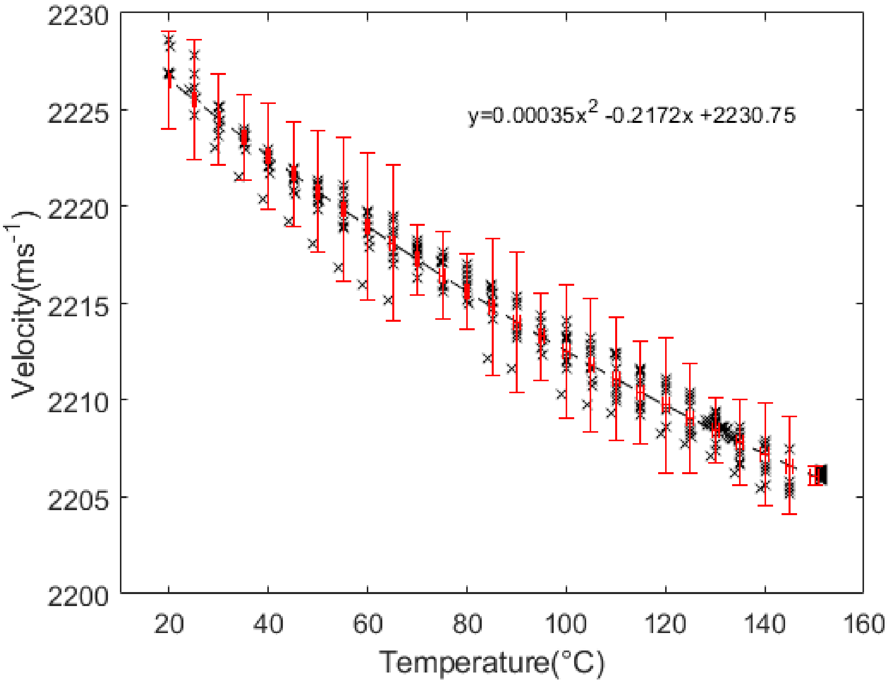

Figure 8-23: Surface wave velocity calibration of CI liner specimen with emit and receive transducers spaced ~40mm apart. Error bars represent 3 standard deviations. Crosses represent the experimental set while the curve is a Least Square Error (LSE) fit of a second order polynomial.

The velocity was found to be different when the transducers were bonded at different locations. Figure 8-24 shows a calibration run conducted with pitch and catch transducers bonded 25.25mm apart.

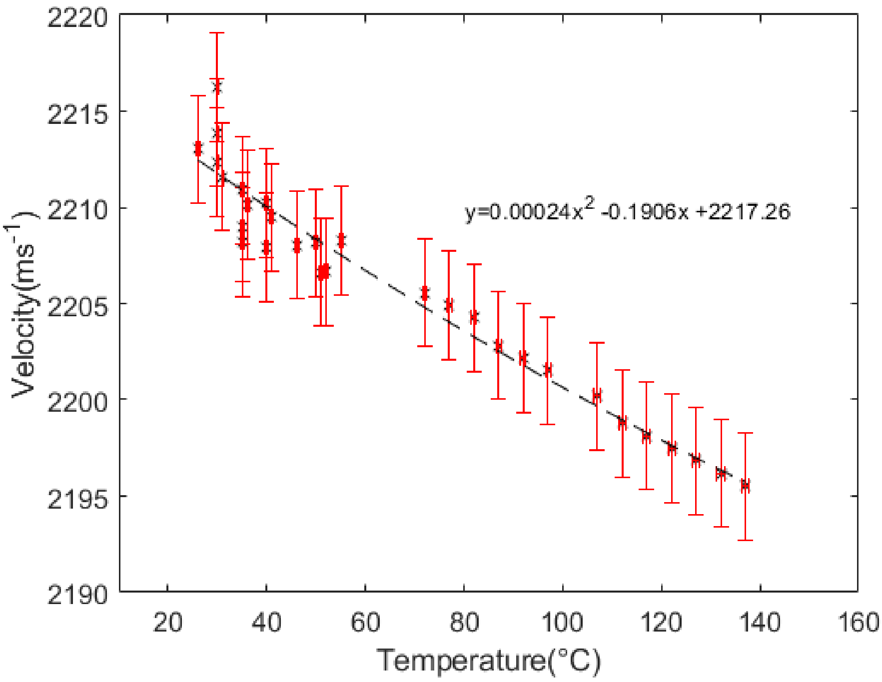

Figure 8-24: Velocity Calibration with *pitch* and *catch* transducers bonded 25.25±0.032mm apart. The error bars are the measurement uncertainty in the reference distance measurement.

Comparing the two calibration figures, reproducibility of the results had ~±15m/s variation in the mean while repeatability was within ±10m/s. Reproducibility error is likely due to human error in reproducing the bond characteristics between the transducer and the substrate, as well as a different error in measuring the initial reference distance. The cast iron material also exhibits a high degree of anisotropy which would contribute to further errors in reproducibility. Repeatability error is attributed to the changing bond characteristics with changing temperature, and the variations in temperature along the wave path. Linearity error is most likely due to wave distortion at the interface. However, linearity is not expected in wave propagation velocity as such an assumption would lead to negative velocity past a certain temperature. Thus, linearity error is assumed to be the same as that of the statical error.

8.6.2 Effect of Temperature Variation Along the Surface Wave Propagation Path

Figure 8-25 presents the outcome of an experiment conducted to measure the wave path length with varying temperature. The temperature distribution measured using the 3 RTD was interpolated using a quadratic function fit then converted to velocity, referring to the presented calibration in Figure 8-23.

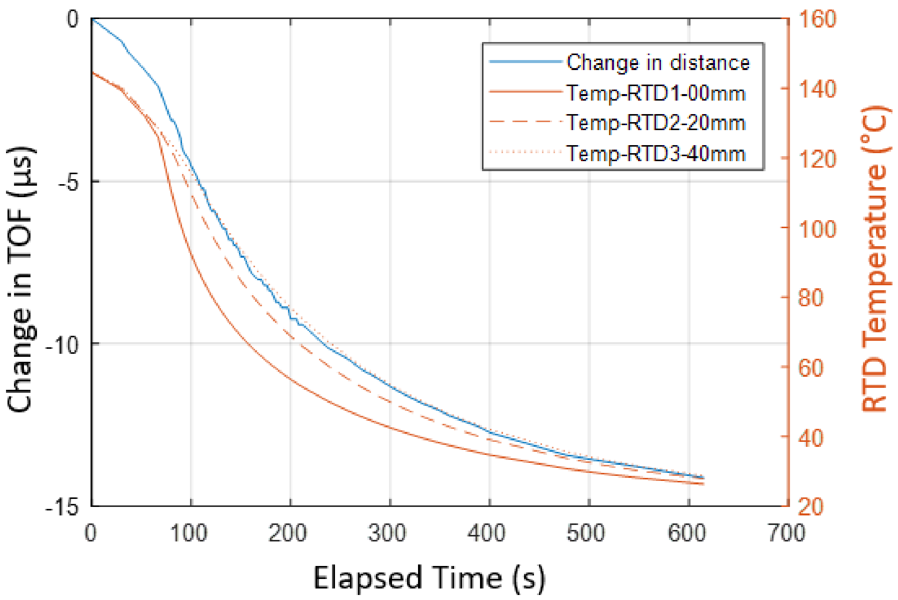

Figure 8-25: Outcome of the study to measure the length of the wave path with varying temperature along the path. Experimental setup presented is presented in Figure 8-14.

Figure 8-25 shows that the change in surface temperature measured using the temperature sensors is reflected in the TOF measurement using one pitch and one catch ultrasonic transducer. While the exact accuracy of the results was not evaluated, it showed the possibility of use a combination of temperature sensors with surface wave ultrasonic transducers TOF measurement using surface waves to find the *true* length of the wave path, in an environment such as an engine. This shows that expansion/contraction of the liner that is attributed to the change in temperature can be subtracted out if the surface temperature is measured using RTD sensors.

8.6.3 One Pitch Three Catch

Figure 8-26 shows waveforms acquired from a one pitch three catch transducer setup, while the specimen was heated from 35°C to 180°C. A the relative change in TOF was obtained for each transducer by using an axis crossing tracking algorithm. Figure 8-27 shows the axis crossing algorithm being employed, while Figure 8-29 shows the tracked change in TOF.

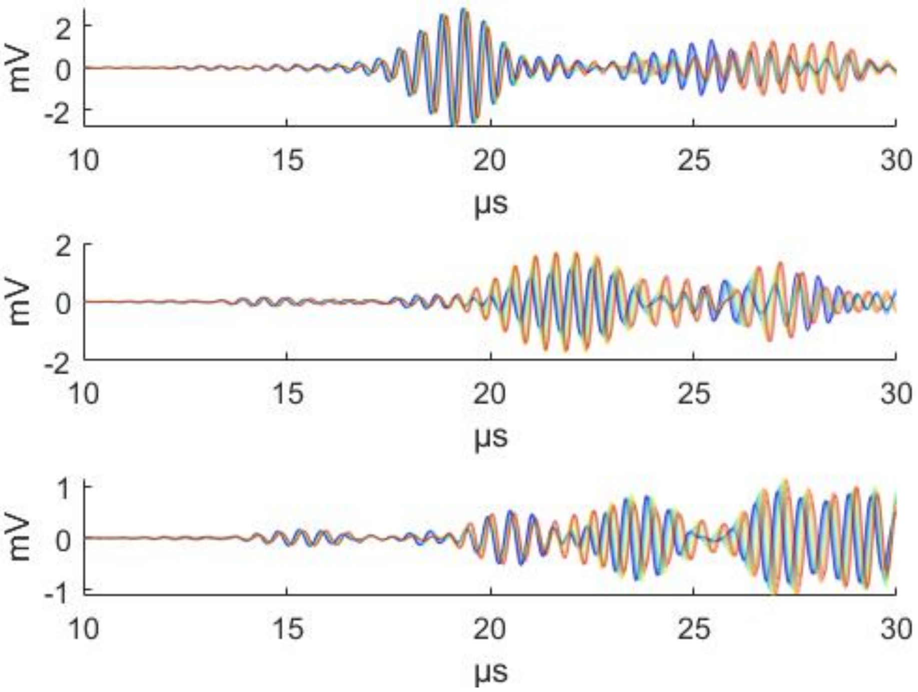

Figure 8-26: Waveforms gathered from 1pitch 3 catch setup. Waveforms in blue are of 20°C while those in red are of 180°C, and those in between are a linear interpolation following the *jet* colour scheme in MATLAB®.

Figure 8-26 shows that the first catch transducer receives a signal with minimal distortion, while due to the obstruction in the wave path from the placement of transducers in the wave path, the second and the third catch transducer receive signals that are higher in distortion — thus the third catch transducer saw the highest wave distortion. The distortions are due to the superposition of waves travelling directly to the receiver transducer with waves that are diffracted as they travelled through the bond interface while travelling under other transducers on the wave path. Nonetheless in all three catch transducers the waveform corresponding to the received signal is prominent enough to use them for distance measurement or change in distance measurement.

While the TOF is seen to increase with increasing temperature, the impact on the amplitude varies for the three receiver transducers. This is most likely due to the varying change in attenuation coefficient as the wave travels through the bond interface (between the transducer and the cast iron specimen).

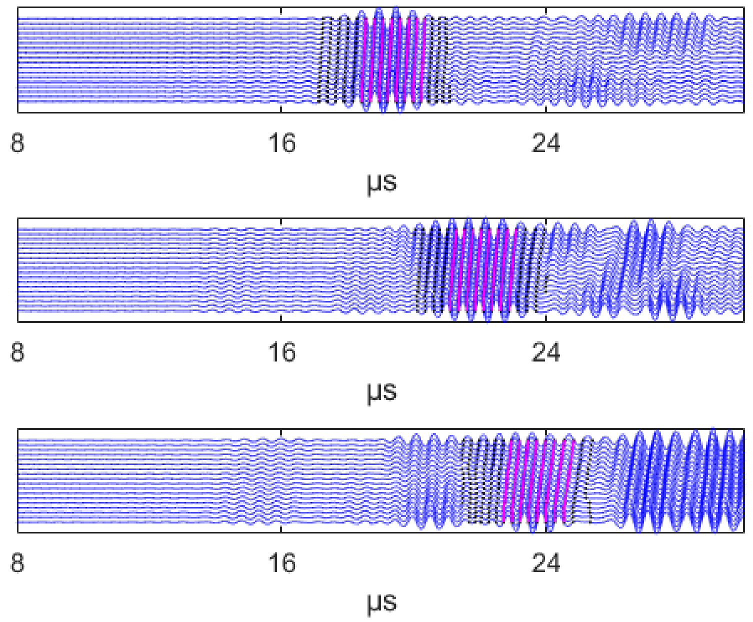

Figure 8-27: Axis tracking algorithm employed to track the change in TOF/ Pink lines show the tracked crossings. The tracked axis crossings were 3 crossings either side of the locations of maximum correlation.

Figure 8-27 shows the use of an axis tracking algorithm to track the TOF and its change as the temperature changes, for the waveform collected using the three receiver transducers. Figure 8-28 shows the wave arrival time (TOF) from the emitter transducer to the three receiver transducers, S1, S2 and S3, respectively.

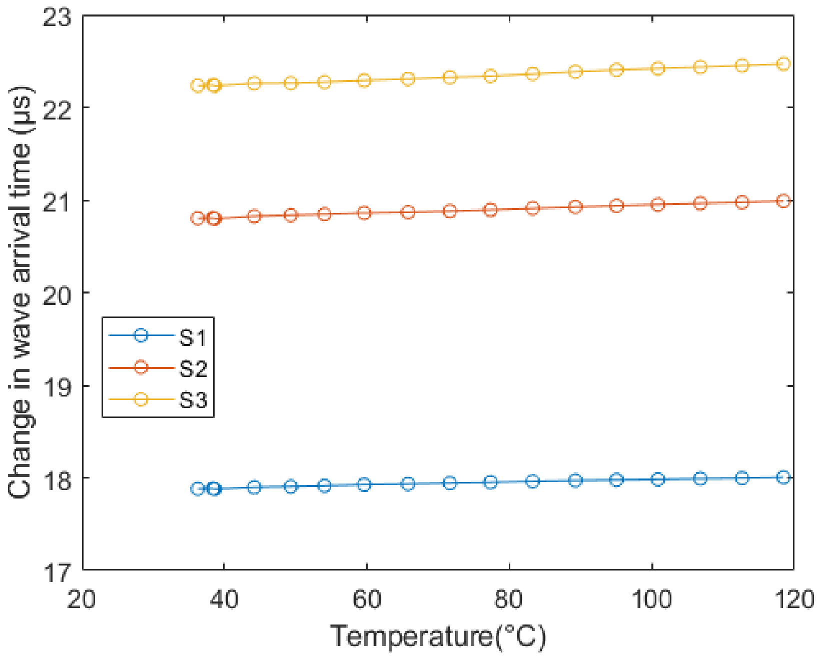

Figure 8-28: Temperature vs change in arrival time of the wave. Distance of receiver transducer from emitter transducer at 2.55°C: S1= 39.75mm, S2= 43.87mm and S3 = 46.7mm.

Figure 8-28 shows the TOF measurements change linearly with changing temperature. The average of the crossings tracked in Figure 8-27 were used to obtain the difference in TOF measurement presented in Figure 8-29.

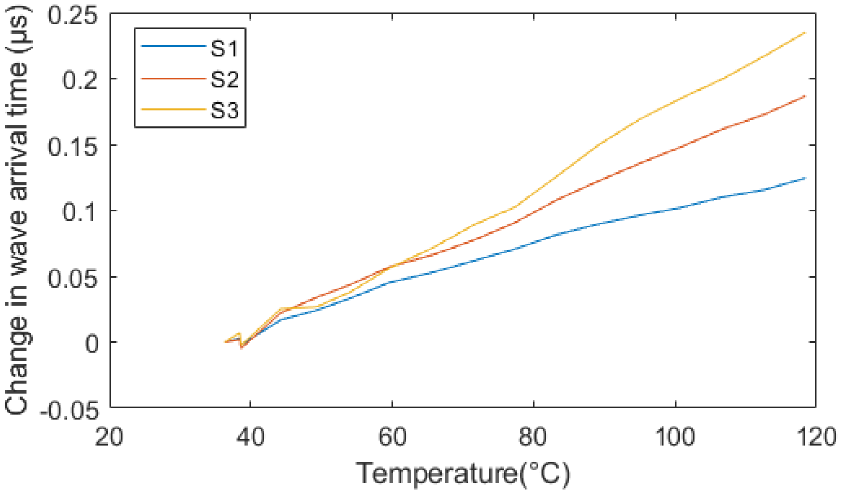

Figure 8-29: Relative change in arrival time of the ultrasonic pulse of the three receiver transducers in Figure 8-10.

The wave arrival time (TOF) shown in Figure 8-29 shows that with increasing temperature the wave arrival time also increases, due to the thermal expansion of the specimen as well as reduction in wave propagation velocity. The measurement made using the third transducer is shown to be susceptible to greater error, likely due to the 2 receive transducers in front of it which obstruct the wave path.

Figure 8-30 shows the gathered data converted to velocity measurement using the theoretical length based on the measured temperature and TOF.

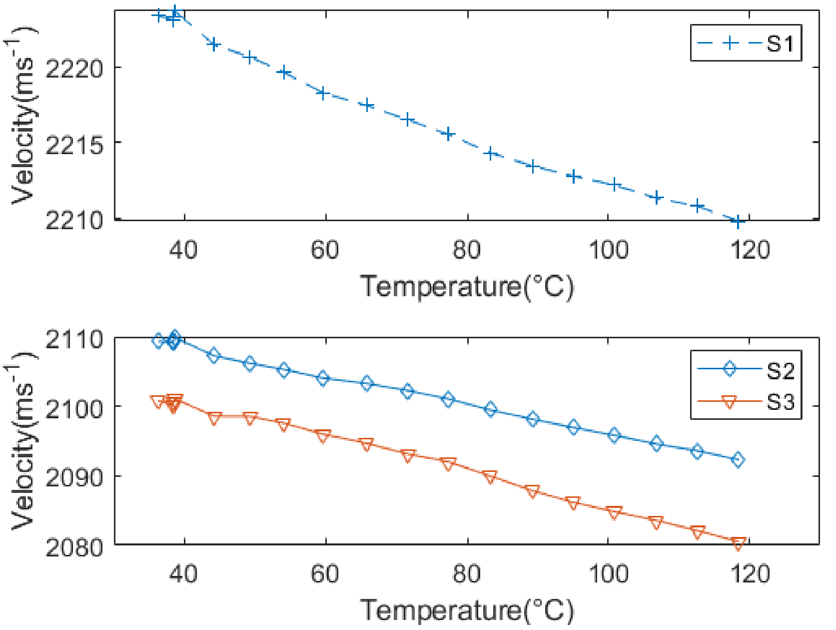

Figure 8-30: Velocity measured using S2 and S3 transducers in Figure 8-10.

It can be seen that the velocity measured by the second and the third transducers are lower. This was likely because the surface wave while travelling through the boundary interface (i.e. adhesive) propagated as an interface wave (Stoneley wave), travelling at different wave velocity (Claus and Kline, 1979). The condition for existence of an interface wave such as a Stoneley wave is that the material constants for the two bonded media must be "suitably related".

Stoneley waves are sensitive to the properties of the bond and have been used to study interfaces properties e.g. by Jahanbin (2021).

The following observations are made from the results:

1. Locally measuring the temperature at the location of receiver transducers (that are within a few millimetres of each other) can account for the change in wave velocities as a function of temperature in all three probes.
2. The effect of the bond layer on the propagation velocity of the wave propagating through it with changing temperature, is linear.
3. With all the velocities a linear function of the temperature, the relative change in TOF that was obtained in the results presented can just be subtracted from the results of an actual measurement. The distortion (coupled with stress effects) would be the difference that remains.

The ability of the surface waves to propagate through the bond interface suggests an improvement to the presented method is possible. The wave propagation path could be protected using a thin layer of adhesive to make it suitable for use in an environment where water or other path contaminating material is present. This is elaborated in the further work section.

While not covered at present, ultrasonic surface waves are known to exhibit change in wave velocity depending on the direction of stress application relative to direction of propagation (Thomas Mase and Johnson, 1987). Thus, with proper calibration methods and smart placement of sensors, surface acoustic waves could be made more sensitive to distortion, while the impact of temperature is mitigated with the method that was presented.

8.7 Conclusions

Impact on the wave propagation velocity due to rapidly changing temperature was evaluated for bulk longitudinal wave (BAW) and for surface/interface waves. The method utilised bare piezoceramic transducer elements bonded on the surface of a *bar specimen* cut from a cast iron cylinder liner.

The impact of through thickness temperature variation of the liner, on BAW, was found to be significant enough to make using it to measure bore distortion, to the high accuracy declared, a challenging task.

A method for generating and detecting SAW using piezoceramic transducers on cast iron liner material was found. The method was found to give linearity and repeatability within ~0.2% with varying temperature. While the reproducibility was found to have higher error, the problem could be averted by performing local temperature calibration, or by improving the repeatability of the transducer gauging process.

Surface waves showed a distinct advantage over bulk waves when operating in an environment with rapidly changing temperature, due to better predictability of the temperature along the wave propagation path by physical measurement.

A method was proposed where one transducer emits a pulse, and 3 transducers receive simultaneously, while a local RTD records the temperature local to the 3 receiver transducers.

While the viability of using surface waves has been investigated, the investigation into the capacity of the method can only be investigated in a fired engine; such tests are left for the future.

9 Conclusions

The goal of engine manufacturers has long been to minimise the distortion of cylinder liner bores, which is a leading cause of conformability issues between piston ring and liner wall. Potential for the use of ultrasonic waves to measure the bore form during honing manufacturing, and the use of ultrasonic waves to measure bore distortion, namely that of overcoming the temperature effects, were investigated.

The work presented within the thesis has shown ultrasound to be viable method of measuring cylinder liner bore form in honing machines, to and accuracy of ±3.5μm, improving on the current measurement system which has an accuracy of ±10μm. Combining surface acoustic waves, produced using PZT transducers, and temperature measurement taken using RTD sensors was found to be a suitable method in measuring in-situ cylinder liner bore distortion.

This chapter draws the conclusions from all the previous experimental chapters.

9.1 Air Coupled Sensor Design

Commercially available air coupled ultrasonic sensors were found to be outside the price range for a feasibility study into the use of ultrasonic sensors to measure bore form during honing. The literature pointed to the possibility of using material commonly available in the lab to manufacture a low MHz air-coupled probe. Thus, a probe working in the MHz region was designed. The probe design consisted of:

1. Araldite and tungsten backing material to minimise reverberations and widen the bandwidth of the probe.
2. An outer matching layer of nylon membrane filters to bridge the gap of acoustic impedance mismatch.
3. Intermediate matching layer to widen the bandwidth of the probe.
4. 3D printed casing.

Steps required in manufacturing the probe were outlined. Method for the use of low viscosity adhesive as an intermediate matching layer was outlined. Heating the adhesive to the point of near complete solidification was found to be a suitable method of bonding the filtration membrane.

It was found difficult to control resonant frequency of the probe; the probe's resonant frequency varied from 0.9MHz to 1.4MHz. This was most likely due to the variability in the thickness of the matching layers.

The proposed probe design had a cost of under £20GBP if components to manufacture it are derived from an existing material stock bought for other uses, or if the probes are manufactured in bulk quantity.

The Bandwidth of the probe was found to be around 20% and the insertion loss was found to be around 74dB. The insertion loss is around 44dB higher than that reported by other authors – most likely due to the use of backing material and low thickness control of the intermediate matching layer. However, a direct comparison was not possible as the other authors used steady state measurements by exciting the probe with many cycles, while at present the probes were excited by only 5-10 cycles.

9.2 Sensor design evaluation using KLM model

KLM model was subsequently used to study the intermediate layer parameters which could have resulted in the high insertion loss observed. The study investigated the effects of varying thickness, impedance, and attenuation of intermediate matching layers.

Varying the intermediate layer thickness was found to affect the resonant characteristics. A change of 50% from quarter wave resonant thickness resulted in the probe losses being significant. The thickness control requirement for the intermediate layer was found to be more stringent than reported in the literature.

Lower impedances favoured lower frequency, most likely due to lower attenuation at lower frequency. However, impedance of the intermediate layer was not found to significantly affect the resonant characteristics of the probe model, provided the probe was excited at the resonant frequency of the intermediate layer.

The model showed that the attenuation coefficient of the intermediate matching layer likely does not impact the probe response when it is low compared to other modes of attenuation; other modes are likely to be dominant. However, increasing the attenuation coefficient past a certain point caused rapid attenuation as the attenuation within the layer became the dominant mode. As the attenuation coefficient raised past this point, the increase in attenuation was exponential. The probe model showed this limit to be around 0.14Np per thickness of the layer for 1MHz probes. Similar modes of reasoning will likely apply for the outer matching layer as well.

9.3 Sensor Evaluation

The 1.4MHz probe manufactured was analysed to see its performance in range/distance measurement applications.

A review of the literature on air-coupled measurement showed air temperature would be the dominant mode of measurement error if the temperature is not accounted for. When the probe was used to measure a distance of 10mm, assuming the variation in temperature to be within ±0.15°C, the measurement error due to change in temperature was found likely to be limited to ±2.5μm in the literature.

A bench top rig was designed and manufactured by adapting a stage micrometer onto a bespoke vertical stand to conduct the range measurement accuracy experiments.

The obtained data was found to give lower variance for when axis crossing between two subsequent echo was used to measure TOF. Thus, the axis-crossing method was adapted in the final precision evaluation and it was found that the probe measured to 10mm distance with an accuracy of ±2.2μm microns when used to measure the distance from itself to a flat surface reflector, and ±3.2μm when the reflector was curved (radius = 41.5mm). Adding these to the effect of potential error in temperature measurement, the accuracy of the measurement system was found to be ±3.35μm and ±4.07μm, respectively.

9.4 Bore Form Measurement

The capability of the 1.4MHz probe for use in cylinder liner bore form measurement during honing was evaluated using a bespoke rig. A semi-automatic axis-crossing detecting algorithm was employed to obtain the relative change in the inner bore form of the cylinder.

The rig was found to result in various measurement errors due to misalignment of the cylinder liner and the spindle that the sensor is mounted on. Methods used in correcting the misalignment error were presented.

The probes were found to perform bore form measurement to within ±3.48μm for spindle speeds of up to 60RPM and ±3.79μm while the rig was running to 200RPM. Accounting for measurement uncertainty in temperature measurement of ±0.15 °C, the resulting error in velocity used would cause errors of ±4.30μm and ±4.55μm, respectively.

While the correction for relative shift in the spinning axis compared to cylinder axis is seen as insignificant, the correction of the relative tilt of the axes by removing second order distortion from both the ultrasound and reference CMM data was not likely the greatest limitation to the rig used.

Another factor not accounted for was the error associated with not knowing the temperature of the bore surface during honing. This may potentially pose the most significant challenge. At present such work is left for the future, and an alternative method to mitigate against errors resulting from the rig used is presented in Chapter 10.

9.5 Bore Distortion Measurement

A review of the literature on current bore distortion measurement tools found them to be limited in their accuracy due to uncertainties associated with knowing the exact position of the piston onto which the sensors are mounted. A study of textbooks on engine parameters meanwhile highlighted the high variability in through thickness temperatures of the liner.

Thus, an investigation into the suitability of using through thickness longitudinal and surface waves was carried out. The through thickness measurement of velocity was found to contain errors in the range of 20ms^{-1} between the heating and cooling cycles, due to variation in through thickness temperature during the heating and cooling cycles even when the temperature sensor measured the same temperature. The temperature calibration of the surface wave was found to result in 3 standard deviations error, $\sigma_{3SDV} = 10\text{ms}^{-1}$. Thus, surface waves were found to minimise measurement uncertainties due to temperature change compared to bulk longitudinal waves.

The effect of fast varying surface temperature on distance measurement made using ultrasonic surface waves was evaluated. With the mean wave velocity corrected for by local temperature measurements, the TOF reading was converted into measurement of the distance between the pulsing and receiving probes. The measured change in distance between the transducer with cooling was found to mimic the measured temperature profile. This showed the credibility of combining ultrasonic sensors and temperature sensors to measure bore distortions, while minimising the impact of temperature variations.

A method where one transducer sent out a pulse and 3 others received the transmitted pulse, with changing temperature of the liner medium propagating the waves, was presented. It was found necessary to consider the slowing of the wave as it propagated under a receiver transducer (as interface/Stoneley wave) while travelling to the next in line receiver. The method still displayed good linearity with changing temperature, and therefore can most likely be adapted to the environment of an engine to perform bore distortion measurement whilst being able to mitigate against the effects of changing temperature.

10 Future Work

From the various feasibility studies conducted, it was expected to obtain some key findings while also leaving some avenues of work for the future. This section presents the various avenues of research that the present author assumes to be relevant to the work presented within the thesis.

10.1 Sensor Design

While the transducer was found suitable for the application requirement at present, the effect of lack of thickness control of the intermediate layers was found to cause significant issues.

10.1.1 Intermediate Layer

The outcome of studying the transducer design with varying intermediate layer parameters using the KLM model had shown a requirement for an improvement in thickness control of the intermediate layer.

The probe design had utilised 3D printed PLA, which has a tolerance of ±0.1mm, for the casing. It is assumed that by replacing the 3D manufactured cap component with one that is machined from a metal would result in better thickness control. Given such a cap would be reusable, this would likely not add significantly to the cost of the probe.

An alternative solution could be to use a different intermediate matching layer with higher thickness control and low loss, such as 0.45mm polypropylene or other material such as a Perspex sheet of set thickness. Authors such as Desilets et al. (1978) point out that using a quarter wave resonant layer of higher impedance would not significantly lower the probe transmission. This was also observed from the KLM model of the probe.

10.1.2 Electrical Tuning

While the study into the transmission line model was carried out in hindsight, it highlighted the benefit of combining all the probe material parameters and presenting them in terms of input impedance. Therefore, naturally the literature on the potential benefit of electrically turning the transducer was investigated. Silk (Silk, 1984, pp. 32–33) highlights a simple modification of the electronic circuit in the transducer by introduction of an inductor parallel to the capacitor for cases where load impedance is very high, shunting the clamped capacitance C_0 of the transducer. The resonant frequency of the modified probe is at $F_T = 1/[2\pi L C_0]$.

Probe tuning can be evaluated by adding a step after obtaining the input impedance of the transducer where lumped electrical components are added in parallel or series depending on their placement. Similarly, the two port network can also be used to evaluate the addition of various electronic component as shown, in Chapter 5

10.1.3 Waterproofing the Probe

Brekhovskikh (1960, p. 50) shows that plane waves incident to a $\lambda/2$ wavelength thick layer submerged in a lossless, infinite medium (e.g. steel plate submerged in water) has no impact on the transmitted wave. Lynnworth (1965) had shown the loss needs to be considered, but also highlighting that the use of thin membranes of higher acoustic impedance and low attenuation coefficient in front of the material does not drastically impact the performance of wave emitted by the probe. The theory was investigated using the KLM model, and the corresponding results is presented in Figure 10-1.

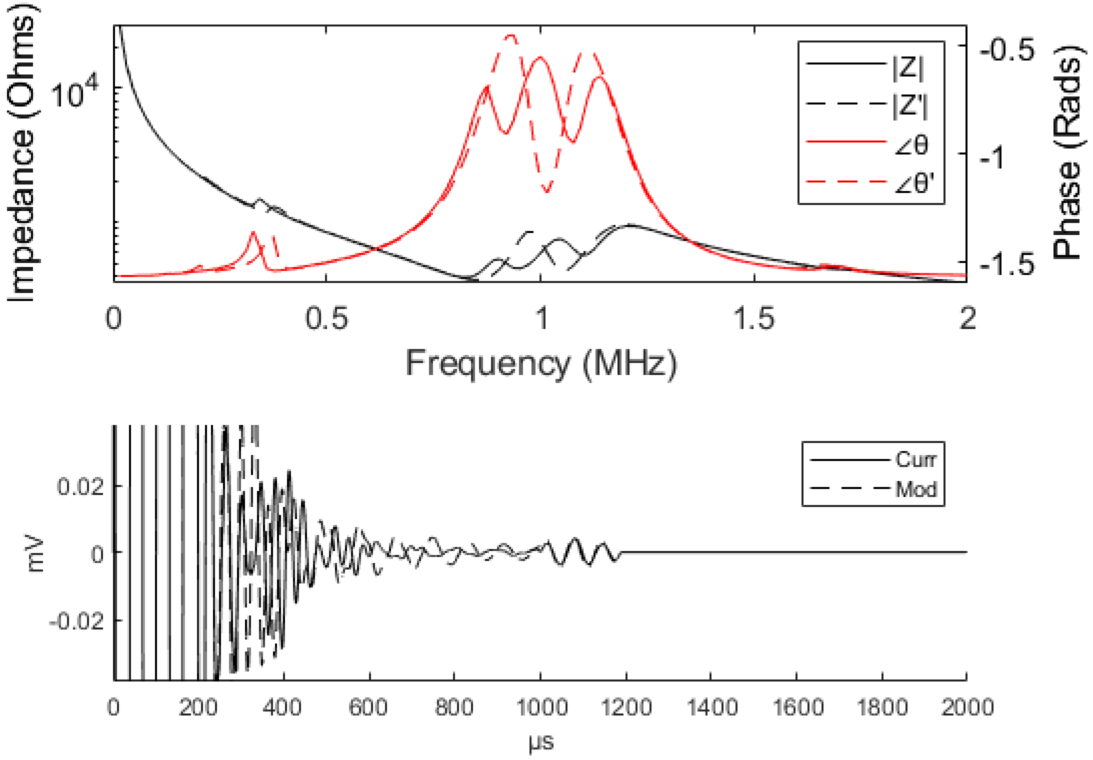

Figure 10-1: Modified probe impedance (Z') and phase($\angle\theta'$) with protective waterproof HDPE layer (v=1950m/s, ρ=920, α = 2.4dB, Z=1.79MRayls, thickness=0.3mm) in front of the outermost matching layer to make the probe design water resistant. This is compared to current design (Curr). Bottom plot shows the time domain response to 3 cycle sine waves.

The model shows that both the probe frequency and the probe bandwidth would change slightly. However, the impact on insertion loss seems minimal.

10.2 Sensor Evaluation

Whilst the accuracy of the probe was established, the impact of surface temperature variation of the reflector is left to be explored for future work. Hickling and Marin (1986) reported an error of 0.1mm for change in air temperature of 20°C while measuring the distance to a target that is 138.3mm away. It is likely the variability would be much lower for a target 10mm away (distance of the probe to inner surface of liner used in the bore form measurement rig).

10.3 Bore Form Measurement

One of the sources of error in measurement was found to be the rig itself and the accuracy to which it could be designed. It is assumed that some problems present in the rig at present, such as that the impact of turbulence (due to spinning tool head) may still be present.

Alvarez-Arenas and Diez (2017) show the possibility of using air coupled probes as endoscopes in industrial applications when measuring internal diameter and wall thickness of pipe/vessels using a conical reflector to direct the sound beam emitted from the axial facing probe, 90°; see Figure 10-2. The setup proposed in the figure would offer a higher accuracy and possibly an easier to implement system for bore form measurement.

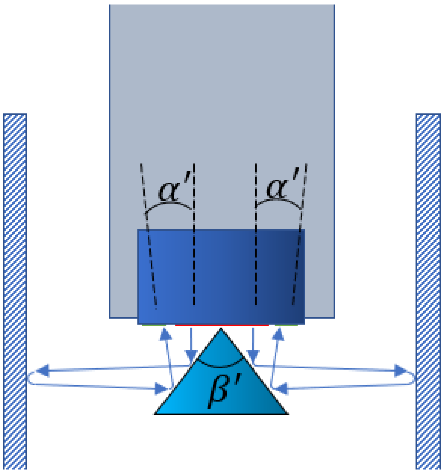

Figure 10-2: Setup with conical reflector (RHS) at the tip of the honing tool or (LHS) at the end of the probe to angle the airborne waves to cylinder wall and measure bore form profile – one axial cross-section at a time. Blue arrows represent the path of ultrasonic wave.

Figure 10-3 shows a modification to the probe proposed by Alvarez-Arenas and Diez (2017) such that higher resolution of the profile is achievable.

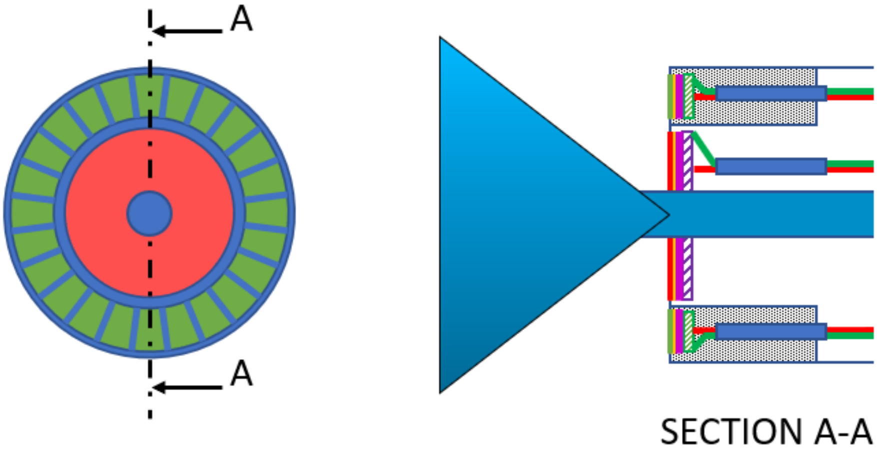

Figure 10-3: Schematic of a probe design which could enable the measurement of bore form, measuring 24 points around the liner.

If the probe is designed with a central section to function as a narrow bandwidth probe with much greater transmission gain, a method such as stepped frequency modulation, such as that presented by Saad et al. (2011) could be implemented to increase the measurement range.

Modifications could be made to the cone structure by replacing it with as many hyperbolic concave reflectors as the number of receiver transducers, to allow the focusing of the sound waves and ensure it is focused into a smaller surface point. Information on such designs can be found in literature (Robertson *et al.*, 2002; Alvarez-Arenas, Camacho and Diez, 2017).

10.3.1.1 Surface Roughness Measurement

While not covered at present, air coupled probes have been used as a surface roughness parameter measurement tool – Rq (Blessing and Eitzen, 1989) and the skewness, Rsk (Saniman *et al.*, 2020). The requirement was for the use of probes in pitch catch mode. Air coupled probes could therefore measure the bore form using arrival time of the echo, while the amplitude of the echo be used to give a reading of the surface roughness of the internal bore surface. The feasibility of using the probes that were manufactured in pitch-catch mode was evaluated by the present author, and is was found that the system worked best when two probes were placed at an angle of 40 degrees. See Figure 10-4.

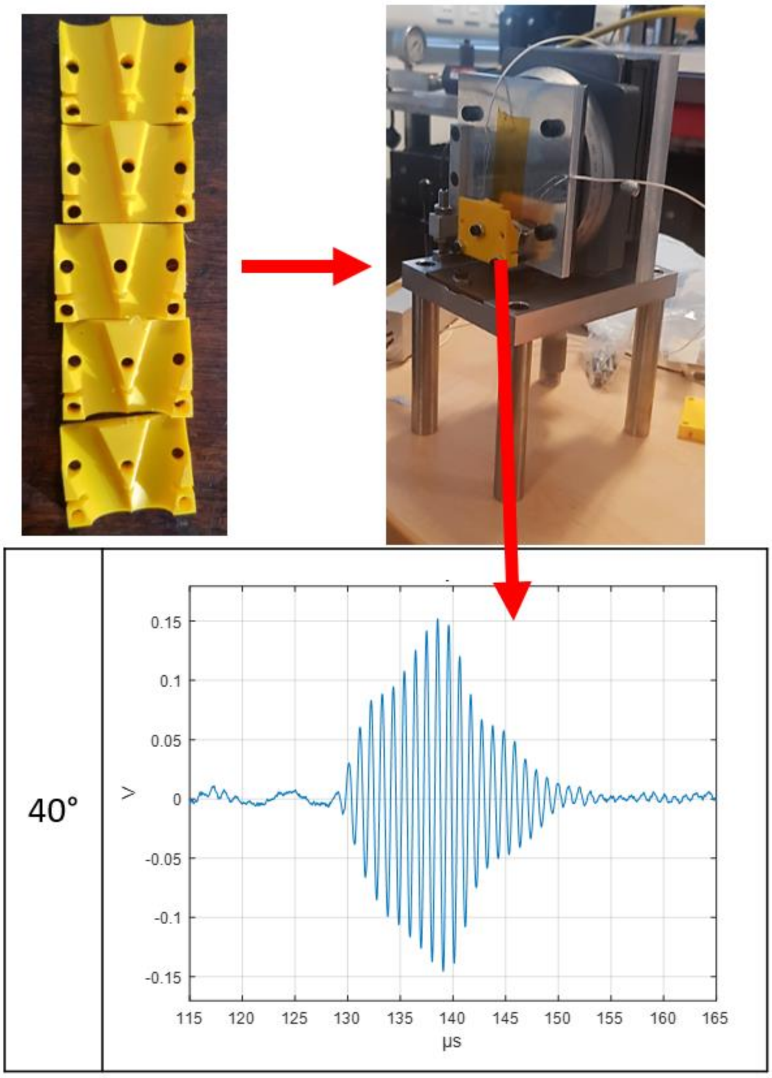

Figure 10-4: Use of manufactured air coupled probes in pitch catch setup

10.4 Bore distortion measurements

As it was mentioned in Chapter 8 (§8.6.3), further work is required to study the effect of stress on the wave propagating through the surface of the liner. A tensile test specimen machined from the same cast iron liner material used could be gauged with piezoceramic transducers and loaded using a tensile test machine. The ultrasonic transducers would perform pitch-catch measurements to measure effect of changing stress on wave propagation velocity, using the same ultrasonic method as the one utilised.

Additional methods could be used, such as using shear horizontal surface waves, and/or strain gauges, to minimise the measurement uncertainty that results from the stress the liner can be subjected to.

10.4.1 Alternative Methods

The work presented showed the feasibility of using one pitch and multiple catch transducers bonded on the liner surface such that they can be used to measure in situ bore distortion without being impacted by the temperature variation. An added complication did however result from the setup, which meant the ultrasound waves had to travel through the interface of the glue as Stoneley waves that are known to be sensitive to the properties of the interface.

A modification could be made to simplify the measurement by placing the receiver transducers either side of emitter transducer as shown in Figure 10-5.

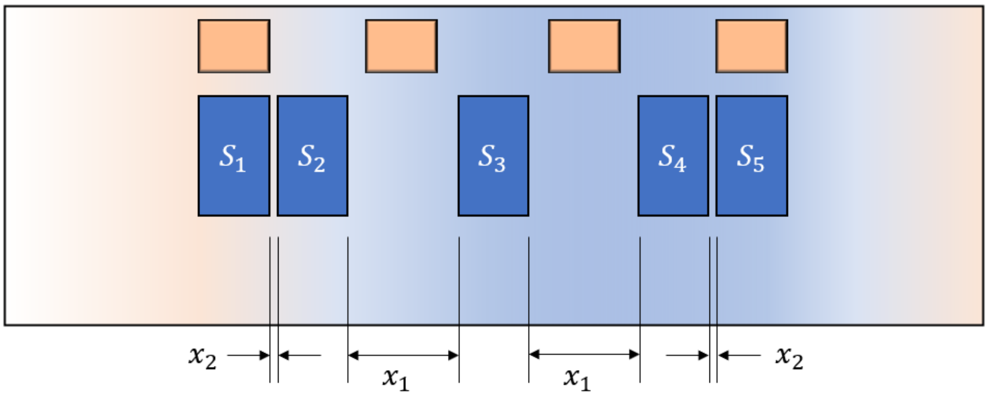

Figure 10-5: Proposed setup of piezoceramic transducers emitting and detecting surface waves.

Figure 10-6 presents another avenue of research where interface waves could be used to measure bore distortion while the wave propagation path is completely isolated from environmental factors. Experiments could be conducted to see if such a mode of wave excitation is possible. On success of the method, a temperature calibration followed by a stress calibration would need to be conducted. Various epoxies could be evaluated to find the one most suitable.

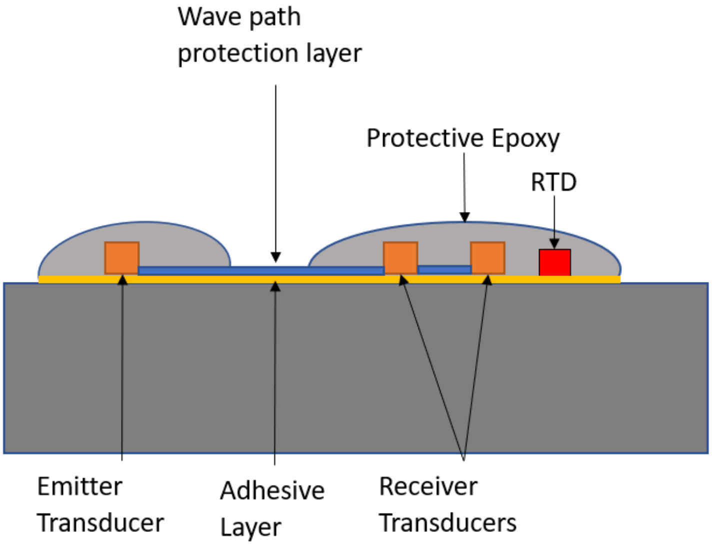

Figure 10-6: Method proposed to use interface waves to measure bore distortion.

11 References

Alshwawra, A. *et al.* (2020) ‘Enhancing the geometrical performance using initially conical cylinder liner in internal combustion engines-A numerical study’, *Applied Sciences (Switzerland)*, 10(11), p. 3705. doi: 10.3390/app10113705.

Alshwawra, A. *et al.* (2021) ‘Increasing the roundness of deformed cylinder liner in internal combustion engines by using a non-circular liner profile’, *International Journal of Engine Research*, 22(4), pp. 1214–1221. doi: 10.1177/1468087419893897.

Álvarez-Arenas, T. E. G. (2004) ‘Acoustic impedance matching of piezoelectric transducers to the air’, *IEEE Transactions on Ultrasonics, Ferroelectrics, and Frequency Control*, 51(5), pp. 624–633. doi: 10.1109/TUFFC.2004.1320834.

Alvarez-Arenas, T. G., Camacho, J. and Diez, L. (2017) ‘Cylindrical and quasi-cylindrical focalization of air-coupled single element and linear array transducers’, in *IEEE International Ultrasonics Symposium, IUS*. IEEE, pp. 1–4. doi: 10.1109/ULTSYM.2017.8092727.

Alvarez-Arenas, T. G. and Diez, L. (2017) ‘Air-coupled and water immersion sectorized array transducers for industrial and medical endoscopy’, in *IEEE International Ultrasonics Symposium, IUS*. IEEE Computer Society. doi: 10.1109/ULTSYM.2017.8091795.

Andersson, P., Tamminen, J. and Sandström, C. E. (2002) ‘Piston ring tribology: A literature survey’, *VTT Tiedotteita - Valtion Teknillinen Tutkimuskeskus*, (2178), pp. 3–105. Available at: https://cris.vtt.fi/en/publications/piston-ring-tribology-a-literature-survey (Accessed: 28 July 2021).

‘ANSI/IEEE Standard on Piezoelectricity’ (1988) *ANSI/IEEE Std 176-1987*, pp. 0_1-. doi: 10.1109/IEEESTD.1988.79638.

Arm, M., Lambert, L. B. and Silverberg, B. (1962) ‘Electro-Optical transfer characteristics of liquid delay-line light modulators’, *1962 IRE National Convention*, pp. 79–89. doi: 10.1109/IRENC.1962.1536166.

Arunachalam, N., Anand Kumar, R. and Ramamoorthy, B. (2011) ‘A preliminary investigation on the application of air-coupled ultrasound to evaluate surface condition of the grinding wheel’, *International Journal of Abrasive Technology*, 4(3), pp. 266–278. doi: 10.1504/IJAT.2011.042823.

Avan, E. Y., Mills, R. and Dwyer-Joyce, R. (2010) ‘Ultrasonic Imaging of the Piston Ring Oil Film During Operation in a Motored Engine-Towards Oil Film Thickness Measurement’, in *SAE International Journal of Fuels and Lubricants*, pp. 786–793. doi: 10.4271/2010-01-2179.

Barbieri, S. G. *et al.* (2019) ‘A Simplified Methodology for the Analysis of the Cylinder Liner Bore Distortion: Finite Element Analyses and Experimental Validations’, in *SAE Technical Papers*. doi: 10.4271/2019-24-0164.

Bass, H. E. *et al.* (1995) ‘Atmospheric absorption of sound: Further developments’, *Journal of the Acoustical Society of America*. Acoustical Society of AmericaASA, pp. 680–683. doi: 10.1121/1.412989.

Berlincourt, D. A., Curran, D. R. and Jaffe, H. (1964) ‘Piezoelectric and Piezomagnetic Materials and Their Function in Transducers’, in Mason, W. P. (ed.) *Physical Acoustics*. Elsevier, pp. 169–

270. doi: 10.1016/b978-1-4832-2857-0.50009-5.

Bernard Jaffe, William R. Cook and Hans Jaffe (1971) *Piezoelectric Ceramics (Non-Metallic Solids)*. Edited by J. . Roberts and P. Poppers. London: Academic Press Inc. (London) LTD. doi: 10.1016/B978-0-12-379550-2.X5001-7.

Bird, L. E. and Gartside, R. M. (2002) 'Measurement of Bore Distortion in a Firing Engine', in *SAE Technical Papers*. SAE International. doi: 10.4271/2002-01-0485.

Birring, A. S. and Kwun, H. (1989) 'Ultrasonic measurement of wear', *Tribology International*, 22(1), pp. 33–37. doi: 10.1016/0301-679X(89)90006-6.

Blessing, G. V. and Eitzen, D. G. (1989) 'Ultrasonic Sensor For Measuring Surface Roughness', in *Surface Measurement and Characterization*. SPIE, p. 281. doi: 10.1117/12.949180.

Blomme, E., Bulcaen, D. and Declercq, F. (2002) 'Air-coupled ultrasonic NDE: Experiments in the frequency range 750 kHz-2 MHz', *NDT and E International*, 35(7), pp. 417–426. doi: 10.1016/S0963-8695(02)00012-9.

Brekhovskikh, L. M. (1960) *Waves in Layered Media*. Edited by D. (translated by) Lieberman, F. . Frenkiel, and G. Temple. London: Academic Press.

Brekhovskikh, Leonid Maksimovich and Godin, Oleg A. (1990) 'Plane Waves in Discretely Layered Fluids', in *Acoustics of Layered Media 1: plane waves and quasi-plane waves.*, pp. 17–40. doi: 10.1007/978-3-642-52369-4_2.

Brekhovskikh, Leonid M. and Godin, O. A. (1990) 'Basic Equations for Wave Processes in Fluids and Solids', in, pp. 1–16. doi: 10.1007/978-3-642-52369-4_1.

Canali, C. *et al.* (1982) 'A Temperature Compensated Ultrasonic Sensor Operating in Air for Distance and Proximity Measurements', *IEEE Transactions on Industrial Electronics*, IE-29(4), pp. 336–341. doi: 10.1109/TIE.1982.356688.

Castillo, M., Acevedo, P. and Moreno, E. (2003) 'KLM model for lossy piezoelectric transducers', *Ultrasonics*, 41(8), pp. 671–679. doi: 10.1016/S0041-624X(03)00101-X.

Chimenti, D. E. (2014) 'Review of air-coupled ultrasonic materials characterization', in *Ultrasonics*. Elsevier, pp. 1804–1816. doi: 10.1016/j.ultras.2014.02.006.

Chittenden, R. J. and Priest, M. (1993) 'Analysis of the piston assembly, bore distortion and future developments', *Tribology Series*, 26(C), pp. 241–270. doi: 10.1016/S0167-8922(08)70014-2.

Claus, R. O. and Kline, R. A. (1979) 'Adhesive bondline interrogation using Stoneley wave methods', *Journal of Applied Physics*, 50(12), pp. 8066–8069. doi: 10.1063/1.325943.

Cramer, O. (1993) 'The variation of the specific heat ratio and the speed of sound in air with temperature, pressure, humidity, and CO2 concentration', *Journal of the Acoustical Society of America*, 93(5), pp. 2510–2516. doi: 10.1121/1.405827.

Dahiya, R. S. and Valle, M. (2014) *Robotic Tactile Sensing: Technologies and System*. London: Springer.

Dahlmann, D. and Denkena, B. (2017) ‘Hybrid tool for high performance structuring and honing of cylinder liners’, *CIRP Annals - Manufacturing Technology*, 66(1), pp. 113–116. doi: 10.1016/j.cirp.2017.04.032.

Davis, J. R., Lampman, S. R. and Zorc, T. B. (eds) (1989) ‘Honing’, in *ASM Handbook, Volume 16 - Machining*. ASM International, pp. 472–491. doi: 10.31399/asm.hb.v16.a0002153.

Deka, M. (1987) ‘AIR-COUPLED ULTRASONIC TRANSDUCER FOR NDE.’, in *Ultrasonics Symposium Proceedings*. IEEE, pp. 543–546. doi: 10.1109/ultsym.1987.199017.

Desilets, C. S. *et al.* (1978) ‘The Design of Efficient Broad-Band Piezoelectric Transducers’, *IEEE Transactions on Sonics and Ultrasonics*, 25(3), pp. 115–125. doi: 10.1109/T-SU.1978.31001.

Dolatabadi, N. *et al.* (2015) ‘A transient tribodynamic approach for the calculation of internal combustion engine piston slap noise’, *Journal of Sound and Vibration*, 352, pp. 192–209. doi: 10.1016/J.JSV.2015.04.014.

Dwyer-Joyce, R. S. (2005) ‘The application of ultrasonic NDT techniques in tribology’, *Proceedings of the Institution of Mechanical Engineers, Part J: Journal of Engineering Tribology*, 219(5), pp. 347–366. doi: 10.1243/135065005X9763.

Dwyer-Joyce, R. S. *et al.* (2006) ‘The Measurement of Liner - Piston Skirt Oil Film Thickness by an Ultrasonic Means’, in *SAE Technical Paper*. doi: 10.4271/2006-01-0648.

EN50324-2 (2002) ‘European Standard, EN50324-2:2002; “Piezoelectric properties of ceramic materials and components. Part 2: Methods of measurement - low power”’, *CENELEC European Committee for Electrotechnical Standardization*, EN 50324-2.

Fahy, F. (2003) *Foundations of Engineering Acoustics*, *Foundations of Engineering Acoustics*. Elsevier Ltd. doi: 10.1016/B978-0-12-247665-5.X5000-0.

Fang, C. *et al.* (2019) ‘Toward fingertip non-contact material recognition and near-distance ranging for robotic grasping’, in *Proceedings - IEEE International Conference on Robotics and Automation (ICRA)*. Institute of Electrical and Electronics Engineers Inc., pp. 4967–4974. doi: 10.1109/ICRA.2019.8793922.

Fang, Y. *et al.* (2017) ‘Review of the use of air-coupled ultrasonic technologies for nondestructive testing of wood and wood products’, *Computers and Electronics in Agriculture*. Elsevier B.V., pp. 79–87. doi: 10.1016/j.compag.2017.03.015.

Farahanchi, F. and Shaw, S. W. (1994) ‘Chaotic and periodic dynamics of a slider-crank mechanism with slider clearance’, *Journal of Sound and Vibration*, 177(3), pp. 307–324. doi: 10.1006/jsvi.1994.1436.

Fox, J. D., Khuri-Yakub, B. T. and Kino, G. S. (1983) ‘HIGH-FREQUENCY ACOUSTIC WAVE MEASUREMENTS IN AIR’, in *Ultrasonics Symposium Proceedings*. IEEE, pp. 581–584. doi: 10.1109/ultsym.1983.198123.

Fujimoto, H. *et al.* (1991) ‘Measurement of cylinder bore deformation during actual operating engines’, in *SAE Technical Papers*. SAE International. doi: 10.4271/910042.

Ghasemi, A. (2012) ‘CAE Simulations for Engine Block Bore Distortion’, in *SAE Technical Paper*.

doi: 10.4271/2012-01-1320.

Goeldel, B. *et al.* (2013) ‘Flexible right sized honing technology for fast engine finishing’, *CIRP Annals*, 62(1), pp. 327–330. doi: 10.1016/J.CIRP.2013.03.075.

Goll, J. H. and Auld, B. A. (1975) ‘Multilayer Impedance Matching Schemes For Broadbanding of Water Loaded Piezoelectric Transducers and High Q Electric Resonators’, *IEEE Transactions on Sonics and Ultrasonics*, 22(1), pp. 52–53. doi: 10.1109/T-SU.1975.30776.

Gómez-Ullate, Y. and De Espinosa, F. M. (2004) ‘Ultrasonic air-coupled metrology of material surfaces’, in *Proceedings - IEEE Ultrasonics Symposium*, pp. 2298–2301. doi: 10.1109/ULTSYM.2004.1418300.

Gómez Álvarez-Arenas, T. E. (2003) ‘A nondestructive integrity test for membrane filters based on air-coupled ultrasonic spectroscopy’, *IEEE Transactions on Ultrasonics, Ferroelectrics, and Frequency Control*, 50(6), pp. 676–685. doi: 10.1109/TUFFC.2003.1209555.

Gómez, T. E. *et al.* (2001) ‘Low-impedance and low-loss customized materials for air-coupled piezoelectric transducers’, *Proceedings of the IEEE Ultrasonics Symposium*, 2, pp. 1077–1080. doi: 10.1109/ULTSYM.2001.991906.

Government, T. U. (2021) *Transitioning to zero emission cars and vans: 2035 delivery plan*. https://www.gov.uk/. Available at: https://www.gov.uk/government/publications/transitioning-to-zero-emission-cars-and-vans-2035-delivery-plan (Accessed: 10 November 2021).

Grandia, W. A. and Fortunko, C. M. (1995) ‘NDE applications of air-coupled ultrasonic transducers’, in *Proceedings of the IEEE Ultrasonics Symposium*. IEEE, pp. 697–709. doi: 10.1109/ultsym.1995.495667.

Grewe, M. G. *et al.* (1992) ‘Acoustic properties of particle/polymer composites for ultrasonic transducer backing applications’, *NDT & E International*, 25(3), p. 149. doi: 10.1016/0963-8695(92)90387-V.

Hayward, G. and Gachagan, A. (1996) ‘An evaluation of 1–3 connectivity composite transducers for air-coupled ultrasonic applications’, *The Journal of the Acoustical Society of America*, 99(4), pp. 2148–2157. doi: 10.1121/1.415402.

Heywood, J. (1988) ‘THERMAL LOADING AND COMPONENT TEMPERATURES’, in *Internal combustion engine fundamentals*. New York, NY: McGraw-Hill Education, p. 699. Available at: https://www.accessengineeringlibrary.com/content/book/9781260116106 (Accessed: 29 July 2021).

Hickling, R. and Marin, S. P. (1986) ‘The use of ultrasonics for gauging and proximity sensing in air’, *Journal of the Acoustical Society of America*, 79(4), pp. 1151–1160. doi: 10.1121/1.393387.

Hill, S. L., Bury, B. and Gray, J. O. (1994) ‘A Multifrequency AM-Based Ultrasonic System for Accuracy Distance Measurement’, *IEEE Transactions on Instrumentation and Measurement*, 43(6), pp. 861–866. doi: 10.1109/19.368084.

Holmberg, K., Andersson, P. and Erdemir, A. (2012) ‘Global energy consumption due to friction in passenger cars’, *Tribology International*, 47, pp. 221–234. doi: 10.1016/j.triboint.2011.11.022.

Hull, D., Kautz, H. and Vary, A. (1985) 'Measurement of ultrasonic velocity using phase-slope and cross-correlation methods'. Available at: https://ntrs.nasa.gov/search.jsp?R=19860028454 (Accessed: 4 August 2021).

Ihara, I. and Takahashi, M. (2007) 'A new method for internal temperature profile measurement by ultrasound', in *Conference Record - IEEE Instrumentation and Measurement Technology Conference*. doi: 10.1109/imtc.2007.379364.

Jahanbin, M. (2021) 'Application of interface guided waves for structural health monitoring of hybrid bonded joints', *IOP Conference Series: Materials Science and Engineering*, 1060(1), p. 012006. doi: 10.1088/1757-899x/1060/1/012006.

Kagnici, F. and Akalin, O. (2014) 'The effect of cylinder bore distortion on lube oil consumption and blow-by', *ASME 2012 11th Biennial Conference on Engineering Systems Design and Analysis, ESDA 2012*, 4(1), p. 011103. doi: 10.1115/ESDA2012-82968.

Kalghatgi, G. (2018) 'Is it really the end of internal combustion engines and petroleum in transport?', *Applied Energy*. Elsevier Ltd, pp. 965–974. doi: 10.1016/j.apenergy.2018.05.076.

Karafotias, G. *et al.* (2018) 'Mid-air tactile stimulation for pain distraction', *IEEE Transactions on Haptics*, 11(2), pp. 185–191. doi: 10.1109/TOH.2017.2781693.

Kaźmierczak, A. (2004) 'Computer simulation of piston-piston ring-cylinder liner coactions in combustion engines', *Proceedings of the Institution of Mechanical Engineers, Part D: Journal of Automobile Engineering*, 218(12), pp. 1491–1501. doi: 10.1243/0954407042707678.

Kelly, S. P., Hayward, G. and Alvarez-Arenas, T. E. G. (2004) 'Characterization and assessment of an integrated matching layer for air-coupled ultrasonic applications', *IEEE Transactions on Ultrasonics, Ferroelectrics, and Frequency Control*, 51(10), pp. 1314–1323. doi: 10.1109/TUFFC.2004.1350960.

Kelly, S. P., Hayward, G. and Gomez, T. E. (2001) 'An air-coupled ultrasonic matching layer employing half wavelength cavity resonance', in *Proceedings of the IEEE Ultrasonics Symposium*, pp. 965–968. doi: 10.1109/ultsym.2001.991880.

van Kervel, S. J. H. and Thijssen, J. M. (1983) 'A calculation scheme for the optimum design of ultrasonic transducers', *Ultrasonics*, 21(3), pp. 134–140. doi: 10.1016/0041-624X(83)90033-1.

Khuri-Yakub, B., Kim, J. and Chou, C. (1988) 'A new design for air transducers', in *IEEE 1988 Ultrasonics Symposium Proceedings*, pp. 503–506.

Kim, G. *et al.* (2019) 'Application of KLM Model for an Ultrasonic Through-Transmission Method', *International Journal of Precision Engineering and Manufacturing*, 20(3), pp. 383–393. doi: 10.1007/S12541-019-00050-Y.

Kim, G. *et al.* (2020) 'Development of phased array ultrasonic system for detecting rail cracks', *Sensors and Actuators, A: Physical*, 311. doi: 10.1016/j.sna.2020.112086.

Kinsler, L. E. . *et al.* (2000) *Fundamentals of Acoustics: Fourth Edition*, *Wiley*. Available at: https://www.amazon.co.uk/Fundamentals-Acoustics-Lawrence-Kinsler/dp/0471847895 (Accessed: 24 September 2020).

Knaus, O. (2017) *AVL EXCITE™ Piston & Rings introduces the new 3D Ring Simulation*, *avl.com*. Available at: https://www.avl.com/-/avl-excite-piston-rings-introduces-the-new-3d-ring-simulati-1 (Accessed: 28 July 2021).

Koch, F., Fahl, E. and Haas, A. (1995) 'A new technique for measuring the deformation of cylinder bores during engine operation', *SAE Technical Papers*, (950540). doi: 10.4271/950540.

Kossoff, G. (1966) 'The Effects of Backing and Matching on the Performance of Piezoelectric Ceramic Transducers', *IEEE Transactions on Sonics and Ultrasonics*, 13(1), pp. 20–30. doi: 10.1109/T-SU.1966.29370.

Krautkrämer, J. and Krautkrämer, H. (1987) *Ultrasonic testing of materials*, *Ultrasonic testing of materials*. Springer-Verlag. doi: 10.1115/1.3167589.

Krautkrämer, J. and Krautkrämer, H. (1990a) 'Transit-Time Methods', in *Ultrasonic Testing of Materials*. Springer Berlin Heidelberg, pp. 222–238. doi: 10.1007/978-3-662-10680-8_12.

Krautkrämer, J. and Krautkrämer, H. (1990b) 'Ultrasonic Waves in Free Space', in *Ultrasonic Testing of Materials*. Springer Berlin Heidelberg, pp. 4–14. doi: 10.1007/978-3-662-10680-8_2.

Krimholtz, R., Leedom, D. A. A. and Matthaei, G. L. L. (1970) 'New equivalent circuits for elementary piezoelectric transducers', *Electronics Letters*, 6(13). doi: 10.1049/el:19700280.

Krynkin, A. (2015) 'MEC6448 - Acoustics: Waves in solids'. Mechanical engineering department, The University of Sheffield, pp. 1–31.

Littlefair, B. *et al.* (2014) 'Transient tribo-dynamics of thermo-elastic compliant high-performance piston skirts', 53(1), pp. 51–70. doi: 10.1007/S11249-013-0243-6.

Lynnworth, L. C. (1965) 'Ultrasonic Impedance Matching from Solids to Gases', *IEEE Transactions on Sonics and Ultrasonics*, pp. 37–48. doi: 10.1109/T-SU.1965.29359.

Maassen, F. *et al.* (2001) 'Analytical and empirical methods for optimization of cylinder liner bore distortion', in *SAE Technical Papers*. SAE International. doi: 10.4271/2001-01-0569.

Magori, V. and Walker, H. (1987) 'Ultrasonic Presence Sensors with Wide Range and High Local Resolution', *IEEE Transactions on Ultrasonics, Ferroelectrics, and Frequency Control*, 34(2), pp. 202–211. doi: 10.1109/T-UFFC.1987.26933.

Marioli, D., Sardini, E. and Taroni, A. (1988) 'Ultrasonic Distance Measurement for Linear and Angular Position Control', *IEEE Transactions on Instrumentation and Measurement*, 37(4), pp. 578–581. doi: 10.1109/19.9817.

Mason, W. P. (1948) *Electromechanical transducers and wave filters*. 2nd edn. New York: D. Van Nostrand Co.

McClure, F. and Tian, T. (2008) *A simplified piston secondary motion model considering the dynamic and static deformation of piston skirt and cylinder bore in internal combustion engines*. SAE Technical Paper.

McCormick, H. and Meara, T. (2002) 'Summary of results of development and validation of hot honing system to provide improved engine performance', in *SAE Technical Papers*. doi:

10.4271/2002-01-3299.

McSkimin, H. J. (1964) 'Ultrasonic Methods for Measuring the Mechanical Properties of Liquids and Solids', in *Physical Acoustics*. Elsevier, pp. 271–334. doi: 10.1016/b978-1-4832-2857-0.50010-1.

Melikov, A. K. *et al.* (1997) 'Air temperature fluctuations in rooms', *Building and Environment*, 32(2), pp. 101–114. doi: 10.1016/S0360-1323(96)00034-0.

Mills, R. and Dwyer-Joyce, R. (2014) 'Ultrasound for the non-invasive measurement of IC engine piston skirt lubricant films', *Proceedings of the Institution of Mechanical Engineers, Part J: Journal of Engineering Tribology*, 228(11), pp. 1330–1340. doi: 10.1177/1350650114538616.

Mills, R. S., Avan, E. Y. and Dwyer-Joyce, R. S. (2012) 'Piezoelectric sensors to monitor lubricant film thickness at piston–cylinder contacts in a fired engine', *Journal of Engineering Tribology*, 227(2), pp. 100–111. doi: 10.1177/135065011246483.

Mohammed, U. A. *et al.* (2015) *Analysis of Parameters Affecting Liner Bore Distortion in DI Diesel Engines*, *SAE Technical Papers*. SAE International. doi: 10.4271/2015-26-0178.Copyright.

Nihtianov, S. (2014) 'Measuring in the Subnanometer range: Capacitive and eddy current Nanodisplacement Sensors', *IEEE Industrial Electronics Magazine*, 8(1), pp. 6–15. doi: 10.1109/MIE.2013.2285240.

Oh, S. J. *et al.* (1995) *Surface Roughness Measurement by Ultrasonic Sensing for In-Process Monitoring*, *Journal of Engineering for Industry*. American Society of Mechanical Engineers Digital Collection. doi: 10.1115/1.2804352.

Papadakis, E. P. (1976) 'Ultrasonic Velocity and Attenuation: Measurement Methods with Scientific and Industrial Applications', in *Physical Acoustics*, pp. 277–374. doi: 10.1016/B978-0-12-477912-9.50010-2.

Pulkrabek, W. (1997) *Engineering Fundamentals of the Internal combustion engine*. Second Edi. Patrice Hall, Upper Saddle River, New Jersey 07458. Available at: https://books.google.co.uk/books?id=LSVuQgAACAAJ.

Queirós, R. *et al.* (2015) 'A multi-frequency method for ultrasonic ranging', *Ultrasonics*, 63, pp. 86–93. doi: 10.1016/j.ultras.2015.06.018.

Reilly, D. and Hayward, G. (1991) 'Through air transmission for ultrasonic non-destructive testing', in *Proceedings - IEEE Ultrasonics Symposium*. Institute of Electrical and Electronics Engineers Inc., pp. 763–766. doi: 10.1109/ULTSYM.1991.234087.

Robertson, T. . J. *et al.* (2002) 'Surface metrology using reflected ultrasonic signals in air', *Ultrasonics*, 39(7), pp. 479–486. doi: 10.1016/S0041-624X(01)00086-5.

Saad, M. M., Bleakley, C. J. and Dobson, S. (2011) 'Robust high-accuracy ultrasonic range measurement system', in *IEEE Transactions on Instrumentation and Measurement*. Institute of Electrical and Electronics Engineers Inc., pp. 3334–3341. doi: 10.1109/TIM.2011.2128950.

San Emeterio, J. L. and Ramos, A. (2004) 'Models for Piezoelectric Transducers Used in Broadband Ultrasonic Applications', in *Piezoelectric Transducers and Applications*. Springer

Berlin Heidelberg, pp. 55–67. doi: 10.1007/978-3-662-05361-4_3.

Saniman, M. N. F. *et al.* (2020) 'Quantitative Roughness Characterization of Non-Gaussian Random Rough Surfaces by Ultrasonic Method Using Pitch-Catch and Pulse-Echo Configurations', *IJMME: International Journal of Mechanical and Mechatronics Engineering*, 20(01), pp. 80–87.

Saniman, M. N. F. and Ihara, I. (2014) 'Application of air-coupled ultrasound to noncontact evaluation of paper surface roughness', in *Journal of Physics: Conference Series*, p. 12016. doi: 10.1088/1742-6596/520/1/012016.

Sasaki, K. *et al.* (2009) 'Air-coupled ultrasonic time-of-flight measurement system using amplitude-modulated and phase inverted driving signal for accurate distance measurements', *IEICE Electronics Express*, 6(21), pp. 1516–1521. doi: 10.1587/elex.6.1516.

Sayers, C. M. and Tait, C. E. (1984) 'Ultrasonic properties of transducer backings', *Ultrasonics*, 22(2), pp. 57–60. doi: 10.1016/0041-624X(84)90022-2.

van Schaik, W. *et al.* (2010) 'High accuracy acoustic relative humidity measurement in duct flow with air', *Sensors*, 10(8), pp. 7421–7433. doi: 10.3390/s100807421.

Schiller, S. *et al.* (1990) 'Novel High-Frequency Air Transducers', in *Review of Progress in Quantitative Nondestructive Evaluation*. Springer US, pp. 795–798. doi: 10.1007/978-1-4684-5772-8_100.

Schindel, D. W. and Hutchins, D. A. (1995) 'Through-thickness characterization of solids by wideband air-coupled ultrasound', *Ultrasonics*, 33(1), pp. 11–17. doi: 10.1016/0041-624X(95)00011-Q.

Schindel, D. W., Hutchins, D. A. and Grandia, W. A. (1996) 'Capacitive and piezoelectric air-coupled transducers for resonant ultrasonic inspection', *Ultrasonics*, 34(6), pp. 621–627. doi: 10.1016/0041-624X(96)00063-7.

Sherrit, S. *et al.* (1999) 'Comparison of the Mason and KLM equivalent circuits for piezoelectric resonators in the thickness mode', in *Proceedings of the IEEE Ultrasonics Symposium*. IEEE, pp. 921–926. doi: 10.1109/ultsym.1999.849139.

Sherrit, S. and Mukherjee, B. K. (2007) 'Characterization of Piezoelectric Materials for Transducers', *arXiv preprint*. Available at: http://arxiv.org/abs/0711.2657.

Silk, M. G. (1984) *Ultrasonic transducers for non-destructive testing*, *NDT & E International*. Bristol: Adam Hilger Ltd. doi: 10.1016/0963-8695(92)90234-8.

Smith, P. T. (2003) *Analysis and Application of Capacitive Displacement Sensors To Curved Surfaces*, *University of Kentucky Master's Thesis*. Available at: https://uknowledge.uky.edu/gradschool_theses/311 (Accessed: 8 December 2020).

Söderfjäll, M. *et al.* (2014) 'The effect of three-dimensional deformations of a cylinder liner on the tribological performance of a piston ring-cylinder liner system', *Proceedings of the Institution of Mechanical Engineers, Part J: Journal of Engineering Tribology*, 228(10), pp. 1080–1087. doi: 10.1177/1350650114529266.

Stor-Pellinen, J. and Luukkala, M. (1995) ‘Paper roughness measurement using airborne ultrasound’, *Sensors and Actuators A: Physical*, 49(1–2), pp. 37–40. doi: 10.1016/0924-4247(95)01011-4.

Sukmana, D. D. and Ihara, I. (2005) ‘Application of Air-Coupled Ultrasound to Noncontact Surface Roughness Evaluation’, *Japanese Journal of Applied Physics*, 44(6B), pp. 4417–4420. doi: 10.1143/jjap.44.4417.

Sukmana, D. D. and Ihara, I. (2007) ‘Quantitative evaluation of two kinds of surface roughness parameters using air-coupled ultrasound’, *Japanese Journal of Applied Physics, Part 1: Regular Papers and Short Notes and Review Papers*, 46(7 B), pp. 4508–4513. doi: 10.1143/JJAP.46.4508.

Takahashi, M. and Ihara, I. (2008a) ‘Ultrasonic Determination of Temperature Distribution in Thick Plates During Single Sided Heating’, *Modern Physics Letters B*, 22(11), pp. 971–976. doi: 10.1142/S0217984908015693.

Takahashi, M. and Ihara, I. (2008b) ‘Ultrasonic monitoring of internal temperature distribution in a heated material’, *Japanese Journal of Applied Physics*, 47(5 PART 2), pp. 3894–3898. doi: 10.1143/JJAP.47.3894.

Takahashi, S. and Ohigashi, H. (2009) ‘Ultrasonic imaging using air-coupled P(VDF/TrFE) transducers at 2 MHz’, *Ultrasonics*, 49(4–5), pp. 495–498. doi: 10.1016/j.ultras.2008.10.020.

Tan, Y. C. and Ripin, Z. M. (2013) ‘Analysis of piston secondary motion’, *Journal of Sound and Vibration*, 332(20), pp. 5162–5176. doi: 10.1016/j.jsv.2013.04.042.

Tanaka, H. *et al.* (2005) ‘Elastic properties of Sn-based Pb-free solder alloys determined by ultrasonic pulse echo method’, *Materials Transactions*, 46(6), pp. 1271–1273. doi: 10.2320/matertrans.46.1271.

Thomas Mase, G. and Johnson, G. C. (1987) ‘An acoustoelastic theory for surface waves in anisotropic media’, *Journal of Applied Mechanics, Transactions ASME*, 54(1), pp. 127–135. doi: 10.1115/1.3172946.

Toda, M. (2002) ‘New type of matching layer for air-coupled ultrasonic transducers’, *IEEE Transactions on Ultrasonics, Ferroelectrics, and Frequency Control*, 49(7), pp. 972–979. doi: 10.1109/TUFFC.2002.1020167.

Toda, M. (2015) ‘Impedance conversion of matching layer for air ultrasonic transducers’, in *2015 IEEE International Ultrasonics Symposium, IUS 2015*. IEEE, pp. 1–4. doi: 10.1109/ULTSYM.2015.0374.

Tolinski, M. and SME Media (2008) *High-Performance Honing*, *sme.org*. Available at: https://www.sme.org/technologies/articles/2008/high-performance-honing/ (Accessed: 24 July 2021).

Tone, M., Yano, T. and Fukumoto, A. (1984) ‘High-Frequency Ultrasonic Transducer Operating in Air’, *Japanese Journal of Applied Physics*, 23(6), pp. L436–L438. doi: 10.1143/JJAP.23.L436.

Wadley, H. N. G. *et al.* (1986) ‘Ultrasonic measurement of internal temperature distribution’, *Philosophical Transactions of the Royal Society of London A*, 320(1554), pp. 341–361. Available at: http://www.jstor.org/stable/37922 (Accessed: 10 August 2017).

Wei, D. *et al.* (2020) ‘A method for reconstructing two-dimensional surface and internal temperature distributions in structures by ultrasonic measurements’, *Renewable Energy*, 150, pp. 1108–1117. doi: 10.1016/j.renene.2019.10.081.

Wu, Q. *et al.* (2016) ‘Air-coupled transducer with a hollow glass microspheres filled epoxy resin matching layer’, in *2016 Symposium on Piezoelectricity, Acoustic Waves, and Device Applications (SPAWDA)*. IEEE, pp. 305–308. doi: 10.1109/SPAWDA.2016.7830011.

Yano, T., Tone, M. and Fukumoto, A. (1987) ‘Range Finding and Surface Characterization Using High-Frequency Air Transducers’, *IEEE Transactions on Ultrasonics, Ferroelectrics, and Frequency Control*, 34(2), pp. 232–236. doi: 10.1109/T-UFFC.1987.26936.

Young, E. H. (1962) ‘Discussion of Time Delay in Reference to Electrical Waves’, *IRE Transactions on Ultrasonic Engineering*, 9(1), pp. 13–20. doi: 10.1109/t-pgue.1962.29282.

Zhmud, B. and Chobany, D. (2020) ‘Mastering the Art of Cylinder Bore Honing’, in *SAE Technical Papers*. SAE International. doi: 10.4271/2020-01-2238.

Zuckerwar, A. J. (1990) ‘Atmospheric absorption of sound: Update’, *Journal of the Acoustical Society of America*. Acoustical Society of AmericaASA, pp. 2019–2021. doi: 10.1121/1.400176.

Appendix A

This section presents the MATLAB functions used for the models used in the thesis. The units of the variables, where not mentioned, are in S.I base units or derived using S.I base units.

Calculate the sound attenuation coefficient in atmosphere, as a function of frequency, pressure, and temperature. The log of alpha is plotted with log of frequency in the literature, which similar graph is present in Chapter 6.

```
function alpha=Attenuation_In_Air(f,T,Ps,h_r)
% alpha =   AttenAir(f,T,Ps,hr)
% alpha =   Attenuation (Np/m)
% f     =   Frequency (Hz)
% T     =   Temperature (°K)
% Ps    =   Atmospheric Pressure (Pa); Ps0=101325
% h_r   =   Relative humidity (Vapour partial pressure/Saturation vapour partial
pressure)
% Source articles
% [1] Bass, H.E., Sutherland, L.C. and Zuckerwar, A.J., 1990.
% Atmospheric absorption of sound: Update. The Journal of the Acoustical
% Society of America, 88(4), pp.2019-2021.
%
% [2] Bass, H.E., Sutherland, L.C., Zuckerwar, A.J., Blackstock, D.T. and
% Hester, D.M., 1995. Atmospheric absorption of sound: Further
% developments. The Journal of the Acoustical Society of America, 97(1),
% pp.680-683.
% [2] used for Psat (corrected from [1] by the authors).

T0      =   293.15;     % Reference Atmospheric Temperature
Ps0     =   101325;     % Reference Atmospheric Pressure (=1 atm)
T01     =   273.16;     % Triple-point Isotherm Temperature

% Saturated Vapour Pressure
Psat    =  Ps0*10^(...
            10.79584*(1-T01/T)-...
            5.02808*log10(T/T01)+1.50474e-4*...
            (1-10^(-8.29692*(T/T01-1) ) )-...
            4.28730e-4*...
            (1-10^(-4.76955*(T/T01-1) ) )-...
            2.21955983);

h       =   h_r*(Psat/Ps0)*(Ps/Ps0); % Humidity

% Relaxation Frequency of Molecular Nitrogen
f_r_N   =   (Ps/Ps0)*(T0/T)^0.5*...
            (   9   +   280*h*exp(-4.17* ((T0/T)^(1/3) -1) )      );

% Relaxation Frequency of Molecular Oxygen
f_r_O   =   (Ps/Ps0)*...
            (   24  +   4.04e4*h*(0.02+h) * (0.391+h)^(-1)     );

% Attenuation coefficient
alpha   =   f.^2.*...
            (...    % bracket1
            1.84e-11*(Ps/Ps0)^(-1).*(T/T0)^0.5+...
            (T/T0)^(-5/2)*...
            (...    % bracket2
            1.278e-2*exp(-2239.1/T)./(f_r_O+f.^2./f_r_O)+...
            1.068e-1*...
            exp(-3352.0/T)./(f_r_N+f.^2./f_r_N)...
            )...    % bracket2
            );      % bracket1
```

```
End
```

MATLAB function to calculate complex velocity and impedance of the elastic layers:

```
function [V_comp,Z_comp,A]  =...
ElasticsCoefficient_Convert2Complex(V,rho,f_r,method,Value)
% Finds the complex velocity and impedance of elastic material to accounts
% for losses within the material from A, or method (see below).
% V,V_comp  = Velocity
% Z_comp    = Specific Impedance
% A         = Attenuation coefficient
% rho       = Density
% f_r       = Frequency (resonant frequency if experimentally measured
%             3db bandwidth (at f_r) is to be used to find Q, then find A).
% method    = Method used:'atten'=  attenuation coefficient'
%                         '3db'  =  3db bandwidth at f_r
%                         'Q'    =  Mechanical quality factor, Q at f_r
% Value     = óValueô of the specified variable of the ómethodô used
% Source article: H.J. McSkimin, Ultrasonic Methods for Measuring the
% Mechanical Properties of Liquids and Solids, pp. 273-274

w_r             =   2*pi*f_r;   % Angular frequency corresponding to f_r

% % % % % % % % % % % % % % % % % % % % % % % % % % % % % % % % % % % % % %
% Find A from method specified
if strcmpi(method,'atten')      ==1 % A specified
        A       =   Value;

% Method that requires Q; if Constraint: Q>10 is satisfied
elseif strcmpi(method,'3db')    ==1    ||      strcmpi(method,'Q')==1

    if strcmpi(method,'3db')    ==1 % 3dB bandwidth from resonant location
        delta_f =   Value;
        Q       =   f_r./delta_f;
    elseif strcmpi(method,'Q')  ==1 % Q specified
        Q       =   Value ;
    else
        error("Specify either 'atten' or '3db' as the method")
    end

    % Calculate Attenuation
    B       =   w_r./V;       % Wave Number
    A       =   B./(2*Q);   % Attenuation
else
        error("Specify either 'atten', '3db' or 'Q' as the method")
end

% % % % % % % % % % % % % % % % % % % % % % % % % % % % % % % % % % % % % %
% Imaginary Elastic Coefficient
E_i         =   (2.*rho.*V.^2.*A.*V./w_r)./...
                (1+A.^2.*V.^2./w_r.^2).^2;
% Real      Elastic Coefficient
E_r         =   rho.*V.^2.*(1-A.^2.*V.^2./w_r.^2)./...
                           (1+A.^2.*V.^2./w_r.^2).^2;
% Complex   Elastic Coefficient
E_comp      =   E_r+1i.*E_i;
% % % % % % % % % % % % % % % % % % % % % % % % % % % % % % % % % % % % % %
% Complex Velocity
V_comp      =   sqrt(E_comp./rho);

% Complex Impedance
Z_comp      =   rho.*V_comp;
End
```

MATLAB function to find the transducer impedance using the KLM model as per Sherrit et al. (1999):

```
function Z=KLM(w,A,rho_0,cD33,espS33,h33,c_0,t_0,c,z,t,num_BL,num_FL)
% Z=KLM(w,A,rho_0,cD33,espS33,h33,c_0,t_0,c,z,t,num_BL,num_FL)
% Output:
%     Z         =   Impedance of the system in frequency domain
% Inputs:
%     w         =   Angular frequency (Hertz).
%     A         =   Probe cross-sectional area (same for all layers) (m^2).
%     rho0      =   Density (kg/m^3).
%     cD33      =   open circuit complex elastic stiffness.
%     espS33    =   clamped complex permittivity.
%     h33       =   piezoelectric deformation constant.
%     c_0       =   open circuit complex wave propagation velocity.
%     t_0       =   Thickness of transducer.
%     c         =   Wave propagation velocity in elastic layers.
%     z         =   Specific acoustic impedance of elastic layers.
%     t         =   Thickness of elastic layers.
%     num_BL    =   Number of Back Layer.
%     num_FL    =   Number of Front Layer.
% All the elastic and electromagnetic constants are complex to account for
% attenuation.
% Reference: Sherrit, S. and Mukherjee, B.K., 2007. Characterization of
% piezoelectric materials for transducers. arXiv preprint arXiv:0711.2657.

% Electrical Impedance of the Transducer
C0          =       espS33.*A./t_0;         % Capacitance
Z_C0        =       1./(1j*w*C0);           % Capacitive Reactance
Z0          =       A.*sqrt(rho_0.*cD33);   % Specific Acoustic Impedance
Gamma       =       w./c_0;                 % The wave number
% % % % % % % % % % % % % % % % % % % % % % % % % % % % % % % % % % % % % %
% KLM - Transducer circuit parameters
M           =       h33./(w.*Z0); % Elastic to electrical Z coupling
X           =       1i * Z0 .* M.^2 .* sin(Gamma*t_0);  % Reactance
Phi         =       1./(2*M) .* ( 1./sin(Gamma*t_0/2) );% Transformer Ratio


% % % % % % % % % % % % % % % % % % % % % % % % % % % % % % % % % % % % % %
% Input impedances of the front and back elastic layers conversion into one
% back and one front lumped components

% Back layers
Z_b_in          =   z{end}*A;
if num_BL>1
    for n       =   (num_FL+num_BL)-1:-1:num_FL+1
        Gamma_  =   w./c{n};
        Z_b_in  =   Imped_Input(Z_b_in,z{n}*A,t(n),Gamma_);
    end
end

% Front layers
Z_f_in          =   z{1}*A;
if num_FL>1
    for n       =   2:(num_FL+num_BL)-num_BL
        Gamma_  =   w./c{n};
        Z_f_in  =   Imped_Input(Z_f_in,z{n}*A,t(n),Gamma_);
    end
end

% % % % % % % % % % % % % % % % % % % % % % % % % % % % % % % % % % % % % %
```

```
% Input impedance of front side
Z_TR        =       Imped_Input(Z_f_in,Z0,t_0/2,Gamma);

% Input impedance of the back side
Z_TL        =       Imped_Input(Z_b_in,Z0,t_0/2,Gamma);

% Total input impedance of the elastic layers including transducer
Zm          =       ZCombP(Z_TR,Z_TL);

% Corresponding input impedance in the electrical circuit that the probe is
% a part of.
Zm_elec     =       Zin_transformer(Zm,1,Phi);

% Impedance of the electronic counterparts in the KLM model
Ze          =       Z_C0+X;

% Input impedance of the whole probe at the electrical terminals
Z           =       Ze+Zm_elec;
end

% % % % % % % % % % % % % % % % SUB-FUNCTIONS % % % % % % % % % % % % % % %
% Input Impedance Calculation function
function Z_in   =   Imped_Input(Z_in_infront,Zc,d,Gamma)
Num         =       Z_in_infront +       1i*Zc.*tan(Gamma.*d);
Denom       =       Zc +       1i*Z_in_infront.*tan(Gamma.*d);
Z_in        =       Zc.*Num./Denom; % Input impedance including the layer
end

% Lumped impedance of parallel electronic circuit components
function Zp =       ZCombP(Z1,Z2)
Zp          =       (Z1.*Z2)./(Z1+Z2);
end

% Electrical impedance coupled using a perfect transformer
function Z1 =       Zin_transformer(Z2,N1,N2)
Z1          =       (N1./N2).^2.*Z2;
End
```

MATLAB function to find the transducer impedance using the KLM model as per Van Kervel (1983) for a probe with two front matching layers and one backing:

```
function [Ht,Hr,Htr,Ze]=...
        KLM_Kervel(f,Phi,C0,X,Zt,Zb,Z0,Z1,Z2,t0,t1,t2,v0,v1,v2,varargin)
% [Nt,Ht,Hr,Htr,Ze]=KLM_Kervel(f,Phi,C0,X,Zt,Zb,Z0,Z1,Z2,t0,t1,t2,v0,v1,v2)
% Output:
%     Ht        =   Transfer function for transmission
%     Hr        =   Transfer function for reception
%     Htr       =   Transfer function for round trip
%     Ze        =   Impedance of the system in frequency domain
% Inputs:
%     w         =   Angular frequency (Hertz).
%     A         =   Probe cross-sectional area (same for all layers) (m^2).
%     rho0      =   Density (kg/m^3).
%     cD33      =   open circuit complex elastic stiffness.
%     espS33    =   clamped complex permittivity.
%     h33       =   piezoelectric deformation constant.
%     c_0       =   open circuit complex wave propagation velocity.
%     t_0       =   Thickness of transducer.
%     c         =   Wave propagation velocity in elastic layers.
%     z         =   Specific acoustic impedance of elastic layers.
%     t         =   Thickness of elastic layers.
%     num_BL    =   Number of Back Layer.
```

```
%     num_FL    =   Number of Front Layer.

% trig and hyperbolic variables
tao0        =   t0./(2*v0); % time delay in transducer half layer
tao1        =   t1./(v1);   % time delay in first matching layer
tao2        =   t2./(v2);   % time delay in second matching layer

p           =   1i*f*2*pi;

% Input impedance of the backing combined with transducer half-layer
Num         =   Z0.*sinh(p.*tao0)     +       Zb.*cosh(p.*tao0);
Denom       =   Z0.*cosh(p.*tao0)     +       Zb.*sinh(p.*tao0);
ZL          =   Z0.*Num./Denom; % Input impedance including the layer

% Transfer matrix: Storage variables
Nem         =   zeros(2,2,numel(f));  % transducer and backing
Nf          =   zeros(2,2,numel(f));  % front layers

% Transfer matrix: transducer and backing
Nem(1,1,:)  =   1./Phi;
Nem(1,2,:)  = -(C0+X)./(p.*C0.*X.*Phi);
Nem(2,1,:)  =  -1./(Phi.*ZL);
Nem(2,2,:)  =   Phi+(C0+X)./(p.*C0.*X.*Phi.*ZL);

% Transfer matrix: Front Acoustic Layers
sh0=sinh(p*tao0);     ch0=cosh(p*tao0);
sh1=sinh(p*tao1);     ch1=cosh(p*tao1);
sh2=sinh(p*tao2);     ch2=cosh(p*tao2);
c0 =cosh(p*tao0);     c2 =cosh(p*tao2);

% element 11
Nf(1,1,:)=        ch1.*ch2.*ch0+...
        (Z2./Z1).*ch0.*sh1.*sh2+...
        (Z1./Z0).*ch2.*sh0.*sh1+...
        (Z2./Z0).*ch1.*sh0.*sh2;

% element 12
Nf(1,2,:)=   -Z0*sh0.*ch1.*ch2-...
    (Z0*Z2./Z1).*sh1.*sh2.*sh0-...
            (Z1)*sh1.*ch0.*ch2-...
            (Z2)*sh2.*ch1.*c0;

% element 21
Nf(2,1,:)= -(1./Z2)*ch1.*ch0.*sh2-...
            (1./Z1)*sh1.*ch0.*c2-...
            (1./Z0)*sh0.*ch1.*ch2-...
     (Z1./(Z2.*Z0))*sh0.*sh1.*sh2;

% element 22
Nf(2,2,:)=           ch0.*ch1.*ch2+...
            (Z1./Z2)*ch0.*sh1.*sh2+...
            (Z0./Z2)*ch1.*sh0.*sh2+...
            (Z0./Z1)*ch2.*sh1.*sh0;

% Full Transfer Matrix: Storage variable
Nt      =   complex(zeros(2,2,size(Nf,3)));

% Full Transfer Matrix: For each frequency
for pp=1:size(Nf,3)
    Nt(:,:,pp)    =  Nf(:,:,pp)*Nem(:,:,pp);
end

% Full Transfer Matrix: separate variables
N11     =   squeeze(Nt(1,1,:));
N12     =   squeeze(Nt(1,2,:));
N21     =   squeeze(Nt(2,1,:));
```

```
N22     =   squeeze(Nt(2,2,:));
Zt      =   Zt(:);

% Impedance of the transducer
Ze      =   (N22.*Zt-N12)./(N11-N21.*Zt);

% Transfer functions
Ht      =   2*Zt ./  (-Ze.*Zt.*N21 + Ze.*N11 - N12 + Zt.*N22); % Transmission
Hr      =   2*Ze ./  (-Ze.*Zt.*N21 + Ze.*N11 - N12 + Zt.*N22); % Reception
Htr     =   4*Ze.*Zt./(Ze.*Zt.*N21 - Ze.*N11 + N12 - Zt.*N22).^2; % Round-trip

end
```

The MATLAB code used to obtain the piezoceramic transducer material parameters from the PI catalogue is as follows:

```
function pzt=ImportPiezoData
% References
% Bernard Jaffe, W.R Cook Jr., H. Jaffe, 1971, Piezoelectric ceramics
% (Non-metallic solids), Academic Press Inc, London, ISBN:0123795508.
% Berlincourt, 1964, Piezoelectric and Piezomagnetic Materials and Their
% Function in Transducers in Physical Acoustics, Volume 1, Part A, pp.
% 169-270.
% Sherrit, S., Leary, S.P., Dolgin, B.P., Bar-Cohen, Y., 1999. Comparison
% of the Mason and KLM equivalent circuits for piezoelectric resonators in
% the thickness mode, in: Proceedings of the IEEE Ultrasonics Symposium.
% IEEE, pp. 921ï926.
% ANSI/IEEE Standard on Piezoelectricity, 1988. . ANSI/IEEE Std 176-1987
% 0_1-. https://doi.org/10.1109/IEEESTD.1988.79638
% Material data corresponding to PIC255 is used.

%% Imported material parameters
esp_0       =   8.85418782e-12; % permittivity of free space

rho         =   7800;           % density

% % % % % % % % % % % % % % % % % % % % % % % % % % % % % % % % % % % % % %
% Permittivity - Constant elastic stress boundary condition
espT        =   zeros(3,3);
espT(3,3)   =   1750.*esp_0;
espT(1,1)   =   1650.*esp_0;
espT(2,2)   =   espT(1,1);

% % % % % % % % % % % % % % % % % % % % % % % % % % % % % % % % % % % % % %
% phase angle between real and imaginary components of piezo parameters
% small angle approximations of trig functions used
tanDde      =   20e-3;          % Dielectric phase angle
Qm          =   80;             % Elastic
tanQme      =   1./Qm;          % Elastic phase angle

% % % % % % % % % % % % % % % % % % % % % % % % % % % % % % % % % % % % % %
% piezoelectric coupling coefficients
k           =   zeros(3,6);
k(3,1)      =  -0.35;
k(3,2)      =   k(3,1);         % (Berlincourt, 1964)
k(3,3)      =   0.69;           % Bar - Longitudinal axial mode
k(1,5)      =   0.66;           % Plate - Transverse Thickness Mode
k(2,4)      =   k(1,5);         % (Berlincourt, 1964)
kp          =  -0.62;           % Radial
kt          =   0.47;           % Plate - Longitudinal Thickness Mode

% % % % % % % % % % % % % % % % % % % % % % % % % % % % % % % % % % % % % %
% Piezoelectric constant
```

```
d           =   zeros(3,6);
d(3,1)      =  -180*10^-12;
d(3,2)      =   d(3,1);         % (Berlincourt, 1964, pp.174, eq.75)
d(3,3)      =   400*10^-12;
d(1,5)      =   550*10^-12;
d(2,4)      =   d(1,5);         % (Berlincourt, 1964, pp.174, eq.75)

% % % % % % % % % % % % % % % % % % % % % % % % % % % % % % % % % % % % % %
% Elastic Compliance - Short circuit electrode boundary condition
sE          =   zeros(6,6);

sE(1,1)     =   16.1*10^-12;

% poissons ratio (Berlincourt, 1964, pp.191, obtained by rearranging eq.33)
Sigma(1,1)  =   1-2./(kp./k(3,1)).^2;
sE(1,2)     =  -Sigma.*sE(1,1); % (Berlincourt, 1964, pp.191, rearranged eq.33)

% Predicting sE13 assuming same ratio as sE(1,2) times a certian factor
sE12_Bcourt =  -5.74*10^-12;
sE13_Bcourt =  -7.22*10^-12;
ScaleFactor =   0.98505;        % obtained from iteration, set as 1 at st
sE(1,3)     =   sE13_Bcourt.*(sE(1,2)./sE12_Bcourt)*ScaleFactor;

sE(2,3)     =   sE(1,3);        % (Berlincourt, 1964, pp.177)
sE(2,2)     =   sE(1,1);        % (Berlincourt, 1964, pp.177)
sE(3,3)     =   20.7*10^-12;
sE(5,5)     =   (d(1,5)./k(1,5)).^2./espT(1,1);% (Berlincourt, 1964, %pp.191,
rearranged eq.33)
sE(4,4)     =   sE(5,5);        % (Berlincourt, 1964, pp.177)
sE(6,6)     =   2*(sE(1,1)-sE(1,2)); % (Berlincourt, 1964, pp.177)
sE(3,1)     =   sE(1,3);        % symmetrical about diagonal
sE(2,1)     =   sE(1,2);        % symmetrical about diagonal
sE(3,2)     =   sE(2,3);        % symmetrical about diagonal
% % % % % % % % % % % % % % % % % % % % % % % % % % % % % % % % % % % % % %
% Elastic Compliance - Open circuit electrode boundary condition
sD          =   zeros(6,6);
sD(3,3)     =   sE(3,3).*(1 - k(3,3).^2); % (Jaffe 1971, pp. 284-287)
sD(1,1)     =   sE(1,1).*(1 - k(3,1).^2); % (Jaffe 1971, pp. 284-287)
sD(2,2)     =   sD(1,1);        % (Berlincourt, 1964, pp.177)
sD(1,2)     =   sE(1,2) - k(3,1).^2.*sE(1,1); % (Jaffe 1971, pp. 284-287)
sD(1,3)     =   sE(1,3) - d(3,1).*d(3,3)./espT(3,3); % (Jaffe 1971, %pp. %284-287)
sD(5,5)     =   sE(5,5).*(1-k(1,5).^2); % (Jaffe 1971, pp. 284-287)
sD(4,4)     =   sD(5,5);        % (Berlincourt, 1964, pp.177)
sD(2,3)     =   sD(1,3);        % (Berlincourt, 1964, pp.177)
sD(6,6)     =   sE(6,6);        % (Berlincourt, 1964, pp.202)
sD(3,1)     =   sD(1,3);        % symmetrical about diagonal
sD(2,1)     =   sD(1,2);        % symmetrical about diagonal
sD(3,2)     =   sD(2,3);        % symmetrical about diagonal
% % % % % % % % % % % % % % % % % % % % % % % % % % % % % % % % % % % % % %
% Permittivity - Clamped dielectric boundary condition

% (Berlincourt, 1964, pp.193)/(Jaffe, 1971)
A           =   sqrt(2).*sE(1,3)./sqrt(sE(3,3).*(sE(1,1)+sE(1,2)));
B           =   sE(1,3)./sqrt(sE(3,3).*sE(1,1));

%% From sD, sE, espT to cD, cE, BT
% As per Berlincourt (1964, pp.189, eq.25)

BT          =   InvertData(espT);   % convert using sub-function
cD          =   InvertData(sD);     % convert using sub-function
cE          =   InvertData(sE);     % convert using sub-function

%% Find piezo constants e, g, and h
```

```
% from 1987 -179-1987 IEEE standard on piezoelectricity, pp. 10, eq(43)

e           =   zeros(3,6);
g           =   zeros(3,6);
h           =   zeros(3,6);

for pp=1:6
    for ii=1:3
        e(ii,pp) =   sum(arrayfun(@(qq) cE(qq,pp).*...
            d(ii,qq),1:6));
    end
end

for pp=1:6
    for ii=1:3
        g(ii,pp) =   sum(arrayfun(@(qq) BT(ii,qq).*...
            d(qq,pp),1:3));
    end
end

for pp=1:6
    for ii=1:3
        h(ii,pp)    =   sum(arrayfun(@(qq) g(ii,qq).*...
            cD(qq,pp),1:6));
    end
end

%% BS and espS
BS          =   zeros(3,3);
espS        =   zeros(3,3);

% 1987 -179-1987 IEEE standard on piezoelectricity, pp. 10, eq(43)
for jj  =   1:3
    for ii =    1:3
        BS(ii,jj)   =   sum(arrayfun(@(qq) BT(ii,jj)+...
                        g(ii,qq).*h(jj,qq),1:6));
    end
end

% (Jaffe, 1971)
espS(3,3)   =   espT(3,3).*(1-(kp.^2+k(3,3).^2+...
                2*A.*abs(kp.*k(3,3)))./(1-A.^2));
espS(1,1)   =   squeeze((d(1,5)./sqrt(espT(1,1).*sE(4,4))./...
                h(1,5)).^2.*cD(4,4));
espS(2,2)   =   espS(1,1);

%% Convert transducer parameters real to complex
pzt.cD33    =   cD(3,3).*  (1+1i.*tanQme);
pzt.espS33  =   espS(3,3).*(1-1i*tanDde);

% % Find complex kt and h33
pzt.e33     =   kt.*sqrt(abs(pzt.cD33).*abs(pzt.espS33)).*...
                exp(1i*(tanQme+tanDde)/2); % (Sherrit, 1999)
pzt.h33     =   abs(pzt.e33)./abs(pzt.espS33).*...
                exp(1i*(tanQme-tanDde)/2); % (Sherrit, 1999)
pzt.kt      =   pzt.h33.*sqrt(pzt.espS33./pzt.cD33);  % (Sherrit, 1999)

% Velocity and Specific Acoustic Impedance
pzt.vD      =   sqrt(pzt.cD33./rho);
pzt.z       =   rho.*pzt.vD;
end
```

Appendix B

Flow chart to convert the properties of a piezoceramic transducer into its complex counterparts:

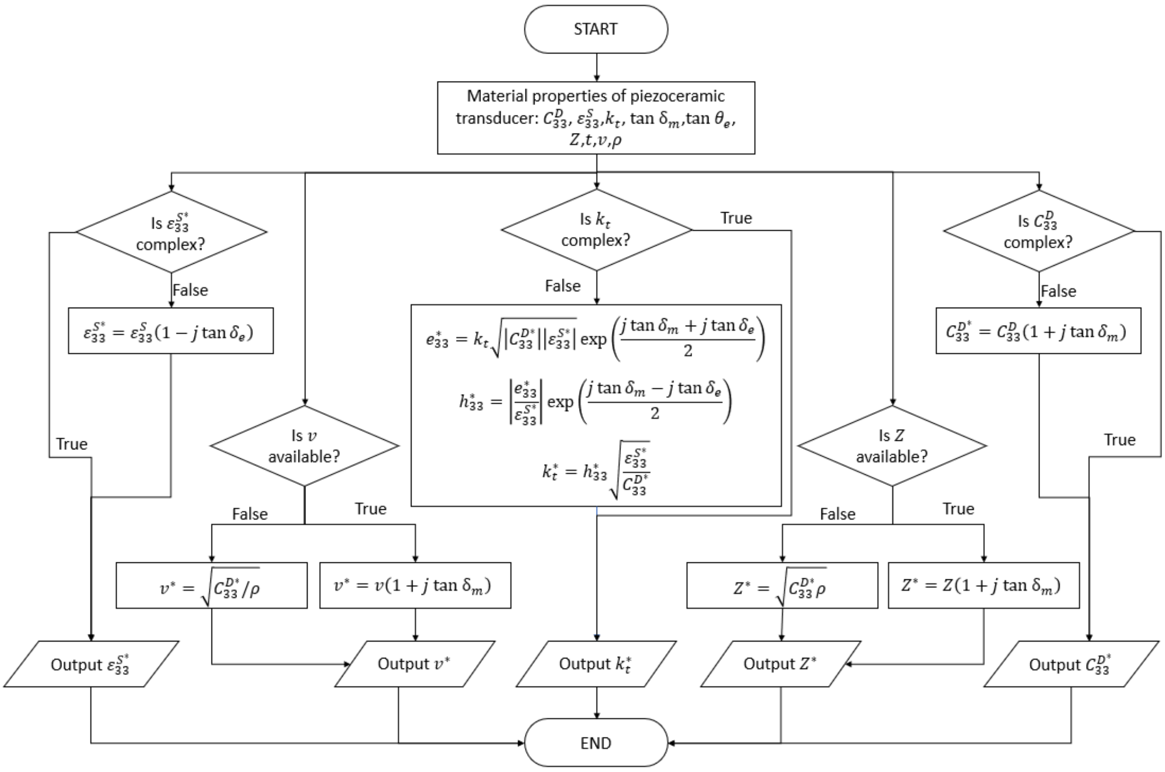

Flow chart to convert the properties of a physical layer into its complex counterpart:

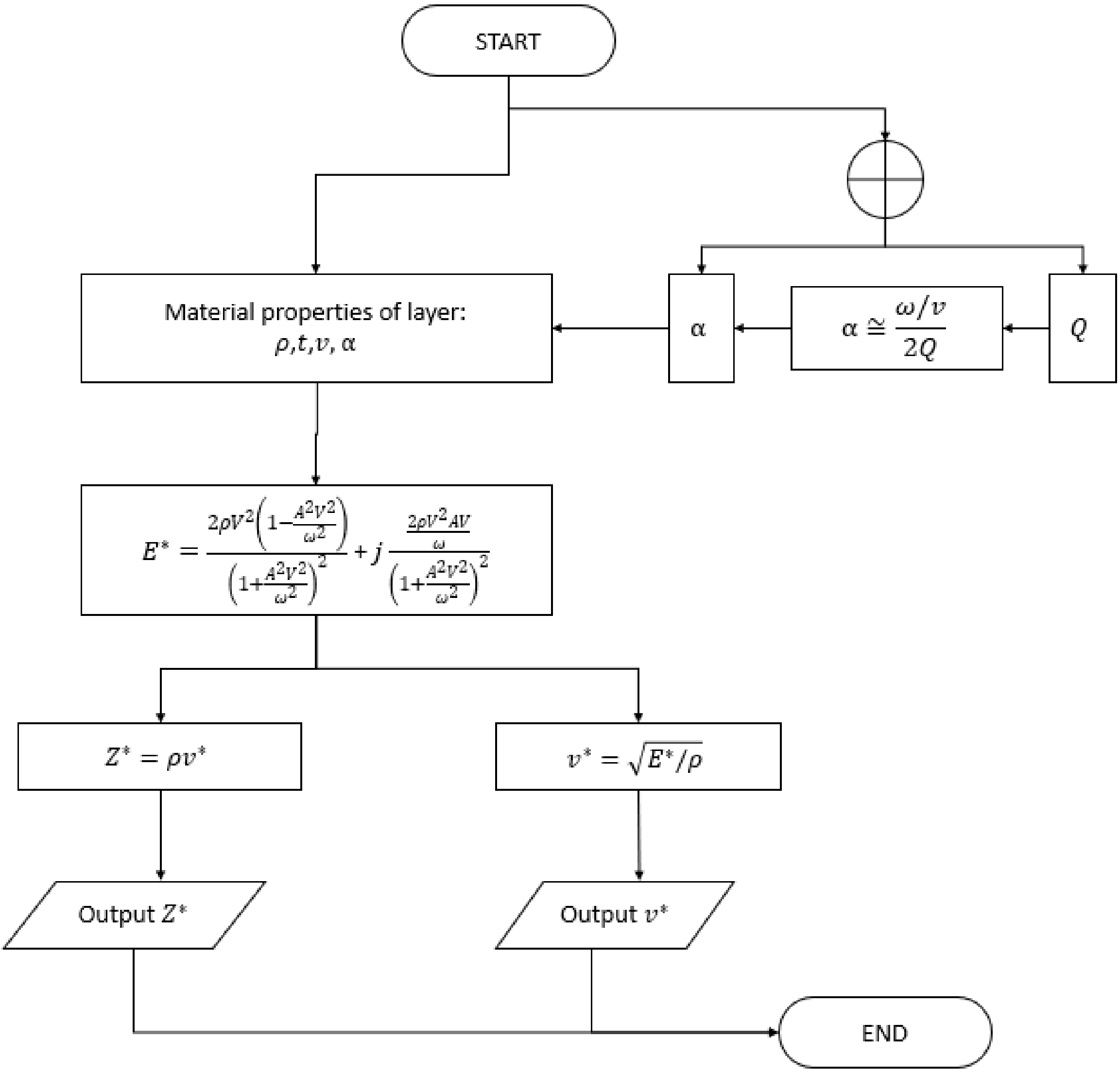

Appendix C

Assembly drawing of the in-situ bore form measurement rig:

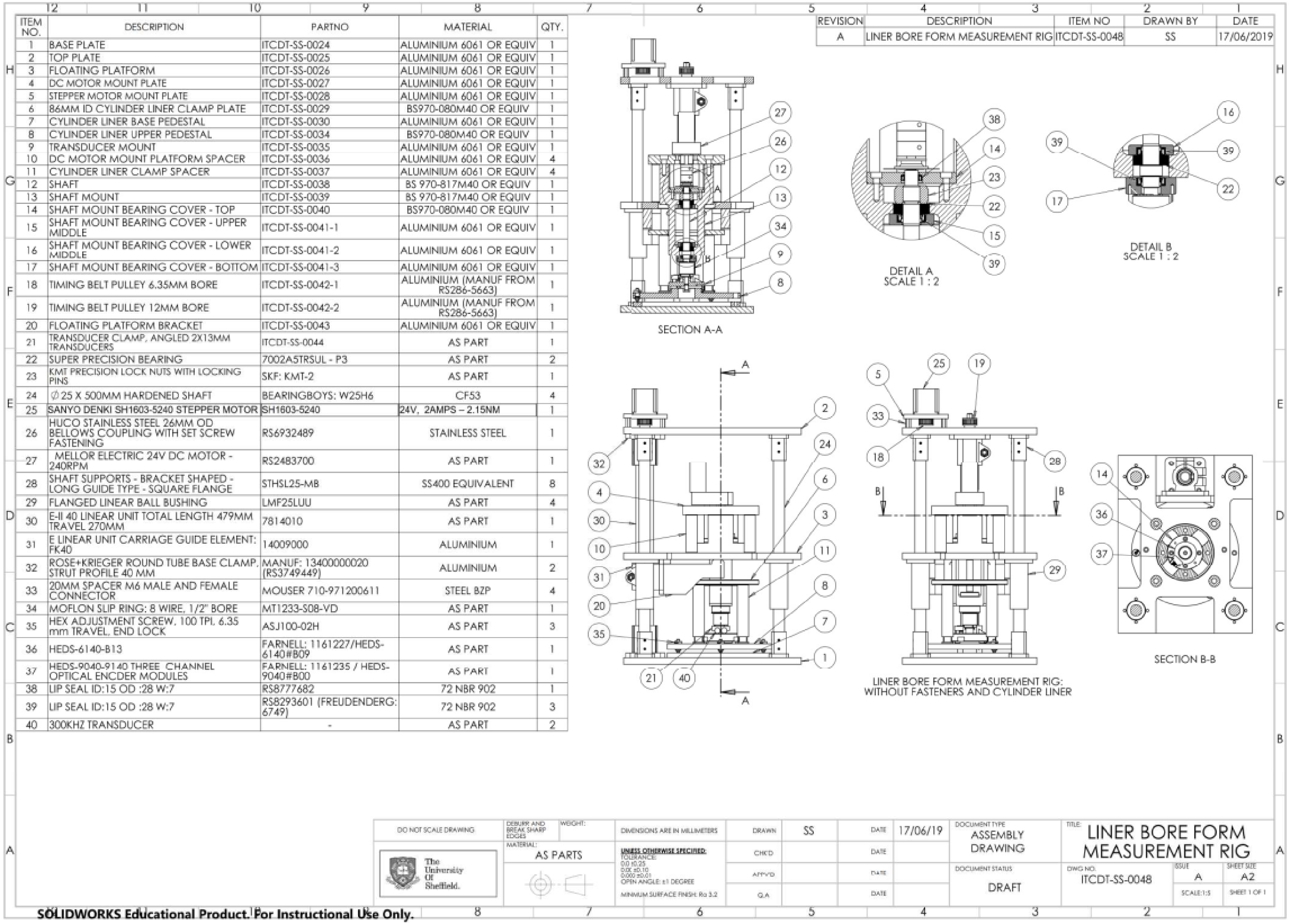

ITEM NO.	DESCRIPTION	PARTNO	MATERIAL	QTY.
1	BASE PLATE	ITCDT-SS-0024	ALUMINIUM 6061 OR EQUIV	1
2	TOP PLATE	ITCDT-SS-0025	ALUMINIUM 6061 OR EQUIV	1
3	FLOATING PLATFORM	ITCDT-SS-0026	ALUMINIUM 6061 OR EQUIV	1
4	DC MOTOR MOUNT PLATE	ITCDT-SS-0027	ALUMINIUM 6061 OR EQUIV	1
5	STEPPER MOTOR MOUNT PLATE	ITCDT-SS-0028	ALUMINIUM 6061 OR EQUIV	1
6	86MM ID CYLINDER LINER CLAMP PLATE	ITCDT-SS-0029	BS970-080M40 OR EQUIV	1
7	CYLINDER LINER BASE PEDESTAL	ITCDT-SS-0030	ALUMINIUM 6061 OR EQUIV	1
8	CYLINDER LINER UPPER PEDESTAL	ITCDT-SS-0034	BS970-080M40 OR EQUIV	1
9	TRANSDUCER MOUNT	ITCDT-SS-0035	ALUMINIUM 6061 OR EQUIV	1
10	DC MOTOR MOUNT PLATFORM SPACER	ITCDT-SS-0036	ALUMINIUM 6061 OR EQUIV	4
11	CYLINDER LINER CLAMP SPACER	ITCDT-SS-0037	ALUMINIUM 6061 OR EQUIV	4
12	SHAFT	ITCDT-SS-0038	BS 970-817M40 OR EQUIV	1
13	SHAFT MOUNT	ITCDT-SS-0039	BS 970-817M40 OR EQUIV	1
14	SHAFT MOUNT BEARING COVER - TOP	ITCDT-SS-0040	BS970-080M40 OR EQUIV	1
15	SHAFT MOUNT BEARING COVER - UPPER MIDDLE	ITCDT-SS-0041-1	ALUMINIUM 6061 OR EQUIV	1
16	SHAFT MOUNT BEARING COVER - LOWER MIDDLE	ITCDT-SS-0041-2	ALUMINIUM 6061 OR EQUIV	1
17	SHAFT MOUNT BEARING COVER - BOTTOM	ITCDT-SS-0041-3	ALUMINIUM 6061 OR EQUIV	1
18	TIMING BELT PULLEY 6.35MM BORE	ITCDT-SS-0042-1	ALUMINIUM (MANUF FROM RS286-5663)	1
19	TIMING BELT PULLEY 12MM BORE	ITCDT-SS-0042-2	ALUMINIUM (MANUF FROM RS286-5663)	1
20	FLOATING PLATFORM BRACKET	ITCDT-SS-0043	ALUMINIUM 6061 OR EQUIV	1
21	TRANSDUCER CLAMP, ANGLED 2X13MM TRANSDUCERS	ITCDT-SS-0044	AS PART	1
22	SUPER PRECISION BEARING	7002A5TRSUL - P3	AS PART	2
23	KMT PRECISION LOCK NUTS WITH LOCKING PINS	SKF: KMT-2	AS PART	1
24	∅ 25 X 500MM HARDENED SHAFT	BEARINGBOYS: W25H6	CF53	4
25	SANYO DENKI SH1603-5240 STEPPER MOTOR	SH1603-5240	24V, 2AMPS – 2.15NM	1
26	HUCO STAINLESS STEEL 26MM OD BELLOWS COUPLING WITH SET SCREW FASTENING	RS6932489	STAINLESS STEEL	1
27	MELLOR ELECTRIC 24V DC MOTOR - 240RPM	RS2483700	AS PART	1
28	SHAFT SUPPORTS - BRACKET SHAPED - LONG GUIDE TYPE - SQUARE FLANGE	STHSL25-MB	SS400 EQUIVALENT	8
29	FLANGED LINEAR BALL BUSHING	LMF25LUU	AS PART	4
30	E-II 40 LINEAR UNIT TOTAL LENGTH 479MM TRAVEL 270MM	7814010	AS PART	1
31	E LINEAR UNIT CARRIAGE GUIDE ELEMENT: FK40	14009000	ALUMINIUM	1
32	ROSE+KRIEGER ROUND TUBE BASE CLAMP, STRUT PROFILE 40 MM	MANUF: 13400000020 (RS3749449)	ALUMINIUM	2
33	20MM SPACER M6 MALE AND FEMALE CONNECTOR	MOUSER 710-971200611	STEEL BZP	4
34	MOFLON SLIP RING: 8 WIRE, 1/2" BORE	MT1233-S08-VD	AS PART	1
35	HEX ADJUSTMENT SCREW, 100 TPI, 6.35 mm TRAVEL, END LOCK	ASJ100-02H	AS PART	3
36	HEDS-6140-B13	FARNELL: 1161227/HEDS-6140#B09	AS PART	1
37	HEDS-9040-9140 THREE CHANNEL OPTICAL ENCDER MODULES	FARNELL: 1161235 / HEDS-9040#B00	AS PART	1
38	LIP SEAL ID:15 OD :28 W:7	RS8777682	72 NBR 902	1
39	LIP SEAL ID:15 OD :28 W:7	RS8293601 (FREUDENDERG: 6749)	72 NBR 902	3
40	300KHZ TRANSDUCER	-	AS PART	2

REVISION	DESCRIPTION	ITEM NO	DRAWN BY	DATE
A	LINER BORE FORM MEASUREMENT RIG	ITCDT-SS-0048	SS	17/06/2019

DO NOT SCALE DRAWING

The University Of Sheffield.

DEBURR AND BREAK SHARP EDGES

WEIGHT:

MATERIAL: AS PARTS

DIMENSIONS ARE IN MILLIMETERS

UNLESS OTHERWISE SPECIFIED:
TOLERANCE:
0.0 ±0.25
0.0X ±0.10
0.000 ±0.01
OPEN ANGLE: ±1 DEGREE
MINIMUM SURFACE FINISH: Ra 3.2

DRAWN	SS	DATE	17/06/19
CHK'D		DATE	
APP'D		DATE	
Q.A		DATE	

DOCUMENT TYPE: ASSEMBLY DRAWING

DOCUMENT STATUS: DRAFT

TITLE: LINER BORE FORM MEASUREMENT RIG

DWG NO. ITCDT-SS-0048

ISSUE: A

SHEET SIZE: A2

SCALE:1:5

SHEET 1 OF 1

Assembly drawing of the ultrasonic air coupled sensor evaluation rig (transducer beam form test rig). The rig can also measure the beam form, as well as testing the frequency response of air-coupled probes and evaluating the sensor range measurement accuracy. The final rig contains some modified components, although the concept and functionality stayed the same.

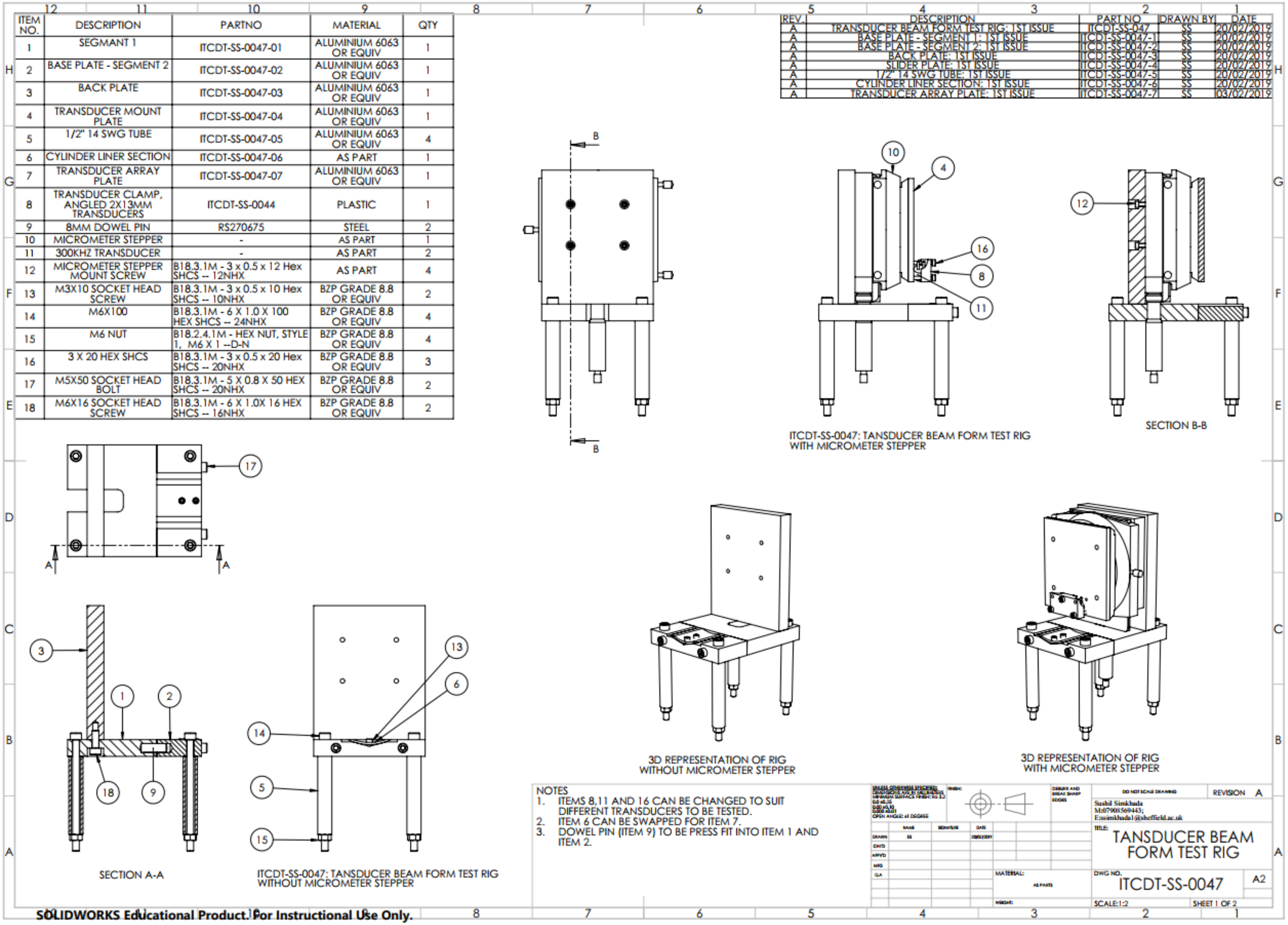

ITEM NO.	DESCRIPTION	PARTNO	MATERIAL	QTY
1	SEGMANT 1	ITCDT-SS-0047-01	ALUMINIUM 6063 OR EQUIV	1
2	BASE PLATE - SEGMENT 2	ITCDT-SS-0047-02	ALUMINIUM 6063 OR EQUIV	1
3	BACK PLATE	ITCDT-SS-0047-03	ALUMINIUM 6063 OR EQUIV	1
4	TRANSDUCER MOUNT PLATE	ITCDT-SS-0047-04	ALUMINIUM 6063 OR EQUIV	1
5	1/2" 14 SWG TUBE	ITCDT-SS-0047-05	ALUMINIUM 6063 OR EQUIV	4
6	CYLINDER LINER SECTION	ITCDT-SS-0047-06	AS PART	1
7	TRANSDUCER ARRAY PLATE	ITCDT-SS-0047-07	ALUMINIUM 6063 OR EQUIV	1
8	TRANSDUCER CLAMP, ANGLED 2X13MM TRANSDUCERS	ITCDT-SS-0044	PLASTIC	1
9	8MM DOWEL PIN	RS270675	STEEL	2
10	MICROMETER STEPPER	-	AS PART	1
11	300KHZ TRANSDUCER	-	AS PART	2
12	MICROMETER STEPPER MOUNT SCREW	B18.3.1M - 3 x 0.5 x 12 Hex SHCS -- 12NHX	AS PART	4
13	M3X10 SOCKET HEAD SCREW	B18.3.1M - 3 x 0.5 x 10 Hex SHCS -- 10NHX	BZP GRADE 8.8 OR EQUIV	2
14	M6X100	B18.3.1M - 6 X 1.0 X 100 HEX SHCS -- 24NHX	BZP GRADE 8.8 OR EQUIV	4
15	M6 NUT	B18.2.4.1M - HEX NUT, STYLE 1, M6 X 1 --D-N	BZP GRADE 8.8 OR EQUIV	4
16	3 X 20 HEX SHCS	B18.3.1M - 3 x 0.5 x 20 Hex SHCS -- 20NHX	BZP GRADE 8.8 OR EQUIV	3
17	M5X50 SOCKET HEAD BOLT	B18.3.1M - 5 X 0.8 X 50 HEX SHCS -- 20NHX	BZP GRADE 8.8 OR EQUIV	2
18	M6X16 SOCKET HEAD SCREW	B18.3.1M - 6 X 1.0X 16 HEX SHCS -- 16NHX	BZP GRADE 8.8 OR EQUIV	2

REV.	DESCRIPTION	PART NO	DRAWN BY	DATE
A	TRANSDUCER BEAM FORM TEST RIG: 1ST ISSUE	ITCDT-SS-047	SS	20/02/2019
A	BASE PLATE - SEGMENT 1: 1ST ISSUE	ITCDT-SS-0047-1	SS	20/02/2019
A	BASE PLATE - SEGMENT 2: 1ST ISSUE	ITCDT-SS-0047-2	SS	20/02/2019
A	BACK PLATE: 1ST ISSUE	ITCDT-SS-0047-3	SS	20/02/2019
A	SLIDER PLATE: 1ST ISSUE	ITCDT-SS-0047-4	SS	20/02/2019
A	1/2" 14 SWG TUBE: 1ST ISSUE	ITCDT-SS-0047-5	SS	20/02/2019
A	CYLINDER LINER SECTION: 1ST ISSUE	ITCDT-SS-0047-6	SS	20/02/2019
A	TRANSDUCER ARRAY PLATE: 1ST ISSUE	ITCDT-SS-0047-7	SS	03/02/2019

NOTES
1. ITEMS 8,11 AND 16 CAN BE CHANGED TO SUIT DIFFERENT TRANSDUCERS TO BE TESTED.
2. ITEM 6 CAN BE SWAPPED FOR ITEM 7.
3. DOWEL PIN (ITEM 9) TO BE PRESS FIT INTO ITEM 1 AND ITEM 2.